Development of Highly Active Internal Steam Methane Reforming Catalysts for Intermediate Temperature Solid Oxide Fuel Cells



Jiexun Di

Department of Engineering Science

Wolfson College

A thesis submitted for degree of Doctor of Philosophy

Michaelmas Term, 2012

Abstract

Fuel processing is one of the essential parts for development of intermediate solid oxide fuel cells (IT-SOFC). Natural gas (methane) is considered as the most abundant and cost effective fuel for the production of hydrogen for IT-SOFC. The primary aim of this thesis is to use a novel precursor material—layered double hydroxide (LDH) – for developing a new type of cost effective, highly active and long lasting catalyst which can reform natural gas in IT-SOFC anode environment. Small amount of noble metals Pd, Rh and Pt are used as promoters to enhance the catalyst's performance as while maintaining the cost relatively low. The research objectives are achieved by a series of studies including catalysts synthesis, characterisation and the catalytic activities.

The thesis initially gives a comprehensive review on fuel cell and SOFC technology, steam methane reforming and reforming catalyst to provide better understanding of the research.

Experimental studies include the effects of the synthetic conditions of the LDH precursors and thermal treatments on the physical, chemical behaviours and catalytic activities of the catalysts and promotional effects by noble metals.

The LDH derived catalysts compositions, promoter quantities and operating conditions are optimised for the best performance in the IT-SOFC anode environment.

A new method for the development of precursor sol for easy coating of the anode is developed and studied. The sol preparation is achieved by acid attack. The sol developed is found to produce better coating and has very high catalytic properties after activation.

The catalysts developed were tested for their stability and self-activation ability to ensure its use in the commercial cells.

The findings of the present study indicate that the catalysts developed show excellent catalytic performance and these catalysts have very high potential for further commercialisation in IT-SOFC.

Statements on originality and intellectual ownership

I declare that the content of this D.Phil thesis is my own work except of the following parts:

- The EDX of as-prepared LDHs were acquired at Oxford Materials Characterisation Service by the employee Mr Chris Salter. The relevant sample preparation and analysis of the data were performed by me. The results were presented in 'actual metal molar ratio' part in Tables 3.1, 5.1 and 6.1.
- The TEM micrographs presented in Figures 3.11, 5.6, 6.11 and 7.2 were performed by Mr Simon Fairclough and me. The relevant sample preparation and analysis of the data were performed by me.
- The elemental mapping presented in Figure 5.7 were acquired by Dr Neil Young and these experiments were performed under 'EPSRC scheme for UK visitors'. The relevant sample preparation and analysis of the data were performed by me.
- The SEM micrographs presented in Figures 3.5, 6.4 and 6.6 were performed by Dr Antal koos and me. The relevant sample preparation and analysis of the data were performed by me.

All the experiments (including the above mentioned ones) in this thesis were designed by me. No part of my thesis have been accepted or is currently being submitted for any degree, diploma or other qualification in this university or elsewhere.

Jiexun Di

Acknowledgements

I would like to express my gratitude and sincere thanks to Professor Ashok Bhattacharya for his sheer determination to offer me the opportunity to carry out research in the field of nanocatalysis at the University of Oxford, the greatest university in the world. I am also thankful for his valuable guidance and considerable support throughout this study. I would like to express my heartfelt thanks to Dr Nicholas Hankins for kindly accepting the request to supervise me in my final year when Professor Bhattacharya's research group moved to another university. During this year, he gave me constant support to my study, which allowed me to complete all remaining experimental work and finish writing the thesis.

My greatest thanks are due to Dr Manickam Jaymurthy. He stood there as a day-to-day supervisor and offered me continuous and comprehensive support during the entire period of my study, including equipment set-up, introducing me to the field, discussing problems and helping in preparation of this thesis, etc. Beside academic aspects, he was always there to advise me a lot even on the daily life which helped me a better living in this country. I also thank other members in the group – Dr Anastasia Pashigreva who shared many personal thoughts and helped me to understand better in some of the research concept and knowledge; Dr David Pyke, Dr Costantinos Komodromos and Dr Adrian Hartridge for sharing their knowledge and expertise on LDH, fuel cell and commercial aspects of catalyst.

I would also like to thank a number of academic personnel and organizations in Oxford, for the advices, expertise and support on my research work. Mr Simon Fairclough, Mr Richard Turner, Dr Antal Koos and Dr Neil Young all from Department of Materials who gave the expertise and helps in TGA, SEM, TEM, and Elemental Mapping; Mr Fred Wondre, Department of Physics, who kindly provided XRD facility in my third year when our own facility was not available; The Oxford EM group who provided training and EM facilities; The 'EPSRC scheme for UK visitors' to provide access and funding for the EDX/Elemental mapping studies.

I am very grateful to Dr Helen Daly and Dr Alexandre Goguet, CenTACat, Queen's University, Belfast. As the hosts, they not only gave me a warm welcome but also patiently and freely provided their expertise and facilities for my DPhil study.

I thank all the people in Oxford University Begbroke Science Park and Wolfson College, Oxford for providing warm, nice, and peaceful environment for my study and life. Without this pleasant environment, I could not have finished my work.

Finally, I would like to give my special thanks my lovely wife, Han, for her love, encouragements and all her sacrifices. During these years, she offered her love and support whenever I need to overcome any difficulties. I would like to record my sincere apology to her for not attending any of her needs during my busy days. This study couldn't have been possible without the love, affection and financial supports from my beloved parents. They always encouraged me in spite of their sufferings for which I do not find an appropriate word to express my feelings.

Dedicated to my outrageously loving and supportive wife, Han and my always encouraging, ever faithful parents, Jilong and Yuzhi.

Contents

Chapter 1. Introduction 1
1.1 Background 2
1.2 Fuel Cells (FCs) 4
1.2.1 Introduction to FCs 4
1.2.2 Electrochemistry aspects 5
1.2.3 Thermodynamic aspects of FC 6
1.2.4 Types of FCs 7
1.3 Solid oxide fuel cell (SOFC) 10
1.3.1 Introduction to SOFC 10
1.3.2 Electrochemistry aspects and cell materials 11
1.3.2.1 Cathode (Air electrode) 12
1.3.2.2 Anode (Fuel electrode) 12
1.3.2.3 Electrolyte 13
1.3.3 Challenges for SOFC 13
1.3.4 Intermediate temperature-SOFC (IT-SOFC) 14
1.3.4.1 Benefits of IT-SOFC 14
1.3.4.2 Development of cell materials for IT-SOFC 15
1.4 Steam methane reforming (SMR) 19
1.4.1 Introduction to SMR 19
1.4.2 Thermodynamic aspects 22
1.4.3 Steam to carbon ratio (S/C ratio) 23
1.5 Catalysts for SMR 24
1.5.1 Fundamentals of catalysis 24
1.5.1.1 Introduction to catalysts 24
1.5.1.2 Heterogeneous catalysis 26
1.5.2 Active metals for SMR reactions 28
1.5.3 Catalyst support 29
1.5.4 Catalyst preparation methods 30
1.5.4.1 Deposition 30
1.5.4.2 Precipitation 31

1.5.4.3 Other methods 32
1.5.5 Impact issues for catalyst performance 32
1.5.6 Catalyst deactivation 33
1.5.6.1 Poisoning 33
1.5.6.2 Sintering 34
1.5.6.3 Oxidation 35
1.5.6.4 Carbon deposition 35
1.5.7 Improvement of catalysts 36
1.6 Layered double hydroxide (LDH) 37
1.6.1 Overview of LDH 37
1.6.2 Advantages of LDH as a catalyst precursor 39
1.6.3 LDH precursors for preparing SMR catalysts 39
1.6.4 Preparation methods 40
1.6.4.1 CP method 41
1.6.4.2 Ion-exchange method 42
1.6.4.3 Rehydration method 43
1.6.5 Takovite 44
1.7 Scope of the thesis 46
1.7.1 Research objectives 46
1.7.2 Structure of this thesis 48
Chapter 2. General experimental methods 50
2.1 Introduction 51
2.2 Preparation of LDHs 51
2.2.1 Preparation of Ni/Al LDHs 51
2.2.1.1 Mixing 52
2.2.1.2 Aging 52
2.2.1.3 Washing, filtering and drying 53
2.2.2 Preparation of noble metal substituted Ni/Al LDHs 54
2.3 Calcination 54
2.4 Catalytic performance studies 55
2.4.1 Experimental set-up 55
2.4.2 Catalyst activation 57
2.4.3 Catalytic studies 57

2.4.3.1 Activity measurement 57
2.4.3.2 Stability test 58
2.4.3.3 Self-activation 59
2.4.3.4 Purged DSS operation 59
2.4.4 Calculation methods 60
2.5 Catalyst characterisation 61
2.5.1 X-ray diffraction (XRD) 61
2.5.1.1 Purpose 61
2.5.1.2 Fundamental principle 61
2.5.1.3 Experimental method 63
2.5.2 BET surface area measurement 64
2.5.2.1 Purpose 64
2.5.2.2 Fundamental principle 64
2.5.2.3 Experimental method 65
2.5.3 Thermo-gravimetric analysis (TGA) 65
2.5.3.1 Purpose 65
2.5.3.2 Fundamental principle 66
2.5.3.3 Experimental method 66
2.5.4 Temperature programmed reduction (TPR) 66
2.5.4.1 Purpose 66
2.5.4.2 Fundamental principle 67
2.5.2.3 Experimental method 67
2.5.5 Scanning electron microscopy (SEM) 68
2.5.5.1 Purpose 68
2.5.5.2 Fundamental principle 68
2.5.5.3 Experimental method 69
2.5.6 Transmission electron microscopy (TEM) 70
2.5.6.1 Purpose 70
2.5.6.2 Fundamental principle 70
2.5.6.3 Experimental method 71
2.5.7 Energy dispersive X-ray spectroscopy (EDX) 72
2.5.7.1 Purpose 72
2.5.7.2 Fundamental principles 72

2.5.7.3 Experimental method 73
2.5.8 Infrared spectroscopy (IR) 73
2.5.8.1 Purpose 73
2.5.8.2 Fundamental principle 74
2.5.8.3 Experimental method 74
Chapter 3. Effect of synthetic conditions on Ni/Al and noble metals substituted Ni/Al LDHs and catalytic activity of the derived catalysts 76
3.1 Introduction 77
3.2 Experimental 77
3.3 Results and discussion 78
3.3.1 Compositions of LDHs 78
3.3.2 Structure of LDHs 81
3.3.3 Structure of catalysts 83
3.3.4 SEM observation 86
3.3.5 Thermal decomposition analysis 86
3.3.6 TPR analysis 89
3.3.6.1 Effect of Ni:Al ratio on the reducibility of the catalysts 89
3.3.6.2 Effect of preparative conditions of LDH on reducibility of the derived catalysts 90
3.3.6.3 Effect of preparative conditions of noble metal substituted LDH on reducibility of the derived catalysts 91
3.3.7 TEM observation 95
3.3.8 Catalyst activity 97
3.3.8.1 Effect of Ni/Al ratio on catalytic activity 97
3.3.8.2 Effect of preparative conditions on catalyst activity 98
3.3.8.3 Reaction pathways 101
3.4 Conclusions 103
Chapter 4. Effect of thermal treatments on Ni/Al LDHs and noble metals substituted Ni/Al LDHs and catalytic activity of the derived catalysts 104
4.1 Introduction 105
4.2 Experimental 105
4.3 Results and discussion 106
4.3.1 Effect of calcination temperature on the surface area of the calcined oxides 106

4.3.2 Structure of catalysts 107
4.3.2.1 Calcination at 450, 550 and 700°C 107
4.3.2.2 Calcination at 1000°C 111
4.3.2.3 Calcination for 4 h and 20 h 111
4.3.3 TPR analysis 112
4.3.3.1 Calcination at 450, 550 and 700°C 112
4.3.3.2 Calcination at 1000°C 116
4.3.3.3 Calcination for 4 h and 20 h 118
4.3.4 Catalyst activity 119
4.3.4.1 Activity as a function of calcination temperature 119
4.3.4.2 Activity as a function of calcination time 122
4.4 Conclusions 123
Chapter 5. Effect of quantity of promoters on noble metal promoted Ni/Al LDHs and activities of the derived catalysts 124
5.1 Introduction 125
5.2 Experimental 125
5.3 Results and discussion 126
5.3.1 Compositions of LDHs 126
5.3.2 Structure of LDHs 128
5.3.3 Structure of catalysts 130
5.3.4 TEM observation 134
5.3.5 Elemental mapping analysis 136
5.3.6 FTIR analysis 139
5.3.7 TPR analysis 141
5.3.8 Catalyst activity 144
5.4 Conclusions 147
Chapter 6. Development of LDH sol for SOFC anode coating 148
6.1 Introduction 149
6.2 Experimental 150
6.3 Results and discussion 152
6.3.1 Preparative conditions of NA-LDHs 152
6.3.2 Compositions of LDHs 154
6.3.3 Structure of LDHs 154
6.3.3.1 Structure of raw-LDHs and NA-LDHs 154

6.3.3.2 Effect of nitric acid quantity on structure of NA-LDHs 156
6.3.4 SEM observation 157
6.3.5 FTIR analysis 159
6.3.6 Thermal decomposition analysis 161
6.3.7 Structure of catalysts 162
6.3.7.1 Structures of catalysts derived from raw-LDHs and NA-LDHs 162
6.3.7.2 Structures of catalysts derived from NA-LDHs treated with different quantities of nitric acid 164
6.3.8 TEM observation 165
6.3.9 TPR analysis 166
6.3.10 Catalyst Activity 168
6.4 Conclusions 171
Chapter 7. Stability, self-activation and self-regeneration studies over LDH derived catalysts 172
7.1 Introduction 173
7.2 Experimental 174
7.3 Results and discussion 175
7.3.1 Long-term stability test 175
7.3.2 Self-activation of Pd and Rh promoted Ni(Al)O catalysts 176
7.3.3 Self-regeneration of Pd and Rh promoted Ni/Al catalysts 177
7.4 Conclusions 180
Chapter 8. Summary and recommendations 181
8.1 Summary 182
8.2 Recommendations for future study 185
Bibliography 187
Appendices 196
Appendix A. List of chemicals and gases used in experiments 197
Appendix B. List of CP method prepared LDHs 198
Appendix C. List of sol/nitric acid attack method prepared LDHs 199
Appendix D. List of calcined catalysts derived from LDHs prepared by CP method 200
Appendix E. List of calcined catalysts derived from LDHs prepared by sol/nitric acid attack method 202

Appendix F. List of reduced catalysts derived from LDHs prepared by CP method 203

Appendix G. List of reduced catalysts derived from LDHs prepared by sol/nitric acid attack method 204

List of Figures

Figure 1.1 World primary energy substitution [8]. 3
Figure 1.2 Working principle of H_2-O_2 FC[13]. 5
Figure 1.3 Working principle of SOFC [12]. 11
Figure 1.4 Gradual internal steam reforming of methane at SOFC anode [74]. 21
Figure 1.5 (A) Langmuir-Hinshelwood and (B) Eley-Rideal mechanisms [96]. 27
Figure 1.6 Structure of LDH (Example: $[Mg_{3-x}Ni_xAl(OH_8)]1/2CO_3^{2-}\cdot 2H_2O$) [140]... 38
Figure 2.1 Schematics for the preparation of Ni/Al LDH. 53
Figure 2.2 Schematic diagram for catalytic testing in micro-reactor unit. 56
Figure 2.3 Diffraction of X-rays by a crystal [179]. 62
Figure 2.4 Schematic diagrams showing the operation of (A) SEM and (B) TEM [171]. 69
Figure 3.1 Ground and sieved LDHs (A) NiAl40, (B) Pd(1.3)NiAl40 and (C) Rh(1.1)NiAl40. 79
Figure 3.2 XRD patterns of LDH precipitates dried at 90°C for 12 h. 81
Figure 3.3 (A) Comparison of XRD peaks of NiAl40, NiAl70 and NiAl70L LDHs corresponding to (003) and (006) reflection lines; (B) Comparison of XRD peaks of NiAl40, Pd(1.3)NiAl40 and Rh(1.1)NiAl40 LDHs corresponding to (003) and (006) reflection lines. 83
Figure 3.4 XRD patterns of catalysts prepared by calcination of LDH precursors at 550°C for 4 h. 84
Figure 3.5 SEM images of (A) NiAl40, (B) Pd(1.3)NiAl40, (C) Rh(1.1)NiAl40 and (D) NiAl70L LDHs. 86
Figure 3.6 TG-DTA curves of (A) NiAl40, (B) Pd(1.3)NiAl40, (C) Pd(2.1)NiAl70B and (D) Rh(1.1)NiAl40. 87
Figure 3.7 TPR profiles of NiAl(2:1)40-C550 and NiAl40-C550 catalysts. 89
Figure 3.8 TPR profiles of Ni(Al)O catalysts. S_A, S_B and S_C are the areas of the Ni reduction peaks in the TPR curves of NiAl40-C550, NiAl70-C550 and NiAl70L-C550 91
Figure 3.9 TPR profiles of Rh promoted Ni(Al)O catalysts. S_A and S_B are the areas of the Ni reduction peaks in the TPR curves of Rh(1.1)NiAl40-C550, and Rh(1.1)NiAl70L-C550 92
Figure 3.10 TPR profiles of Pd promoted Ni(Al)O catalysts. S_A, S_B and S_C are the areas of the Ni reduction peaks in the TPR curves of Pd(1.3)NiAl40-C550, Pd(1.8)NiAl70L-C550 and Pd(2.1)NiAl70B-C550 93
Figure 3.11 TEM images of (A) NiAl40-C550, (B) NiAl70L-C550, (C) Pd(1.3)NiAl40-C550, (D) NiAl40-C550-R700, (E) NiAl70L-C550-R700 and (F) Pd(1.3)NiAl40-C550-R700. 96
Figure 3.12 Comparison of (A) CH_4 consumption and (B) H_2 productivity as a function of reaction temperature in SMR over NiAl(2:1)40-C550-R700 (Ni:Al=2:1)

and NiAl40-C550-R700 (Ni:Al=3:1) catalysts (CH_{4inlet}= 16.2ml/min, S:C=3:1, 1 atm). 97
Figure 3.13 Comparison of (A) CH_4 consumption and (B) H_2 productivity of SMR over NiAl40-C550-C700, NiAl70-C550-C700 and NiAl70L-C550-C700 catalysts (CH_{4inlet} = 16.2ml/min, S:C=3:1, 1 atm). 98
Figure 3.14 Comparison of (A) CH_4 consumption and (B) H_2 productivity of SMR over Rh(1.1)NiAl40-C550-R700 and Rh(1.1)NiAl70L-C550-R700 catalysts (CH_{4inlet}= 16.2ml/min, S:C=3:1, 1 atm). 99
Figure 3.15 Comparison of (A) CH_4 consumption and (B) H_2 productivity of SMR over Pd(1.3)NiAl40-C550-R700, Pd(1.8)NiAl70L-C550-R700 and Pd(2.1)NiAl70B-C550-R700 catalysts (CH_{4inlet}= 16.2ml/min, S:C=3:1, 1 atm).....99
Figure 3.16 (A) CO and (B) CO_2 evolution (%) during SMR over (A) NiAl40-C550-R700, (B) Pd(1.3)NiAl40-C550-R700 and (C) Rh(1.1)NiAl40-C550-R700 catalysts. 102
Figure 4.1 Effect of calcination temperature of (A) NiAl40, (B) Pd(1.3)NiAl40 and (C) Rh(1.1)NiAl40 on surface area. 107
Figure 4.2 XRD patterns of the Ni(Al)O and Pd and Rh promoted Ni(Al)O catalysts calcined at 450, 550, 700 and 1000°C for 4 h. (■) Ni(Al)O; (□) $NiAl_2O_4$ spinel; (○) PdO. 108
Figure 4.3 XRD patterns of NiAl40LDH precursor calcined at 550°C for 4 h (NiAl40-C550) and 20 h (NiAl40-C550L). 112
Figure 4.4 TPR profiles of (A) Ni(Al)O, (B) Pd promoted Ni(Al)O and (C) Rh promoted Ni(Al)O catalysts calcined at 450, 550 and 700°C. 113
Figure 4.5 TPR profile of pure NiO from calcination of $Ni(NO_3)_2 \cdot 6H_2O$ at 450°C for 4 h. 114
Figure 4.6 TPR profiles of 1000°C calcined samples. 117
Figure 4.7 TPR of Ni(Al)O catalysts calcined at 550°C for 4 and 20 h. 118
Figure 4.8 Comparison of (A) CH_4 consumption and (B) H_2 productivity of SMR over Ni/Al catalysts calcined at 400, 550 and 700ºC (CH_{4inlet}=16.2ml/min, S:C=3:1, 1 atm). 119
Figure 4.9 Comparison of (A) CH_4 consumption and (B) H_2 productivity of SMR over Pd promoted Ni/Al catalysts calcined at 400, 550 and 700ºC (CH_{4inlet}= 16.2ml/min, S:C=3:1, 1 atm). 121
Figure 4.10 Comparison of (A) CH_4 consumption and (B) H_2 productivity of SMR over Rh promoted Ni/Al catalysts calcined at 400, 550 and 700ºC (CH_{4inlet}= 16.2ml/min, S:C=3:1, 1 atm). 121
Figure 4.11 Comparison of CH_4 consumption (A) and (B) H_2 productivity of SMR over Ni/Al catalysts clacined for 4 and 20 h (CH_{4inlet}= 16.2ml/min, S:C=3:1, 1 atm). 122
Figure 5.1 Pd substitued ground LDH powders: (A) Pd(0.3)NiAl40, (B) Pd(0.6)NiAl40, (C) Pd(1.3)NiAl40, (D) Pd(1.9)NiAl40, (E) Pd(2.3)NiAl40 and (F) Pd(4.0)NiAl40. 127

Figure 5.2 Rh substitued ground LDH powders: (A) Rh(0.5)NiAl40, (B) Rh(1.1)NiAl40, (C) Rh(1.6)NiAl40, (D) Rh(2.1)NiAl40, (E) Rh(3.1)NiAl40 and (F) Rh(4.2)NiAl40. 127
Figure 5.3 XRD patterns of Ni/Al LDH (in both Figure A and B) and, (A) Pd and (B) Rh substituted Ni/Al LDHs. 129
Figure 5.4 XRD patterns of Ni(Al)O (in both Figure A and B) and (A) Pd and (B) Rh promoted Ni(Al)O catalysts calcined at 550°C for 4 h. (■) Ni(Al)O; (○) PdO..... 132
Figure 5.5 XRD patterns of Ni/Al (in both Figure A and B) and (A) Pd and (B) Rh promoted Ni/Al catalysts obtained from H_2-reduction of calcined catalysts at 700°C for 1 h. (•) Ni; (■) Ni(Al)O. 133
Figure 5.6 TEM images of (A) NiAl40-C550-R700, (B) Pd(1.3)NiAl40-C550-R700, (C) Pd(4.0)NiAl40-C550-R700 and (D) Rh(4.2)NiAl40-C550-R700. 135
Figure 5.7 Elemental map of Pd(1.3)NiAl40-C550-R700 catalyst. 137
Figure 5.8 Elemental map of Rh(1.1)NiAl40-C550-R700 catalyst. 137
Figure 5.9 Elemental map of Pd(4.0)NiAl40-C550-R700 catalyst. 138
Figure 5.10 Elemental map of Rh(4.2)NiAl40-C550-R700 catalyst. 138
Figure 5.11 FTIR spectra after admission of CO on reduced Ni/Al, and Pd and Rh promoted Ni/Al catalysts at ambient temperature. 140
Figure 5.12 TPR profiles of (A) Pd and (B) Rh promoted Ni(Al)O catalysts. 143
Figure 5.13 CH_4 consumption and H_2 productivity of SMR reactions over Ni/Al and Pd promoted Ni/Al catalyst with different loading amounts of Pd. (CH_{4inlet}= 16.2ml/min, S:C=3:1, 1 atm). 145
Figure 5.14 CH_4 consumption and H_2 productivity of SMR reactions over Ni/Al and Rh promoted Ni/Al catalyst with different loading amounts of Rh. (CH_{4inlet}= 16.2ml/min, S:C=3:1, 1 atm). 146
Figure 6.1 Suspension of Ni/Al LDH (A) before and (B) after nitric acid attack treatment. The centrifuged slurry of Ni/Al LDH (C) before and (D) after nitric acid attack. 151
Figure 6.2 XRD patterns of raw-LDHs and NA-LDHs. 155
Figure 6.3 XRD patterns of LDHs treated with different quantities of nitric acid (■) $Ni(NO_3)_2 \cdot 6H_2O$. 156
Figure 6.4 SEM image of silica substrate used for spin coating 157
Figure 6.5 SEM images of (A) NiAl40, (B) NA(1.0)-NiAl40, (C) NA(0.85)-Pd(1.3)NiAl40, and (D) NA(0.88)-Rh(1.1)NiAl40 LDHs. 158
Figure 6.6 SEM images of (A) NiAl40-C550, (B) NA(1.0)-NiAl40-C550, (C) NiAl40-C550-R700, and (D) NA(1.0)-NiAl40-C550-R700 catalysts. 159
Figure 6.7 FTIR spectra of raw-LDHs and NA-LDHs. 160
Figure 6.8 TGA curves of raw-LDHs and NA-LDHs. 161
Figure 6.9 XRD patterns of catalysts obtained from calcination of raw-LDHs and NA-LDHs at 550°C for 4 h. 163
Figure 6.10 Comparison of XRD patterns of (A) Ni(Al)O and (B) Pd promoted Ni(Al)O catalysts derived from LDH precursors treated with different quantities of nitric acid. (■) Ni(Al)O/NiO; (○) PdO 164

Figure 6.11 HR-TEM images of (A) NiAl40-C550, (B) NA(1.0)-NiAl40-C550, (C) NiAl40-C550-R700 and (D) NA(1.0)-NiAl40-C550-R700. 165
Figure 6.12 TPR profiles of the catalysts derived from raw-LDHs and NA-LDHs. .167
Figure 6.13 Comparison of (A) CH_4 consumption and (B) H_2 productivity of SMR over Ni/Al catalysts derived from raw-LDH and NA-LDH (CH_{4inlet}=16.2ml/min, S:C=3:1, 1 atm). 168
Figure 6.14 Comparison of (A) CH_4 consumption and (B) H_2 productivity of SMR over Pd promoted Ni/Al catalysts derived from raw-LDH and NA-LDH (CH_{4inlet}=16.2ml/min, S:C=3:1, 1 atm). 170
Figure 6.15 Comparison of (A) CH_4 consumption and (B) H_2 productivity of SMR over Rh promoted Ni/Al catalysts derived from raw-LDH and NA-LDH (CH_{4inlet}=16.2ml/min, S:C=3:1, 1 atm). 170
Figure 7.1 CH_4 consumption of long-term SMR at 600ºC over tested catalysts (CH_{4inlet}=16.2ml/min, S:C=3:1, 1 atm). 175
Figure 7.2 HR-TEM images of NiAl40-C550-R700 derived catalyst (A) before and (B) after long-term stability tests. 176
Figure 7.3 Self-activation of the tested catalysts during SMR at 600ºC. (CH_{4inlet}=16.2ml/min, S:C=3:1, 1 atm). 176
Figure 7.4 CH_4 consumption of SMR under normal DSS-like conditions over NiAl40-C550-R700, NA-NiAl40-C550-R700 catalysts (CH_{4inlet}=16.2ml/min, S:C=3:1, 1 atm). 178
Figure 7.5 CH_4 consumption of SMR under steam-purged DSS-like conditions over tested catalysts at 600ºC (CH_{4inlet}=16.2ml/min, S:C=3:1, 1 atm). 178
Figure 7.6 XRD patterns of NiAl40-C550-R700 catalysts (A) before and (B) after the steam-purged DSS-like operation. 179

List of Tables

Table 1.1 Currently developed FC types and their characteristic applications [12, 19, 20]. 9
Table 1.2 Possible reactions during SMR [81]. 22
Table 1.3 Range of structures possible in oxide form of co-precipitated Ni/Al catalyst [155]. 45
Table 3.1 Chemical composition and structure studies of synthesised LDHs 80
Table 3.2 Crystallite sizes, BET SA and lattice parameters of all calcined catalysts. . 85
Table 4.1 Structure, chemical composition and surface area of catalysts calcined at 450, 550, 700 and 1000°C 110
Table 5.1 Structure and chemical composition of synthesised LDHs. 128
Table 5.2 Crystal structure details of calcined and reduced catalysts. 131
Table 6.1 Chemical composition and structural parameters of raw-LDHs and NA-LDHs. 153
Table 6.2 Structure and composition of calcined catalysts. 163

Abbreviations

AFC	**A**lkaline **F**uel **C**ell
BET (SA)	**B**runauer – **E**mmett – **T**eller (**S**urface **A**rea)
BSCF	**B**arium **S**trontium **C**obalt iron oxide
CHP	**C**ombined **H**eat and **P**ower
CP	**C**o-**p**recipitation
DCDI	**D**e-**c**arbonated **D**e-**i**onized (water)
D.S.O.I.	**D**isordered **O**xide-**S**pinel **I**ntermediate
EDX or EDS	**E**nergy-**d**ispersive **X**-ray **S**pectroscopy
ESMR	**E**xternal **S**team **M**ethane **R**eforming
FTIR	**F**ourier **T**ransform **I**nf**r**ared Spectroscopy
FWHM	**F**ull **W**idth at **H**alf **M**aximum
GC	**G**as **C**hromatography
GIR	**G**radually **I**nternal **R**eforming
HT	**H**ydrotalcite
HRTEM	**H**igh **R**esolution **TEM**
ICDD	**I**nternational **C**entre for **D**iffraction **D**ata
IR	**I**nfrared **S**pectroscopy
ISMR	**I**nternal **S**team **M**ethane **R**eforming
IT-SOFC	**I**ntermediate **T**emperature **SOFC**
LDH	**L**ayered **D**ouble **H**ydroxide
MFC	**M**ass **F**low **C**ontrol
MOFC	**M**olten **C**arbonate **F**uel **C**ell
PAFC	**P**hosphoric **A**cid **F**uel **C**ell
PE	**P**rimary **E**lectrons
PEMFC	**P**roton **E**xchange **M**embrane **F**uel **C**ell

S/C	**S**team to **C**arbon
SEM	**S**canning **E**lectron **M**icroscopy
S.L.M.	**S**pinel-**l**ike **M**aterial
SMR	**S**team **M**ethane **R**eforming
S.N.O.	**S**ubstituted **N**ickel **O**xide
SOFC	**S**olid **O**xide **F**uel **C**ell
TCD	**T**hermal **C**onductivity **D**etector
TEM	**T**ransmission **E**lectron **M**icroscopy
TGA	**T**hermo-**G**ravimetric **A**nalysis
TPR	**T**emperature **P**rogrammed **R**eduction
TOF	**T**urn**o**ver **F**requency
WGS	**W**ater **G**as **S**hift
XRD	**X**-**r**ay **D**iffraction
YSZ	**Y**ttria-**s**tablized **Z**irconia

Nomenclature

A standard nomenclature is applied to name the LDHs, calcined and reduced catalysts:

A. LDHs

(1) Standard LDH: *A*(*x*)NiAl*y*

Where *A*=Pd, Rh or Pt; *x* ($0 \leq x < 5$); *x* is the atomic ratio of the *A* in the brucite layer of LDH, calculated by $x=\frac{A}{A+Ni+Al}$; NiAl stands for the fundamental composition of system with Ni:Al=3:1(atomic); *y* (*y*=40, 70) is the co-precipitation temperate in °C.

e.g. NiAl40, Pd(1.3)NiAl70, Rh(1.1)NiAl40.

Standard 4 h aging is applied for the precipitate of LDH except for precipitates aged for 24h or critical, specified with suffix L or B after *y*, where L=24h, B=100°C/0.5 (hour) aging.

e.g. Rh(1.1)NiAl70L, Pd(2.1)NiAl70B.

(2) Sol/nitric acid attack-route prepared LDH: NA(*z*)-A(*x*)NiAl*y* (also referred as NA-LDHs in Chapter 6-7)

Where a prefix NA(*z*)- is added before the name of the parent LDH (referred as raw-LDH in Chapters 6 and 7) stands for nitric acid treatment, *z* is the relevant quantity of

nitric acid used during preparation. The quantity of nitric acid used for a standard Ni/Al LDH sample (name: NA(1.0)-NiAl40) is set as *z*=1.0.

e.g. NA(1.0)-NiAl40, NA(0.85)-Pd(1.2)NiAl40.

B. Calcined catalysts: *A*(*x*)NiAl*y* -C*h* or NA(*z*)-*A*(*x*)NiAl*y*-C*h*

A suffix –C*h* is added after the name of the LDH precursor, where C standards for calcination, *h* (*h*=450, 550, 700 or 1000) is the calcination temperature in °C. LDHs are calcined for 4 h except one sample NiAl40-C550L, L standard for 20 h.

e.g. NiAl40-C450, Pd(1.3)NiAl40-C700, NA(0.88)-Rh(1.0)NiAl40-C550.

C. H_2 reduced catalysts: *A*(*x*)NiAl*y* -C*h*-R700 or NA(*z*)-*A*(*x*)NiAl*y*-C*h*-R700

Only 700°C is used for catalyst reduction, a suffix –R700 is added after the name of calcined catalyst, R stands for reduction.

e.g. NiAl40-C550-R700, NA(0.88)-Rh(1.0)NiAl40-C550-R700.

Chapter 1. Introduction

1.1 Background

Increasing energy demands and environmental problems are critical challenges to the world. Alternative energy, such as wind, solar and nuclear power, is considered to be the solution, but their deployment is restricted by cost, efficiency, location, and security issues. Thus, traditional hydrocarbon fuels will still dominate the global energy supply in the near future [1].

Among the current primary hydrocarbon fuels, natural gas (predominantly methane) is regarded as a relatively cheap and clean fuel compared with oil and coal in terms of the energy and environmental costs. The existing global proved reserve of natural gas is sufficient for over 60 years' supply at the current production and consumption levels [2]. Moreover, improved extraction technologies (e.g. shale gas extraction) significantly improve the resource profile and hence the cost of using natural gas will remain low in the long term [3]. Low emissions from natural gas usage compared with oil and coal imply an increased use of natural gas in the next few decades (Figure 1.1).

Currently, electricity generation accounts for about 20% (34% in the USA [4] and 45% in the UK [5]) of global natural gas usage, entailing 21% of world electricity production. This proportion will constantly increase due to high pressure on reducing CO_x and NO_x emissions from burning coal [6]. Globally, the major power generation method is the burning of gas to drive gas turbines and steam turbines [7]. However, internal combustion results in low system efficiency and relatively high emissions.

Developing an alternative method for a better use of natural gas is extremely important for global energy security and the low carbon economy.

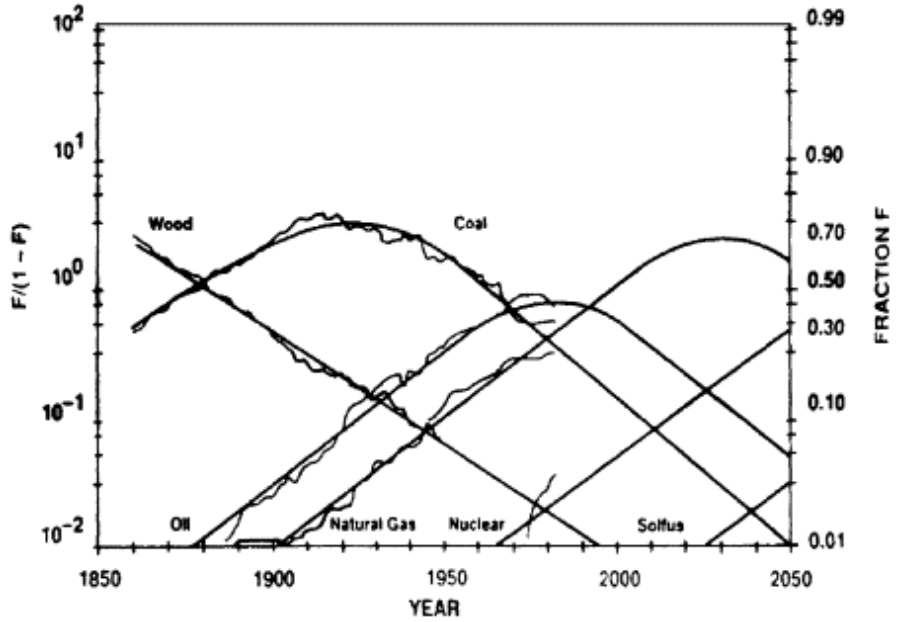


Figure 1.1 World primary energy substitution [8].

Solid oxide fuel cells (SOFC) offer a highly efficient (over 60% in theory) solution in terms of the power conversion of natural gas, with relatively low levels of pollution. By using internal steam reforming, natural gas can be directly used as fuel in SOFC without combustion. This technology is a promising solution for the power generation industry [9-11] and is currently under development for a variety of stationary and portable electric power generations. Among these research works, one essential aspect for the further deployment of SOFC is an enhancement of the fuel processing. This thesis investigates low temperature steam methane reforming (SMR) catalysts specifically for the next generation SOFC (intermediate temperature SOFC). In order to give a comprehensive understanding of the research background, this introductory chapter introduces fuel cells, SOFCs, steam methane reforming, the reforming catalysts and a novel catalyst precursor—layered double hydroxide (LDH), followed

by a discussion of research objectives and an outline of the structure of the whole thesis.

1.2 Fuel Cells (FCs)

1.2.1 Introduction to FCs

An fuel cell (FC) is an electrochemical device that directly convert chemical energy into electrical energy [12]. The technology is expected to play a significant role in a future sustainable energy system due to its high efficiency, and the possibility of using renewable fuels, such as biogas.

An FC operates like an engine or a battery. However, unlike the most widely used electricity generators such as internal combustion turbines, the FC has no moving parts. Electrical energy is released when fuel undergoes chemical reaction with oxygen or an oxidising agent without combustion. There is no intermediate conversion of fuel to thermal or mechanical energy during this process. Unlike a battery, the FC does not store energy but works continuously to generate electricity by consuming the fuel. There is a variety of fuel choices for FC, depending on the type of FC and the applications. Hydrogen, one type of direct fuel, is the most commonly used fuel. Hydrocarbons, such as natural gas and alcohol, have also been used as indirect fuel to provide hydrogen after fuel processing.

1.2.2 Electrochemistry aspects

The basic physical structure of an FC consists of three major parts – an electrolyte layer in contact with a porous anode and cathode on either side. The anode is the electrode where the oxidation takes place, whereas reduction occurs on the cathode. The electrolyte conducts charged ions between two electrodes during the operation of an FC. It also provides a physical barrier to prevent charges from moving between two electrodes. These three parts together are referred to the membrane assembly. A schematic representation of a typical H_2-O_2 FC with reactants and product gases and ion conduction flow is shown in Figure 1.2. A fuel, mostly, hydrogen is supplied to the anode and an oxidant (normally oxygen but sometimes air) is brought to the cathode.

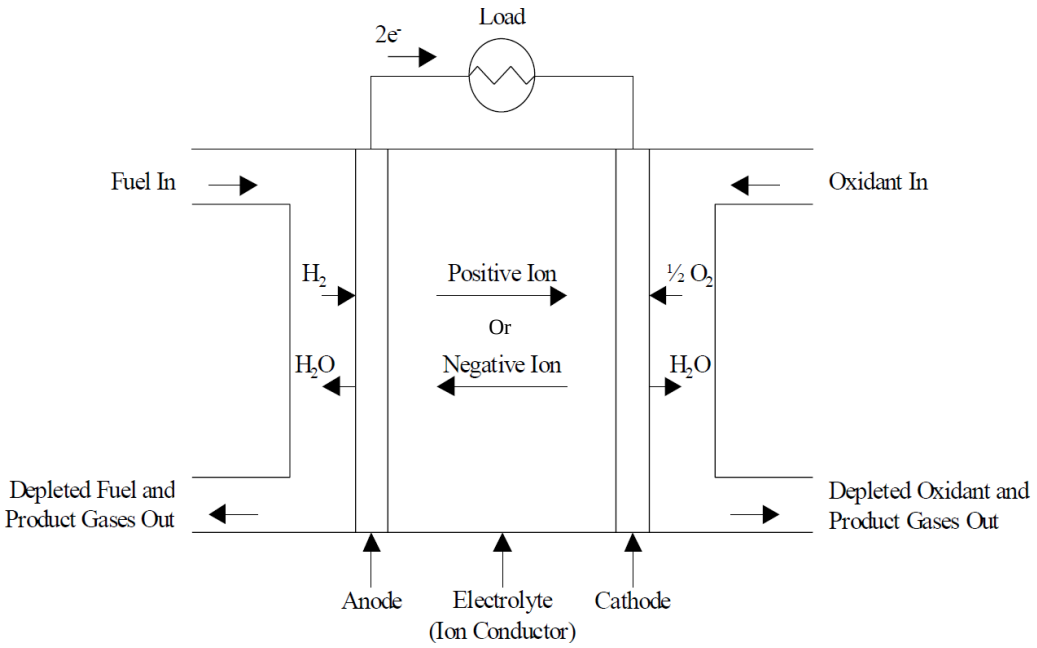


Figure 1.2 Working principle of H_2-O_2 FC[13].

According to Atkins [14], the basic principle and primary reaction encountered in an FC is based on the redox reaction:

$$H_2 + \frac{1}{2}O_2 = H_2O \quad (1.1)$$

Although the half-cell reaction occurring at each electrode may vary depending on the type of the cell, the fundamental principle of different types of FC remains the same [13, 15].

1.2.3 Thermodynamic aspects of FC

Thermodynamics is the study of the conversion of energy which is connected with heat and its relation to other forms of energy and/or work. FC converts the free-energy change of an electrochemical reaction into electrical energy. When an FC operates at a constant temperature and pressure, the system will reach equilibrium. The maximum electrical work in the system can be expressed by the Gibbs Free Energy of the electrochemical reaction:

$$W = \Delta G = -nFE \quad (1.2)$$

where ΔG is the free-energy change, n is the number of moles of electrons involved, E is the reversible potential of the FC and F is Faraday's constant. Once the reactants and products are in their own standard states, the equation can be written as:

$$\Delta G^{\circ} = -nEF^{\circ} \quad (1.3)$$

Under standard conditions of temperature and pressure (T = 298 K, $P_{H_2} = P_{O_2} =$ 1 atm, H_2O in liquid state), where the ΔG corresponding to equation (1.2) is -229 kJ/mol, n = 2, F = 96500 C/mol electron, the calculated E is 1.229V.

Under variable conditions, the variations of reversible potential E with temperature and pressure are expressed by the equation:

$$E = E^{\circ} + \frac{\Delta S}{nF}(T - 298) \quad (1.4)$$

where ΔS is entropy change. It is easy to see that the revisable potential decreases with an increase in temperature, whereas the behaviour is opposite with an increase in pressure. For reaction (1.1), ΔS is negative. This means heat would always be released from an FC even if there is no efficiency losses in an H_2-O_2 FC system [12, 16, 17].

1.2.4 Types of FCs

Various FCs exist and are in different stages of development. All the FCs have a similar cathode–electrolyte–anode structure. FCs are classified into different categories depending on the type of electrolyte used, with different combination of fuel, operating temperature and applications. The most common classification of FCs being commercialised and used for large-scale applications today include: 1) alkaline

fuel cell (AFC); 2) proton exchange membrane electrolyte fuel cell (PEMFC); 3) phosphoric acid fuel cell (PAFC); 4) molten carbonate fuel cell (MCFC); and 5) SOFC. Table 1.1 summarises their characteristics and applications. In addition to the classifications mentioned, there are other types of FCs, for example direct methanol FCs, which are currently in the development stage. The MCFC and SOFC are operated at relatively high temperature (600-1000°C) and hence they have the ability to utilise methane directly in the FC with high inherent generation efficiency (45–60% for common fuels such as natural gas, 75% with heat recovery) [18].

Table 1.1 Currently developed FC types and their characteristic applications [12, 19, 20].

	Electrolyte	Charge carrier	Anode reaction	Cathode reaction	Operating temperature	Fuel	Electric efficiency (System)	Power range/ application	Partition (generation/ temp)	Advantages	Disadvantages
Alkaline FC (AFC)	KOH	OH^-	$H_2 + 2(OH)^- \rightarrow 2H_2O + 2e^-$	$1/2O_2 + H_2O + 2e^- \rightarrow 2(OH)^-$	60-120°C	Pure H_2	35-55%	<5kW, niche markets (defence, space)	1st /low temp	Cathode reaction faster in alkaline electrolyte, leads to high performance Low-cost components Low temperature	Sensitive to CO_2 in fuel and air Electrolyte management
Proton exchange membrane FC (PEMFC)	Solid Polymer	H^+	$H_2 \rightarrow 2H^+ + 2e^+$	$1/2\ O_2 + 2H^+ + 2e^+ \rightarrow H_2O$	50-100°C	Pure H_2 (tolerates CO_2)	35-45%	Automotive, CHP (5-250kW)	1st /low temp	Solid electrolyte reduces corrosion and electrolyte management problems Low temperature Quick start-up	Expensive catalysts Sensitive to fuel impurities Low temperature waste heat
Phosphoric acid FC (PAFC)	Phosphoric acid	H^+	$H_2 \rightarrow 2H^+ + 2e$	$1/2\ O_2 + 2H^+ + 2e^- \rightarrow H_2O$	~220 °C	Pure H_2 (,1% CO)	40%	CHP(200kW)	1st /intermediate temp	Higher temperature enables CHP Increased tolerance to fuel impurities	Expensive Pt catalyst Long start-up time Low current and power
Molten carbonate FC (MCFC)	Lithium and potassium carbonate	CO_3^{2-}	$H_2 + CO_3^{2-} \rightarrow H_2O + CO_2 + 2e^-$ $CO + CO_3^{2-} \rightarrow 2CO_2 + 2e^-$	$1/2\ O_2 + CO_2 + 2e^- \rightarrow CO_3^{2-}$	~650 °C	H_2, CO, CH_4, other hydrocarbons (tolerates CO_2)	50%	200kW-MW range, CHP and standalone	2nd /high temp	High efficiency Fuel flexibility Variety of catalysts available Suitable for CHP	High temperature corrosion and breakdown of cell components Long start-up time Low power density
Solid oxide FC (SOFC)	Solid oxide electrolyte	O^{2-}	$H_2 + O_2\text{-} \rightarrow H_2O + 2e^-$ $CO + O2^- \rightarrow CO_2 + 2e^-$ $CH_4 + 4O^{2-} \rightarrow 2H_2O + CO_2 + 8e^{2-}$	$1/2\ O_2 + 2e^- \rightarrow O^{2-}$	800-1000 °C	H_2, CO, CH_4, other hydrocarbons (tolerates CO_2)	50%-60%	1kW-MW range, CHP and standalone	3rd high temp	High efficiency Fuel flexibility Variety of catalysts available Suitable for CHP Solid electrolyte	High temperature corrosion and breakdown of cell components Long start-up time Low power density Solid diffusion

1.3 Solid oxide fuel cell (SOFC)

1.3.1 Introduction to SOFC

Solid oxide fuel cell (SOFC) belongs to the third generation FC. Among various types of FCs, SOFC has attracted significant interest due to its technological advantages. It is considered as a potential future energy solution with high efficiency and low emissions of pollutants to the environment [21-23]. SOFC is an all-solid power system which operates at high temperature to ensure the adequate ionic and electronic conductivity of its components. The typical operating temperature is currently between 800 and 1000°C. The electrolyte is made of hard ceramic materials. SOFC has several advantages over other types of FC due to its all solid state behaviour [24]. Firstly, the solid ceramic construction of the cell has no principal restriction on the configuration. The cell can be designed in planar, tubular or monolithic structures. Moreover, the two-phase contact in SOFC significantly reduces the rate of corrosion and eliminates electrolyte management problems compared with a liquid electrolyte FC [13, 20]. The high operating temperature of SOFC also offers several benefits: Activation overpotential is low during the cells' operation and hence noble metal catalysts are not needed for the electrochemical reaction. Hydrocarbons such as natural gas could be potentially internally reformed for the *in-situ* hydrogen production at the anode of the cell [25]. The resulting high-quality steam from FC reaction can be directly used as reactant for the internal reforming. Operating at a high temperature also makes the free energy of formation less negative than at room temperature, so that the open circuit potential at practical gas utilisations is about

0.9V. In spite of this, more than 50% thermal efficiencies can be achieved (corresponding to 0.75V) for chemical-to-electrical energy conversion in SOFCs [17].

1.3.2 Electrochemistry aspects and cell materials

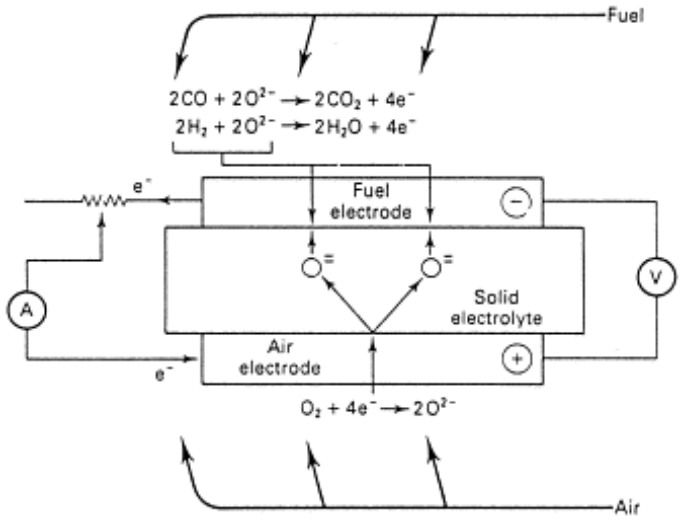


Figure 1.3 Working principle of SOFC [12].

SOFCs consist of three basic components: anode, cathode and electrolyte. Figure 1.3 illustrates the common structure of a typical SOFC. The operating principle is the same as the working principle of the general H_2-O_2 FC, with the overall reaction being:

$$H_2 + \frac{1}{2}O_2 = H_2O \tag{1.1}$$

This is accompanied by the release of electrons to the external circuit. Normally, several SOFCs are connected together in a series to form an SOFC stack via interconnects. The electricity generated by individual cells can be combined together.

1.3.2.1 Cathode (Air electrode)

The cathode, also called the air electrode, is a thin porous structure layer where oxygen reduction occurs. The reaction in anode can be written as:

$$\frac{1}{2}O_2 + 2e^- \rightarrow O^{2-} \quad (1.5)$$

The material of the cathode should be very stable and highly electronically conductive, as well as exhibiting a good activity for oxygen reduction under high operating temperatures. Its firing shrinkage and thermal expansion coefficient must also match with other cell components. Otherwise, the cell may crack due to the thermal expansion/contraction under critical operating conditions [17, 26].

Perovskite materials, with a general formula ABO_3, have been widely used as cathode materials. Here A and B are cations with a total charge of +6. The current SOFC cathode material choice for commercial application is strontium-doped lanthanum manganite (LSM, $La_{1-x}\,Sr_xMnO_3$), which has a perovskite structure with very good compatibility with zirconia electrolyte [27].

1.3.2.2 Anode (Fuel electrode)

The ceramic anode, or fuel electrode, is a porous layer which has fuel to flow towards the electrolyte. The reaction is expressed as:

$$H_2 + O^{2-} \rightarrow H_2O + 2e^- \quad (1.6)$$

If the fuel gas (e.g. syngas) consists of CO, the CO can also combine with O^{2-} and the anode reaction is:

$$CO + O^{2-} \rightarrow CO_2 + 2e^- \quad (1.7)$$

Same as the cathode, the anode material must be stable with high electronic conductivity. Nickel-zirconia cermet substrate with yttria-stablized zirconia (YSZ) is commonly used as anode material. This composition also enables an internal reforming reaction of methane (i.e. SMR) due to the catalytic behaviour of the nickel in content.

1.3.2.3 Electrolyte

The electrolyte of SOFC is a dense layer with high ionic and negligible electronic conductivity layers to prevent losses from leakage currents. Considering the availability and cost, the most common used electrolyte material currently is the stabilised zirconia with conductivity based on oxygen ions (O^{2-}), especially YSZ [28].

1.3.3 Challenges for SOFC

Currently, SOFC needs to run at about 800-1000°C in order to achieve sufficiently high current densities and power output [29]. This high operating temperature offers several benefits to SOFC, especially in terms of internal fuel reforming. Nevertheless, the high operational temperature is also a key issue that limits the further development and deployment of SOFC: First, it limits the materials selection and may involve a

difficult fabrication processes. The expensive high temperature alloys and ceramics used for cell fabrication and interconnections lead to a high system cost. Balancing the thermal stress of each component at high temperature conditions is extremely difficult [30, 31]. Second, the high operating temperature results in a higher degradation rate of the cell's performance. Problems like thermal expansion/contractions and metal diffusion within the system significantly reduce the lifetime of the SOFC. Third, the large amount of nickel used in Ni/YSZ anode (a minimum of 30% to ensure the required performance [32]) also leads a poor tolerance of sulphur (impurity in hydrocarbon fuels) and carbon deposition (due to cracking of hydrocarbons) when using hydrocarbon as the fuel. Fourth, internal steam reforming is a very fast endothermic reaction which causes a sharp temperature gradient and thermal tension. Additionally, the high operating temperature requires slow start-up and shutdown cycles, which limits the applicability of such SOFCs in the portable power and transportation sectors. To operate at a high temperature, the system also needs to include significant thermal shielding to protect personnel and to retain heat [12, 23, 33-35].

1.3.4 Intermediate temperature-SOFC (IT-SOFC)

1.3.4.1 Benefits of IT-SOFC

Lower operating temperature has been recognised worldwide as the key point for low-cost SOFCs. Operating at an intermediate temperature, i.e. between 500-700°C, would still retain the advantages of improved electrode kinetics and the ability to

internally reform hydrocarbons [18]. Moreover, such a reduction in the temperature makes a reality of using cheaper interconnecting and structural components, such as stainless steel. A lower temperature can also reduce the thermal stress in active ceramic structures, implying to a longer expected lifetime of the system as well as a shorter start-up time [30, 31].

1.3.4.2 Development of cell materials for IT-SOFC

Operating the SOFC at intermediate temperature, between 500-700°C, is considered a future solution in development of the SOFC technology. However, current SOFC cell materials are designed for high temperature conditions, the performance of an SOFC is very sensitive; a 10% drop in temperature results in roughly a 12% drop in cell performance, due to the increase in internal resistance to the flow of oxygen ions [36]. Hence, research efforts have predominantly focused on developing alternative materials for fabricating SOFCs which are suitable for operating at the intermediate temperature range.

Electrolyte materials

YSZ has material imitations of ionic conductivity at low temperature, especially below 700°C. To achieve sufficiently high ionic conductivity at intermediate temperature, several different materials are under development as a replacement for YSZ. Notable candidates include strontium, magnesium-doped lanthanum gallate (LSGM), scandia-stabilised zirconia (ScSZ) and gadolinium or samarium doped ceria (CGO or GSO). However, they all have disadvantages. LSGM (formula

$La_{0.8}Sr_{0.2}Ga_{0.8}Mg_{0.2}O_3$) has significant advantages as a perovskite-type material, with negligible electronic conductivity in a large range of oxygen partial pressures at 400-700°C [37]. The shortcoming of LSGM is its restriction to nickel-containing electrodes. Huang *et al.* [38] found that LSGM reacted with the nickel anode and formed $LaNiO_3$, resulting in a degradation of the Ni/LSGM anode. ScSz (formula $Sc_xZr_{1-x}O_{2-x/2}$) also has excellent ionic conductivity at intermediate temperature. According to Archi *et al*. [39], ScSZ compositions with 8-12 mol % scandia have the highest oxide ion conductivities among all the zirconium oxides. The material currently suffers from synthesis difficulties and a sintering problem that hinder wide adaption. CGO or GSO is another attractive candidate because of its high ionic conductivity and comparability with high performance electrodes' materials. Its disadvantage is due to the narrow region of oxide ionic conductivity under reducing conditions, which produces a short circuit and low output voltage [40].

A number of methods, such as optimisation of doping level, are under development to solve these problems.

Cathode materials

New cathode materials are also needed since oxygen reduction is responsible for much of the loss in performance [23]. To ensure good performance, one task is to reduce the overpotential at intermediate operating temperature to a proper level. LSM is difficult to operate below 800°C due to the shortage of oxygen vacancies for the reduction of oxygen to the three-phase boundary regions [27]. A number of alternative perovskite materials have been proposed and developed for low

temperature SOFC. Among them, a potential one is barium strontium cobalt iron oxide (BSFC, formula: $Ba_{0.5}Sr_{0.5}Co_{0.8}Fe_{0.2}O_{3-\delta}$), which was proposed by Shao and Haile [41]. It has been shown to deliver high power densities up to a power density of 1 W cm^{-2} at 600°C when the anode has minimal losses. However, the conductivity of BSFC is lower compared with common SOFC cathode materials. Another popular material is $Sm_{0.5}Sr_{0.5}CoO_{3-\delta}$ (SSC), which belongs to strontium-doped samarium cobaltite (general formula $Sm_{1-x}Sr_xCoO_{3-\delta}$) material. Liu *et al.* [42] made a nanocomposite SSC cathode with a high power density of 385 W cm^{-2} at 600°C, but the conductivity is much lower than BSFC. Some researchers, like Zhu *et al.* [43], also proposed a SSC-BSFC composite cathode with better performance than just a pure SSC or BSFC cathode. Apart from SSC and BSFC, other potential materials for IT-SOFC cathodes include $Ln_{0.6}Sr_{0.4}MnO_3$ (by Ishihara *et al.* [44, 45]), $La_{1-x}Sr_xFe_{1-y}Co_yO_3$ (LSCF, by Steele *et al.*[46, 47]), and $LaNi_{0.6}Fe_{0.4}O_3$ (by NTT Japan, [48-50]).

Anode materials

Ni/YSZ works properly as anodes, although it is sensitive to sulphur and carbon deposition at high temperatures. Direct reducing the operating temperature of the Ni-YSZ electrolyte causes a dramatic decline in electronic conductivity. One solution is applying substitutial materials to the current system. Murray *et al.* [51] deposited $(Y_2O_3)_{0.15}(CeO_2)_{0.85}$ (YDC) porous film between YSZ electrolyte and Ni-YSZ anode and achieved a 0.37 W cm^{-2} power density at 650°C without carbon deposition.

Another solution is partial or complete replacement of the nickel content. Intensive research efforts are being put on this aspect. Copper, cerium are the most widely investigated compostions, because of their tolerance of carbon formation. Extensive investigations of Cu, Ce cermets anode material have also been reported by several other researchers [52-58], For example, Gorte *et al.* [59] reported that composites containing copper and ceria or samaria-doped ceria had replaced nickel in operations at low temperatures. Perovskite (including bi-perovskite, or doped perovskite)' compositional flexibility and stability in the presence of a large number of oxygen vacancies make it as a potential replacement of nickel. Goodenough *et al.* [60, 61] developed a perovskite $Sr_2Mg_{1-x}Mn_xMoO_{6-x}$, which had long-term stability and sulphur tolerance at 600°C, using methane as the fuel. Its performance was further enhanced by substituting a small quantity of La.

These alternative materials have been considered as the solution of anode for IT-SOFCs. Although, they are still associated with significant problems at present. Compared with Ni/YSZ, the biggest one is insufficient ability for fuel processing [21, 62, 63]. To avoid using an external reformer, high performance catalysts are necessarily required to retain the fuel processing internally.

1.4 Steam methane reforming (SMR)

1.4.1 Introduction to SMR

One of the great advantages of SOFC in comparison with other FCs is its fuel processing ability through the reforming of hydrocarbons. Among various fuels, natural gas is the most promising choice for SOFC, especially for large-scale application. This is due to its low cost, abundant resource and convenient distribution. SMR is also employed as an established process for large-scale production of hydrogen, which currently accounts for 48% of global hydrogen production [64-67]. SMR consists of three major reversible reactions:

$$CH_4 + H_2O \leftrightarrows 3H_2 + CO \quad \Delta H^\circ_{298} = +206 \text{ KJ/mol} \tag{1.8}$$

$$CO + H_2O \leftrightarrows H_2 + CO_2 \quad \Delta H^\circ_{298} = -41 \text{ KJ/mol} \tag{1.9}$$

$$CH_4 + 2H_2O \leftrightarrows CO_2 + 4H_2 \quad \Delta H^\circ_{298} = +165 \text{ KJ/mol} \tag{1.10}$$

The industrial SMR reactions operate at around 800-900°C over nickel-based catalysts in a large-scale reformer reactor [68]. This temperature range is almost the same as the current operating temperature for SOFC. For an SOFC system, the SMR reaction can be conducted both externally and internally [69, 70].

External steam methane reforming (ESMR) is similar to the industrial SMR process, which places a pre-reformer outside the SOFC stack. The benefit of using an external reformer is the avoidance of several engineering and mechanical problems such as the thermal tension from the temperature gradient. Normally, one reformer can fuel several stacks or even a matrix of SOFCs. Because the reformer cannot directly use the steam generated in the electrochemical reactions, there is a need to use extra steam. Accordingly, this leads to a complex system and a low overall efficiency.

Internal steam methane reforming (ISMR) can take place directly or indirectly. For an SOFC with indirect ISMR fuel processing, the SMR reactions take place in a reformer but the reformer is integrated as a part of the cell in a close contact to with the anode. In contrast, reactions in direct ISMR occur simultaneously with the electrochemical reactions at the anode. Compared with ESMR, the ISMR approach has several advantages as a fuel route for SOFC: Without an external reformer, the structure of the whole system is simplified and accompanied with a higher reliability and flexibility. The heat and high quality of steam realised from the electrochemical reaction can be regenerated and used by the SMR reaction. Strong endothermic SMR reactions, on the other hand, decrease the requirement for cell cooling. These significantly reduce running costs and provide high overall system efficiency [71-73]. The disadvantage of ISMR is the temperature gradient effect and possibility of carbon deposition (when using nickel catalyst), which is even more severe in the case of direct ISMR.

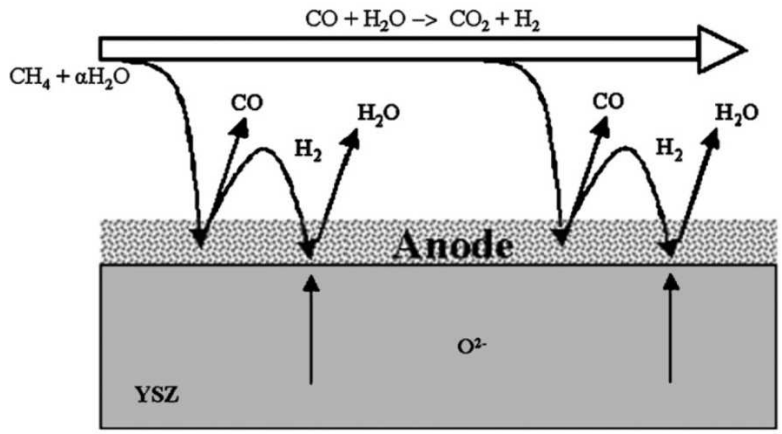


Figure 1.4 Gradual internal steam reforming of methane at SOFC anode [74].

There are several methods to solve these difficulties. The most effective one is operating SMR at lower temperature. Since the ISMR operates at the same temperature as the electrochemical reaction, the whole system's operating temperature should be reduced. Another potential solution is gradual internal forming (GIR). This is an enhancement based on the current ISMR principle. The concept was proposed in 1998 by Vernoux *et al.* [74-79] and received considerable interest. The idea is to associate locally a catalyst for steam reforming and an electrocatalyst for hydrogen electrochemical oxidation. As shown in Figure 1.4, water vapour produced from the local electrochemical oxidation of hydrogen is used progressively for the SMR along the fuel pathway. With gradual reforming, only a small quantity of steam has to be added to inlet fuel and the anode cooling effect is uniformly distributed. By using GIR, a large amount of high-quality steam from electrochemical reactions can be saved and regenerated for a subsidiary application such as CHP to increase overall system efficiency. Because of these benefits, GIR of methane at an intermediate temperature is thought to be a premier fuel processing solution for IT- SOFC [72, 74, 80].

1.4.2 Thermodynamic aspects

Thermodynamics are widely studied to discover the reactions involved and energy conversions in the SMR process in order to study the limits in the reforming process and discover the maximum conversion efficiency [81-85]. Xu and Froment [81] developed reaction schemes with 11 possible reactions occurring during SMR, as shown in Table 1.2.

Table 1.2 Possible reactions during SMR [81].

No.	Reactions	$\Delta H_{298}°$, kJ/mol	Equation
I	$CH_4 + H_2O = CO + 3H_2$	+206.1	(1.8)
II	$CO + H_2O = CO_2 + H_2$	−41.15	(1.9)
III	$CH_4 + 2H_2O = CO_2 + 4H_2$	+165.0	(1.10)
IV	$CH_4 = C + 2H_2$	+74.82	(1.11)
V	$CH_4 + CO_2 = 2CO + 2H_2$	+247.3	(1.12)
VI	$CH_4 + 3CO_2 = 4CO + 2\ H_2O$	+330.0	(1.13)
VII	$2CO = C + CO_2$	−173.3	(1.14)
VIII	$CO + H_2 = C + H_2O$	−131.3	(1.15)
IX	$CO_2 + 2H_2 = C + 2\ H_2O$	−90.13	(1.16)
X	$CH_4 + 2CO = 3C + 2\ H_2O$	−187.6	(1.17)
XI	$CH_4 + CO_2 = 2C + 2\ H_2O$	−15.3	(1.18)

The dominant reactions are (I), (II) and (III). Reactions (I) and (III) are both strongly endothermic reforming reactions accompanied with a molar increase, with the reaction equilibriums being towards H_2 under high temperature and low pressure conditions. The reactions proceed to the right, approaching equilibrium at a longer

contact time [86]. Reaction (II) is a moderately exothermic water-gas shift (WGS) reaction and not appreciably affected by the pressure, although its equilibrium is at a lower temperature compared with (I) and (III). It should be noted that reaction (III) should not only be considered a combination of reactions (I) and (II). The three reactions take place simultaneously, such that CO_2 production not only results from reaction (II) but also directly via a steam-reforming reaction (III) [81, 87-89]. The major productions of SMR are hydrogen, carbon monoxide and carbon dioxide.

For the industrial SMR process, a high temperature shift reactor, mainly performing reaction (I) and (III) with a high S/C (stream to carbon) ratio and a low temperature shift reactor, performing reaction (II) with a low S/C ratio, are connected to the main SMR reformer for a further WGS process to produce hydrogen [90]. In SOFC anode, the primary reactions (I), (II), and (III) are integrated together in the whole SMR. To ensure high rates of methane conversion to hydrogen, a proper S/C ratio is important for ISMR in order to maximise the CO conversion to hydrogen via reaction (II), as well as preventing carbon formation from reaction (IV).

1.4.3 Steam to carbon ratio (S/C ratio)

S/C ratio is a crucial factor for all steam reforming of hydrocarbons. For SMR, S/C ratio equals to S/M (steam to methane) ratio. There are variety of S/C ratios reported in literature, depending on the nature and purpose of the studies. For theoretical modelling, such as in thermodynamics and kinetic studies, an S/C ratio$\leq$2 is often used. A value from 2 up to 6.5 has been mostly reported for industrial SMR reactions

[84, 90]. In practice, a value of 3 to 3.5 is commonly adapted, as suggested by Twigg [90] and Rostrup-Nielsen [67, 91, 92].

A high S/C ratio can suppress the carbon formation from the cracking of methane. It also enhances methane conversion, pushing the three dominant SMR reactions towards hydrogen production. Industrially, a high S/C ratio requires an additional amount of steam, which incurs a high consumption of energy and the large steam inlet also need an increase of volume of the reactor. The unused steam in the mixed resultant gas also derives a dilution of hydrogen and increases the cost of separation. In contrast, a low S/C ratio decreases the methane conversion rate and increases the chance of carbon deposition over a conventional nickel-based catalyst. The carbon deposition also blocks the gas inlet and causes the destruction of the cell.

1.5 Catalysts for SMR

1.5.1 Fundamentals of catalysis

1.5.1.1 Introduction to catalysts

Understanding the nature and fundamental working mechanisms of the catalyst is of great importance for catalyst researchers. A catalyst acts by providing an alternative reaction path with lower activation energy. It does not disturb the final equilibrium composition of the system, only the rate at which that equilibrium is approached [14]. The catalyst has three cardinal parameters: activity, selectivity and lifetime.

Activity

The activity is the ability of the catalyst to convert reactant into products and can be measured by the conversion rate of the reactant or the productivity of the resultant. The unit often used is kg (or mol, L) reactant (or resultant) converted (or produced), depending on the scale of the reaction and nature of the study. The most commonly used unit is $h^{-1} \cdot g$ (or Kg) cat^{-1}. In this thesis, we use mol $(H_2) \cdot h^{-1} \cdot gcat^{-1}$ to express the productivity of H_2 from SMR reactions. Another measurement approach is turnover frequency (TOF), which is the number of molecules of products formed per unit time per surface atom or per unit surface area (SA) of the catalyst.

Selectivity

With the same reactants, the catalyst sometimes activates several reactions at the same time. The selectivity is the ability of the catalyst to give the desired product, out of all products. Generally, the selectivity of a catalytic reaction can be expressed as:

$$Sel_{a_i}\% = \left(\frac{a_i}{\sum a}\right) \times 100 \quad (1.19)$$

where a_i is the desired product concentration and $\sum a$ is the sum of the total product concentrations.

Lifetime

The lifetime is the sum of the net time of the catalyst. It requires a sufficient level of activity and/or selectivity during this period.

1.5.1.2 Heterogeneous catalysis

Generally, catalysis can be either heterogeneous or homogeneous, which depends on whether the catalyst used is in the same phase as the reactants. In heterogeneous catalysts the reactants and the catalysts are in different phase. Currently, more than 90% of the chemical manufacturing processes in the world are controlled by heterogeneous catalysis, including the production of plastics, energy sources, synthetic fibres, paper products, polymers, pharmaceuticals, modern building materials and agricultural products. Most heterogeneous catalysts are solids that act on the reactions using liquid or gas as reactants [93, 94]. SMR reactions typically use solid catalyst acting on gaseous reactants. The major benefit of using a heterogeneous catalyst is the ease of separation of the catalyst in continuous chemical reactions. Furthermore, recycling and process control are also relatively easy.

The key issues of heterogeneous catalysis are adsorption and modification. A heterogeneous catalytic reaction normally involves at least one reactant rapidly adsorbed and modified on the surface of the catalyst. There are many different sites on the surface of the catalyst with different characteristics in terms of reactions. Taylor [95] originally proposed the idea of an “active site” as the surface site where the reactant molecules are adsorbed and modified. Diverse mechanisms of

heterogeneous catalysis on active surface sites have been proposed. The most important one is the Langmuir-Hinshelwood mechanism in which reactions occur by encounters between molecular fragments and atoms adsorbed on the surface (Figure 1.5A). Almost all thermally activated surface catalysed reactions are thought to take place via the Langmuir-Hinshelwood mechanism [14].

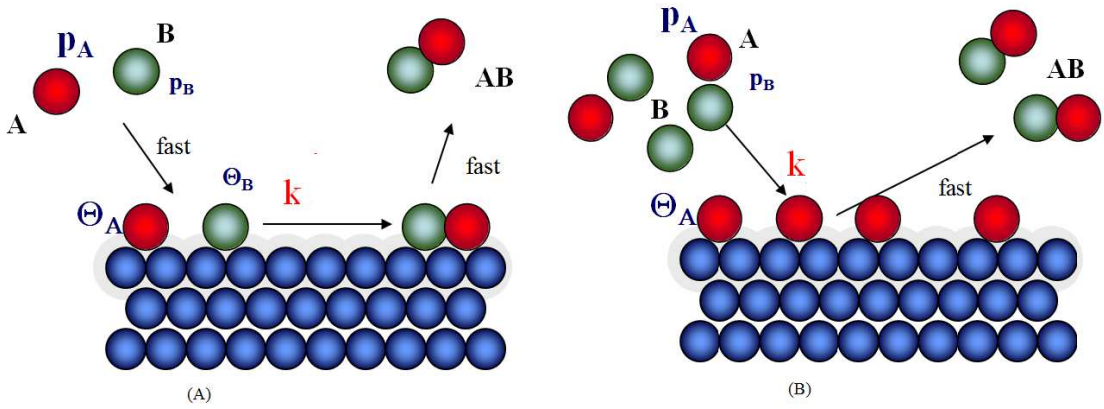


Figure 1.5 (A) Langmuir-Hinshelwood and (B) Eley-Rideal mechanisms [96].

For example, if a bimolecular reaction occurs as follows:

$$A_{ads} + B_{ads} \rightarrow AB$$

The reaction should then depend on the partial pressure of A and B, meaning the rate therefore is as follows:

$$v = k\theta_A\theta_B \qquad (1.20)$$

Where θ is the surface coverage and k is rate constant.

The Eley-Rideal mechanism is another important mechanism in which a gas-phase molecule collides with another molecule already adsorbed on the surface (Figure 1.5B). For example, the adsorbed molecule *B* can directly be modified with the gas-phase molecular *A* without the need for the adsorption A on the catalyst surface, in a bimolecular reaction:

$$A_{ads} + B_{gas} \rightarrow AB$$

The rate of the equation can be expressed by:

$$v = kp_B\theta_A \tag{1.21}$$

where θ_A is the surface coverage of *A*, p_B is the partial pressure of gas *B*, and *k* is the rate constant.

1.5.2 Active metals for SMR reactions

The most commonly used active metal for SMR is the inexpensive nickel metal. It accounts for most industrial hydrogen production from steam reforming of natural gas. Besides nickel, other Group VIII metals are also used as active metals for SMR reactions. Among them, palladium (Pd), rhodium (Rh), platinum (Pt), ruthenium (Ru), osmium (Os) and iridium (Ir) belongs to noble metals, which have outstanding catalytic properties. They have similar physical and chemical properties, and are commonly referred to 'platinum group' metals. Compared with nickel, these noble metals are less sensitive to carbon formation and oxidation in SMR reactions. This

may be explained by the fact that the noble metals do not dissolve carbon [97, 98]. There have been a number of investigations reported by different groups seeking to compare the activity of different active metals. Rostrup-Nielsen and Kikuchi [99] reported their experimental results from steam reforming of methane and ethane over a series of transaction metals at 500°C. They found relative activity in the order: Rh, Ru>Ni, Pd, Pt>Co. Kikuchi *et al.* [100] did the SMR experiments between 350 and 600°C and obtained similar results: Rh-Ru > Ni > Ir > Pd~Pt >> Co, Fe. Qin *et al.* [101] conducted a similar SMR experiment as Rostrup-Nielsen in the temperature range 600-800°C, but only using platinum group metals. The order obtained was: Ru > Rh > Ir > Pt > Pd. All these tests were carried out under atmospheric pressure with minimal support effect. The results showed a common agreement in terms of the order of active metals. Of the pure metal catalysts, Ru and Rh are the most active, Ni and Ir are intermediate and Pd and Pt are less active [102].

1.5.3 Catalyst support

Support is another important part of heterogeneous catalysts affecting catalyst performance. Commonly used supporting materials for SMR catalysis include *a*-Al_2O_3, MgO, $MgAl_2O_4$, SiO_2, ZrO_2, and CeO_2. These materials are all porous, thermally stabile and catalytically inert [103-105]. Support involves providing a high and stable SA for the active compound. It should be noted that support may also affect the catalyst's performance, as it sometimes participates in a subsidiary reaction which indirectly influences the catalytic reactions. This may be due to the different magnitude of synergetic effects. For example, Isha and Williams [106] studied the effect of catalyst support in SMR reactions via nickel catalysts using *a*-Al_2O_3, MgO

and CaO as support, finding the *a*-Al_2O_3 support catalyst had the highest activity. Bradford *et al.* [107] studied MgO and TiO_2, SiO_2 and activated carbon supported nickel catalysts for CO_2 reforming of methane. They found strong metal-support interaction in the Ni/TiO_2 catalyst led to the migration of TiO_x-species. The migrating TiO_x not only blocked the active sites but also prohibited carbon deposition.

1.5.4 Catalyst preparation methods

There are several approaches for synthesis of heterogeneous catalysts for SMR reactions. The commonly used methods are deposition and precipitation. It is essential to deposit the active metals on a support. After preparation, the prepared precursors should overtake thermal treatments (calcination and reduction) to become an activated catalyst.

1.5.4.1 Deposition

Deposition physically or chemically disperses the catalytic component (e.g. nickel) or the materials containing the catalytic compound (e.g. nickel nitrate) on to the supports. The most commonly used method involves an impregnation of metal salt in aqueous solution on a porous oxide support. There are two major ways of performing an impregnation. One way is incipient wetness impregnation. Typically, a salt solution containing the required quantity of active compounds is well mixed with the support materials. The solvent is then evaporated, leaving a solid dispersed mixture. The preparation is normally held in a rotary container to ensure a more homogeneous dispersion. During the preparation, the volume of the solution should be sufficient to

fully immerse the supports. The other method is called pore volume impregnation. In this method, active compounds are contained in a volume of solution corresponding to the total pore volume of the support. The solution is gradually dipped into the support, with one or several drying process in intervals.

Both of the methods are straightforward in terms of handling and cost effective. There are also a variety of selection of active metal and supports [108].

1.5.4.2 Precipitation

The precipitation method involves mixing two or more solutions containing the active compound and support precursor. These substances are precipitated together under certain conditions. Normally, one solution is added to another solution at a specific rate and temperature (or pressure), followed by a digestion to allow nucleation and growth of particles. The final precipitate is filtered and thermal treated. If this association contains two or more active compounds in the precipitate, it can be referred to co-precipitation (CP). The CP process can be divided into two stages and the mechanism involves adsorption, inclusion and occlusion [109]. In the first stage, the impurity is trapped either on the surface (inclusion or adsorption) or inside (occlusion) the growing crystal. The impurities are then either localised in the vicinity of structural defects (due to occlusion or adsorption) or in the solid phase with an imperfect structure (due to inclusion). In the second stage, surface and structure defection become equalised as a result of the decrease of the defects. At this point, the crystal structure of the precipitate acquires an equilibrium composition at a steady condition [110, 111].

1.5.4.3 Other methods

A special preparation method called deposition-precipitation involves the mechanism of both of the two methods, in which the precipitate is formed immediately or gradually in a changing the condition (e.g. pH, [112, 113] light [114] etc.) of the suspension containing the salt solution of the active component and support materials. A precipitation agent is normally used, such as urea. Some other methods including selective removal, thermal decomposition and the sol-gel method are mostly used for laboratory-scale studies [67].

1.5.5 Impact issues for catalyst performance

The activity of the catalyst normally depends on the density of active sites. For this reason, most catalyst preparations are performed with high surface-area materials, in order to obtain a high dispersion of the active compound on the surface [90]. The catalyst particle sizes are normally at nanoscale. Although the large SA and small particle sizes leads to a large population of active sites, the catalyst's reactivity and stability in heterogeneous reaction (not only reforming reactions) also depend on the raw materials, the preparation method and pre-treatment conditions. In practice, catalysts with the same composition but synthesised by different precursors and/or methods may show different catalytic activity. For instance, Wang *et al.* [115, 116] performed methane reforming over impregnated Ni/Al_2O_3 catalysts derived from a different precursor. Their test result illustrated that catalysts derived from an inorganic precursor (nickel nitrate) are much more active and have a lower deactivation rate than those from organic precursors (nickel acetylacetonate). Van

Beurden *et.al* [87] prepared and tested potassium doped catalyst from steam-reforming reactions. They found that the catalyst prepared via CP methods had a much higher tolerance on deactivation than the impregnated catalyst. Wang *et al.* [115, 116] also studied methane reforming with CO_2 and found that the impregnated Ni/MgO-catalyst had better stability than the CP one.

Activation condition is another impact factor in the catalysts' composition and performance. Abelló *et al.* [117] studied partial hydrogenation via Ni/Al catalyst derived from LDH. They used a different calcination temperature range from 500 to 900°C and found that a lower temperature made the catalyst more active. A similar result was reported by Smola´kova´ *et al* [118].

1.5.6 Catalyst deactivation

Catalyst deactivation is a crucial problem of great and continuing concern in the practice of industrial catalytic processes [119, 120]. It is a complex phenomenon which results in a number of unwanted chemical and physical changes. SMR reactions operate at high temperature (commonly 800-1000°C), which creates a severe environment for the catalyst. During operation, the nickel-based catalyst faces four major type of deactivation: poisoning, sintering, oxidation and carbon deposition.

1.5.6.1 Poisoning

Poisoning is a phenomenon in which the catalyst is deactivated by strong chemisorption of impurities from the feed. It divides into temporary (reversible) and

permanent (irreversible) poisoning. During the reaction process, poisons from the reactants or resultants may block the active surface sites or/and change the atomic surface structure. Sulphur is the major poison for steam-reforming catalysts. The small amount of hydrogen sulphide contained in raw materials like natural gas can be chemisorbed on a nickel catalyst:

$$H_2S + Ni_{surface} \rightleftarrows Ni_{surface}–S + H_2. \quad (1.22)$$

This reaction results in a block of the active sites of the catalyst. A filter is normally used to reduce H_2S content in the hydrogen plant and power plant. Nevertheless, a small amount of H_2S in the feed gas can still reach and be chemisorbed on the surface of the nickel catalyst at ppb level even after de-sulfurization. The sulphur tolerance is therefore an important catalyst parameter for steam-reforming catalysts. In this thesis, methane (99.5% purity) containing H_2S impurity was used in order to simulate the practical operating conditions of SMR.

1.5.6.2 Sintering

The sintering of a heterogeneous catalyst is a process of growth of large particles at the expense of smaller particles. It causes a loss of surface as well as a reduction of active sites. Nickel catalyst particles grow and agglomerate during the SMR reaction. The mechanism involves either particle migration or atom migration (Oswald ripening) [121]. The rate of sintering is influenced by several factors, such as catalyst materials, crystallite size, active metal distributions and, most importantly, temperature. According to Sehested's [122, 123] experiment, the speed of this growth

is considerably faster with temperature over 600ºC due to a change in the sintering mechanism from particle migration to Ostwald ripening via atom migration at the support.

1.5.6.3 Oxidation

Oxidation of the nickel particles often occurs at a high S/C ratio and a low catalyst activity. Nickel is activated by reduction in a hydrogen-rich environment prior to the steam reforming operation. At low temperatures, preferential oxidation of nickel catalysts readily occurs. Consequently, the reduction of metallic nickel on the catalyst surface causes the deactivation. Matsumura *et al.* [68] reported that the effect is even stronger than carbon deposition and catalyst sintering when the reaction operates below 500°C. Once the regular reforming conditions are reached, sufficient hydrogen will be present to keep most of the active nickel surface reduced. The activity of the catalyst is then recovered.

1.5.6.4 Carbon deposition

Carbon deposition is a physical deposition of carbon species from the gas phase onto the catalyst surface. In SMR reactions, CH*x*-species from methane may decompose and deposit a thick layer of inactive carbon that cover the actives site of catalyst. Sometimes, a large amount of carbon deposition even blocks the gas inlet.

1.5.7 Improvement of catalysts

Nickel is the most commonly used reforming catalyst mainly due to its low cost, although its activity and carbon tolerance are not as good as noble metals. Practically, it is necessary to improve its performance as well as maintaining the lower cost. An excellent way to do this is by modifying the nickel particles with a small amount of promoters during the preparation stage. After activation, a bimetallic (or tri-metallic) surface with metal-to-metal bonds will be formed. The charge transfer due to these bonds in the bimetallic surface can produce larger perturbations in the electronic, chemical and catalytic properties [124, 125]. Thus, the promoted catalysts have a number of possible benefits in comparison to monometallic ones.

Noble metals, especially platinum group metals, are excellent catalytic materials. Amongst them, Pt, Pd and Rh are most frequently used for reforming at both laboratory scale and industrial level. Ru, Ir and Os are normally used at a laboratory scale [126]. Due to their high cost, a small amount of noble metals are normally substituted for the nickel catalyst. Several research groups have reported their investigations on nickel-based catalysts modified with noble metal precursors. For example, Foletto *et al.* [127] studied a small amount of Pt promoted Ni/$MgAl_2O_4$ catalysts and their results showed that the activity of catalysts in SMR reactions are significantly improved by the addition of Pt. Miyata *et al.* [128] investigated the promoting effect of Pt, Pt and Rh promoted Ni/Mg/Al(O) catalysts for daily start-up and shut-down (DSS) like SMR. The addition of the noble metals they used not only increased the catalysts activity but also exhibited a high suppression of nickel oxidation. Hou *et al.* [129] reported that their use of Rh promoter resulted in a higher

decomposition activity in terms of carbon formation in methane reforming. A common finding from these experiments is that the additions of promoters increase the dispersion of nickel particles by increasing the SA and reducing the crystalline size of the catalyst.

Apart from activity and resistance to deactivation, noble metal promoters also bring some extra beneficial features to the catalyst, such as self-activation and regenerative activity. Li *et al.* [130-132] developed a series of Pt, Rh and Ru doped Ni/Mg(A)O catalysts derived from rehydrated hydrotalcite (HT) precursors. The noble metal promoted catalysts were self-activated under the methane/steam stream in both stationary SMR and DSS-like SMR. Similar results were reported by Hyeok *et al*. [133] using Ru-doped impregnated Ni/$MgAl_2O_4$ catalysts.

1.6 Layered double hydroxide (LDH)

1.6.1 Overview of LDH

Conventional nickel-based or promoted nickel-based catalysts are usually prepared by the impregnation method. A common problem in this method is an inhomogeneity of metal distribution on the surface. Moreover, the catalyst and support are in separate phases, which may cause a potential sintering problem due to migrations on the surface [134-136]. Therefore, the preparation method for increasing the homogeneity inside the structure has attracted considerable research interests and efforts in the last two decades.

Layered double hydroxides (LDHs), also known as hydrotalcite (HT)-like materials, fulfil these requirements as catalyst precursors. Figure 1.6 illustrates the basic structure of a typical LDH. It is based on a brucite ($Mg(OH)_2$) structure with two types of layers: positively charged brucite-like layers (also called the host layer) containing divalent and trivalent cations and negatively charged compensating ions along with water molecules located in between (also called interlayer or guest layer). It can be generally represented by the formula $[M^{II}_{1-x}M^{III}_{x}(OH)_2]^{x+}(A^{n-})_{x/n} \cdot yH_2O$, where M^{II} (M^{II}: Ni^{2+}, Mg^{2+}, Zn^{2+}, Co^{2+}, Pt^{2+}, Pd^{2+}…) and M^{III} (M^{III}: Al^{3+}, Rh^{3+}, Ga^{3+}, Cr^{3+}, Mn^{3+}, Fe^{3+}…) are divalent and trivalent cations and A^{n-} (A^{n-}: $CO_3^{2-}, NO_3^{2-}, Cl^-$ ...) is the anion. In the brucite-like layers, the divalent metal cations are located in the centre of oxygen octahedron and two-dimensional infinite layers are formed by edge-sharing of octahedron [137]. Theoretically, the value of x is generally between $0.2 \leq x \leq 0.33$. Some LDH studies reported a composition beyond this limit, but they may not exist in a single phase [137-139].

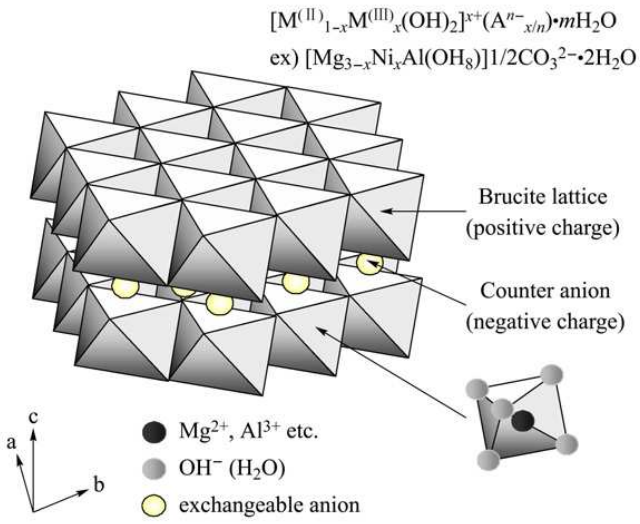


Figure 1.6 Structure of LDH (Example: $[Mg_{3-x}Ni_xAl(OH_8)]1/2CO_3^{2-} \cdot 2H_2O$) [140].

1.6.2 Advantages of LDH as a catalyst precursor

LDHs and their derived materials have great applications in catalysis. They can be modified by altering either the types or molar ratio of M^{II}/M^{III} cations, or the types of compensating A^{n-} anion in the interlayer space. As a catalytic material, the LDHs can be directly used as an actual catalyst in some reactions but mostly they are applied as the catalyst precursors for metal oxide or metal-based heterogeneous catalysts. After calcination and/or reduction, highly dispersed supported mixed metal oxides or metal particles over mixed oxide matrix are formed, along with a large SA and good thermal stability [141].

One significant advantage of LDH compared with the conventional impregnated method is the easiness it engenders in the fabrication of the SOFC anode [142]. This is extremely important for ISMR- or GIR-based SOFC since the quality of the catalyst layer on the anode surface directly influences system performance. The dried impregnated catalyst power, either as precursor or calcined catalyst, is hardly incorporated on the surface of the anode. In contrast, the as-prepared aqueous LDH slurry, with good viscosity, can easily be coated and pre-treated on the anode surface.

1.6.3 LDH precursors for preparing SMR catalysts

Two naturally occurring LDHs are mostly used and reported as catalyst precursor for preparing SMR catalysts from previous reviews. One LDH is hydrotalcite (HT) with a general formula $Mg_6Al_2(OH)16CO_3 \cdot 4H_2O$ (or written as general LDH form

$Mg_{0.75}Al_{0.25}(CO_3)_{0.125}(OH)_2]\cdot nH_2O$). Pure HT does not contain active metal for the reforming reaction; hence parts of the Mg are normally replaced by the Ni or noble metal during synthesis. The other one is called takovite with a general formula of $Ni_6Al_2(OH)_{16}CO_3\cdot 4H_2O$ (or written as general LDH written form: $Ni_{0.75}Al_{0.25}(CO_3)_{0.125}(OH)_2]\cdot nH_2O$). The Ni/Al ratio varies between 2.5 and 3 in practice. An HT-like precursor is normally applied for preparation of low percentage nickel loading catalyst or investigation of pure noble metal loading catalyst. Its derived catalyst contains a large weight percentage of Mg-Al mixed oxide support, which has very good thermal stability at high operating temperatures (800-1000°C). The low percentage nickel or noble metal loading also reduces deactivation from carbon deposition. Commercially, HT is a thermal treated at high temperature (>700°C) and employed in reformer-based SMR reactions, such as industrial H_2 production or ESMR-based PEMFC [132, 143, 144]. Several phases normally co-exist in the derived catalyst. The takovite -like material has a very high nickel proportion but remains a high surface dispersion of nickel for catalysis. High levels of exposed nickel on the anode surface are beneficial to direct ISMR, especially GIR reactions [75]. For SMR at low temperatures, it is possible to compensate the activity loss when the reaction occurs at a lower temperature. Experimental results in this thesis show the reactivity of SMR is higher when using a high nickel loading LDH-derived catalyst (Chapter 3).

1.6.4 Preparation methods

There are more than 10 synthetic techniques reported and applied for making LDHs, including CP, ion-exchange method, rehydration, urea hydrolysis method, sol-gel

method, and intercalation [141, 145]. In this chapter, we only introduce the three most commonly employed methods: CP, ion-exchange and rehydration. The CP method is a basic method for preparing LDHs. Ion-exchange and rehydration are methods for modifying the LDHs prepared earlier. They are mostly useful when the CP method is not applicable for direct synthesis of some LDHs.

1.6.4.1 CP method

The most common used preparative method is CP, which works by precipitating an aqueous solution of M^{2+} and M^{3+} with CP agent solution containing anion at a given condition. The method allows a variety of divalent and trivalent cations and anionic species to be selected for making different types of catalysts. To ensure simultaneous precipitation of two or more cations, it is necessary to synthesise the LDH under the conditions of supersaturation [137]. This can be achieved by two methods: low supersaturation and high supersaturation.

Low supersaturation is performed by slowly mixing the addition of mixed solution of calculated amount of desired M^{2+} and M^{3+} ions to the CP agent solution containing the desired interlayer anions. The pH value is simultaneously maintained at an optimum value by adding another pH-controlling solution at a given rate. After co-precipitation, the precipitates are aged by maintaining them at a particular temperature to increase the crystallinity. In order to prevent a competing reaction of metal salt combing the M^{2+} or/and M^{3+} ions with anions, the anions chosen must have a higher affinity towards LDH and should be present in excess. Carbonate anions have a higher affinity to LDH layers and therefore a mixture of NaOH and Na_2CO_3 solution

is the most commonly used as CP agent to provide anions for LDH preparation. Compared with other cations, the monovalent Na^+ has almost no affinity to LDH and is easily washable. Nitrates have low selectivity to LDHs and, therefore, metal nitrates are commonly used as raw materials for preparing takovite-like (Ni/Al) or HT-like (Ni/Mg/Al) LDH. Many studies of steam reforming over Ni/Al or Ni/Mg/Al catalysts derived from LDH have been reported. A constant pH of 10 is the most commonly used to perform the supersaturation condition [140, 146-148]. Noble metal promoters could be incorporated into the LDH's layers, forming a homogeneous coordination. According to Basile *et al* [149], a small quantity of platinum group metal ions Pd^{2+}, Rh^{3+}, Ir^{3+}, Ru^{3+} and Pt^{2+} were successfully incorporated to the brucite layer of the LDH at a pH of 10.

In high supersaturation precipitation, on the other hand, the mixed solution of interlayer anions is added into a solution containing the desired ratio of M^{2+} and M^{3+} ions. Compared with low supersaturation, this method often gives lower crystalline LDH because of the higher number of nuclei. The continuous change of pH during synthesis also results in an undesired M(II)/M(III) ratio and $M(OH)_2$ and/or $M(OH)_3$ phase [137].

1.6.4.2 Ion-exchange method

In the ion-exchange procedure, external guest ions are exchanged with anions in the interlayers of synthesised LDH. This method can be expressed as follows:

$$LDH \cdot A^{m-} + X^{n-} \rightarrow LDH \cdot (X^{n-})_{m/n} + A^{m-} \quad (1.23)$$

Or

$$LDH \cdot A^{m-} + X^{n-} + mH^{+} \rightarrow LDH \cdot (X^{n-})_{m/n} + H_mA \quad (1.24)$$

Guest ions can be provided from acid or salt. Bish [150] first proposed this method and successfully exchanged the carbonate with chloride, nitrate and sulphate. The method is easily achievable and has now received increasing attention in relation to catalysis, biological applications and from the drug industry [151, 152]. One essential condition of the ion-exchange method is that the anions in the interlayers of the parent LDH must be weakly interacting with two neighbour brucite layers. Furthermore, the radii of gust anions also have not to exceed the limits of the interlayer expansion. Ion-exchange can be performed by either an acid attack or slow permeation, which depends on the property of the parent LDH. A low pH value is favoured for liberation of the original ions, although high acidic conditions may also destroy the structure of the parent LDH [137].

1.6.4.3 Rehydration method

Rehydration using the structural “memory effect” is another synthetic method. It consists of two steps during preparation. Firstly, the LDH is thermally deconstructed at a certain temperature, forming mixed metal oxides. Then, the calcined oxide is immersed in an aqueous solution containing anions for regeneration after cooling. The LDH structure is gradually recovered under this condition. Here, the anions can either be the same as the original one or an alternative one. This ‘memory effect’ is sensitive to the calcination temperature. An increase in calcination temperature may result in a

longer reconstruction time. A higher calcination temperature (e.g. >800°C) may also cause a partial of wholly loss of the 'memory effect' due to the migration of Al^{3+} to the tetrahedral site. Non-recoverable $MgAl_2O_4$, $NiAl_2O_4$, γ-Al_2O_3 will be formed under this condition [153].

The rehydration method is normally used to intercalate large organic or inorganic guest anions, and particularly large ions are intercalated. Sometimes, it is also applied for the substitution of promoters to LDH brucite lattices [137]. Takehira *et al.* [130, 132, 140, 143, 154] successfully prepared a series of Pd, Rh, Pt and Ru promoted Ni/Mg(Al)O catalysts for SMR using rehydration methods. However, it was found that not all the noble metals were incorporated in to the M(II)/M(III) sites, with some of them being physically trapped in the layered structure. This causes a phase separation and an inhomogeneous dispersion of noble metal.

1.6.5 Takovite

Takoviate (Ni/Al HT) is a naturally existing LDH material. The Ni/Al ratio is normally about 3:1, though variations exist and can be made up to 1:2 in a synthetically produced approach. After calcination and reduction, mixed crystalline metallic oxides can be obtained with high nickel loading, high metal (inter) dispersion, large SA and small particle sizes. After thermal treatments, the oxide and reduced materials have very strong thermal stability compared with the supported materials prepared by impregnation method. Several reactions are involved in this procedure:

$$Ni_6Al_2(OH)_{16}CO_3 \cdot 5H_2O \rightarrow Ni_6Al_2O_9 + 13H_2O + CO_2 \quad (1.25)$$

$$Ni_6Al_2O_9 \rightarrow 5NiO + NiAl_2O_4 \quad (1.26)$$

$$Ni_6Al_2O_9 \rightarrow 6NiO + \gamma\text{-}Al_2O_3 \quad (1.27)$$

Reaction (1.25) can take place at a wide temperature range from 350 to 800°C. Reaction (1.26) and (1.27) require a huge energy input for the formation of $NiAl_2O_4$ and γ-Al_2O_3 hereby occurs at a high temperature (>800°C). Based on the cubic structure of nickel oxide and nickel aluminate, Puxley *et al.* [155] describe the mixed oxide system as an metastable state without the presence of pure NiO and γ-Al_2O_3 (Table 1.3).

Table 1.3 Range of structures possible in oxide form of co-precipitated Ni/Al catalyst [155].

Structure	Probable site occupation		Aluminium content or calcination temperature
	Octahedral	Tetrahedral	
NiO	Ni^{2+}		Low
Substituted nickel oxide (S.N.O.)	Ni^{2+}, Al^{3+}		
Disordered oxide – spinel intermediate (D.O.S.I.)	Ni^{2+}, (Al^{3+})	Al^{3+}	
Spinel-like material (S.L.M.)	Ni^{2+}, Al^{3+}	Al^{3+}	
$NiAl_2O_4$	Ni^{2+}, Al^{3+}	Al^{3+}	
NiAl2O4 /γ-Al_2O_3	Ni^{2+}, Al^{3+}	Al^{3+}	
/γ-Al_2O_3	Al^{3+}	Al^{3+}	High

After reduction in H_2, the mixed oxide becomes a homogeneous supported Ni/Al catalyst. No clear border can be detected from the nickel and support [156]. Nickel metal is present in the paracrystalline structure. The lattices of each nickel crystalline are disturbed and strained by random point defects (e.g. aluminate group) [155]. Unlike an impregnated catalyst, the metal and support in the LDH derived catalyst are

intracrystallined in the same phase, with very strong metal to support interaction. Sintering effects are therefore weakened, due to the inhibition of particle migration in different phases [68].

1.7 Scope of the thesis

1.7.1 Research objectives

SOFC, using natural gas as fuel, will play a greater role in the future electricity generation. The development of materials will mean that SOFC operation at lower temperatures becomes a reality. The ideal operating temperature of the next generation of SOFC is between 500 and 700°C. To achieve this target, highly active catalysts for lower temperature SMR reactions must be developed. Commercial nickel-based impregnated and HT-derived catalysts are primarily designed for high temperature reformer reactors rather than fuel cells. They have disadvantages in terms of their low nickel loading and surface separation. Also, it is difficult for the impregnated catalysts to be coated firmly and uniformly on the surface of SOFC anode.

The principle aim (and research question) of this thesis is to develop catalysts which are suitable for steam reforming capable of operating internally in an IT-SOFC anode environment ***(as research question 1)***. The initial requirements of catalysts are simple and easy preparation as well as inclusion of these catalysts within the anode of SOFC during their fabrication. They should also be cost effective with good activity,

stability and tolerance to deactivation at intermediate operating temperatures. Moreover, the catalyst should also be suitable for SMR reactions operating at both stationary and daily start-up and shout-down (DSS) modes.

Investigations are carried out on Ni/Al LDH-derived catalysts with Pd and Rh promoters. It is clear from a literature review that there is no systematic study available for SMR at low or intermediate temperature range using LDH-derived catalysts. Research on low or intermediate temperature SMR have mostly been carried out over impregnated catalysts. The main aim of these studies was to reduce the energy consumption in the industrial SMR process for producing hydrogen [68, 157-161]. LDH-derived catalysts have mostly been reported in studies of ethanol [147, 162, 163] and methanol reforming [164], hydrogenation [117, 165-168], dehydrogenation [118, 169, 170] and high temperature SMR [131, 132]. Hence, this thesis also aims to conduct a systematic study of LDHs and the derived catalysts, with particular focus (research questions) on: the effect of catalyst preparation and calcination conditions on catalyst performance ***(as research question 2)****;* the role and promoting effect of some noble metals on catalytic performance and possible mechanisms ***(as research question 3)***; and new preparation methods to produce LDH which can easily be coated on SOFC anodes ***(as research question 4)***. The synthesised LDHs and their derived catalysts have been characterised using a variety of techniques, including X-ray diffraction (XRD), temperature programmed reduction (TPR), thermo-gravimetric analysis (TGA), BET surface area measurement (BET), scanning electron microscopy (SEM), transmission electron microscopy (TEM), energy-dispersive X-ray analyser (EDX) and Fourier Transform Infrared (FTIR). Catalytic studies were carried out using an indigenous-built tubular micro-reactor.

1.7.2 Structure of this thesis

The present work is compiled and presented in eight chapters.

Chapter 1: A comprehensive overview of FCs, SOFC, SMR reactions, catalysts for SMR reactions and LDHs are reviewed.

Chapter 2: Methodologies for catalysts synthesis, pre-treatment, testing and their characterisation and the instruments used for such studies are given in this chapter.

Chapter 3: Effect of preparation condition on the composition/structure of LDH precursors and the activities of derived catalysts are investigated. A series of Ni/Al, noble metal substituted LDHs and derived catalysts are prepared and tested.

Chapter 4: The impact of calcination temperature on catalytic activity and the promoting effect of noble metals were studied on Ni/Al, Pd and Rh promoted Ni/Al Ni/Al catalysts derived from their as-prepared LDHs.

Chapter 5: Detailed studies on promoter quantities for the SMR reactions were carried out.

Chapter 6: A new method for synthesising fine LDHs for easy coating on the anode surface is developed.

Chapter 7: Stability, self-activation and self-regeneration behaviour of promoted catalysts are also investigated.

Chapter 8: Overall conclusions of this thesis and possible future work are finally summarised.

Chapter 2. General experimental methods

2.1 Introduction

The first part of this chapter describes the catalyst preparation methods. This includes a detailed description of the CP procedure of LDH and subsequent thermal treatments adopted in this thesis. The second part describes catalytic studies in the micro-reactor and product analysis method. Several different methods for testing the catalyst's activity, selectivity, stability and self-activation behaviours have been developed for SMR in simulated SOFC anode operating conditions. The final part gives the functions and fundamental principles of various methods employed in characterising the catalysts and catalytic reactions.

2.2 Preparation of LDHs

LDHs can be prepared by several different methods as discussed in Chapter 1. In the present study, the cost-effective and easy CP technique was used to prepare the LDH precursors. A low-supersaturation synthesis method was developed similar to the one reported by Rives *et al.* [146], albeit with minor modifications. Figure 2.1 demonstrates the preparation procedure for Ni/Al LDHs and noble metal promoted Ni/Al LDHs.

2.2.1 Preparation of Ni/Al LDHs

Nickel was chosen as the active metal since it is the most cost-effective option and is commonly used as a catalyst for steam reforming of natural gas. Palladium, rhodium

and platinum were used as promoters to enhance the catalytic performance. Ni/Al LDH, with a nominal Ni/Al ratio of 3:1, known as takovite $Ni_6Al_2(OH)_{16}CO_3{\bullet}5H_2O$ (or by common LDH formula $[Ni_{0.75}Al_{0.25}(CO_3)_{0.125}(OH)_2] \bullet nH_2O$), was prepared as the base catalytic precursor. The syntheses were performed at near ambient temperature in air. De-carbonated de-ionised (DCDI) water was used throughout the preparation to prevent absorption of CO_2. There are several basic steps involved in the preparation process, which are presented below.

2.2.1.1 Mixing

40g NaOH and 53g Na_2CO_3 were respectively dissolved in 1 L DCDI water in glass-stoppered bottles to give (a) 1 mol/L sodium hydroxide and (b) 0.5 mol/L sodium carbonate stock solution. The CP agent solution, a mix of 80 mL solution (a) and 80 mL solution (b) with 80 mL DCDI water in a glass beaker, was gently heated to 40, or 70°C under controlled vigorous stirring. Then, a freshly prepared 2 mol/L transparent metal ion solution containing 23.78g $Ni(NO_3)_2 \cdot 6H_2O$ and 10.23g $Al(NO_3)_3 \cdot 9H_2O$ in 55 mL DCDI water was slowly dropwised to the CP agent solution at a constant pH of 10. Green slurry of LDH was formed during the mixing process.

2.2.1.2 Aging

The co-precipitated LDH slurry was aged at 40, or 70°C for 4, or 24 h with constant stirring at a constant pH of 10. The pH was maintained by adding small quantities of the CP agent. The aim of aging is to provide a further crystallisation of the LDHs.

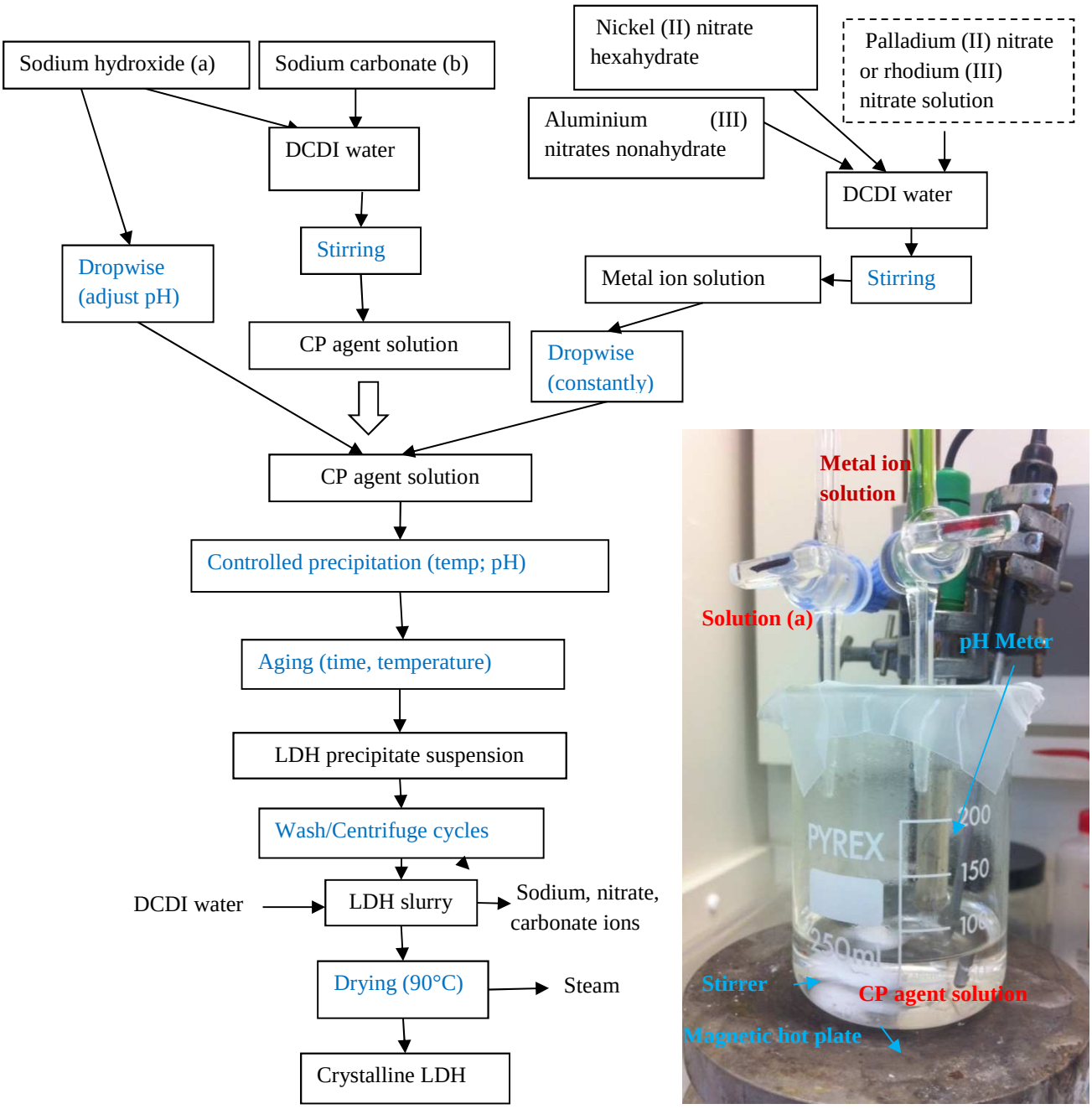


Figure 2.1 Schematic diagram for the preparation of Ni/Al LDH.

2.2.1.3 Washing, filtering and drying

The aged precipitate was washed several times with DCDI water to remove all sodium ions and other residential ions. The washing and filtration processes were

repeated until the pH of the filtrate became neutral. The precipitate was then dried at 90°C in the air for 12 h to obtain a high crystalline LDH.

2.2.2 Preparation of noble metal substituted Ni/Al LDHs

For the preparation of Pd, Rh or Pt substituted LDHs, calculated amounts of palladium (II) nitrate (Assay 8.16%) solution or rhodium (III) nitrate solution (Assay 13.21%) or teraammine platinum (II) powder (99.995% metals basis) were used to substitute part of nickel nitrate in the mixed metal ion solution prior to the preparation to obtain the required ratio. This was done following the same procedure described earlier.

A series of Pd and Rh substituted Ni/Al LDH samples, with common formula $([A_xNi_{0.75-x}Al_{0.25}\ (CO_3)_{\ 0.125+\delta}\ (OH)_2]\bullet nH_2O$, where A is Pd or Rh ($0<x\leq0.05$) were prepared with different molar ratios, and/or by different preparative conditions (CP temperature, aging temperature and time). Pt was found unflavoured to the LDH and study on this aspect can be referred in Chapter 3. All LDHs were characterised by XRD and EDX to confirm the structure and compositions.

2.3 Calcination

The mixed oxide steam reforming catalysts Ni(Al)O, Pd promoted Ni(Al)O or Rh promoted Ni(Al)O were obtained by calcination of the relevant as-prepared LDH precursors. The LDHs were pressed, gently crushed and sieved to obtain the fraction

with a particle size of 0.2–0.4 mm. The separated grains were calcined in a muffle furnace in a static air atmosphere by elevating the temperature from 50°C to the chosen temperature range from 450°C to 1000°C (represented by '-C+calcination temperature' in the catalyst name, e.g. -C550) at a rate of 5°C/min and then kept at the maximum temperature for 4 h.

2.4 Catalytic performance studies

In order to investigate the catalytic behaviour of these as-prepared catalysts, SMR reactions were studied under different test conditions.

2.4.1 Experimental set-up

To simulate the steam reforming under the SOFC anode operating condition, catalyst pre-reduction and catalytic studies were carried out at atmospheric pressure in an indigenously built tubular micro-reactor. The reactor was equipped with a furnace which could be heated to 1000°C at a desired heating rate. A schematic view of the experimental set-up is presented in Figure 2.2. The benefits of using a micro-reactor are the low cost, easy set-up, quick loading, and good distribution of temperature [171]. The catalyst was tightly loaded in the middle of a quartz tube (OØ: 6mm, IØ: 4mm) between quartz wool. The tube was heated in an electrical furnace. Reactor temperature was regulated by a K-type thermocouple placed at the centre of the catalyst tube. The whole system was maintained in an oven at 150°C. This reactor has the facility to feed Ar (99.999%), H_2 (99.999%) and CH_4 (99.5%), which were

supplied by BOC Gases and were used without further purification. The gases were fed into the reactor via mass flow controllers (MFC). DCDI water was introduced to a steamer which was operated at 550°C. The flow rate was controlled by a high-pressure water pump. The steam generated was mixed with CH_4/Ar flow just before entering into the reactor. The outlet gas from the reactor then passed through a condenser/separator kept at -25°C to remove steam/water from the gas product. The de-watered gas mixture was analysed by an online Hewlett Packard 5890 Series II gas chromatograph (GC) equipped with a thermal conductivity detector (TCD) using helium (from BOC) as the carrier gas.

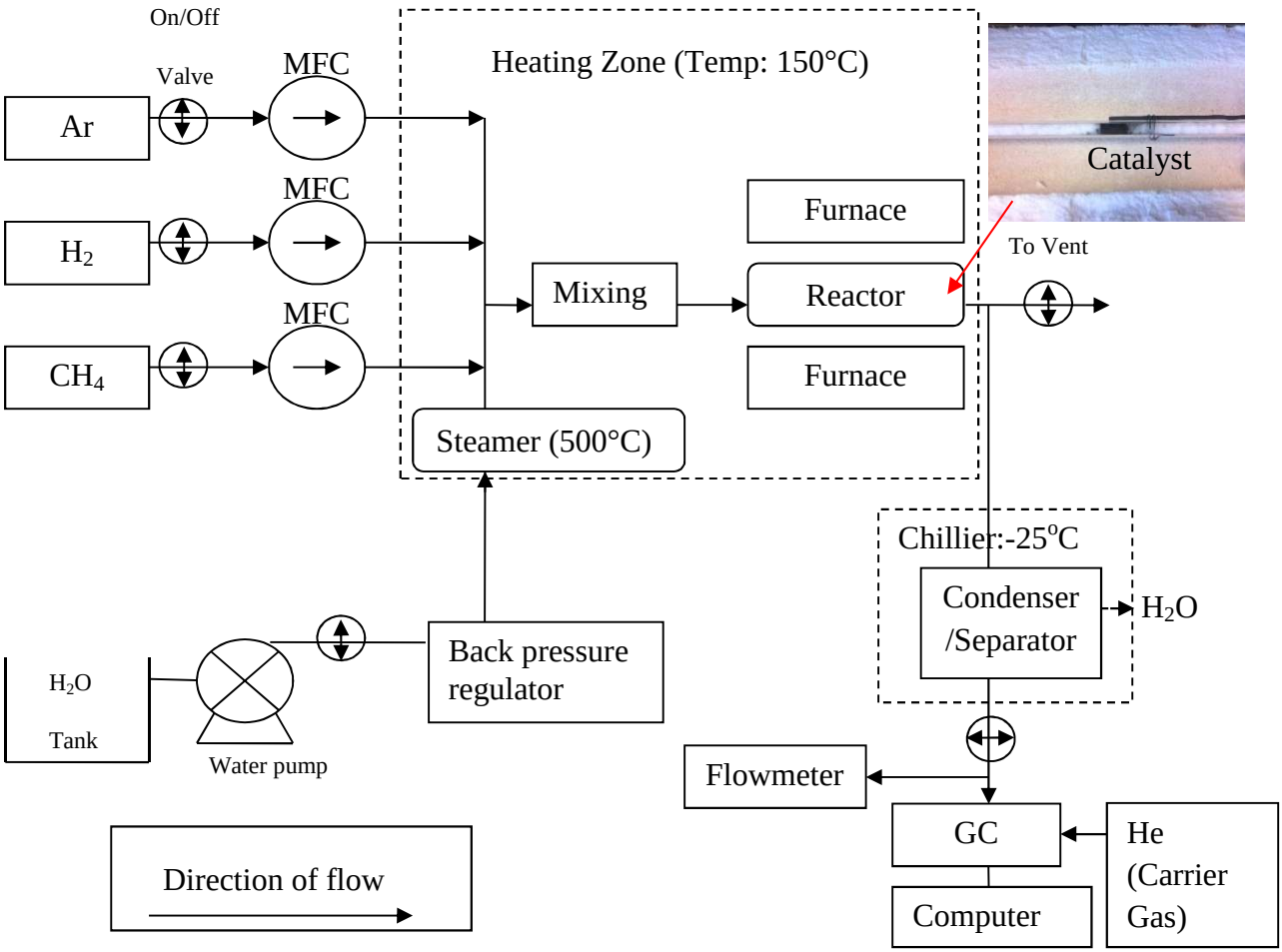


Figure 2.2 Schematic diagram for catalytic testing in micro-reactor unit.

2.4.2 Catalyst activation

130 mg calcined catalysts (derived from about 200 mg LDH) were loaded into the reactor tube. The sample was then preheated in 23.5 mL/min Ar flow at 50°C for 30 minutes and then reduced *in-situ* at 700°C (represented by '-R700' in the catalyst name) for 1 h in a flowing 10% H_2 in Ar. The ramp rate of the furnace was 10°C /min. The reduced catalyst was then cooled down to ambient temperature and kept in Ar atmosphere for at least 30 minutes prior to catalytic study.

2.4.3 Catalytic studies

In the present study, several catalytic studies were performed to evaluate the catalytic activity, stability, self-activation, and tolerance of oxidation and the promotional effect of noble metal promoters. The entire test was performed with a steam to methane ratio (S/C ratio) of 3:1 at ambient pressure.

2.4.3.1 Activity measurement

The SMR was performed on the reduced catalyst in the above-mentioned micro-reactor at atmospheric pressure. Argon was used as protection gas as well as the internal standard for calculating the methane consumption (conversion) and the productivity of other products.

The reduced catalyst was heated up to 250°C in 23.5 mL/min Ar flow and kept for 10 minutes. Then, 48 mL/min steam followed by 16.2 mL/min CH_4 was introduced into the Ar stream. This order of introducing the reactant gases was maintained to ensure that the methane reacts with sufficient steam at the beginning of the SMR reaction, preventing any carbon deposition on the catalyst due to CH_4 decomposition. The product gas was passed through the condenser/separator unit to remove excess steam/water before being introduced into the GC for analysing. The SMR reactions were step performed from 250°C and 700°C with an interval of 50°C for each elevation. A slow heating rate of 5°C/min was applied when the temperature of the reactor was changed. A 30-minute equilibrium time was allowed at each temperature prior to GC recording. Three measurements were then made at each temperature, with 15-minute intervals.

2.4.3.2 Stability test

Catalyst stability was evaluated by flowing a stream of CH_4/H_2O/Ar (26.8/18.3/54.9 vol.-%) with a constant flow rate of 87.5 mL/min. After *in-situ* reduction of 130 mg calcined catalysts, reaction was started at 250°C following the same procedure as described in Section 2.4.3.1. The reactor temperature was then increased to 600°C at a rate of 5°C/min and kept at this temperature for 110 h. The activity was tested for every 2 h (during daytimes only) throughout this period.

2.4.3.3 Self-activation

Self-activation properties of noble metal promoted catalysts in SMR reaction were reported by several researchers [143, 172-175]. The self-activation property of the catalysts Pd, Rh promoted catalyst were studied in the isothermal mode at 600°C over 130 mg catalyst with 87.5 mL/min CH_4/H_2O/Ar (26.8/18.3/54.9 vol.-%) gas mixture at atmospheric pressure, without a pre-reduction step. Each test was maintained for 180 minutes in order to assess the stability of the self-activated catalysts. Initial GC data collection was done after 30 minutes of operation and subsequent data were collected every 15 minutes.

2.4.3.4 Purged DSS operation

A daily start up and shut down (DSS)-like operation was carried out among chosen catalysts following the procedure reported by Takehira *et al.* [143, 174, 176], with minor modifications. After pre-reduction of 130 mg calcined catalysts, the reactor temperature was cooled down 600°C for the first cycle SMR operation for 90 minutes, under the same condition of the standard activity measurement. Then the methane inlet was cut-off and the reactor was cooled down to 250°C under purging with a 71.5 ml/min steam/argon (67.2/32.8 vol.-%) mixed gas. After keeping the reactor at 250 °C for 30 minutes, the temperature was again increased to 600°C under the purging conditions. When the temperature reached 600°C, the reaction was started by re-introducing 16.2mL/min methane flow the into the purging gas, carried out at 600°C for 90 minutes and followed by steam purging. This cycle was repeated three times to

simulate the DSS-like operation of domestic use SOFC. GC data was collected every 15 minutes.

2.4.4 Calculation methods

The results obtained for CH_4 conversion, H_2 productivity, CO and CO_2 selectivity are defined by the following equations:

$$CH_4\ consumption\ (\%) = \frac{P_{CO}+P_{CO_2}}{P_{outletCH_4}+P_{CO}+P_{CO_2}} \quad (2.1)$$

$$COselectivity(\%) = \frac{P_{CO}}{P_{outletCH_4}+P_{CO}+P_{CO_2}} \quad (2.2)$$

$$CO_2\ selectivity\ (\%) = \frac{P_{CO_2}}{P_{inletCH_4}+P_{CO}+P_{CO_2}} \quad (2.3)$$

$$H_2\ Productivity\ (mol \cdot h^{-1} \cdot g_{cat}^{-1}) = \frac{\frac{P_{H_2}}{P_{outletCH_4}+P_{CO}+P_{CO_2}} \times 16.2 \times 60}{22.4 \times 0.13 \times 1000} \quad (2.4)$$

where *P* is the partial pressure of the gas, 22.4 is the molar volume of ideal gas (25°C, unit: dm^3/mol), 16.2 stands for 16.2ml/min CH_4 inlet flow rate and 0.13 is the weight of catalyst loaded during each test (unit: g). Equations 2.1, 2.2 and 2.3 are based on the conservation of carbon during the reaction.

2.5 Catalyst characterisation

Catalyst characterisation is an essential part of any catalytic study to understand reactions and their mechanisms. In this thesis, several different characterisation methods have been used to probe the state of the Ni/Al and precious metal promoted Ni/Al catalyst systems.

2.5.1 X-ray diffraction (XRD)

2.5.1.1 Purpose

X-ray diffraction (XRD) is one of the most commonly used techniques for characterisation of heterogeneous catalysts since the diffraction patterns may be used to identify the structure and composition of the crystalline materials. It can also yield an estimate of the crystallite size of the micro-crystallite and *d*-spacing, as well as insights into the atomic constituents of the unit cells [177].

2.5.1.2 Fundamental principle

X-rays are radiation produced by bombarding a metal target with high energy (10 – 100 keV), knocking out the core electrons [171]. When a sample with a crystal structure is projected by a monochromatic X-ray beam at the angle θ, diffraction occurs as the beams travel through the planar spacing formed by the sample's atomic structure [178]. The relationship between the wavelength of incident X-ray beam λ,

the angle of diffraction θ and the distance between planes in atomic lattice *d* are expressed mathematically in Bragg's law (equation 2.5), where integer *n* stands for the order of reflection (Figure 2.3):

$$n\lambda = 2\,d\sin\theta;\ n = 1,2,\ldots \tag{2.5}$$

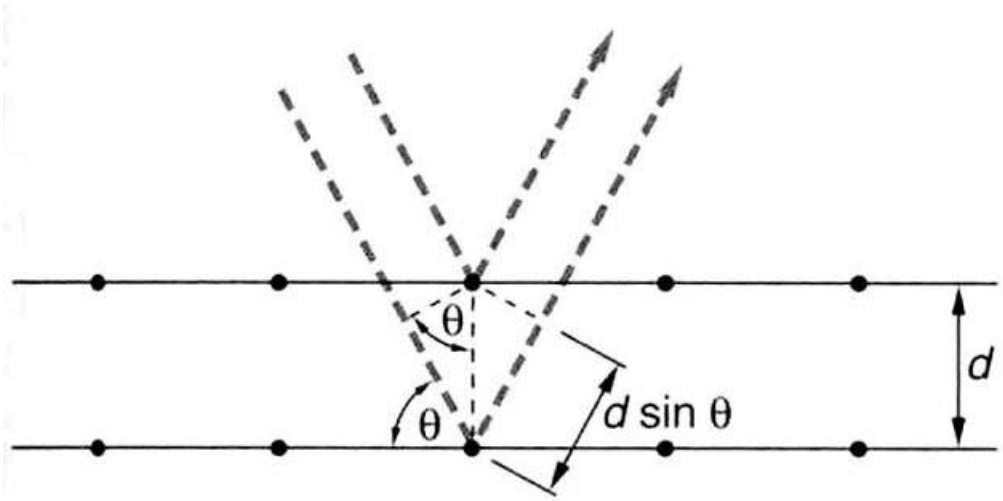


Figure 2.3 Diffraction of X-rays by a crystal [179].

The law is strictly applied for crystals with a perfect parallel attacked by a monochromatic beam. In most circumstances, deviations from ideal conditions must be taken into account when considering real diffraction phenomena.

For very small crystals, fewer planes produce a particular Bragg diffraction. As Bragg's law gives the condition for constructive interference, at θ values slightly higher than the Bragg angle each plane gives a "lag" in the diffracted beam. For many planes, this ends up cancelling out and thus the net diffraction is zero. In small crystals there are relatively fewer planes, causing a "remanent" diffraction [94].

Consequently, this leads to a broadening of the diffracted beam. This phenomenon can be described by the Scherrer equation and provides an approach for determine the average crystallite size:

$$t = \frac{K\lambda}{\beta \cos\theta} \tag{2.6}$$

where t is the thickness of the crystal in the direction perpendicular to the diffracting planes, K is the shape factor typically with a value of about 0.9, λ is radiation wavelength, β is the full width at the half maximum (FWHM) of the peak and θ is the Bragg angle.

2.5.1.3 Experimental method

A PANalytical PW3040 Powder X-ray diffractiometer using Cu Kα (λ =nm) radiation and operating at 40 kV and 40 mA using the θ-2θ model was used for the measurement of the as-prepared LDH precursors and the derived calcined catalysts. Since the freshly reduced catalyst is very active and the catalyst is quickly passivated after contact with the air while handling,, another PANalytical PW3040 XRD but equipped with a high-temperate gas supplied *in-situ* chamber with temperature programme function (ambient temperature to 900°C) was used for the study of freshly reduced catalysts. Both of these XRDs are interfaced with microcomputers for program setting and data collection. Fine powder samples, such as ground LDHs and calcined catalysts, were mounted onto an aluminium plate with a groove cut (or ceramic holder for *in-situ* XRD) and smoothed out flat using a flat glass slide. Diffraction patterns were obtained from 5° to 85° at a rate of 2° per minute. The phase

identification was carried out by comparing the collected diffraction pattern with the available files from the International Centre for Diffraction Data (ICDD) and from published literatures. The particle sizes were calculated using the Scherrer equation from the most intense XRD peaks.

2.5.2 BET surface area measurement

2.5.2.1 Purpose

The BET (Brunauer, Emmett and Teller) is a one of the most widely used methods to measure a catalyst's specific surface area. It involves applying the physical adsorption of nitrogen on the solid sample's surface at liquid nitrogen temperature (-195.8°C).

2.5.2.2 Fundamental principle

BET theory was proposed by Stephen Brunauer, Paul Hugh Emmett and Edward Teller in 1938. Normally, the sample is loaded in a chamber where the temperature can be reduced to liquid nitrogen temperature. An inert gas (normally nitrogen gas) is physically adsorbed on the solid surface until it reaches equilibrium. The amount of nitrogen gas molecules adsorbed is measured over a range of pressures below one bar. The adsorption process is exothermic and several layers of molecules may cover the surface under this condition [180]. The adsorption isotherm for the monolayer adsorption is recorded and the specific SA can be calculated using the BET equation:

$$\frac{P}{v(P_o-P)} = \frac{1}{v_m C} + \frac{(C-1)P}{v_m C P_o} \quad (2.7)$$

where P is equilibrium pressure, P_o is the saturation pressure at the adsorption temperature, v is the adsorbed gas quantity, v_m is monolayer adsorbed gas quantity and C is the constant for a particular temperature and gas system.

2.5.2.3 Experimental method

The BET measurement was performed by a Micromeritics Gemini V BET SA analyser. Calculated amounts of calcined catalyst powder were placed on the quartz sample chamber. Prior to the measurement, the sample was pre-treated at elevated temperature in a vacuum in order to remove any contaminants. The sample chamber was then cooled down to liquid nitrogen temperature (-195.8°C) for the measurement.

2.5.3 Thermo-gravimetric analysis (TGA)

2.5.3.1 Purpose

Thermo-gravimetric analysis (TGA) investigates the change in the weight of the catalyst or precursor upon programmed heating [181]. The technique gives information about the pathways of decomposing the catalytic precursor to form an oxide form of the catalyst.

2.5.3.2 Fundamental principle

The TGA method measures the weight loss of the sample as a function of temperature. A thermo-gravimetric plot of percentage weight as a function of temperature is used in the evaluation of the reaction process, reaction rates, thermal stability and weight loss of the sample [182].

2.5.3.3 Experimental method

TGA was performed using a Perkin Elmer Pyris TGA. The sample, of approximately 20 mg LDH, was loaded and measurement started at ambient temperature using a heating rate of 10 °C/min up to 1000°C under air flow (100 mL/min).

2.5.4 Temperature programmed reduction (TPR)

2.5.4.1 Purpose

Temperature programmed reduction (TPR) is a widely used technique for the characterisation of catalysts. It provides quantitative information of the reducibility of the oxide form catalyst, as well as the heterogeneity of the reducible surface [183].

2.5.4.2 Fundamental principle

During TPR, a reducing gas mixture containing hydrogen and nitrogen or argon was continuously flown over the catalyst bed while the temperature of the bed was raised linearly with time. The consumption of hydrogen was measured at the exit of the catalytic bed, as a function of temperature characterises the reducibility of different species in the sample. The reduction of a metal oxide M_xO_y by H_2 is described by the following equation:

$$M_xO_y + yH_2 \rightarrow xM + yH_2O \quad (2.8)$$

A thermal conductivity detector (TCD) or mass spectrometer is normally used to measure the hydrogen uptake and plotted against temperature. Analysis of the plot for the position, area and shape of the peaks can indicate qualitative and sometimes quantitative information on the reproducibility of the catalyst surface, as well as the chemical changes resulting from promoters or metal/support interactions [180].

2.5.2.3 Experimental method

The H_2 TPR was carried out on a micro-reactor with a similar design to that described in Section 2.4.1. A 50 mg catalyst was carefully weighed and loaded in the quartz tube (OØ: 6mm, IØ: 4mm) between quartz wool and then pre-treated in a flowing stream of Ar (18 ml/min) for 30 minutes at ambient temperature. Then, the gas mixture was switched to 20 ml/min with 10% H_2 in Ar. The TPR was performed at a heating rate of 10°C/min from ambient temperature to 950°C. The H_2 consumption

was measured using a modified Hewlett Packard 5890 Series II GC equipped with TCD, using Ar as the carrier gas. The outlet gas from the TPR unit was passed through a molecular sieve trap to remove any water.

2.5.5 Scanning electron microscopy (SEM)

2.5.5.1 Purpose

An scanning electron microscope (SEM) is a type of electron microscope that uses a focused beam of high-energy electrons to generate a variety of signals by scanning the surface of solid specimens. The signals that derive from electron–sample interactions reveal information about the sample, including its external morphology (texture), crystalline structure, as well as the orientation of the materials making up the sample [184].

2.5.5.2 Fundamental principle

The electron optical arrangement in a SEM is shown schematically in Figure 2.4 (A). In an SEM, electrons are accelerated at voltages in the range of 2 to 40 kV to carry a significant amount of kinetic energy. An incident electron beam is emitted on the solid sample. These fast primary electrons (PE) interact in various ways with the surface layers of the sample. The kinetic energy is dissipated as a variety of signals produced by electron-sample interactions. The size of the interaction volume depends on the electron's landing energy, the atomic number of the specimen and the

specimen's density. The signals produced include secondary electrons, back-scattered electrons (BSE), characteristic X-rays, visible light and heat. Secondary electrons and BSEs are commonly used for imaging samples; secondary electrons are most valuable for showing morphology and topography on samples and BSEs are most valuable for composition analysis [184, 185].

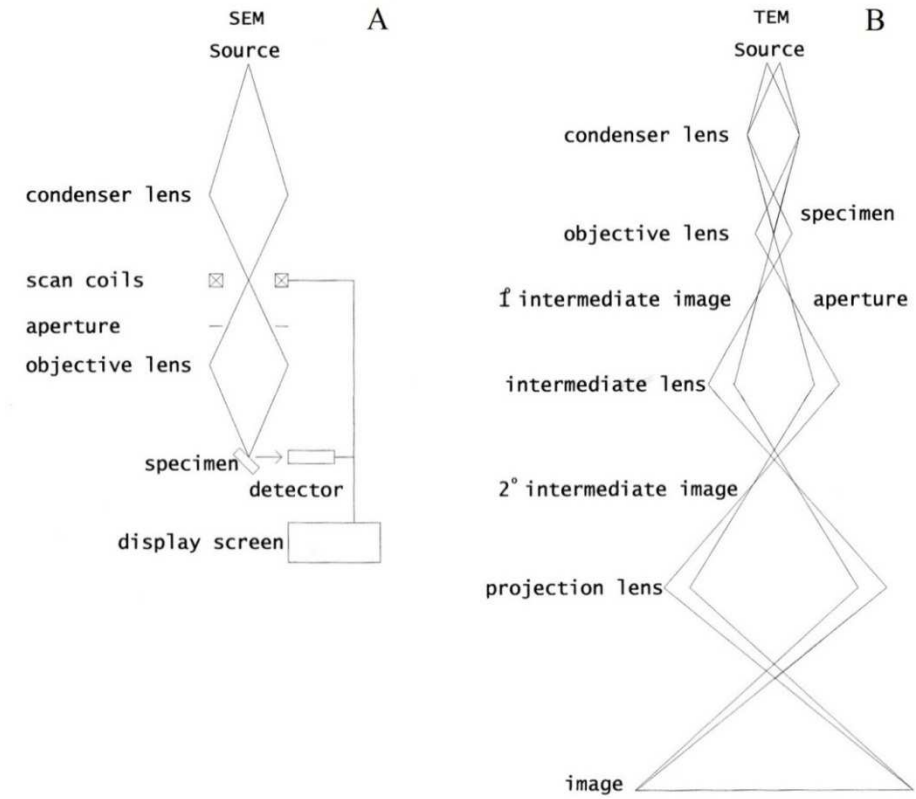


Figure 2.4 Schematic diagrams showing the operation of (A) SEM and (B) TEM [171].

2.5.5.3 Experimental method

SEM was recorded using the JEOL 840F operated at 5 keV. SEM micrographs were used to get information on morphology and particle size for as-prepared LDHs, calcined oxide form catalysts and reduced catalysts. LDH samples for recording SEM were prepared by dispersing a small amount of slurry in a minimum amount of

deionised water. The suspension was spin coated a 1 cm x 1 cm SiO_2 substrate spinning at a speed of 3000 rpm for 20 seconds. The coated substrate was dried at 90°C for 12 h before the SEM recording. SEM images for the calcined or reduced catalysts were recorded after calcination and reduction of the LDH coated substrate in a large diameter tubular reactor. The conductivity of the samples was enhanced by coating an ultra-thin platinum layer on the originally coated surface.

2.5.6 Transmission electron microscopy (TEM)

2.5.6.1 Purpose

Transmission electron microscope (TEM) is another important technique for direct investigation of heterogeneous catalysts. Unlike SEM, which provides an image of the external morphology of samples, TEM probes their internal structure. The main usage of this technique is to examine the specimen's local structure, composition or properties in sub-microscopic detail [184]. It is also used to determine particle size and distribution.

2.5.6.2 Fundamental principle

A TEM operates according to the same principled as a light microscope or projector, but the light source is replaced by a high-energy electron beam. The system is composed of several components, which include an electron gun, a series of electromagnetic lenses and electrostatic plates. It also requires specimen-loading

devices and imaging devices. The whole system should be maintained and operated at high vacuum condition. Figure 2.4 (B) above schematically shows the electron optical arrangement of TEM. The electrons are generated by an electron gun and accelerated by a series of accelerating plates with potential differences, becoming an incident electron beam with high energy. The electron beam is focused by a condenser lens and transmitted through the sample. An image is formed from the interaction of electrons passed through the sample. The image is magnified and focused by an objective lenses and an intermediate lessens, forming an intermediate image. The projection lens focuses the intermediate image to create the final image on an imaging device, normally a fluorescent screen or a CCD camera [171, 184].

2.5.6.3 Experimental method

The TEM samples were investigated using a JEOL 4000EX high-resolution transmission electron microscope (HR-TEM) working at 400 kV. The materials for TEM must be prepared at a very low thickness, which enables the elections to transmit through. Hence, the specimens were prepared by sonicating a small quantity of ground sample in methanol in an ultra-sonic bath for five minutes. The solution was then dropped onto a copper grid with an ultra-thin carbon support (400 mesh, supplied by Agar Scientific). Before loading the specimen to the TEM, the solvent methanol left on the grid has to be completely evaporated.

2.5.7 Energy dispersive X-ray spectroscopy (EDX)

2.5.7.1 Purpose

An energy dispersive X-ray spectroscopy EDX (sometimes also known as an EDS) is an analytical technique used to analyse the elemental composition and distribution of a sample.

2.5.7.2 Fundamental principles

EDX is the investigation of the interaction of a source X-ray excitation on a sample. The fundamental principle is that each element has a unique atomic structure reflecting the unique set of peaks on its X-ray spectrum. The EDX is normally in conjunction with SEM or TEM. It measures the energy values of characteristic X-rays which are elemental specific. The EDX detector uses semiconducting materials, typically a lithium drifted silicon (Si/Li) crystal, to absorb the energy of incoming X-rays by ionisation, yielding free electrons in the crystal that become conductive and produce an electrical charge bias. The X-ray absorption thus converts the energy of individual X-rays into electrical voltages of proportional size, while the electrical pulses correspond to the characteristic X-rays of the element. [185, 186]. There are several limitations of using an EDX to probe the specimen's elemental ratio. First, the accuracy of EDX is affected by several factors, such as the nature of the sample and the overlapping peaks of some elements. Second, the EDX is not suitable for detecting light elements.

2.5.7.3 Experimental method

The composition analysis of the prepared LDHs was conducted using a JEOL 6480 LV SEM equipped with Oxford Instruments EDS 6767 EDX. The ground LDH powder was compressed into a 1 cm diameter pellet applying 5 ton/m^2 pressure. A thin carbon layer was coated on the surface of the sample pellet. Composition analyses on 20 randomly selected areas of each sample pellet were taken and averaged for the calculation of the elemental ratio of the specimen. EDX results were used only to confirm the existence of the elements and for a rough estimate of the elemental ratios of Ni, Al and noble metal (Pd, or Rh), for the purpose of comparing the samples prepared under different synthetic conditions.

The EDX was also used for mapping the element (Ni, Al and Pd or Rh) distribution of the reduced catalysts. The work was carried out by an Oxford Instruments EDX installed on a JEOL 3000F HR-TEM, operating at 300 kV. Specimens were prepared using the same method as for the JEOL 4000EX HR-TEM.

2.5.8 Infrared spectroscopy (IR)

2.5.8.1 Purpose

Infrared (IR) covers the range of the electromagnetic spectrum between 0.78 and 1000 mm [171]. It is used to identify and study the state of the adsorbed atoms/molecules on the surface of the catalyst.

2.5.8.2 Fundamental principle

IR spectroscopy covers a range of techniques which are mostly based on absorption spectroscopy. Among them, the most common used is Fourier Transform infrared spectroscopy (FTIR), which is capable of simultaneously collecting a wide range of spectral data of solid, liquid, gas, microsamples and mixtures [183]. The technique is based on the absorption of infrared radiation exciting the bonds in the sample from one vibrational energy state to another higher vibrational energy state. When IR radiation passes through a sample, some of the infrared radiation is absorbed by the sample while the other part is transmitted. The resulting spectrum represents the molecular absorption bands whose intensity and frequency provide information on the structure and bonding in the molecule. A basic FTIR system consists of several parts, including the beam source, interferometer, sample holder and detector. IR energy is emitted from a glowing back-body source. Before passing through the sample, an interferometer is employed in the collection of spectral information, and the spectrum is calculated as an inverse Fourier Transform of the interferogram. The IR beam passing through the sample is absorbed to various extents at different wavelengths by the atoms/molecules present in the surface. A detector records the intensity of the transmitted IR beam. The absorbance frequency ranges are measured as wave numbers typically over the range 4000 to 600 cm^{-1} [186].

2.5.8.3 Experimental method

Two FTIR facilities were used for the investigation of prepared LDH precursors and fresh reduced catalysts. The analysis of LDH precursor was recorded by a Varian

Excalibur FTS-3000 FTIR spectrometer with a liquid-nitrogen-cooled MCT detector. A small quantity of the grounded LDH sample was dropped on to the sample window before recording the FTIR spectra. The IR spectra were obtained by averaging 128 scans with a resolution of 4 cm^{-1}.

On the other hand, the *in-situ* FTIR of CO adsorption on freshly reduced catalyst was carried out on a Bruker Equinox 55 FTIR with an *in-situ* cell. 35 mg of calcined catalyst was pre-reduced at 700°C in 62.5 mL/min 5% H_2/He for 1 h. The catalyst was then cooled down and maintained at 25°C under a He environment. This reduction procedure is the same as the pre-treatment condition prior to the activity test. A reference FTIR single scan was recorded as a background. The CO was then introduced to the He flow to form a total flow rate of 100 ml/min 2% CO/He before recording the spectra.

Chapter 3. Effect of synthetic conditions on Ni/Al and noble metals substituted Ni/Al LDHs and catalytic activity of the derived catalysts

3.1 Introduction

Ni/Al LDH, also known as takovite, is considered an ideal precursor for preparing multicomponent catalysts for catalytic steam reforming [187-190], dry reforming of hydrocarbons [191], and dehydrogenation [117, 118]. The precursors can easily be substituted with promoters, such as noble metal examples. After thermal treatment, the derived catalyst has large surface area as well as homogeneously mixed oxide structures [141, 149, 187, 192, 193]. An important research objective of this thesis is to develop high performance and cost-effective SMR catalysts for IT-SOFC application. In this chapter, Ni/Al LDHs with noble metal (Pd, Rh and Pt) incorporations were successfully prepared by standard CP method with different preparation temperatures and aging times. The as-prepared LDHs and derived catalysts were characterised and tested to study the impact of the variation in the preparation conditions on the LDHs and their derived catalyst's chemical compositions, thermal decomposition behaviour, reducibility and catalytic performance.

3.2 Experimental

A/Ni/Al LDH (A=Pd, Rh or Pt) precursors (formula: $[Ni_{0.75-x}A_xAl_{0.25}(CO_3)_{0.125+\delta}(OH)_2]\bullet nH_2O$) with an atomic ratio of A:Ni:Al=x:0.75-x:0.25, (x=0.01 for Rh, 0.02 for Pd or Pt) were prepared by CP method described in Section 2.2 of Chapter 2. Some of the properties of the LDHs with different preparative conditions are listed in Table 3.1. In addition to the above compositions, three other

LDH samples were also prepared using different Ni/Al ratio of preparation conditions. One sample, named NiAl(2:1)40 was prepared with a Ni:Al atomic ratio of 0.66:0.34 and two Pd and Pt substituted LDHs, named as Pd(2.1)NiAl70B and Pt(0.1)NiAl70B were co-precipitated at 70°C followed by elevating the suspension temperature to 100°C and kept for 30 minutes. All the LDH samples were calcined at 550°C for 4 hours to obtain oxide form catalyst.

As-prepared LDHs were characterised by EDX, XRD, SEM, TGA and derived catalysts were characterised by XRD, BET, TPR and TEM. Details of these experiments are given in Section 2.5 of Chapter 2. All catalysts were pre-reduced at 700°C and activity measurements were performed from 250-700°C using the method described in Section 2.4.3.1 of Chapter 2.

3.3 Results and discussion

3.3.1 Compositions of LDHs

The as-prepared LDHs are divided into four groups by their chemical compositions: basic Ni/Al LDH series, Pd and Rh-substituted Ni/Al LDH series. As shown Table 3.1, the molar Ni/Al ratios of all as-prepared LDHs, except sample NiAl40(2:1), are very close to the nominal ratio 3:1 in the nickel and aluminium nitrate solution. As shown in Figure 3.1, the colours of Pd and Rh substituted LDHs are uniform and darker than the NiAl40 LDH. The reason could be due to the incorporation of noble metal into the LDHs.

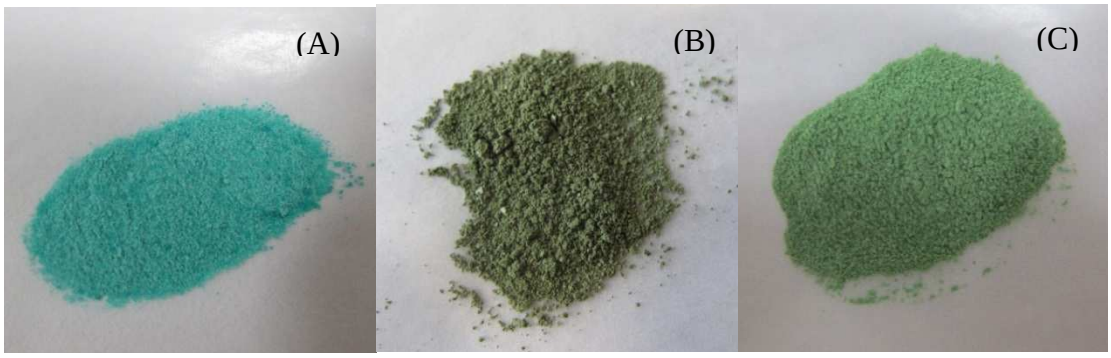


Figure 3.1 Ground and sieved LDHs (A) NiAl40, (B) Pd(1.3)NiAl40 and (C) Rh(1.1)NiAl40.

The chemical compositions were confirmed by EDX. As shown in Table 3.1, Pd and Rh were respectively found incorporated in brucite layers of doped LDHs. The average atomic ratios of Al in all samples are slightly higher by 2% over the nominal 25% (atomic%). The chemical composition of samples in basic Ni/Al and Rh substituted Ni/Al LDHs shows no dependence on the preparative condition. Rh is favourable to be incorporated to the LDH layers and Rh content reaches the nominal ratio 1% (Rh/(Rh+Ni+Al), atomic%) in all three Rh substituted LDHs. Similar results has also been reported by Greenwood and Earnshaw [194]. Pd content in the LDH strongly depends on the preparative conditions. Some Pd was lost during preparation in general condition and the reason being the ionic radii of the Pd^{2+} (0.086nm) is quite close to the limit of the suitable values for entering the brucite layers [149]. Severe synthetic conditions significantly increase the incorporation of Pd in the lattice. For sample Pd(2.1)NiAl70B, the Pd content reaches the nominal ratio 2% (Pd/(Pd+Ni+Al), atomic%) when aged at 100°C, implying a sufficient and high intensive energy input is required to completely incorporate all Pd^{2+} into the LDH. Pt exhibited poor affinity to the LDHs, only 0.1% Pt (Pt/(Pt+Ni+Al), atomic%) was found in the LDH lattice after aging the LDH in critical condition.

Table 3.1 Chemical composition and structure studies of synthesised LDHs

	LDH name	CP temperature (°C)	Aging time (hours)	Expected metal molar ratio % (Solution)			Actual metal molar ratio % (Solid, by EDX)			Crystallite size (nm)[a]		Lattice parameter (Å)		
				A	Ni	Al	A	Ni	Al		Trend	*a*	*c*	Trend
`	NiAl(2:1)40*	40	4	-	66.0	34.0	-	64.6	35.4	13.3		2.974	22.694	
A	NiAl40	40	4	-	75.0	25.0	-	72.8	27.2	16.2	L ↓ H	3.036	23.091	H ↑ L
	NiAl70	70	4	-	75.0	25.0	-	72.4	27.6	23.8		3.034	23.087	
	NiAl70L**	70	24	-	75.0	25.0	-	72.6	27.4	27.7		3.031	23.081	
				Pd			**Pd**							
B	Pd(1.3)NiAl40	40	4	2.0	73.0	25.0	1.3	71.7	27.0	9.9	L ↓ H	3.048	23.136	H ↓
	Pd(1.6)NiAl70	70	4	2.0	73.0	25.0	1.6	71.5	26.9	12.8		3.049	23.139	
	Pd(1.8)NiAl70L**	70	24	2.0	73.0	25.0	1.8	71.3	26.9	20.2		3.052	23.144	
	Pd(2.1)NiAl70B***	70	100°C/0.5	2.0	73.0	25.0	2.1	71.2	26.7	24.1		3.057	23.149	
				Rh			**Rh**							
C	Rh(1.1)NiAl40	40	4	1.0	74.0	25.0	1.1	72.2	26.7	11.5	L ↓ H	3.042	23.118	H ↑ L
	Rh(1.1)NiAl70	70	4	1.0	74.0	25.0	1.1	72.3	26.6	14.3		3.041	23.114	
	Rh(1.1)NiAl70L	70	24	1.0	74.0	25.0	1.1	72.2	26.7	21.9		3.031	23.109	
				Pt			**Pt**							
D	Pt(0)NiAl40	40	4	2.0	73.0	25.0	0	72.5	27.5	14.0	L ↓ H	3.038	23.089	H ↑ L
	Pt(0.1)NiAl70B	70	100°C/0.5	2.0	73.0	25.0	0.1	72.6	27.3	26.5		3.036	23.081	

Green number in catalyst name indicates the difference in co-precipitation temperature (°C).
Red number in catalyst name indicates the difference in Pd, Rh or Pt content in overall Ni+Al+Pd, Ni+Al+Rh or Pt+Ni+Al (%).
*Ni:Al=2:1, **L=long aging period, ***B=ageing at 100°C (Boiling) for 0.5 h.
[a] Mean value obtained from reflections (003) and (006), ref ICDD 15-0087.
A is the basic Ni/Al LDH series, B is the Pd substituted Ni/Al LDH series, C is the Rh substituted Ni/Al LDH series and D is the Pd substituted Ni/Al LDH series.

3.3.2 Structure of LDHs

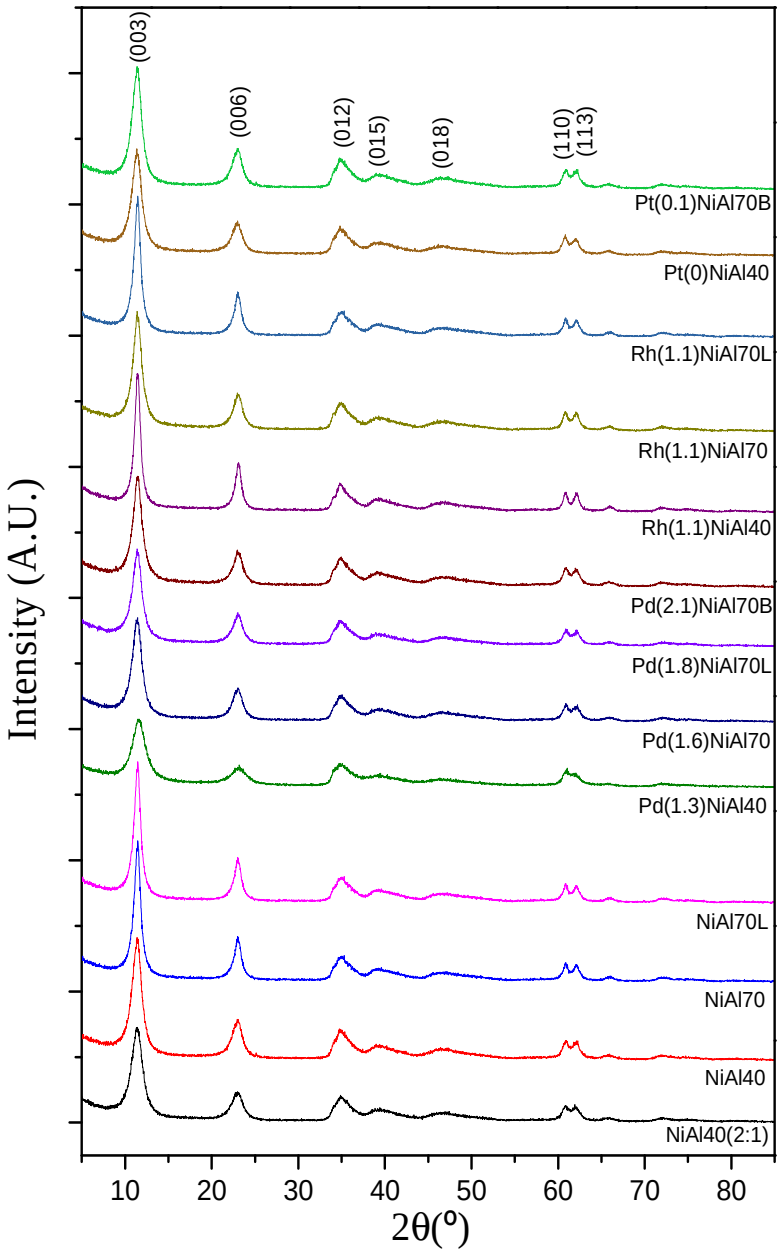


Figure 3.2 XRD patterns of LDH precipitates dried at 90°C for 12 h.

Figure 3.2 compares the XRD patterns of all as-prepared LDHs. All the patterns show only well-crystallised takovite phase (ICDD: 15-0087), with narrow, symmetric and intensive peaks at the low 2θ range and weaker, while less symmetric lines at high 2θ

range. No other phase segregations are found in any of the LDHs. Two common features are found from the vertical and horizontal comparisons of the XRD patterns and lattice profiles of LDHs in each series:

Firstly, within each series, the LDH co-precipitated at higher temperature and/or with a longer aging time have sharper reflective peaks, indicating an enhancement on both crystallinity and crystallite sizes (Figures 3.3A and Table 3.1). The lattice parameters *a* and *c* of basic Ni/Al and Rh substituted Ni/Al LDHs slightly decrease as a function of increased CP temperature and aging time. This could be attributed to the strengthening interaction between interlayer anions and hydroxide layers as a result of the increased crystallinity [195, 196]. For the Pd substituted LDHs, both the lattice parameters *a* and *c* increase with the increasing CP temperature and aging time, due to their enhancing Pd incorporation into the LDHs. All these trends are indicated the red and blue arrows in Table 3.1.

Secondly, for the LDHs prepared at the same condition, the incorporations of noble metal ions (Pd or Rh) caused a lattice distortion and this significantly reduced the crystallinity and crystallite sizes of the LDHs. The large Pd^{2+} and Rh^{3+} (Pd^{2+}>Ni^{2+}>Al^{3+}, Ni^{2+}>Rh^{3+}>Al^{3+}) in the lattice also lead lattice expansion on both *a* and *c* directions (Table 3.1). These behaviours are proved from Figure 3.3B as the reflective peaks in the two Pd and Rh substituted LDHs slightly shift to lower 2θ range and become less intensive, compared with the basic Ni/Al40 LDH.

For the Pt substituted LDHs, the absence of Pt in the brucite layers makes their structure same as the basic Ni/Al LDHs. Therefore, it is decided not to use Pt as promoters in the further studies.

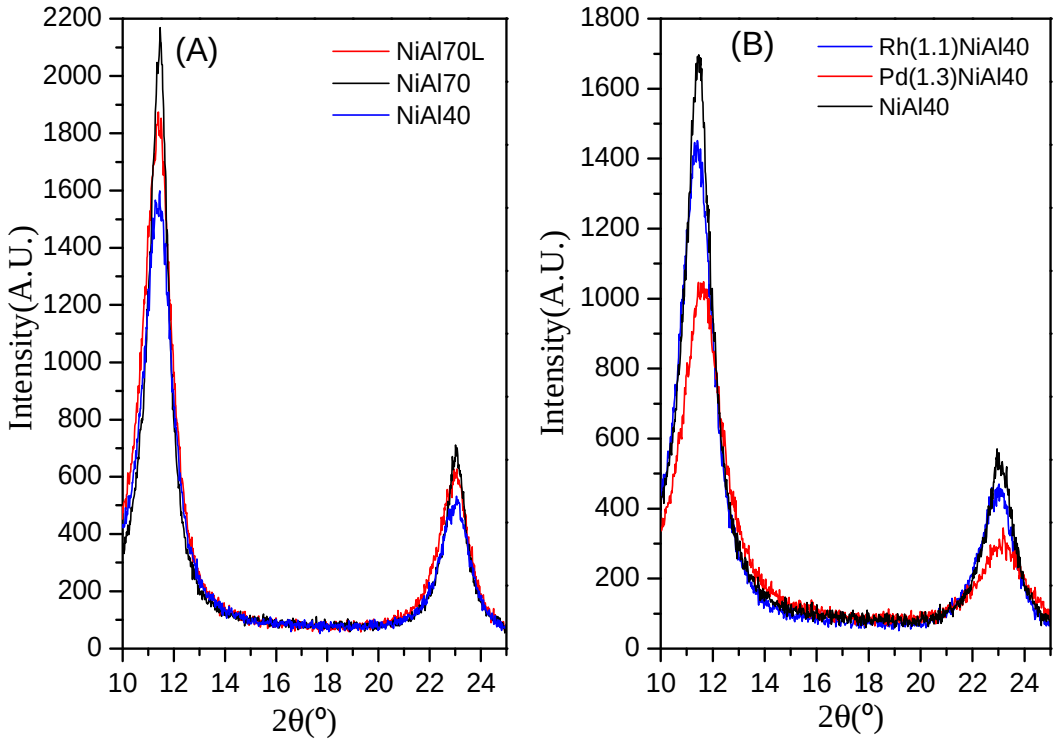


Figure 3.3 (A) Comparison of XRD peaks of NiAl40, NiAl70 and NiAl70L LDHs corresponding to (003) and (006) reflection lines; (B) Comparison of XRD peaks of NiAl40, Pd(1.3)NiAl40 and Rh(1.1)NiAl40 LDHs corresponding to (003) and (006) reflection lines.

3.3.3 Structure of catalysts

Calcination of the LDHs at 550°C completely destroyed the layered structure. As shown in Figure 3.4, all calcined catalysts have quite similar single phase diffraction patterns. Clear peaks at 2θ=37°, 43° and 63° corresponding to reflections of (111), (200) and (220) lines suggest the existence of NiO-like phase (ICDD: 47-1049).

Compared with the pure nickel oxide, the reflection peaks in these catalysts are broader and less intensive, indicating a lower crystallinity. The broad baseline without distinct Al-containing phases is mainly due the incorporation of Al^{3+} cations into the nickel oxide lattice, forming highly disordered metastable Ni(Al)O solid solution without a clear distinction between the nickel and aluminium supports [155].

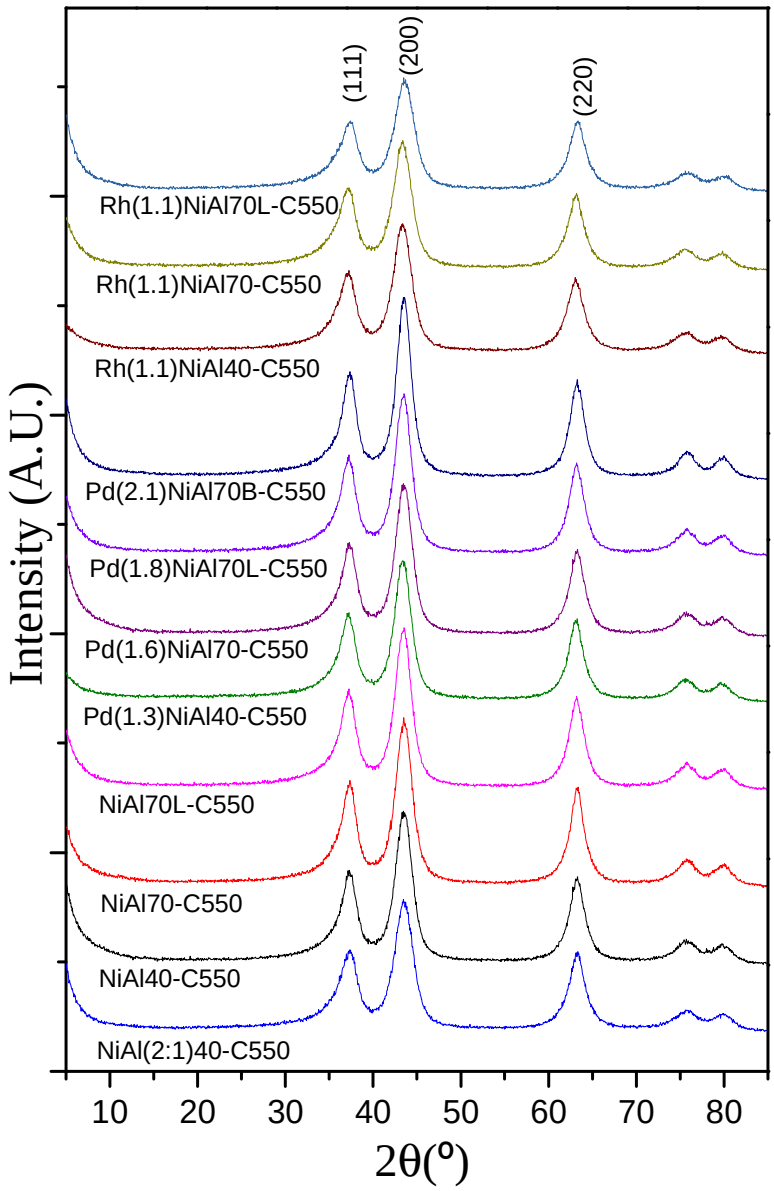


Figure 3.4 XRD patterns of catalysts prepared by calcination of LDH precursors at 550°C for 4 h.

Table 3.2 Crystallite sizes, BET SA and lattice parameters of all calcined catalysts.

Sample name	Crystallite size of the catalysts (nm)[a]		BET SA of the catalysts (m^2/g)		Lattice parameter *a* (Å)	
		Trend		Trend		Trend
NiAl40(2:1)-C550*	11.0		146.4		4.104	
NiAl40-C550	13.5	L ⇩ H	137.7	H ⇧ L	4.159	H ⇧ L
NiAl70-C550	14.2		135.4		4.153	
NiAl70L-C550**	14.6		129.2		4.151	
Pd(1.3)NiAl40-C550	8.4	H ⇧ L	184.9	L ⇩ H	4.186	L ⇩ H
Pd(1.6)NiAl70-C550	7.7		188.0		4.188	
Pd(1.8)NiAl70L-C550**	6.9		208.6		4.197	
Pd(2.1)NiAl70B-C550***	6.2		217.2		4.201	
Rh(1.1)NiAl40-C550	9.7	L ⇩ H	179.5	H ⇧ L	4.177	H ⇧ L
Rh(1.1)NiAl70-C550	10.2		175.6		4.175	
Rh(1.1)NiAl70L-C550	12.8		168.1		4.172	

*Ni:Al=2:1, **L=long aging period, *** B=Boiled.

[a].Mean values obtained from reflections (111), (200) and (220): ref ICDD 47-1049

The calcined catalysts retain some of the properties of their precursors known as 'memory effect' [197-199]. The two features previously found in the LDH precursors are still applied in their derived catalysts. This can be evident from comparison of catalysts crystallite size, BET SA and lattice parameter in accordance with the data and trend of their precursors (compare the red and blue arrows in Table 3.1 and 3.2). The change in BET SA of each catalyst exhibits similar trend as the lattice parameter *a*. One exception finding is the crystallite sizes of the Pd promoted catalysts decrease as a function of the increasing CP temperature and aging time applied in preparation of their precursors. This trend (the green arrow in Table 3.2) is opposite to the trend found in their precursors. The result is not unexpected since the enhanced preparation condition increase the Pd content in LDH. After calcination, the higher amount of Pd incorporated in Ni(Al)O enhanced the distortion of the catalyst lattice, the crystallinity and crystallite sizes hence both decline.

3.3.4 SEM observation

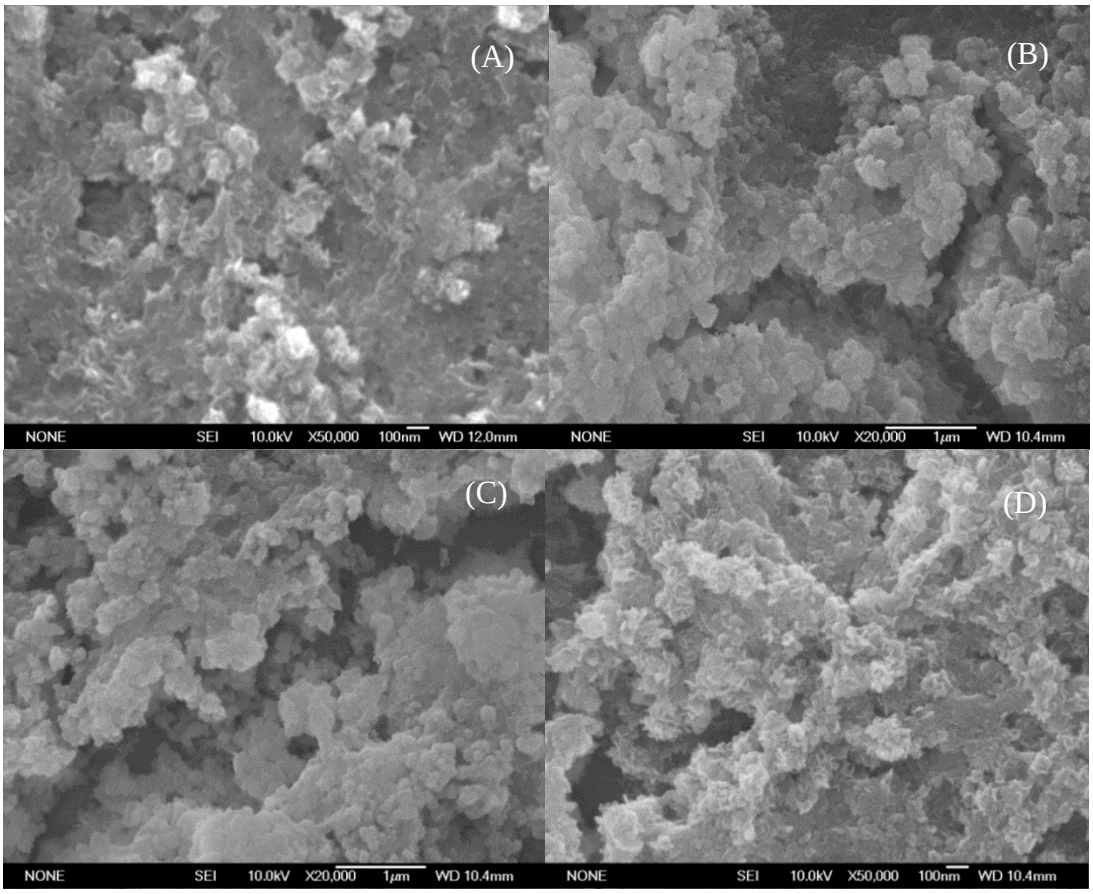


Figure 3.5 SEM images of (A) NiAl40, (B) Pd(1.3)NiAl40, (C) Rh(1.1)NiAl40 and (D) NiAl70L LDHs.

SEM images of selected LDH are shown in Figure 3.5. All of the samples contain similar overlapped and embedded plate-shaped nodules with narrow size distribution.. There are no distinguishable differences observed.

3.3.5 Thermal decomposition analysis

The thermal decomposition of selected LDH samples was conducted by TG-DTA from ambient temperature up to 800°C

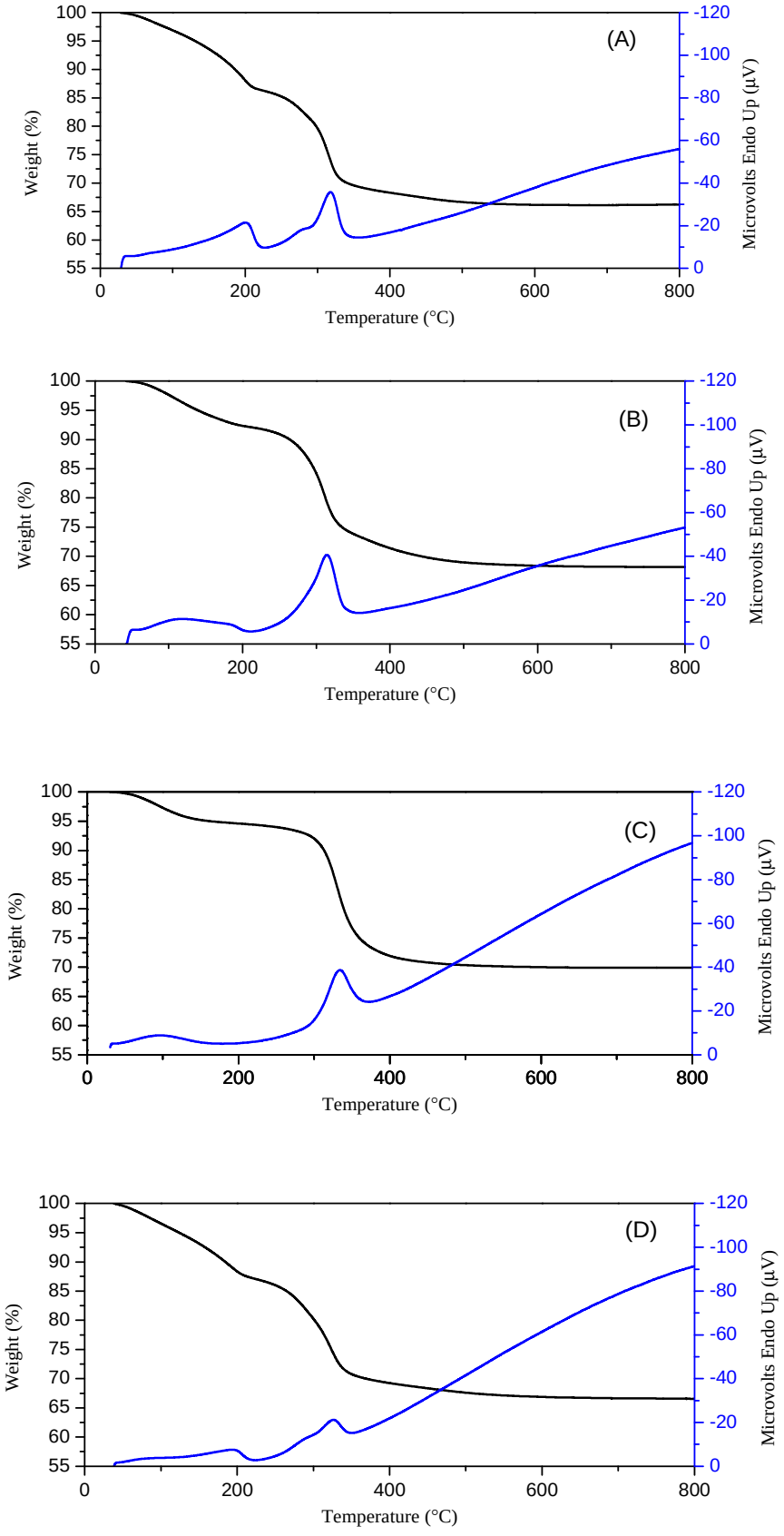


Figure 3.6 TG-DTA curves of (A) NiAl40, (B) Pd(1.3)NiAl40, (C) Pd(2.1)NiAl70B and (D) Rh(1.1)NiAl40.

Figure 3.6 shows quite similar weight loss and differential curves, with only a marginal difference. In general, the thermal decomposition contains two consecutive stages weight losses, corresponding to the decompositions of HT-like LDH [141, 200, 201]. Both of these two steps are endothermic from the DTA results. The first peak at the low temperature range (around 200°C) in TGA accounts for the removal of the water present in the interlayers and physically adsorbed on the surface of the LDH. For the samples Pd(1.3)NiAl40 and Pd(2.1)NiAl70B, the weight loses are lower in comparison with NiAl40. Accordingly, their DTA peaks are less intensive and broader. In agreement with the XRD results, this could be due to the increased thickness of brucite-like layers (in *c* direction) due to the substitution of Pd ions into the lattice, caused shrinkage in the space between the compensating layers. Consequently, the amount of structural water accommodated within the interlayers goes down. Pd(2.1)NiAl70B has the smallest weight lost at this stage when compared with the NiAl40. This is due to the shrinkage of this interlayer distance.

Rh(1.1)NiAl40, on the other hand, its lattice parameter *c* is affected marginally when compared with the parent NiAl40, its weight loss on this step is comparable to the parent LDH. Major weight loss in all LDHs for the second intensive peak is due to the brucite-like layer dehydrogenation, hydroxyl groups and compensating carbonate anions decomposition at this stage.

The above TG-DTA results indicate the layered structures are still well maintained in the Pd, Rh substituted LDHs. The noble metal ions were incorporated into the layers during preparation, causing changes in lattice parameter of the system.

the substitution of noble metal ions did not change the structure of the LDHs but only influence the lattice profiles of the LDHs.

3.3.6 TPR analysis

H_2-TPR was carried out to investigate the influence of the preparative conditions on the reducibility and internal structure of the derived catalysts.

3.3.6.1 Effect of Ni:Al ratio on the reducibility of the catalysts

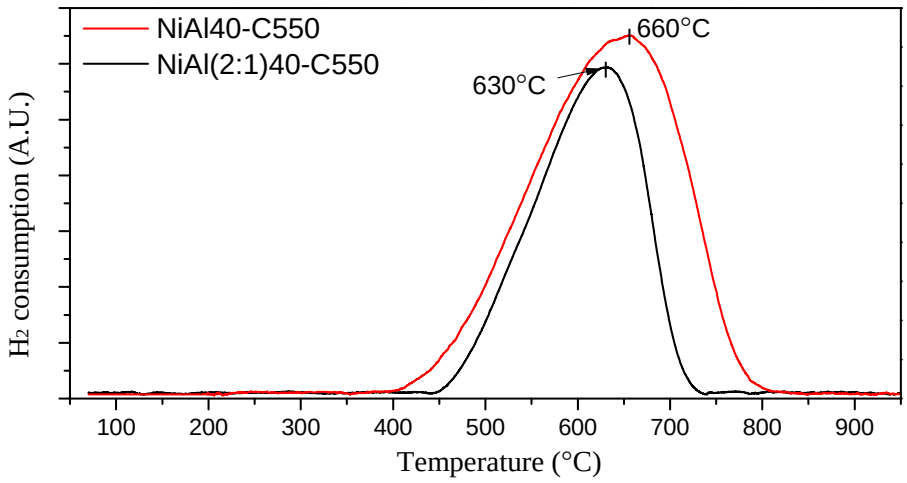


Figure 3.7 TPR profiles of NiAl(2:1)40-C550 and NiAl40-C550 catalysts.

Figure 3.7 compares the reducibility of unpromoted catalysts prepared with different Ni:Al ratios. Both NiAl40(2:1)-C550 (Ni:Al=2:1, atomic%) and NiAl40-C550 (Ni:Al=3:1, atomic%) follow a similar reduction trend with a board assymmetrical reduction peak from 400 to 800°C corresponding to the reduction of Ni(Al)O. Puxley *et. al.* [155] developed a model, dividing the relationship between co-existed Ni and

Al within the Ni(Al)O into three types, according to the difference in the aluminium coordination within the lattices — substituted nickel oxide (S.N.O), discorded oxide-spinel intermediate (D.O.S.I.) and spinel-like material (S.L.M). The Ni(Al)O metastable structure starts to break down to ordered nickel oxide and nickel aluminate from 800°C. The reduction temperatures of these two catalysts at 630 and 660°C are closer to nickel aluminate, unlike pure nickel oxide which gets reduced in the range 370-430°C, The structure of the present catalyst may be assigned to be predominantly S.L.M. [202].

NiAl40(2:1)-C550 catalyst has a smaller reduction area compared to the 3:1 catalysts mainly due to the reduced nickel content in Ni(Al)O. Its reduction temperature is also lower than the NiAl40-C550 catalyst. Similar results have been reported by Smoláková *et. al*. [118]. Smaller crystallite size produced by the calcination of NiAl(2:1)40 LDH may be responsible for the lower reduction maximum.

3.3.6.2 Effect of preparative conditions of LDH on reducibility of the derived catalysts

Figure 3.8 shows the TPR profiles of the Ni(Al)O catalysts derived from Ni/Al LDH (Ni:Al=3:1) prepared with different preparative conditions. All three catalysts show very similar TPR profiles. However, the reduction maximum is found be shifting to higher temperature slightly as a function of increase in preparation temperature and aging time. Abelló *et. al.* [117] and Arnoldy *et.al.* [203] found that the reducibility of Ni(Al)O catalyst is determined by interaction between nickel and aluminium because Al^{3+} causes a ligand effect – polarise the surrounding Ni^{2+} – making Ni(Al)O hard to

reduce, compared with pure nickel oxide. The severe preparative conditions tend to reduce the lattice parameter *a* in the LDH and thus result in a smaller lattice cell of the derived Ni(Al)O catalyst. The interaction between nickel and aluminium are therefore become stronger, making the nickel more ionic and less reducible [117]. The H_2 consumption in reduction of nickel during TPR is S_A:S_B:S_C =139:124:123. This indicates the high CP temperature and prolonged aging slightly influence the nickel dispersions of the calcined catalysts.

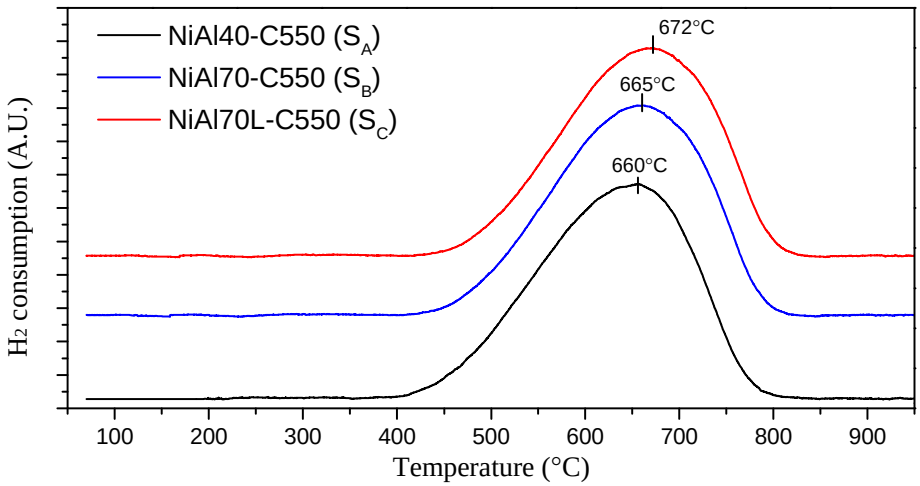


Figure 3.8 TPR profiles of Ni(Al)O catalysts. S_A, S_B and S_C are the areas of the Ni reduction peaks in the TPR curves of NiAl40-C550, NiAl70-C550 and NiAl70L-C550

3.3.6.3 Effect of preparative conditions of noble metal substituted LDH on reducibility of the derived catalysts

Addition of Pd, Rh promoters in the LDH lattices drastically enhance the reducibility of the derived catalysts. Figures 3.9 and 3.10 show the TPR profiles of Rh and Pd promoted catalysts. The reduction maxima of the promoted catalysts shift to lower temperature compared to the unpromoted catalysts in Figure 3.8. This is due to the

synergetic effect of the noble metal promoters as it significantly reduces the polarisation of nickel by the aluminate. The Ni-Al bond is weakened by the presence of even relatively low level of promoters. On the other hand, the internal structure of the Ni(Al)O is also affected by Pd or Rh promoter. Large amount of nickel gets reduced at lower temperature indicating predominant amount of nickel present in Ni(Al)O system is close to pure nickel oxide.

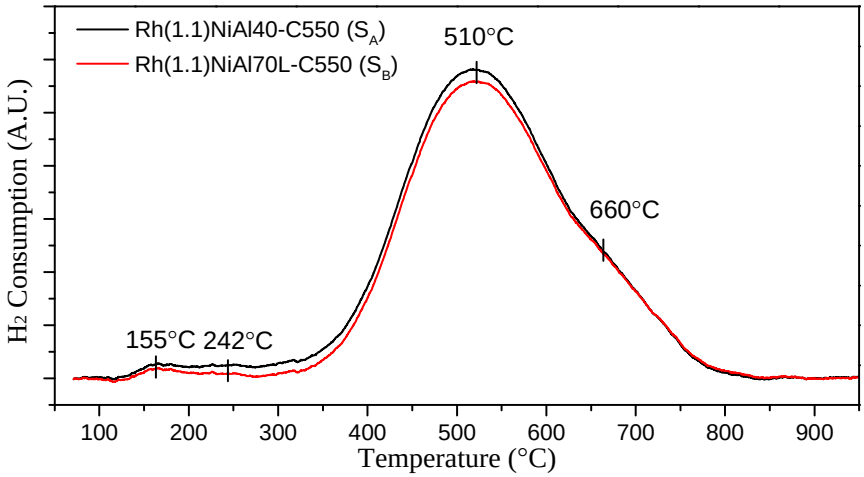


Figure 3.9 TPR profiles of Rh promoted Ni(Al)O catalysts. S_A and S_B are the areas of the Ni reduction peaks in the TPR curves of Rh(1.1)NiAl40-C550, and Rh(1.1)NiAl70L-C550

Rh promoted catalysts

In Figure 3.9, the reduction profiles of Rh promoted catalysts show little or no dependence on the preparative conditions. The reduction maxima for both the catalysts appear at 510°C. The reason for this behaviour is that there is no change in the internal structure of Rh promoted Ni(Al)O though the reduction maxima are considerably lower than the unpromoted catalyst. A shoulder at 660°C with similar shape and intensity are found in both the catalysts which may be due to a small

portion of S.L.M. form present in the structure. The H_2 consumption during reduction of nickel is S_A:S_B=138:129. This result agrees with the TPR study of the unpromoted catalysts in Figure 3.8 as the preparative conditions marginally show their influences on the catalysts and intensive energy input during CP and aging caused lower dispersion and reducibility of the nickel in these catalysts.

There are two small peaks at low temperature range at 155°C and 242°C due to the reduction of Rh. Since there is no segregation of any Rh found in XRD, these two peaks may be due to surface exposed Rh^{3+} located at different sites.

Pd promoted catalysts

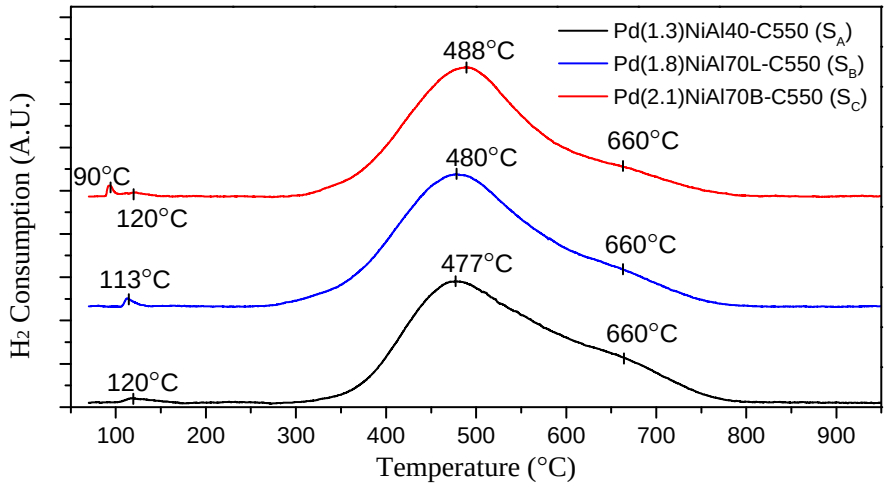


Figure 3.10 TPR profiles of Pd promoted Ni(Al)O catalysts. S_A, S_B and S_C are the areas of the Ni reduction peaks in the TPR curves of Pd(1.3)NiAl40-C550, Pd(1.8)NiAl70L-C550 and Pd(2.1)NiAl70B-C550

The reduction maxima of Pd promoted catalysts (Figure 3.10) appear in the range 470-480°C which are very close to the reduction peak of pure nickel oxide, indicating existence of predominantly S.N.O. form in the internal structure. The shoulders at 660°C are assigned to small quantity of S.L.M. in the catalyst. The reduction maxima of the Pd promoted catalysts have slight variation with change in the preparative conditions. The reduction maximum for mild preparative conditions (40°C/4h) is found to be 477°C and the intermediate preparative conditions (70°C/24h) is at 480°C whereas the severe conditions (boiled/30min) shows at 488°C. The amount of Pd incorporated in the LDH precursor also varied with the conditions as may be seen from the Table 3.1. The reason for these changes is due to small increase in the crystallite size and changes in the internal structure of the Ni(Al)O by Pd promoters. This is as evidenced by a closer look at low temperature region of the TPR profiles: a small peak at 120°C for Pd(1.3)NiAl40-C550 and 113°C for Pd(1.8)NiAl70L-C550, possibly due to the reduction of surface exposed Pd^{2+} in the lattices. For Pd(2.1)NiAl70B-C550 catalyst, this peak locates at 120°C and decreases as a small shoulder. An additional well-defined reduction peak formed at 90°C could be assigned to the reduction of well-dispersed PdO particles [204, 205]. The small particle sizes make these segregated particles undetectable by XRD. The further TPR analyses in Chapter 5 further confirm this conclusion. In this case, the emerging Pd segregation in catalyst Pd(1.8) NiAl70L-C550 and Pd(2.1)NiAl70B-C550 may cause a local accumulation of Pd in the lattice. The promotional effect is hence weakened and catalysts become less reducible.

Same as the series of unpromoted and Rh promoted catalysts, the H_2 consumption of three selected Pd promoted catalyst during TPRs is S_A:S_B:S_C=131:121:116, which

show the dependence of the dispersion of nickel in the calcined catalyst with the initial preparative condition of the precursors. However, nickel reduction peak areas of Pd promoted catalysts, in comparison to unpromoted and Rh promoted catalysts are relatively smaller. This reveals that the additional Pd adoption in the Ni(Al)O system has reduces the nickel dispersion.

3.3.7 TEM observation

The TEM image of the catalyst NiAl40-C550 catalyst is shown in Figure 3.11A. The escape of water and carbon dioxide did not result in a significant structure reengagement. Due to the 'memory effect' behaviour, the general morphology is recalled as the original LDH shapes and the thin nodular strip structures are observed again. The nodular shapes are also observed in NiAl70L-C550 and Pd(1.3)NiAl40-C550 catalysts (Figures 3.11B and C). The change in preparative conditions and the incorporation of noble metal promoters did not make any obvious differences to the morphology of the catalysts, although it seems the particle size of Pd(1.3)NiAl40-C550 is slight smaller than the other two samples, possibly due to the small crystallite size of its LDH precursor.

After reduction at 700°C, the lamellar shape structure disappeared. Instead, almost elliptical nanoparticles are observed in Figures 3.12D, E, and F. Again, no obvious differences in terms of the morphology are found among these samples. The particle sizes of the reduced catalysts range from 15 to 30 nm, slightly larger than their calcined catalysts. Because of the magnetic behaviour of nickel, the reduced particles agglomerate forming large lumps of nanoparticles

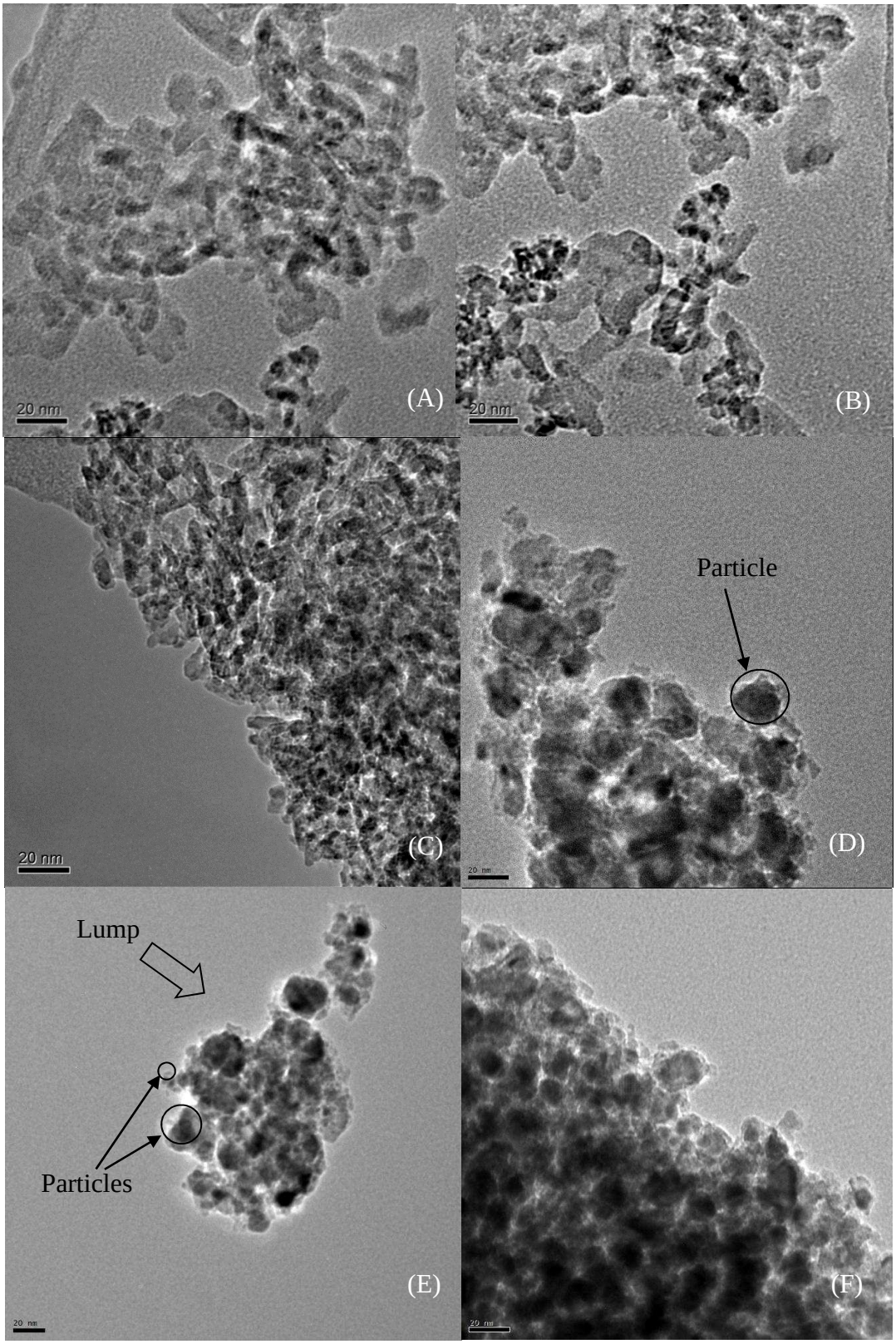


Figure 3.11 TEM images of (A) NiAl40-C550, (B) NiAl70L-C550, (C) Pd(1.3)NiAl40-C550, (D) NiAl40-C550-R700, (E) NiAl70L-C550-R700 and (F) Pd(1.3)NiAl40-C550-R700.

3.3.8 Catalyst activity

3.3.8.1 Effect of Ni/Al ratio on catalytic activity

Figure 3.12 shows the apparent reactivity of SMR reactions over NiAl(2:1)40-C550-R700 (Ni:Al=2:1) and NiAl40-C550-R700 (Ni:Al=3:1) derived catalysts. Both the catalysts have light-off for SMR reactions at temperatures between 250 and 300°C. The activity of the NiAl40-C550-R700 catalyst is higher than the NiAl(2:1)40-C550-700 catalyst in the whole testing range, meaning smaller crystallite size in the latter catalyst does not compensate the loss in activity due to the decrease of the number of nickel active sites.

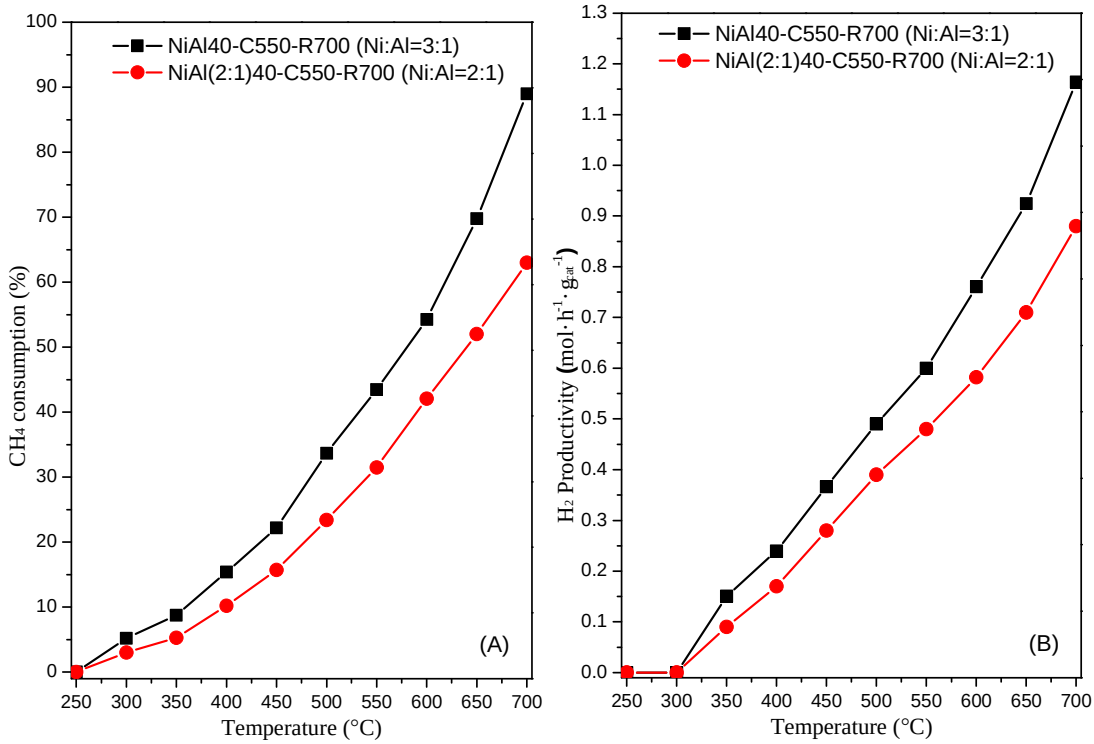


Figure 3.12 Comparison of (A) CH_4 consumption and (B) H_2 productivity as a function of reaction temperature in SMR over NiAl(2:1)40-C550-R700 (Ni:Al=2:1) and NiAl40-C550-R700 (Ni:Al=3:1) catalysts (CH_{4inlet}= 16.2ml/min, S:C=3:1, 1 atm).

3.3.8.2 Effect of preparative conditions on catalyst activity

Figure 3.13 comprises the catalytic activities of NiAl40-C550-C700, NiAl70-C550-C700 and NiAl70L-C550-C700 catalysts. As expected, catalysts show very similar activity in SMR reactions due to their similar structure and chemical compositions. CH_4 consumption reached around 90% at 700°C. Between 500 and 700°C, the NiAl40-C550-R700 catalyst exhibit marginally higher activity in comparison with the other two catalysts, possibly due to the smaller crystallite sizes and higher nickel dispersion.

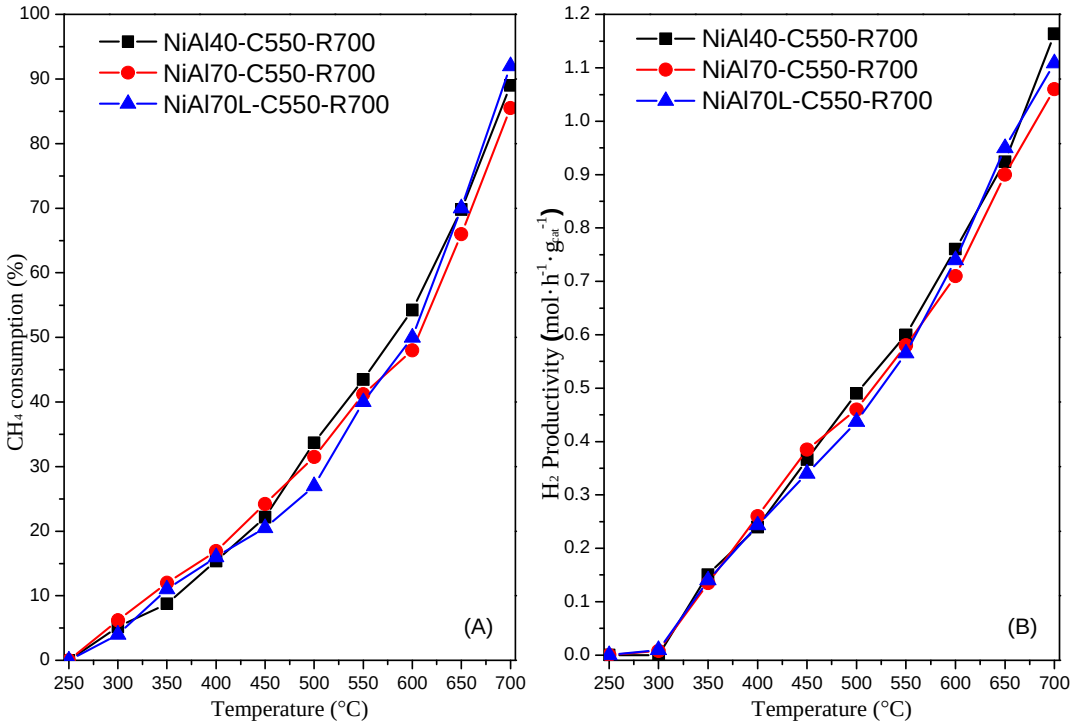


Figure 3.13 Comparison of (A) CH_4 consumption and (B) H_2 productivity of SMR over NiAl40-C550-C700, NiAl70-C550-C700 and NiAl70L-C550-C700 catalysts (CH_{4inlet} = 16.2ml/min, S:C=3:1, 1 atm).

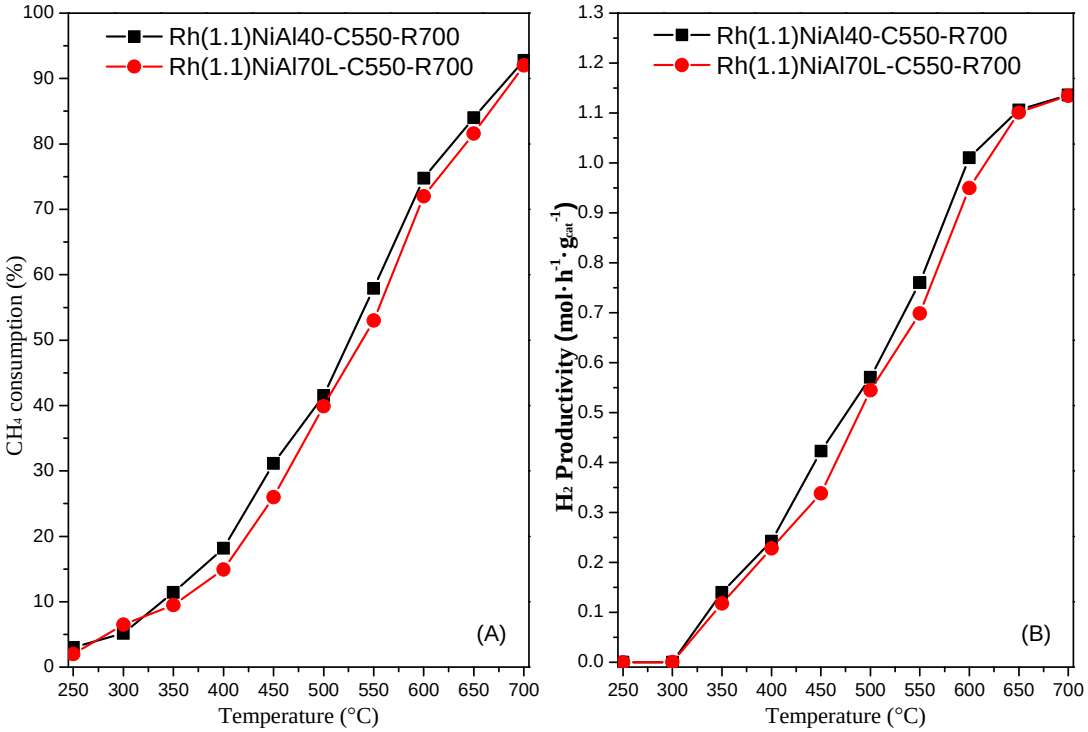


Figure 3.14 Comparison of (A) CH_4 consumption and (B) H_2 productivity of SMR over Rh(1.1)NiAl40-C550-R700 and Rh(1.1)NiAl70L-C550-R700 catalysts (CH_{4inlet}= 16.2ml/min, S:C=3:1, 1 atm).

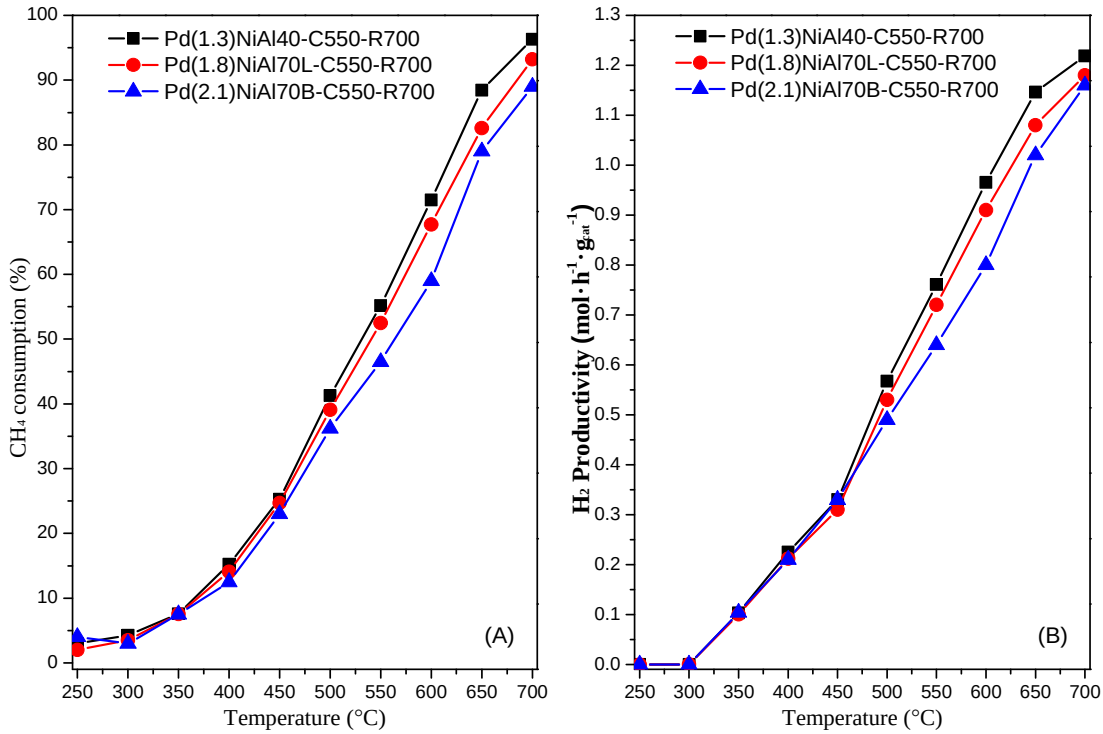


Figure 3.15 Comparison of (A) CH_4 consumption and (B) H_2 productivity of SMR over Pd(1.3)NiAl40-C550-R700, Pd(1.8)NiAl70L-C550-R700 and Pd(2.1)NiAl70B-C550-R700 catalysts (CH_{4inlet}= 16.2ml/min, S:C=3:1, 1 atm).

Compared with the unpromoted catalysts, the Pd and Rh promoted catalysts exhibited much higher activity for SMR, especially at intermediate temperature range (500-700°C). This is because the noble metal promoters not only contribute an increase of catalyst SA, but also result in a strong synergetic effect. As shown in Figures 3.14 and 3.15, the SMR reactions begin at temperatures below 250°C on all the tested Pd and Rh promoted catalysts, indicating a reduction in activation energy of SMR reactions.

In Figure 3.14, the Rh(1.1)NiAl40-C550-R700 catalyst achieved the highest activity with 74.8% CH_4 consumption and 1.011 $mol \cdot h^{-1} \cdot g_{cat}^{-1}$ H_2 output at 600°C, which is equal to a 15-20% enhancement in catalytic activity compared to the NiAl40-C550-R700 catalyst. The activity of the Rh(1.1)NiAl70L-C550-R700 catalyst was slightly lower than that of the Rh(1.1)NiAl40-C550-R700 catalyst, possibly due to the large crystallite size. A significant enhancement on the activity by Pd promoter is also found in the three promoted catalysts (Figure 3.15). The best performance in this series is achieved by Pd(1.3)NiAl40-C550-R700 catalyst, with a 71.5% CH_4 consumption and 0.965 $h^{-1} \cdot g_{cat}^{-1}$ H_2 output at 600°C. A decrease on activity is found in the other two Pd promoted catalysts, with precursors prepared under the severe preparative conditions. This result is as expected since the synergetic effect in these catalysts is possibly weakened by the poor distribution of Pd or even a segregation of PdO.

On the other hand, the lower nickel dispersion of nickel in the Pd promoted catalyst (detected from TPR analyses) does not influence the promoting effect on catalysts activity. This result reveals that internal structure play predominant role compared with the nickel dispersion in this type of LDH derived catalyst system.

At about 700°C, the promoting effect became less significant since the reactions of SMR reactions were close to thermodynamic equilibrium.

3.3.8.3 Reaction pathways

Three major primary reactions occur during methane steam reforming.

$$CH_4 + H_2O \leftrightarrows 3H_2 + CO \qquad \Delta H°_{298} = +206 \text{ KJ/mol} \tag{3.1}$$

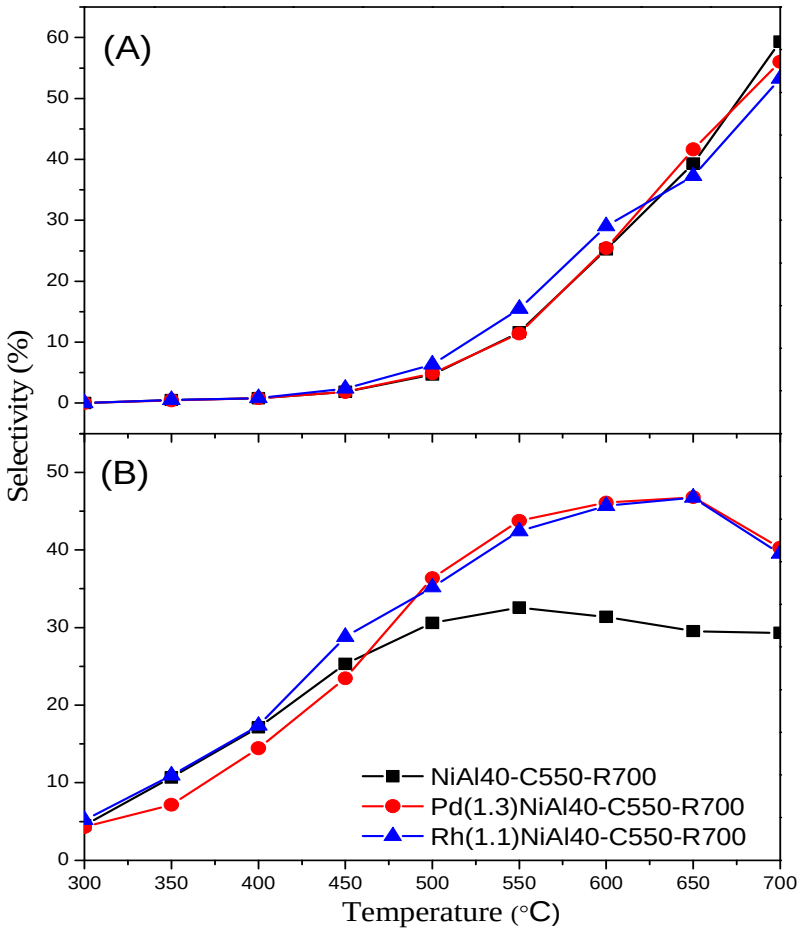
$$CO + H_2O \leftrightarrows H_2 + CO_2 \quad \Delta H°_{298} = -41 \text{ KJ/mol} \tag{3.2}$$

$$CH_4 + 2H_2O \leftrightarrows CO_2 + 4H_2 \quad \Delta H°_{298} = +165 \text{ KJ/mol} \tag{3.3}$$

The SMR reactivity may be enhanced over promoted catalyst by improved adsorption of methane.

Figure 3.16 shows CO and CO_2 evolution during SMR over NiAl40-C550-R700, Pd(1.3)NiAl40-C550-R700 and RhNiAl-550-R700 catalysts. In Figure 3.16A CO evolution from unpromoted catalyst NiAl40-C550-R700 and the two noble metal promoted catalysts show a similar and comparable trend indicating little or no promotional effect on reaction (3.1). The CO_2 evolution profiles in Figure 3.16B, on the other hand, show a considerable difference between the unpromoted and promoted catalysts. At 600°C, CO_2 evolution in the product gas reaches 46.2% and 47.1% for the Pd(1.3)NiAl-550-R700 and RhNiAl-550-R700 catalysts compared with only 31.4% from unpromoted NiAl40-C550-R700. CO_2 production by the reaction (3.2) can

easily be ruled out as the CO evolution profiles are unchanged. The above observations confirm the fact that hydrogen production is enhanced by the promoted catalyst by accelerating the forward reaction of reaction (3.3). The enhancement on activity is also due to an increase in surface area by noble metal promoters and the surface exposed promoted nickel metal becoming labile to adsorb and react with the reactant species, forming more hydrogen.



#

Figure 3.16 (A) CO and (B) CO_2 evolution (%) during SMR over (A) NiAl40-C550-R700, (B) Pd(1.3)NiAl40-C550-R700 and (C) Rh(1.1)NiAl40-C550-R700 catalysts.

3.4 Conclusions

The Ni/Al and noble metal promoted N/Al LDHs were successfully prepared by co-precipitation at different temperatures and digestion times. The samples are well characterised. The results indicate high CP temperature and long aging time increased the LDH's crystallinity and crystal sizes and reduced their lattice constant in *a* and *c* directions. Rh showed very high preference to the brucite layers of the LDHs and its content had no significant dependence on the preparative conditions. The incorporation of Pd is mainly determined by the energy input during preparation and Pt has less affinity to the LDH lattice making it difficult to incorporate into the LDH system.

Homogeneously mixed Ni(Al)O catalysts and active Ni/Al catalysts have been obtained by calcination and reduction. After calcination, the calcined catalyst regained some of the physical and chemical properties of their LDH precursors. The incorporation of noble metal ions in the catalysts exhibited strong synergetic effect and this not only changed the internal structure but also enhanced the catalysts reducibility and activity. It is found that the activity of Pd promoted catalysts decreased with the severe preparative conditions of their LDH precursors since the high Pd loading result in a segregation of PdO and poor distribution of the Pd in the catalysts after thermal treatment; whereas, the Ni/Al and Rh promoted Ni/Al showed no dependence on this aspect, due to their unchanged chemical composition and internal structure.

Chapter 4. Effect of thermal treatments on Ni/Al LDHs and noble metals substituted Ni/Al LDHs and catalytic activity of the derived catalysts

4.1 Introduction

Catalytic ability is one of the most important segments of the commercially used catalyst and it can be affected by many factors. The effect of preparative conditions on the catalyst activity is investigated in the previous chapter. Beside preparative conditions, thermal treatment is another important factor which affects the catalyst structure, chemical composition and the catalytic ability of the LDH derived catalysts [206, 207]. Normally, LDH precursors are calcined and reduced to get the active catalysts. Pre-reduction of these oxides is not necessary for noble metal promoted catalysts due to their self-activation behaviour [130, 131, 140, 172, 173]. H_2 is produced in SMR reaction so that the catalysts are always in H_2 environment that keeps the catalysts in the active state. The catalysts in the present study are pre-reduced at 700°C which is the same as the highest temperature at which the activity tests are conducted. [105]. It is assumed that the reduction temperature has little or no effect on the activity and hence the investigation of thermal treatment is only focused on the calcination temperature. In this chapter, Ni/Al, Pd and Rh substituted Ni/Al LDHs are calcined at different temperatures or durations and well characterised to study the effect of calcination condition on catalyst structure, reducibility and catalytic ability of SMR reactions.

4.2 Experimental

LDH NiAl40, Pd(1.3)NiAl40 and Rh(1.1)NiAl40 were selected for the study in this chapter since the derived catalysts showed highest activity in the series of catalysts

studied in the previous chapter. These LDHs were calcined in static air environment at different temperatures (100, 200, 400, 450, 500, 550, 700, 800, 900 and 1000°C) for 4 h. In addition, a 20-h calcination of NiAl40 LDH was carried out separately in order to find the effect of calcination time on the catalytic performances.

The calcined catalysts were characterised by XRD, BET and TPR methods. Catalysts were pre-reduced at 700°C and activity measurements were performed from 250-700°C using the method described in Section 2.4.3.1 of Chapter 2.

4.3 Results and discussion

4.3.1 Effect of calcination temperature on the surface area of the calcined oxides

Figure 4.1 presents the SA of NiAl40, Pd(1.3)NiAl40 and Rh(1.1)NiAl40 LDHs calcined at different temperatures. All three samples show similar trend with the temperature of calcination. At low temperature range (below 200°C), SA of all the samples are low, between 80 and 100 m^2/g. Thermal decomposition of LDH starts from 100°C with continuous increase in the SA with elevating temperature. SA values reach maximum at around 450°C for all the samples. Pd and Rh substituted samples show higher SA than the NiAl40 samples in the whole decomposition range. The SA of the samples starts going down when the calcination temperature goes over 500°C. The decrease in SA at high temperature calcination is due to the change of internal structure of the mixed oxides. It is known that the calcined Ni(Al)O catalyst is

composed of highly disordered metastable mixed oxide with structural properties between pure nickel oxide and nickel aluminate. The increasing temperature makes the final oxides more like nickel aluminate[155].

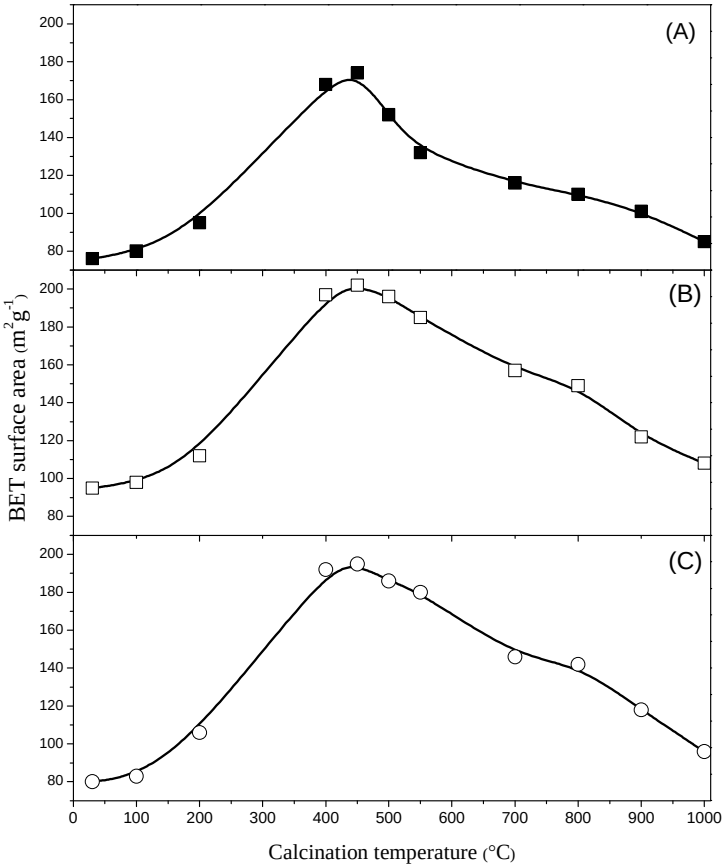


Figure 4.1 Effect of calcination temperature of (A) NiAl40, (B) Pd(1.3)NiAl40 and (C) Rh(1.1)NiAl40 on surface area.

4.3.2 Structure of catalysts

4.3.2.1 Calcination at 450, 550 and 700°C

In Figure 4.2, Ni/Al, Pd and Rh promoted Ni/Al LDHs after calcination at 450, 550 and 700°C exhibit typical NiO-like diffractions (ICDD: 47-1049), with broad

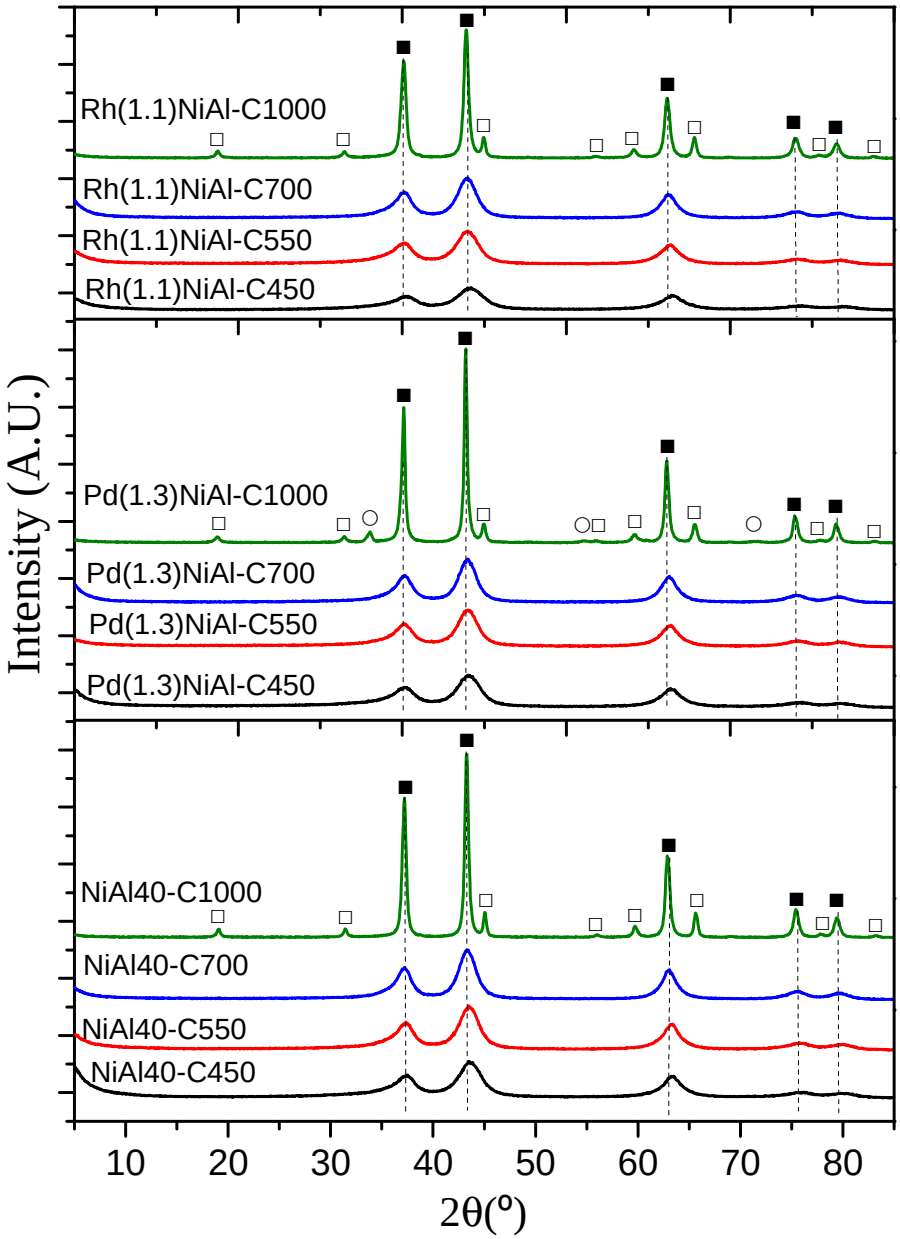


Figure 4.2 XRD patterns of the Ni(Al)O and Pd and Rh promoted Ni(Al)O catalysts calcined at 450, 550, 700 and 1000°C for 4 h. (■) Ni(Al)O; (□) $NiAl_2O_4$ spinel; (○) PdO.

baselines and low intensity diffraction peaks at 2θ=37°, 43°, and 63° compared with pure nickel oxide. The absence of aluminium oxide peak and the small displacement of all diffraction peaks to higher 2θ range suggests an aluminium substitution in the nickel oxide lattice, forming metastable Ni(Al)O [117, 208, 209]. There is no distinctive phase corresponding to nickel aluminate, palladium or rhodium oxide. At

these temperatures sufficient energy may not be realised for the formation of spinel crystallization [195, 210]. However, the high calcination temperature, enhance the crystallinty and increase crystallite sizes of the Ni(Al)O in all the cases (Table 4.1).

For the unpromoted Ni(Al)O catalysts, the lattice parameters decrease as a function of increasing calcination temperature, indicating the shrinkage of the lattice cell during high temperature calcination. This may cause a stronger Ni-Al coordination in the catalyst structure.

Pd or Rh addition in the catalyst produce smaller crystallite sizes and larger lattice parameters and higher SA when compared with unprompted Ni(Al)O catalysts calcined at the same temperature, indicating good incorporation of Pd, or Rh promoters in the catalysts. Unlike the unpromoted Ni(Al)O, the lattice constant of both Pd, and Rh promoted Ni(Al)O series follow a trend as $a_{c550} > a_{c450} > a_{c700}$. This phenomenon may be related to the distribution of Pd and Rh in the lattice. The Ni:Al ratios on the surface and bulk of the Ni(Al)O are different irrespective of the catalyst calcination temperature as known from the literature [195, 211-213]. The surface of the catalyst is enriched by aluminium and hence Ni:Al ratio in the bulk is higher than the surface. The distribution of Pd and Rh in the Ni(Al)O may not be uniform due to the same reason. It may be proposed that higher Pd and Rh distribution at surface layer in the 450°C calcined catalysts whereas in the 700°C calcination, the noble metal migrates to the bulk, making Pd or Rh rich bulk. It is likely that intermediate temperature (550°C) calcination results in a relatively uniform distribution across the whole Ni(Al)O nanoparticle, hence causing a larger average lattice constant.

Table 4.1 Structure, chemical composition and surface area of catalysts calcined at 450, 550, 700 and 1000°C

LDH precursors	Calcined catalysts						
	Sample name	**Calcination temperature (°C)**	**Calcination time (h)**	**Phase**	**Crystallite size (nm)[a]**	**Lattice parameter *a* (Å)**	**BET SA (m^2/g)**
NiAl40 Crystallite size: 16.2nm Ni:Al=72.8:27.2 (Atomic %) Lattice parameter: *a*=3.036, *c*=23.091	NiAl40-C450	450	4	Ni(Al)O	10.9	4.165	173.6
	NiAl40-C550	550	4	Ni(Al)O	13.5	4.159	137.7
	NiAl40-C700	700	4	Ni(Al)O	15.7	4.151	115.9
	NiAl40-C1000	1000	4	NiO, $NiAl_2O_4$	24.8 (NiO)	4.188 (NiO)	85.72
	NiAl40-C550L*	550	20	Ni(Al)O	16.2	4.156	123.6
Pd(1.3)NiAl40 Crystallite size: 9.9nm Pd:Ni:Al=1.3:71.7:27.0 (Atomic %) Lattice parameter: *a*=3.048, *c*=23.136	Pd(1.3)NiAl40-C450	450	4	Pd/Ni(Al)O	5.2	4.181	202.1
	Pd(1.3)NiAl40-C550	550	4	Pd/Ni(Al)O	8.4	4.186	184.9
	Pd(1.3)NiAl40-C700	700	4	Pd/Ni(Al)O	9.6	4.176	157.3
	Pd(1.3)NiAl40-C1000	1000	4	NiO, PdO Pd/NiO $NiAl_2O_4$	28.7(NiO)	4.192 (NiO)	102.1
Rh(1.1)NiAl40 Crystallite size:9.7nm Rh:Ni:Al=1.1:72.2:26.7 (Atomic %) *a*=3.042, *c*=23.118	Rh(1.1)NiAl40-C450	450	4	Rh/Ni(Al)O	6.7	4.173	194.7
	Rh(1.1)NiAl40-C550	550	4	Rh/Ni(Al)O	9.7	4.177	179.5
	Rh(1.1)NiAl40-C700	700	4	Rh/Ni(Al)O	10.8	4.168	146.2
	Rh(1.1)NiAl-C1000	1000	4	Rh/NiO, $Rh/NiAl_2O_4$	22.7 (NiO)	4.186	91.3

Brown number in the catalyst name indicates calcination temperature (°C).

*L=long calcination duration (20 hours)

[a]. Mean values from reflections (111), (200) and (220), ref ICDD 00-047-1049.

4.3.2.2 Calcination at 1000°C

XRD pattern of the 1000°C calcined samples are given in Figure 4.2. In all the causes a structural rearrangement of the catalysts with sharp and narrow diffraction peaks at around 2θ=37°, 43°, and 63° assigned to pure nickel oxide (ICDD: 00-047-1049) along with a series of low intensive but clear diffraction peaks corresponding to nickel aluminate (ICDD: 00-001-1154). The aluminium oxide may exist as amorphous or γ-Al_2O_3 state since there is no clear diffraction found in all cases.

The diffraction pattern of Pd(1.3)NiAl40-C1000 shows small peaks at around 2θ=33.7°, 54.7° and 71°, suggesting the formation of segregated PdO (ICDD: 01-075-0584), whereas no observable peaks corresponding to rhodium oxide are found in Rh(1.1)NiAl40-C1000 sample. Similar results have also been reported by Basile *et. al.* [149, 214] in the study of Ni/Mg/Al LDHs derived catalyst, where the Rh^{3+} are preferentially located in nickel oxide and spinel phases, randomly distributed with Al^{3+}.

4.3.2.3 Calcination for 4 h and 20 h

The prolonged calcination time also cause an increase in crystallinity and crystallite size of the Ni(Al)O as shown in Figure 4.3 and Table 4.1. The diffraction peaks also shift slightly to lower 2θ along with a decreased lattice constant due to shrinkage of the crystal lattice.

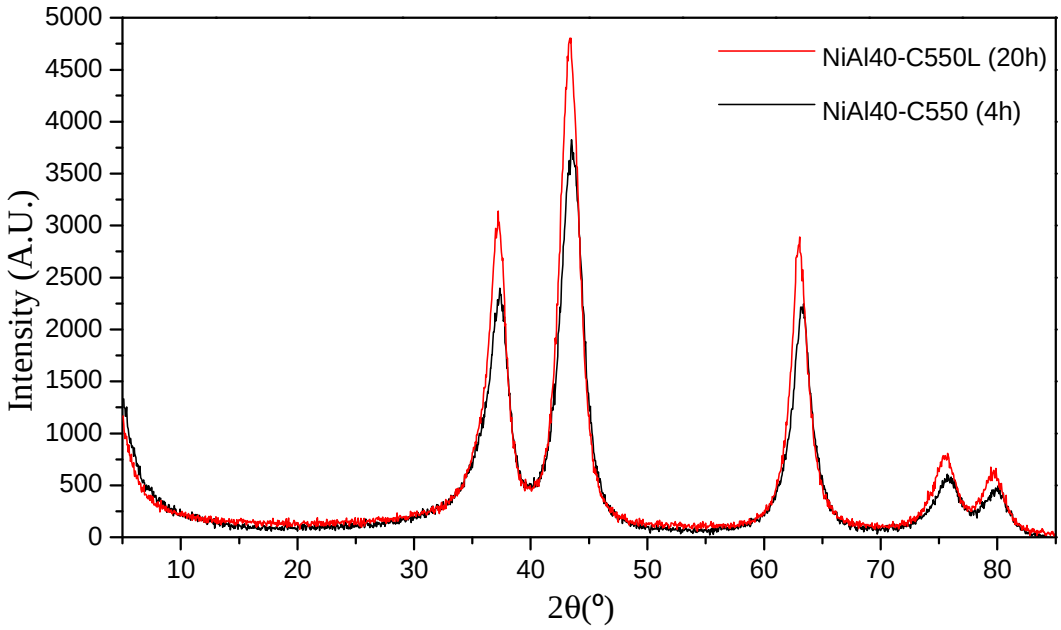


Figure 4.3 XRD patterns of NiAl40LDH precursor calcined at 550°C for 4 h (NiAl40-C550) and 20 h (NiAl40-C550L).

4.3.3 TPR analysis

TPR were be used to investigate the impacts of calcination temperature on the reducibility and internal structures of the catalysts.

4.3.3.1 Calcination at 450, 550 and 700°C

Figure 4.4A displays the TPR results of Ni(Al)O catalysts obtained from different calcination temperatures. The reduction of nickel occurs in a broad range from 400 to 900°C, depending on their calcination temperature.

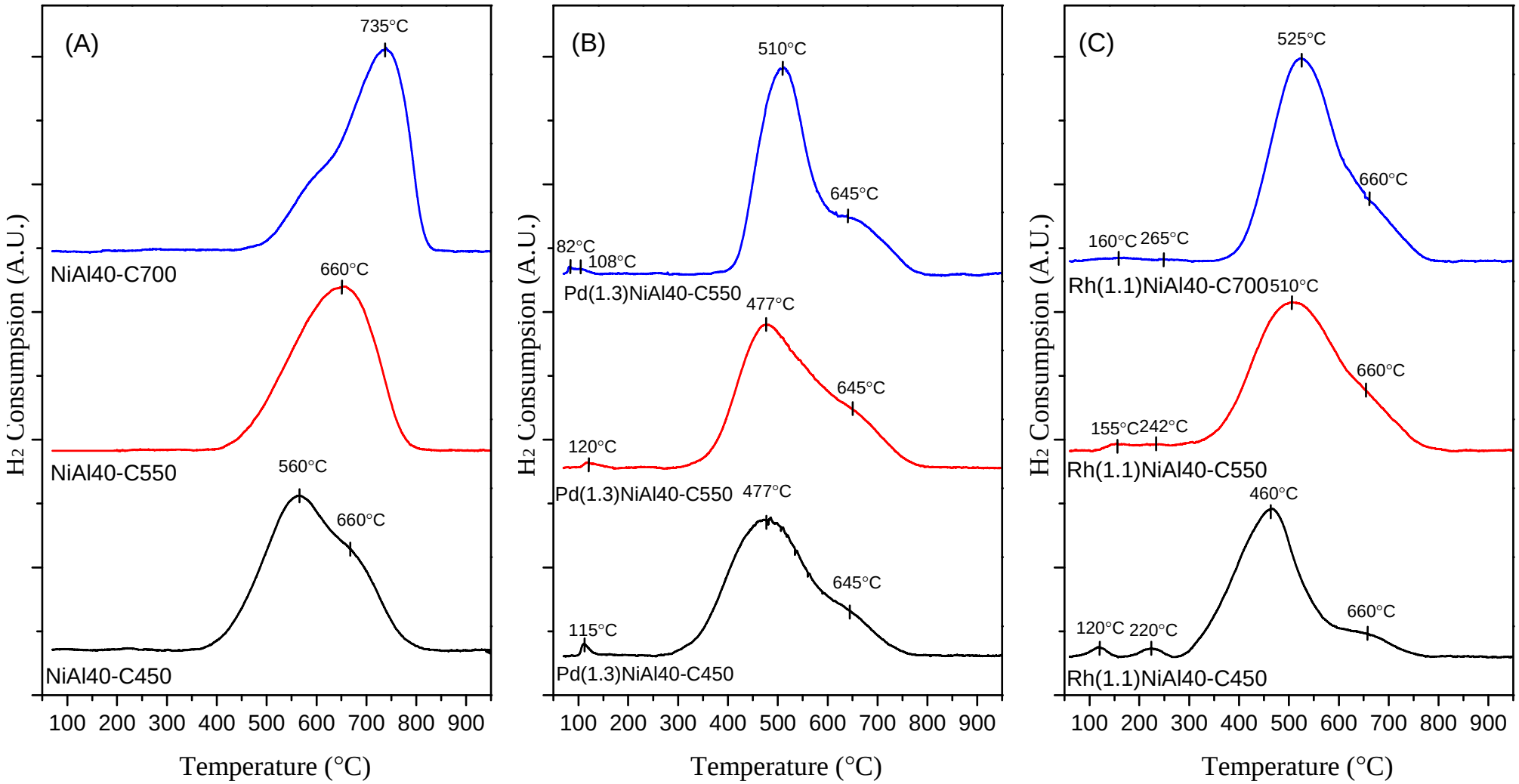


Figure 4.4 TPR profiles of (A) Ni(Al)O, (B) Pd promoted Ni(Al)O and (C) Rh promoted Ni(Al)O catalysts calcined at 450, 550 and 700°C.

The 450°C calcined catalyst, NiAl40-C450 shows reduction peak is around 560°C, which is higher than the reduction temperature of pure NiO (around 412°C, Figure 4.5). This is due to the integration of Al in the NiO mixed oxide. Al^{3+} surrounded by Ni^{2+} polarizes more or less the covalent Ni-O bonds, making the bonds more ionic and stronger. This ligand effect makes the Ni(Al)O less reducible. Moreover, the reduction occurs at a wide range of temperatures in comparison with the single narrow peak for pure NiO, indicating Ni^{2+} is in different coordination with Al^{3+} in the structure [155].

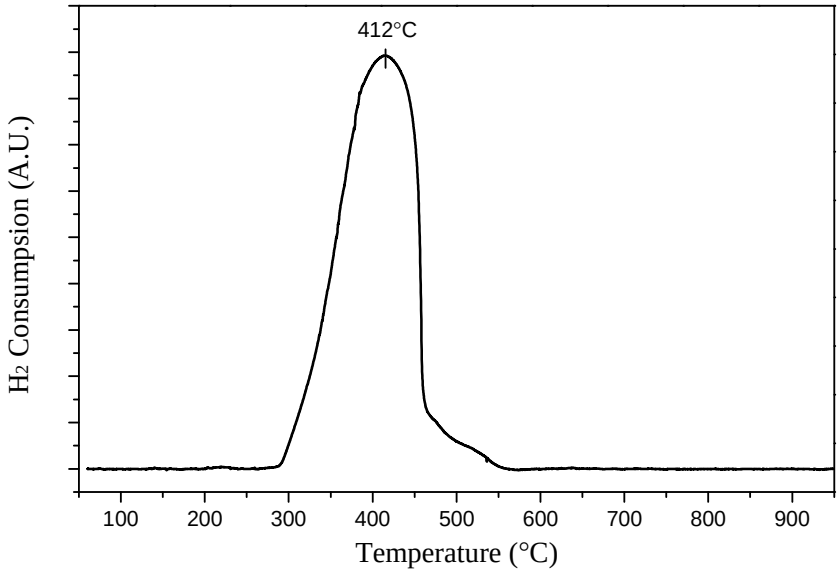


Figure 4.5 TPR profile of pure NiO from calcination of $Ni(NO_3)_2 \cdot 6H_2O$ at 450°C for 4 h.

The reduction temperature increases as increasing the calcination temperature. For the 550 and 700°C calcined Ni(Al)O catalysts, the reduction maxima shift to 660 and 735°C, respectively. Similar results were reported in the literature [117, 118]. The high temperature calcination makes the crystal lattice more compact (Table 4.1) and

hence the Ni-Al bonds are strengthened and have an increase in the charge of nickel, making the catalyst more close to nickel aluminate and less reducible.

The reducibility of the catalysts is significantly enhanced when Pd and Rh promoters are incorporated into the catalyst system. Figures 4.4B and C show Pd and Rh promoted catalysts calcined at 450°C reduction, being reduced at around 460-480°C. This reduction temperature is very close to the pure nickel oxide (Figure 4.5). It is likely that the presence of Pd and Rh in the lattice caused a synergetic effect which weakens the polarisation of nickel by the surrounding aluminium. This effect is significantly higher than the ligand effect caused by aluminium seen in the high temperature calcined catalysts. Hence even the high temperature calcined (700°C) samples show reduction maxima below 530°C. The internal structure of Ni(Al)O may also be changed by Pd and Rh incorporation and hence the main reduction peaks in these catalysts are arisen from S.N.O or D.O.S.I whereas the shoulder at 640-660°C are due to S.L.M. form. Along with the increasing calcination temperature, the content of S.L.M form gradually goes up.

It should be noticed that very low temperature reduction peaks appear due to reduction of surface exposed Pd or Rh. For Pd(1.3)NiAl40-C450 catalyst, a small peak at 115°C is observed. This peak becomes less intense, shifting to 120°C for Pd(1.3)NiAl40-C550 catalyst. When the calcination temperature is further increased to 700°C, the peak splits into two features: one at 82°C and another at 108°C. The 108°C peak is assigned to reduction of surface exposed Pd^{2+} and the 82°C peak is assigned the reduction of segregated PdO [204, 205].

The Rh promoted Ni(Al)O shows two small symmetric peaks at low temperature range. Since XRD patterns (Figure 4.2) and TPR profiles of 1000°C calcined sample (Figure 4.6) do not identify any rhodium oxide, these two reduction peaks should belong to the reduction of substantial Rh^{3+} located in different sites i.e. tetrahedral and octahedral interactions in the Ni(Al)O matrix. The Rh series catalysts, as seen in Pd promoted catalysts, the reduction peaks shift to higher temperature with a decrease in H_2 consumption as a function of increasing calcination temperature of the LDHs. These results agree well with the trend found in the lattice parameter – calcination at low temperature results in a higher ratio of Pd or Rh distributed in the surface layer. When the calcination temperature is increased, the surface exposed Pd and Rh start to migrate to the bulk. Hence, the quantity of surface Pd or Rh goes down causing smaller reduction peaks. On the other hand, the aluminate in the lattice not only polarise the nickel but also influence the charge on Pd or Rh. The decrease in total number of Pd or Rh ions in the surface Al-enriched layers also strengthens the polarisation of these noble metal ions by surrounding aluminium. As a result, the surface exposed Pd or Rh become less reducible.

4.3.3.2 Calcination at 1000°C

Structure rearrangement happens when the calcination temperature is increased to 1000°C. Figure 4.6 shows clear phase segregation in all three samples. NiAl40-C1000 sample shows a sharp narrow peak at 510°C corresponding to NiO generated upon withdrawal of aluminium from the Ni-Al solid solution and another broad peak at about 830°C due to the reduction of $NiAl_2O_4$ formed at high temperatures [215, 216]. Alumina, possibly γ-Al_2O_3 or amorphous form, is also produced at the same time. It

may be noted that the Al_2O_3 formed acts as support for NiO particles. Therefore, the reduction temperature of the NiO phase appears at 510°C, higher than that of unsupported pure NiO. The mechanism is quite similar to the reduction of impregnated Ni/Al_2O_3 catalyst. Strong metal to support interaction exists between NiO and Al_2O_3 support and consequently increases the reduction temperature of NiO [68, 217].

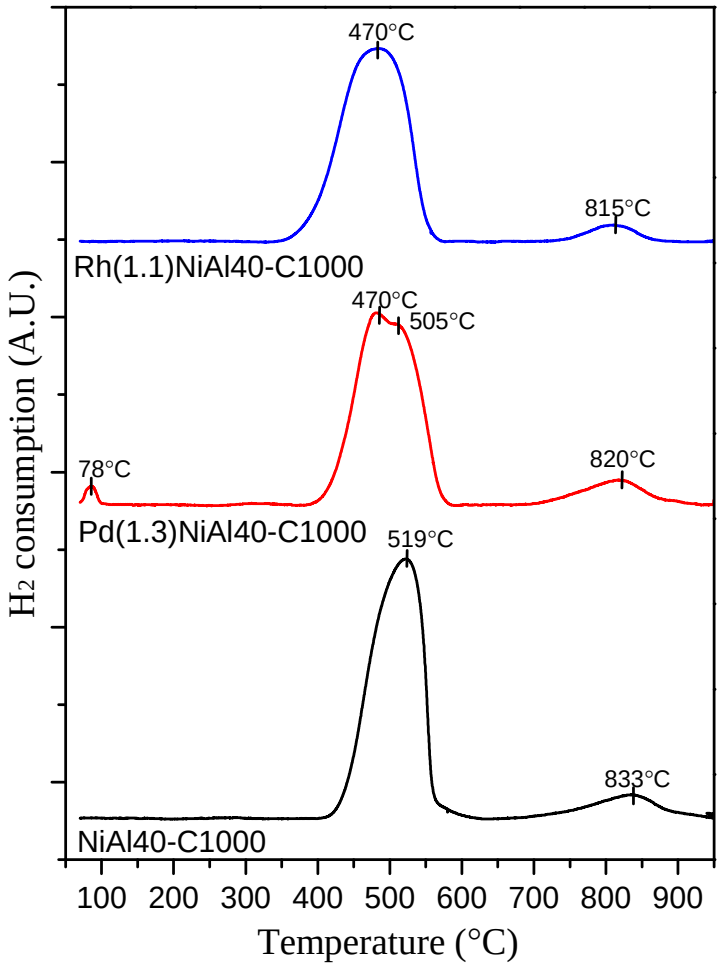


Figure 4.6 TPR profiles of 1000°C calcined samples.

The Rh(1.1)NiAl40-C1000 sample also show two reduction peaks with slight displacement to lower temperatures due to the incorporation of Rh in the nickel oxide

and nickel aluminate. The absence of separate low temperature reduction peaks corresponding to rhodium oxide further confirms this incorporation.

Pd(1.3)NiAl40-C1000 sample shows a split in the main reduction peak at intermediate temperature. The peaks at 470°C and 510°C are found to overlap. The first peak is derived from the reduction of Pd substituted Ni(Al)O system and the second one is assigned to pure Ni(Al)O system without substantial Pd in the crystal lattices. The reduction peak at 830°C shifts to 810°C due to existence of Pd in nickel aluminate formed during calcination. There is only one low temperature reduction peak observed at 78°C in agreement with the XRD results and literature [204, 205] ascribing to the segregated PdO. The TPR and XRD results show a relative low affinity of Pd to LDH [149, 214] implying an occurrence of segregation of Pd when the LDH is calcined at high temperature.

4.3.3.3 Calcination for 4 h and 20 h

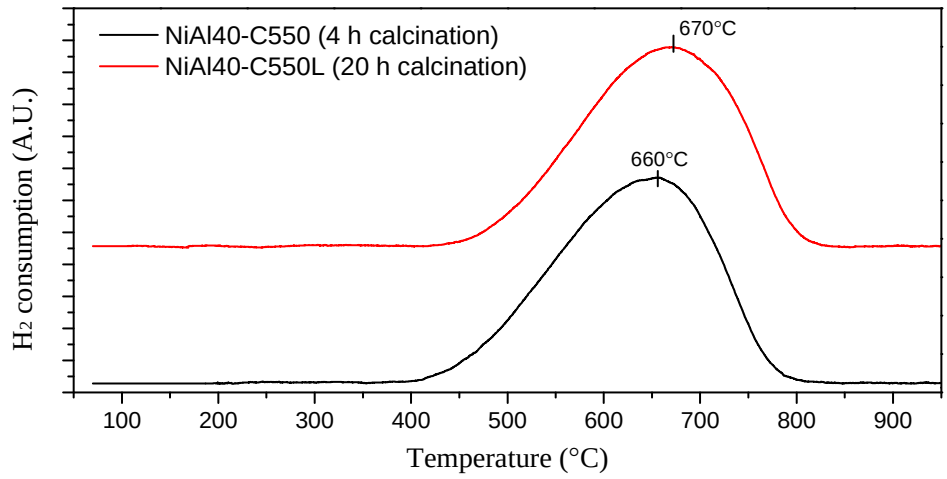


Figure 4.7 TPR of Ni(Al)O catalysts calcined at 550°C for 4 and 20 h.

Figure 4.7, shows similar TPR curves for NiAl40-C550 and NiAl40-C550 catalysts. As noticed in XRD, the prolonged calcination time led shrinkage of the lattice and thus strengthened Ni-Al bond. Hence, the reduction maximum of NiAl40-C550L catalyst shifts to higher temperature.

4.3.4 Catalyst activity

4.3.4.1 Activity as a function of calcination temperature

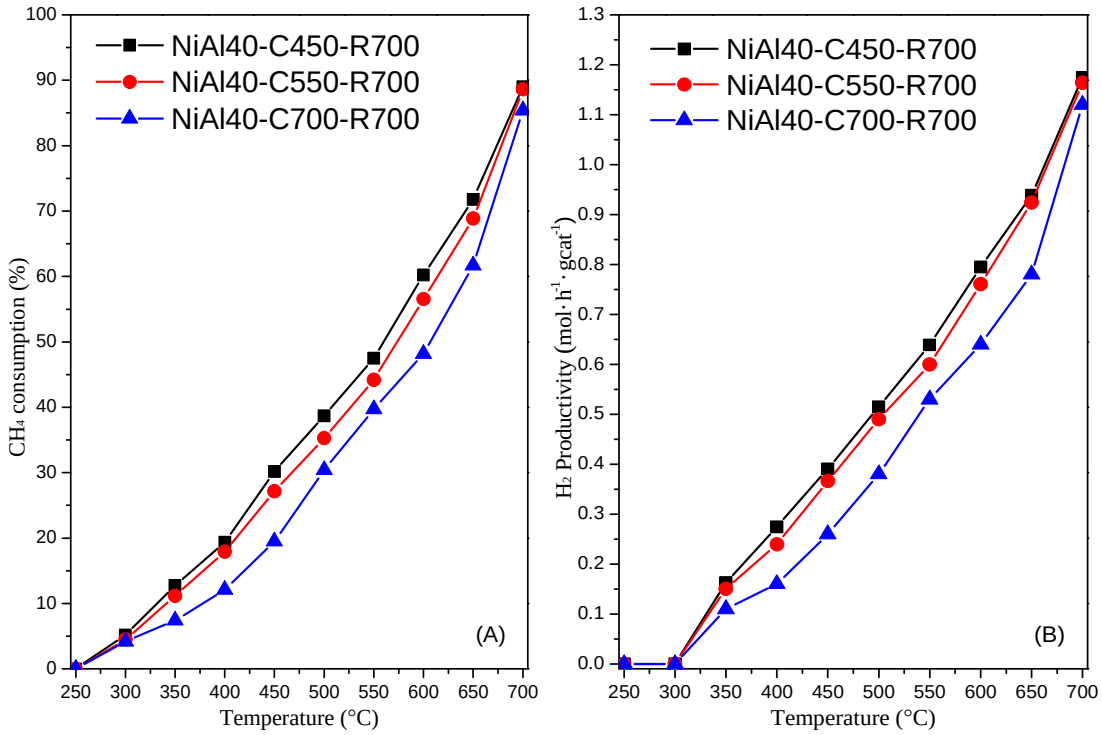


Figure 4.8 Comparison of (A) CH_4 consumption and (B) H_2 productivity of SMR over Ni/Al catalysts calcined at 400, 550 and 700ºC (CH_{4inlet}=16.2ml/min, S:C=3:1, 1 atm).

Figure 4.8 compares of the reactivities of SMR over NiAl40-C450-R700, NiAl40-C550-R700 and NiAl40-C700-R700 catalysts. The light-off temperatures are between

250 and 300°C for all the catalyst. The CH_4 consumption and H_2 productivity continuously increased with increasing temperature from temperatures over 300°C. The activities of all the catalysts decreased with increasing calcination temperatures which is in agreement with the changes of catalyst lattice constant. The smaller lattice parameter of Ni(Al)O may cause stronger Ni-Ni bonds after reduction, hence nickel becomes less labile.

Addition of noble metal promoters increased the activation towards SMR reactions. All Pd and Rh promoted catalysts start up below 250°C (Figures 4.9 and 4.10), indicating a reduction in activation energy. Pd or Rh promoted catalysts show higher catalytic activity when compared to the sample without any noble metal promotion with similar preparative and thermal treatment conditions. On the other hand, both Pd and Rh containing catalysts calcined at 550°C exhibit the highest reactivity in their series, especially at intermediate temperature range. In consideration with the lattice parameter and the mechanism proposed, the promoted catalysts obtained by 550°C calcination have relatively uniform dispersion of noble metal and hence having the strongest synergetic effect. Large amount of surface nickel provide an optimum condition for spill-over of CH_4 and adsorb the product CH_x- (x=1, 2 or 3) on the active sites [68]. In contrast, the high amount of Pd or Rh on the surface of 450°C calcined catalysts can push the equilibrium in the opposite direction. The 700°C calcined catalyst has lower amount of Pd or Rh on the surface, or even segregated noble metal causing a lower promotional effect.

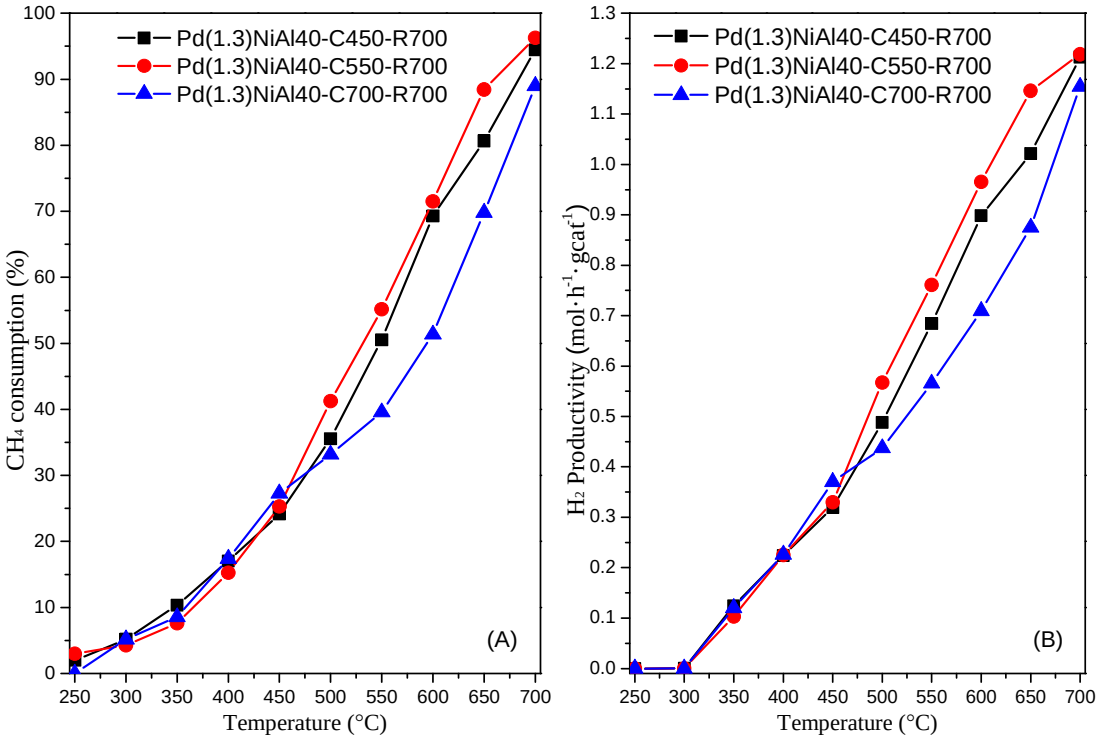


Figure 4.9 Comparison of (A) CH_4 consumption and (B) H_2 productivity of SMR over Pd promoted Ni/Al catalysts calcined at 400, 550 and 700°C (CH_{4inlet}= 16.2ml/min, S:C=3:1, 1 atm).

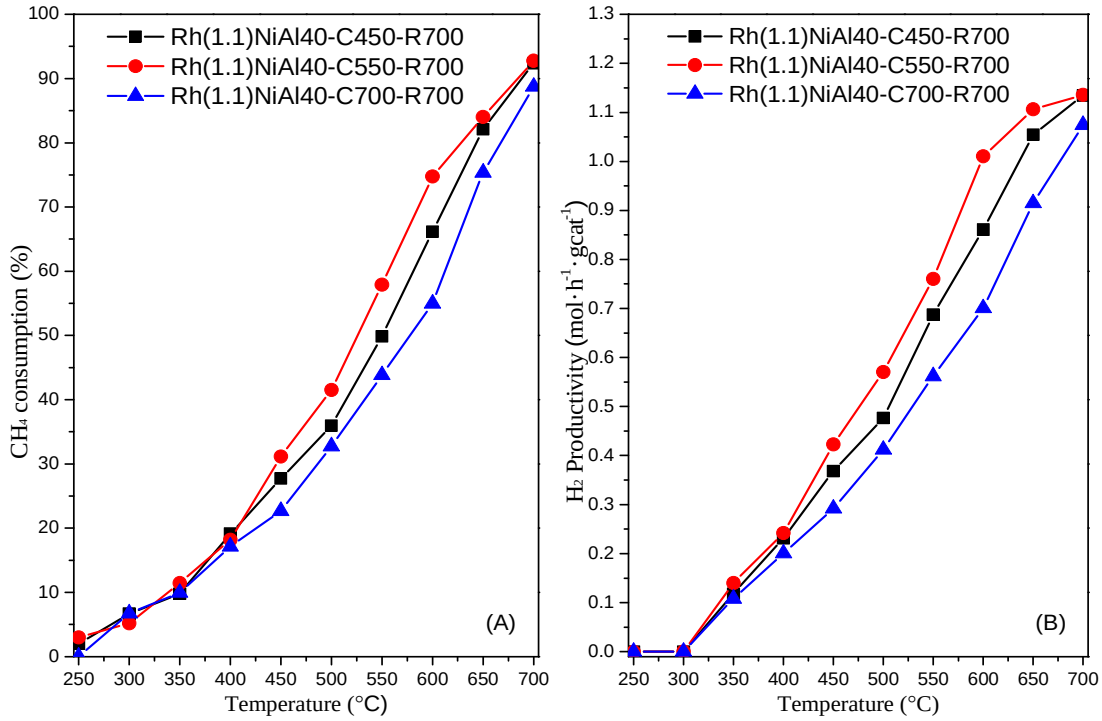


Figure 4.10 Comparison of (A) CH_4 consumption and (B) H_2 productivity of SMR over Rh promoted Ni/Al catalysts calcined at 400, 550 and 700°C (CH_{4inlet}= 16.2ml/min, S:C=3:1, 1 atm).

4.3.4.2 Activity as a function of calcination time

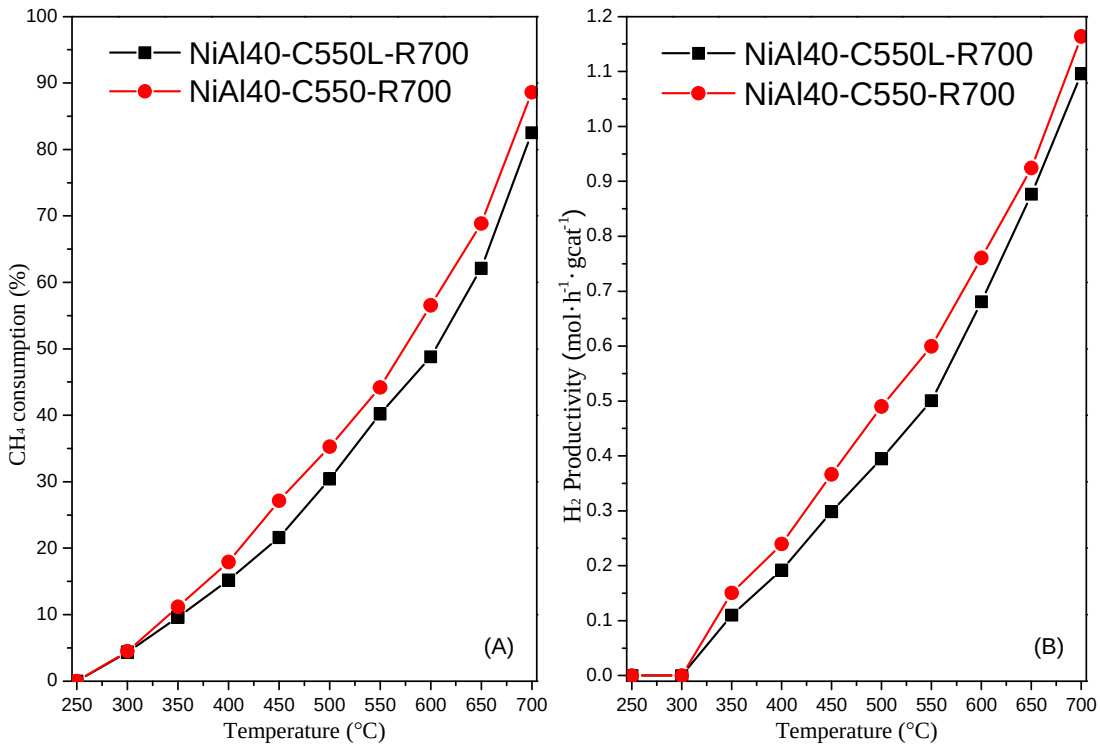


Figure 4.11 Comparison of CH_4 consumption (A) and (B) H_2 productivity of SMR over Ni/Al catalysts clacined for 4 and 20 h (CH_{4inlet}= 16.2ml/min, S:C=3:1, 1 atm).

Figure 4.11 presents the performance of SMR over NiAl40-C550-R700 (4 h calcination) and NiAl40-C550L-R700 (20 h calcination) derived from same LDH precursor but with calcination for 4 h and 20 h (represented by 'L' in the catalyst name) respectively. The light-off temperatures for both the catalysts are between 250 and 300°C. In the whole testing range, the activity of 4-h calcined catalyst shows higher activity than the 20-hour calcined one. The decrease of activity in the latter catalyst should be because the prolonged calcination leads lager crystallite size and lower surface area, as evidenced by XRD and BET results. Also, the smaller Ni(Al)O lattice may also possibly lead a strong Ni-Ni coordination after reduction, leaving less dangling Ni on the surface.

4.4 Conclusions

The experimental results show the calcination condition plays an important role on catalyst structure, reducibility and catalytic ability. A high calcination temperature increased crysatllinity and decreased the surface and reducibility of the unpromoted catalyst. It makes the catalyst structure of Ni(Al)O more prone to the nickel aluminate, causing a small crystal lattice, thus lower activity.

Pd and Rh are proved to be incorporated in the lattice of the catalyst after reduction and significantly enhanced the reducibility by weakening the ligand effect while maintaining the structure and behaviour of the catalyst more close to the NiO. The distribution of Pd and Rh shows strong dependence on the calcination condition. The elemental distribution is found as predominate issue for the catalytic activity of Pd or Rh promoted catalyst (derived from same LDH), in comparison with other issues like crystallite size, SA. An intermediate calcination temperature at 550°C, for the Pd or Rh promoted catalyst, leads largest average lattice constant as well as the highest activity of SMR reactions. The promoters, in this case, have optimum distribution with minimum segregation and with less migration to the bulk.

Chapter 5. Effect of quantity of promoters on noble metal promoted Ni/Al LDHs and activities of the derived catalysts

5.1 Introduction

In the previous chapters, the effect of preparative conditions and thermal treatments of LDH derived catalysts on some of the physical and chemical properties and catalytic activities are investigated. Some of these factors have direct influence on the catalytic behaviour of the catalysts. These parameters have to be optimised for high-quality reforming catalysts that will operate in IT- SOFC.

In this chapter, the effect of promoter quantities on catalytic properties is discussed in detail. Catalysts with different Pd and Rh loadings were prepared in the optimised conditions as discussed in the previous chapters, then characterised and tested for catalytic activity. The results indicate that Pd and Rh still interact with Ni even after H_2 reduction. An optimum amount of prompter is found and plays a key role in the catalytic ability of the catalysts. Indeed, promoter levels in excess of this optimum quantity can cause a migration of the promoter atom from surface to bulk and local accumulation or even segregation in the reduced catalyst.

5.2 Experimental

A/Ni/Al LDH (A=Pd, or Rh) precursors (formula: $[Ni_{0.75-x}A_xAl_{0.25}(CO_3)_{0.125+\delta}(OH)_2]\bullet nH_2O$) with an atomic ratio of A:Ni:Al=x:0.75-x:0.25, ($0 \leq x \leq 0.05$) were prepared by CP method described in Section 2.2 of Chapter 2. All LDHs were prepared by co-precipitation at 40°C, followed by 4 h aging. The LDHs were calcined at 550°C for 4 h to get the oxide form catalysts.

As-prepared LDHs were characterised by EDX, XRD and derived catalysts were characterised by XRD, TEM, FTIR and TPR. Details of these experiments are given in Section 2.5 of Chapter 2. All catalysts were pre-reduced at 700°C before SMR. Activity measurements were carried out from 250-700°C as described in Section 2.4.3.1 of Chapter 2.

5.3 Results and discussion

5.3.1 Compositions of LDHs

A series of Pd/Ni/Al and Rh/Ni/Al LDHs were prepared with different Pd or Rh contents. Finely ground and sieved dry powders of these LDHs are shown in Figure 5.1 and 5.2. The homogenous incorporation of promoters in the LDH samples is evident from the uniform colour of the ground samples. The colour of the Pd or Rh incorporated LDH becomes darker with an increasing amount of promoters.

The chemical compositions of the as-prepared LDHs are listed in Table 5.1. The molar ratios of Ni/Al in all samples are quite close to those in the nitrate solution used in the CP (Ni:Al=3:1) solution, suggesting a complete precipitation of Ni^{2+} and Al^{3+} into the LDHs.

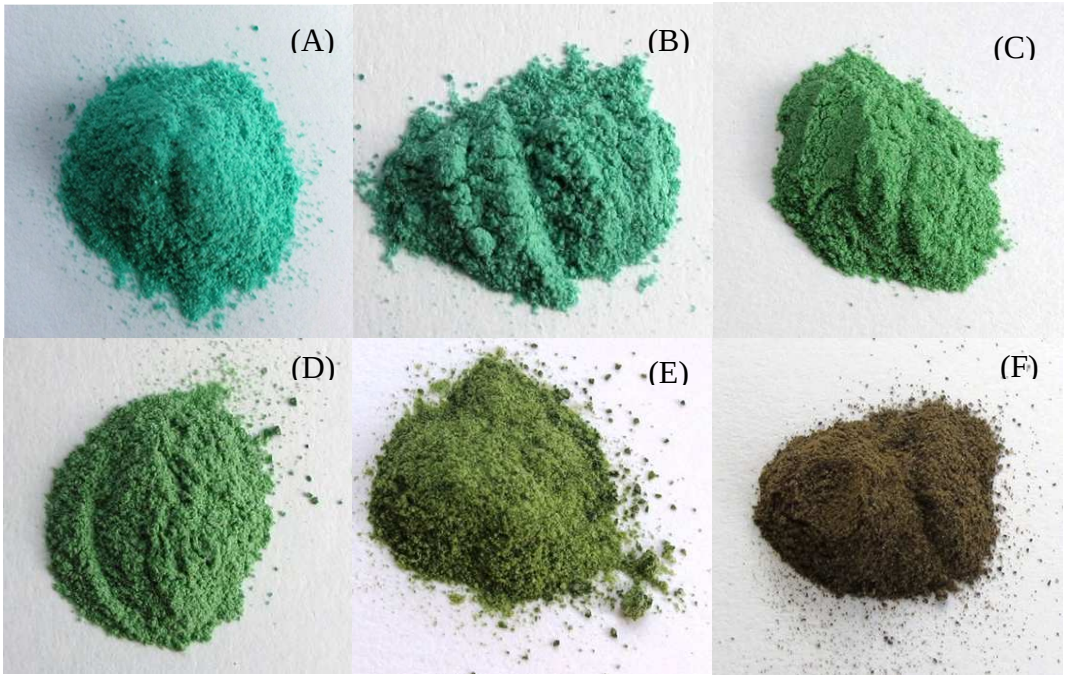


Figure 5.1 Pd substitued ground LDH powders: (A) Pd(0.3)NiAl40, (B) Pd(0.6)NiAl40, (C) Pd(1.3)NiAl40, (D) Pd(1.9)NiAl40, (E) Pd(2.3)NiAl40 and (F) Pd(4.0)NiAl40.

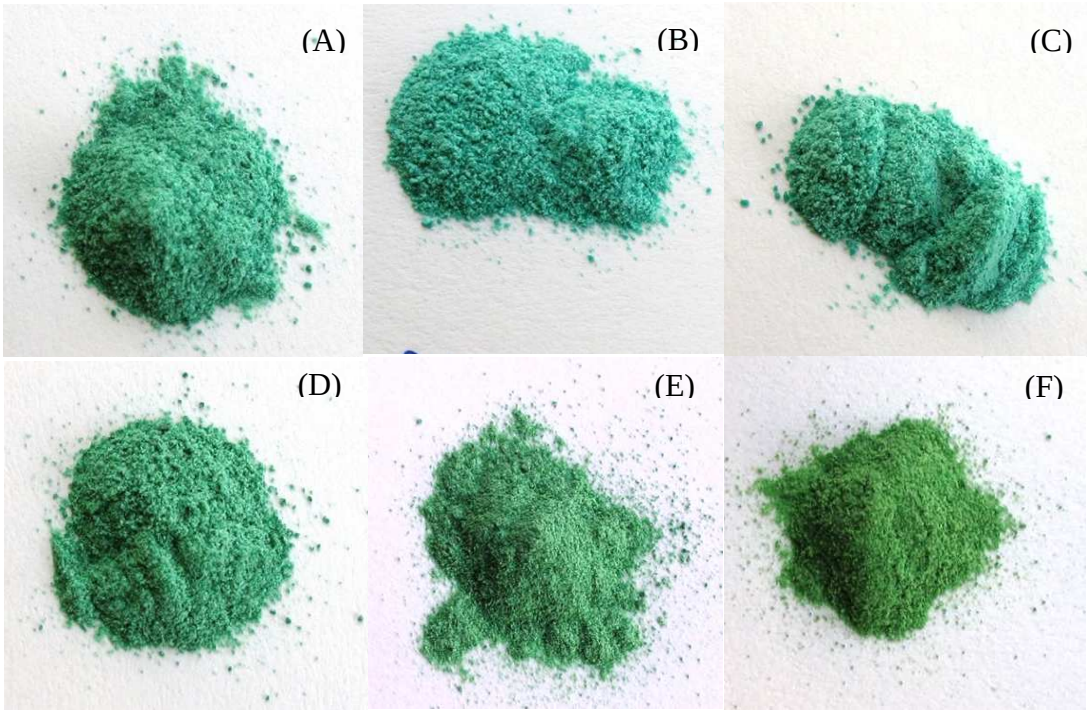


Figure 5.2 Rh substitued ground LDH powders: (A) Rh(0.5)NiAl40, (B) Rh(1.1)NiAl40, (C) Rh(1.6)NiAl40, (D) Rh(2.1)NiAl40, (E) Rh(3.1)NiAl40 and (F) Rh(4.2)NiAl40.

Table 5.1 Structure and chemical composition of as-synthesised LDHs.

LDH precursor	Expected metal molar ratio % (Solution)			Actual metal molar ratio % (Solid, by EDX)			Crystallite size of the precursors (nm)[a]	Lattice parameter (Å)	
	A	Ni	Al	A	Ni	Al		*a*	*c*
NiAl40	-	75.0	25.0	-	72.7	27.3	16.2	3.036	23.091
	Pd			**Pd**					
Pd(0.3)NiAl40	0.5	74.5	25.0	0.3	72.4	27.3	14.5	3.039	23.128
Pd(0.6)NiAl40	1.0	74.0	25.0	0.6	72.3	27.1	12.2	3.045	23.134
Pd(1.3)NiAl40	2.0	73.0	25.0	1.3	71.7	27.0	9.9	3.048	23.136
Pd(1.9)NiAl40	2.5	72.5	25.0	1.9	71.2	26.9	9.1	3.053	23.141
Pd(2.3)NiAl40	3.0	72.0	25.0	2.3	70.9	26.8	8.6	3.055	23.146
Pd(4.0)NiAl40	5.0	70.0	25.0	4.0	69.8	26.2	7.7	3.061	23.150
	Rh			**Rh**					
Rh(0.5)NiAl40	0.5	74.5	25.0	0.5	72.6	26.9	15.3	3.040	23.106
Rh(1.1)NiAl40	1.0	74.0	25.0	1.1	72.2	26.7	11.5	3.042	23.118
Rh(1.6)NiAl40	1.5	73.5	25.0	1.6	71.8	26.6	10.1	3.047	23.122
Rh(2.1)NiAl40	2.0	73.0	25.0	2.1	71.4	26.5	9.6	3.049	23.129
Rh(3.1)NiAl40	3.0	72.0	25.0	3.1	70.6	26.3	8.3	3.052	23.134
Rh(4.2)NiAl40	4.0	71.0	25.0	4.2	69.5	26.3	8.9	3.058	23.142

Red numbers in the catalyst name indicate the ratio of Pd or Rh in the overall Ni+Al+Pd or Ni+Al+Rh (%).
[a] Mean values obtained from reflections (003) and (006), ref ICDD 00-015-0087

5.3.2 Structure of LDHs

The XRD patterns of the crystallised LDHs are given in Figure 5.3. The crystallite sizes and lattice parameters are summarised in Table 5.1. All diffraction patterns show typical reflections of the pure takovite structure (ICDD: 00-015-0087) without excess phases. Pd and Rh are well incorporated into the brucite layers of the LDHs, as evidenced by an expansion of the lattice parameter in *a* and *c* directions. Electrostatic attraction between cationic layers decrease under this condition [201].

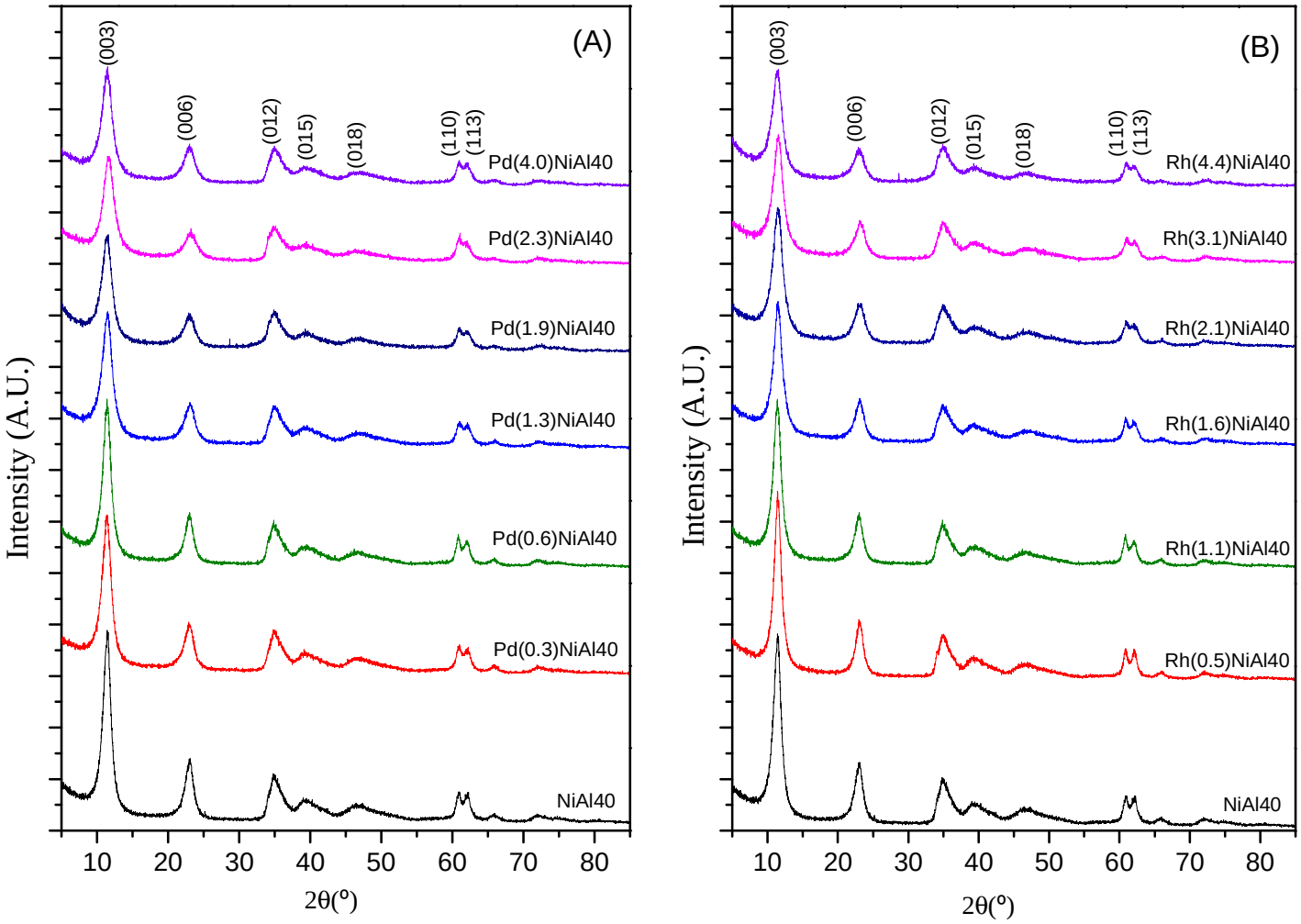


Figure 5.3 XRD patterns of Ni/Al LDH (in both Figure A and B) and, (A) Pd and (B) Rh substituted Ni/Al LDHs.

The peak intensities corresponding to the reflection line (003) and (006) at 2θ=11° and 22° gradually decrease with increasing content of Pd or Rh, indicating severe structure defection in Pd-Ni-Al or Rh-Ni-Al ternary LDH due to the mismatched ionic radii [218]. As a result, both crystallinity and crystallite size are reduced.

5.3.3 Structure of catalysts

Figure 5.4 shows the XRD patterns of 550°C calcined Pd and Rh promoted oxide catalysts derived from LDH precursors. In all the samples, the HT-like phases were completely destroyed during calcination. The dominant peaks are observed at 37°, 43° and 63°, corresponding to the (111), (200) and (220) planes, which are assigned to NiO-like structure (ICDD: 00-047-1049). For each catalyst, the broad bases of the peaks indicate the structure is composed of a mixture of Ni(Al)O cubic matrix, rather than the well-crystallised pure NiO. No phase assigned to alumina could be detected in any of the catalysts. The crystallinity and crystallite sizes decrease as a function of the increasing quantity of promoter ions as noticed in their precursors. An increase in lattice parameter *a* in the Pd and Rh promoted catalysts suggests the presence of a residential amount of Pd^{2+} and Rh^{3+} ions within the structure. For the samples containing Pd, it is found that there is no further increase in the lattice parameter when the Pd atomic ratio is over 1.3% (Pd/(Pd+Ni+Al)%) (Table 5.2). When the Pd content is greater than this ratio, the Pd in the NiO-like phase starts separating. Diffraction peaks at 2θ=33.7°, 54.7° and 71° suggest the segregated phase corresponds to PdO (ICDD: 01-075-0584). The segregated PdO may either be on the surface or within the bulk of the Pd/Ni(Al)O catalyst particles.

Rh promoted catalysts, on the other hand, show no evidence of formation of Rh_2O_3. All samples containing Rh retain the same NiO-like structure as the unpromoted NiAl40-C550 sample. However, the lattice parameter *a* does not continuously increases with increasing Rh content. In fact, the lattice parameter starts decreasing when the ratio of Rh/(Rh+Ni+Al)% is higher than 1.6. This is because a considerable amount of Ni^{2+} (0.069nm) is replaced by Rh^{3+}(0.068nm) in the CP solution during preparation.

Table 5.2 Crystal structure details of calcined and reduced catalysts.

Calcined catalyst			**Reduced catalyst (by H_2)**	
Name	**Crystallite size of the catalysts (nm)[a]**	**Lattice parameter *a* (Å)**	**Name**	**Lattice parameter *a* (Å)**
NiAl40-550	13.5	4.159	NiAl40-C550-R700	3.514
Pd(0.3)NiAl40-550	11.1	4.166	-	
Pd(0.6)NiAl40-550	9.6	4.173	Pd(0.6)NiAl40-C550-R700	3.529
Pd(1.3)NiAl40-550	8.4	4.186	Pd(1.3)NiAl40-C550-R700	3.538
Pd(1.9)NiAl40-550	7.2	4.184	-	
Pd(2.3)NiAl40-550	6.2	4.187		
Pd(4.0)NiAl40-550	5.0	4.188	Pd(4.0)NiAl40-C550-R700	3.541
Rh(0.5)NiAl40-550	10.8	4.164	Rh(0.5)NiAl40-C550-R700	3.516
Rh(1.1)NiAl40-550	9.7	4.177	Rh(1.1)NiAl40-C550-R700	3.521
Rh(1.6)NiAl40-550	7.6	4.179	-	
Rh(2.1)NiAl40-550	6.8	4.175		
Rh(3.1)NiAl40-550	6.1	4.171		
Rh(4.2)NiAl40-550	5.6	4.166	Rh(4.2)NiAl40-C550-R700	3.554

[a] Mean values obtained from reflections (111), (200) and (220): ref ICDD 47-1049

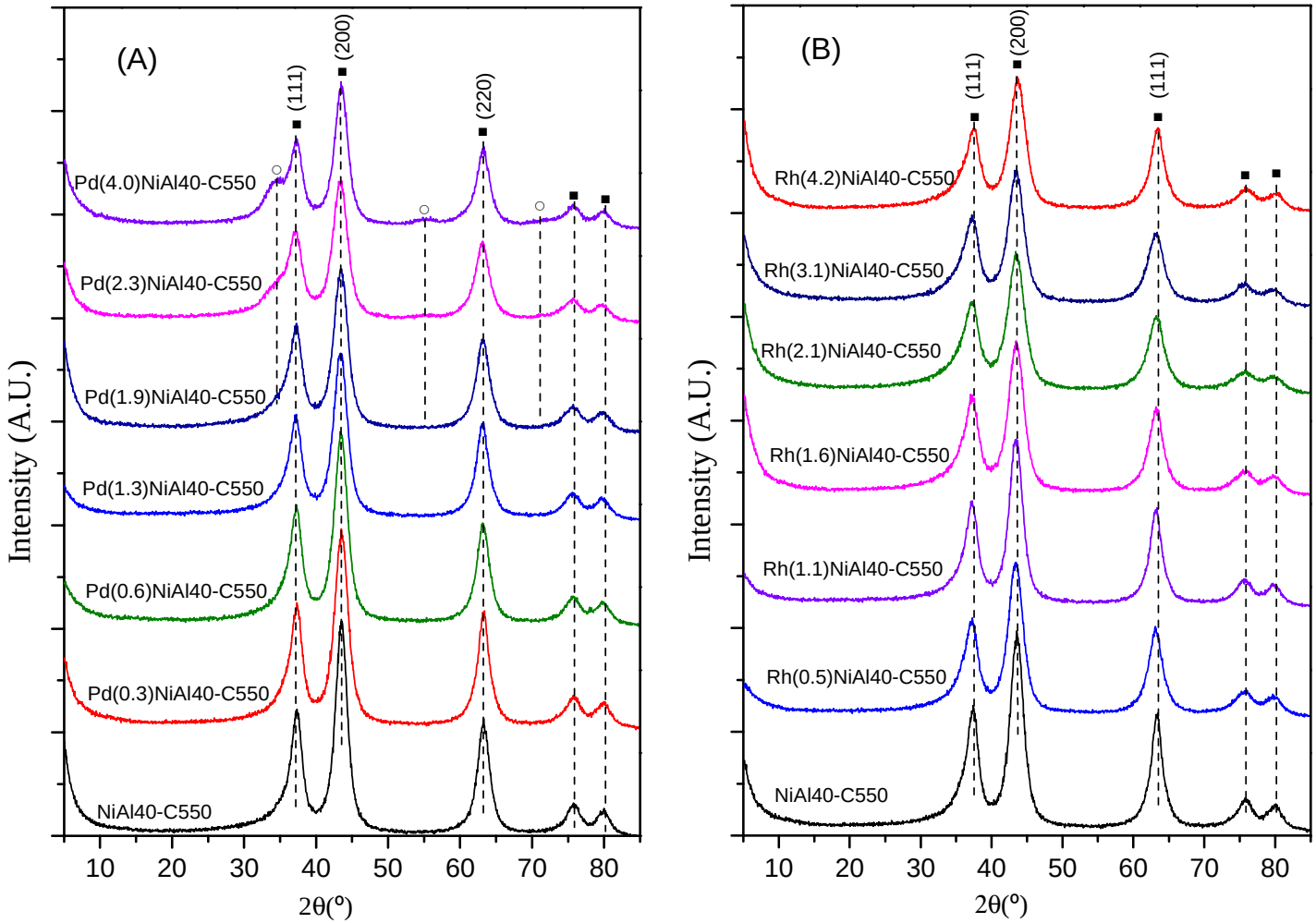


Figure 5.4 XRD patterns of Ni(Al)O (in both Figure A and B) and (A) Pd and (B) Rh promoted Ni(Al)O catalysts calcined at 550°C for 4 h. (■) Ni(Al)O; (○) PdO.

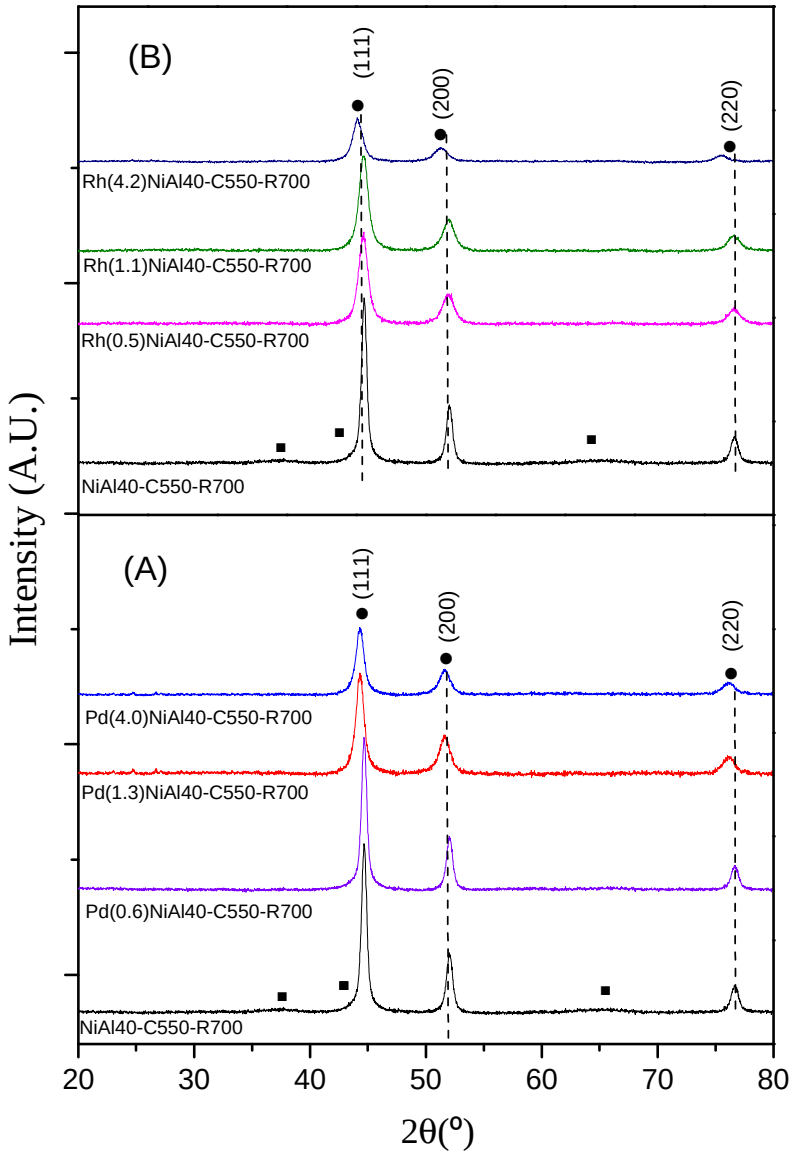


Figure 5.5 XRD patterns of Ni/Al (in both Figure A and B) and (A) Pd and (B) Rh promoted Ni/Al catalysts obtained from H_2-reduction of calcined catalysts at 700°C for 1 h. (•) Ni; (■) Ni(Al)O.

Figure 5.5 displays the XRD patterns of several selected Pd, Rh promoted catalysts after reduction at 700°C for 1 h in Ar/H_2 flow and measured *in-situ.* All catalyst show a typical reflection of pure cubic Ni (ICDD: 00-001-1260) with characteristic peaks corresponding to reflections (110), (200) and (220). No diffractions assigned to aluminium or alumina could appear in any of the catalysts due to the low reduction temperature applied. Alumina may possibly exist in an amorphous form [118, 195]

and/or γ-Al_2O_3 form [208]. The reflections become broader with the increasing amount of Pd and Rh loading, indicating degradation due to the structural defects (Pd, Rh). Peak positions also gradually shift towards a lower 2θ range due to the expansion of lattice parameter *a* (Table 5.2). This fact, again, reveal that the promoting ions are incorporated in the lattices with nickel, forming Pd-Ni or Rh-Ni system in the reduced catalysts.

A small quantity of NiO phase is found in the unpromoted sample NiAl40-C550-R700 even after reduction. This may be a result of the the unreduced Ni(Al)O [117]. No segregated NiO could be detected in the promoted catalysts clearly indicating the enhancement on catalysts' reducibility due to the noble metal promotion. The peak that appeared due to the segregated PdO in calcined catalyst Pd(4.0)NiAl40-C550 disappeared after reduction. This could be because the size of the reduced metallic Pd particles is very small and thus undetectable by the XRD.

5.3.4 TEM observation

TEM micrographs of several selected reduced catalysts are shown in Figure 5.6. All catalysts have similar elliptical nanoparticle morphology, ranging from 10 to 30 nm. There is no evidence of segregated Pd particles or any phase segregation of Ni(Al)O nanoparticles in Pd(4.0)NiAl40-C550-R700 (Figure 5.6C) in agreement with XRD findings. Another common finding of these catalysts is that the crystal structure of the top layers of the nanoparticles is slightly different from the bulk. The XPS results reported by Abelló *et al*. [117] show the aluminium content of these surface layers should be higher than the bulk. Hence, the distribution of nickel and aluminium are

not uniform across the whole catalyst particle and the majority of the heavy nickel is prone to migrate to the bulk during thermal treatments, leaving Al-enriched layers on the surface.

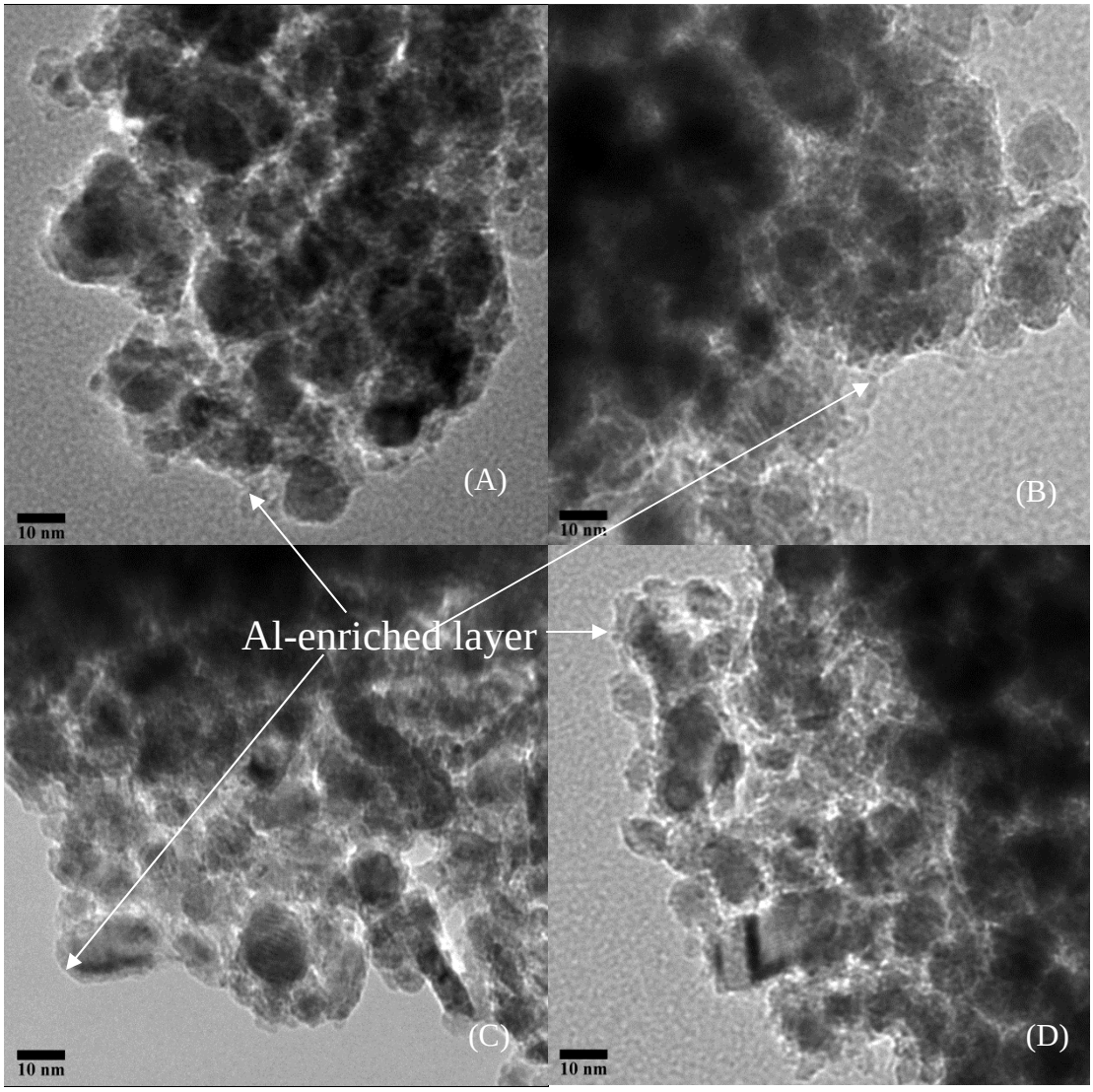


Figure 5.6 TEM images of (A) NiAl40-C550-R700, (B) Pd(1.3)NiAl40-C550-R700, (C) Pd(4.0)NiAl40-C550-R700 and (D) Rh(4.2)NiAl40-C550-R700.

5.3.5 Elemental mapping analysis

Elemental mappings of four selected reduced catalysts – Pd(1.3)NiAl40-C550-R700, Rh(1.1)NiAl40-C550-R700, Pd(4.0)NiAl40-C550-R700 and Rh(4.2)NiAl40-C550-R700 – are shown in Figures 5.7 to 5.10. In all the cases, the mapping shows good agreement with the TEM results in that the top layer of the surface of the nanoparticles mainly consists of the Al-enriched phase. However, the thickness of this layer seems to vary with promoter quantity. In catalysts Pd(1.3)NiAl40-C550-R700 and Rh(1.1)NiAl40-C550-R700, incorporated with low content promoters, the layers are much thinner than those in Pd(4.0)NiAl40-C550-R700 and Rh(4.2)NiAl40-C550-R700 contained high amount of promoters. Also, the Pd, Rh and Ni atoms in these two samples are homogenously distributed throughout the catalyst particles. In contrast, the distributions of Pd and Rh and even Ni are not uniformly distributed throughout the particles in Pd(4.0)NiAl40-C550-R700 and Rh(4.2)NiAl40-C550-R700, and the thicknesses of the Al-enriched surface layers in these two catalysts become higher. Hence, most of Pd, Rh and Ni are hidden underneath thick Al-enriched layers.

The results indicate that an extra Pd or Rh loading over optimised ratio did not contribute to the catalyst structure whereas they significantly enhanced the separation of nickel and aluminium, leading to poor uniformity of component distribution. As a result, the heavy nickel and substantial amount of promoters may be migrating from the surface to the bulk during thermal treatment.

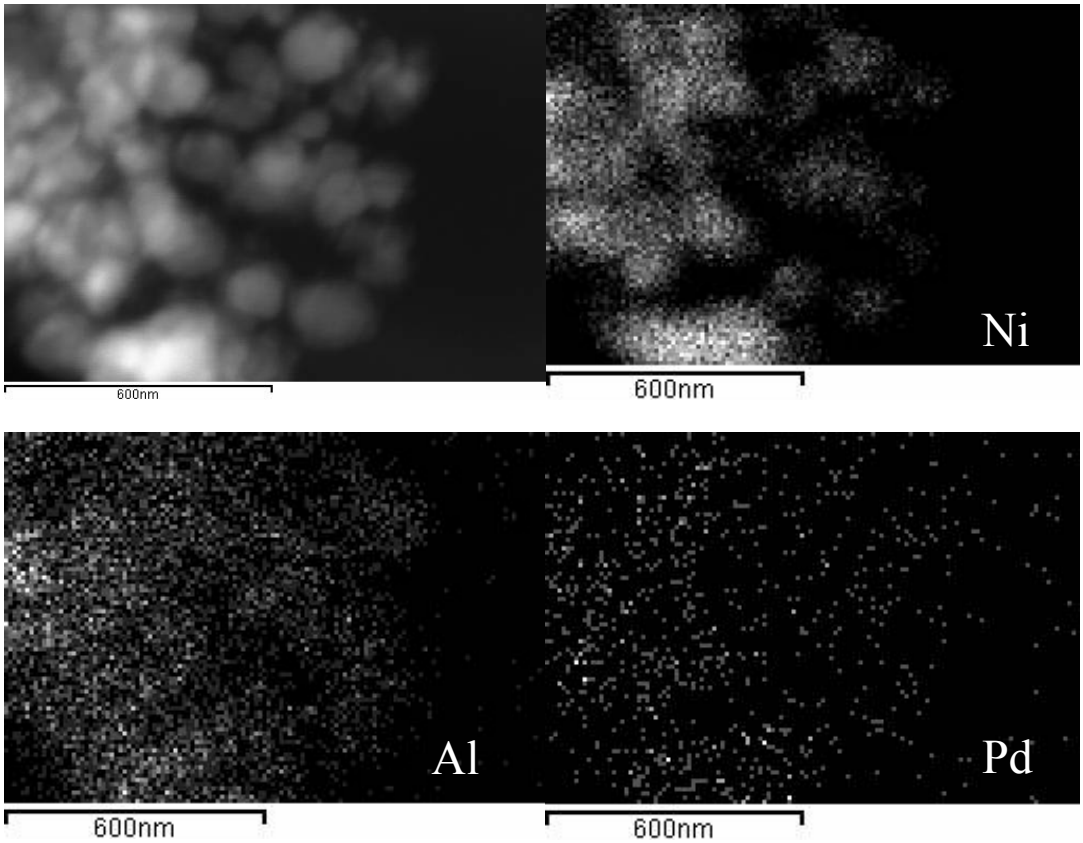


Figure 5.7 Elemental map of Pd(1.3)NiAl40-C550-R700 catalyst.

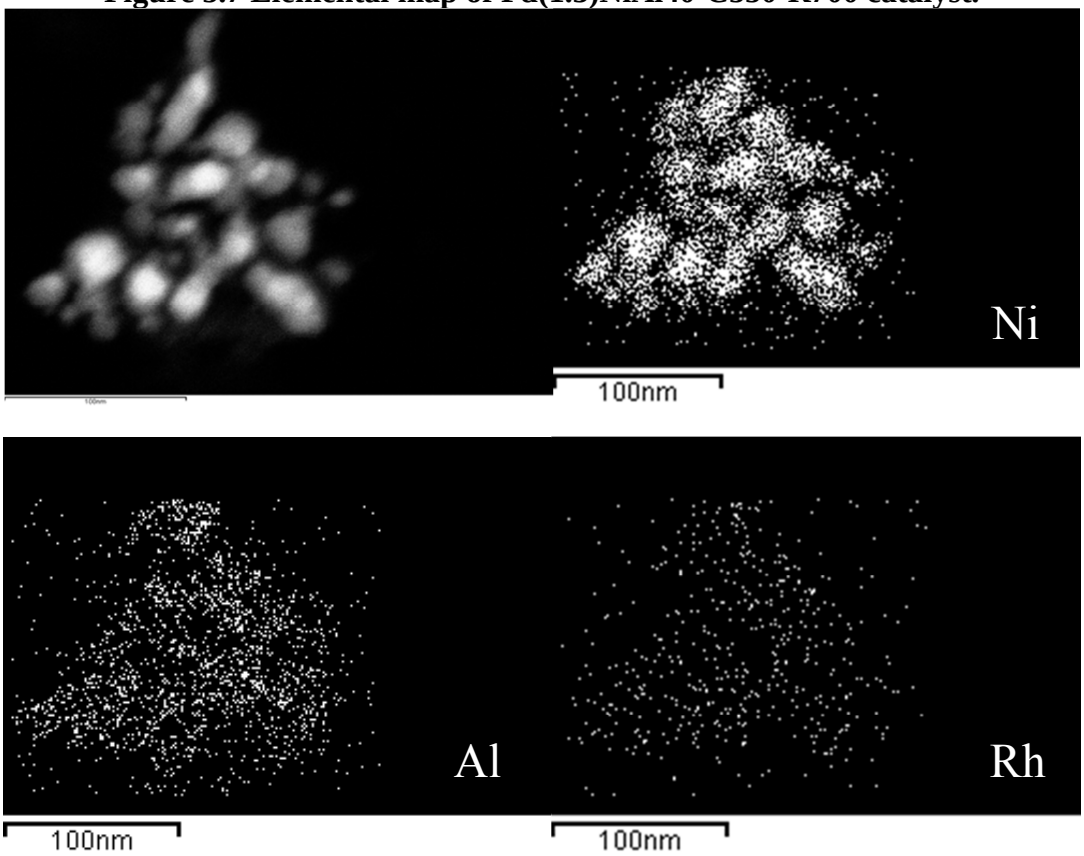


Figure 5.8 Elemental map of Rh(1.1)NiAl40-C550-R700 catalyst.

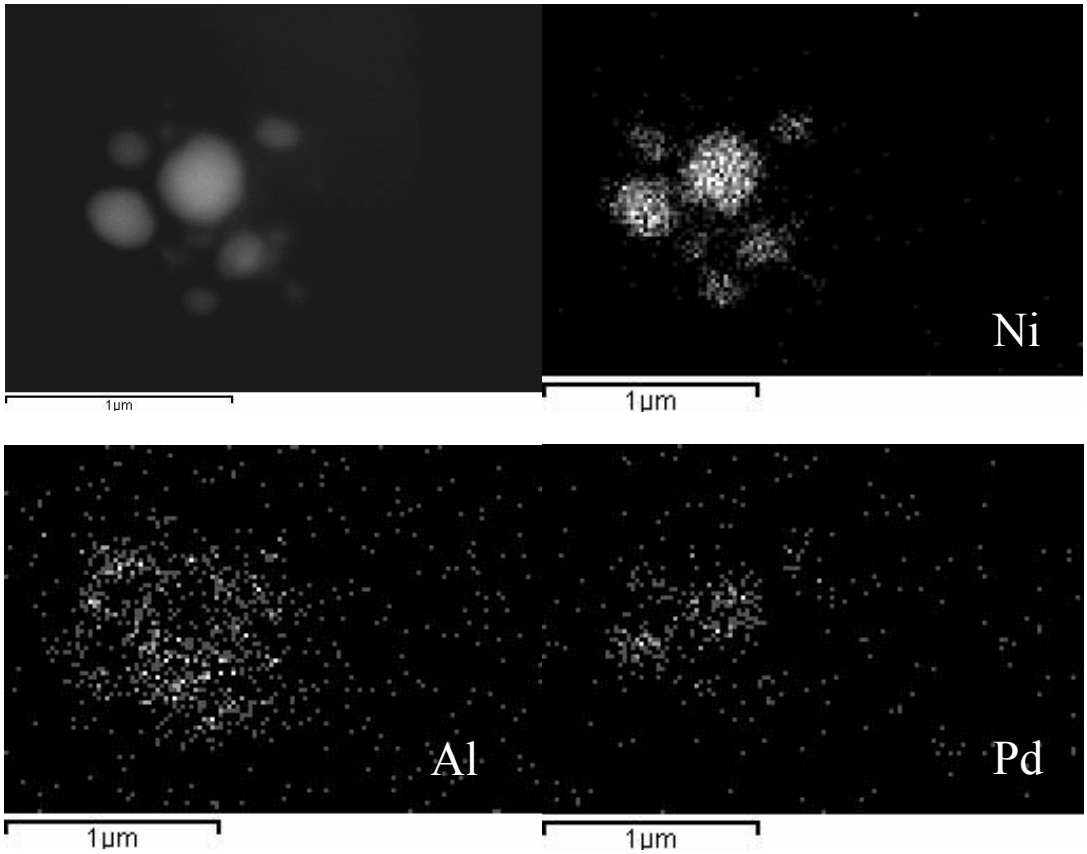


Figure 5.9 Elemental map of Pd(4.0)NiAl40-C550-R700 catalyst.

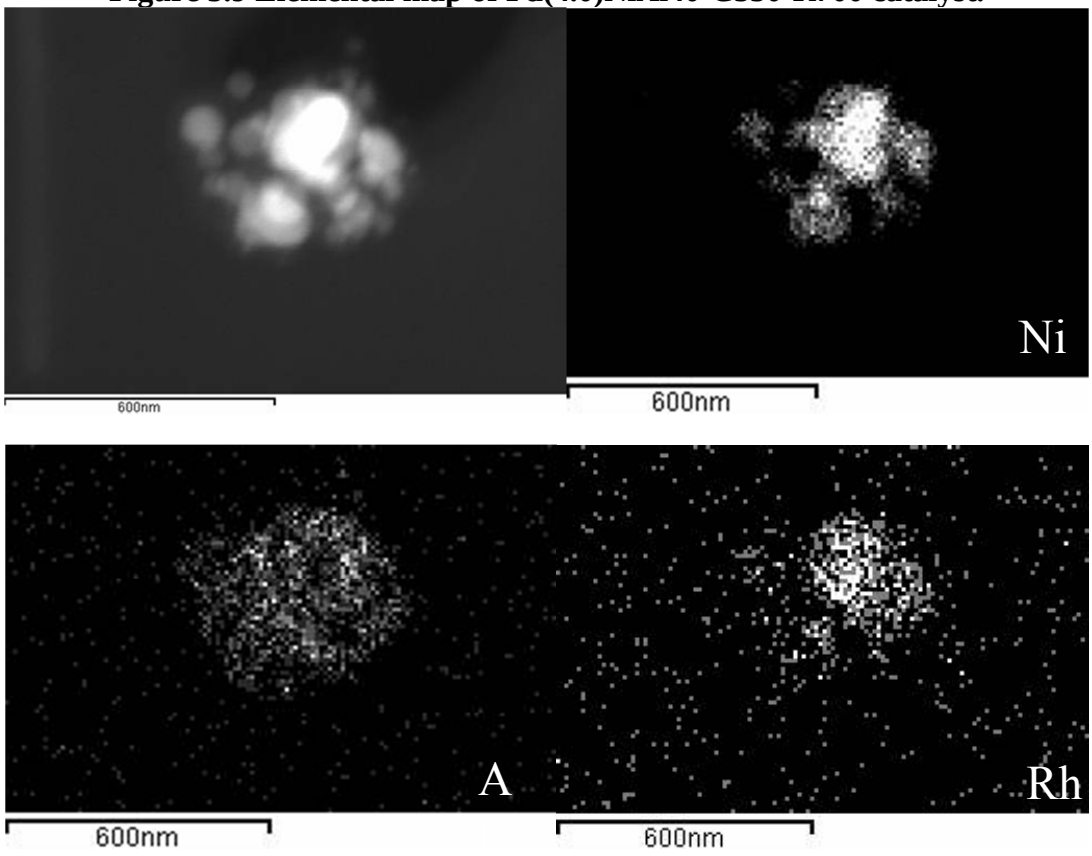


Figure 5.10 Elemental map of Rh(4.2)NiAl40-C550-R700 catalyst.

5.3.6 FTIR analysis

Figure 5.11 shows the FTIR spectra of reduced Ni/Al and selected Pd, Rh promoted Ni/Al catalysts after adsorbing CO at an ambient temperature. A small absorption band at 2129 cm^{-1} and a predominant band at 2057 cm^{-1} are observed in all the samples. These bands are mainly due to the liner carbonyl species adsorbed on metallic nickel [219, 220]. The absence of any absorption band below 1950 cm^{-1} indicates that there is no or less detectable CO adsorbed in bridged form. A shoulder at 1981 cm^{-1} in some samples may be due to liner-adsorbed CO with a small amount of bridge CO coordinated together. The linearly adsorbed CO species is favoured over isolated metal sites (corner, edge, etc.) and bridged CO species are more likely on flat and extensive metal sites [219, 221, 222].

A clear but weak band at 2175 cm^{-1} is found in the spectra of the NiAl40-C550-R700 catalyst, corresponding to the linear CO species adsorbed on Ni^{2+} or Ni^{+} sites [223-225]. In agreement with XRD, this could be due to some surface nickel being re-oxidised during the cooling process after reduction. The intensity of this band sharply turns down in the promoted catalysts with similar treatment. This band almost disappeared in Rh(0.5)NiAl40-C550-R700 and Rh(1.1)NiAl40-C550-R700, which both have low levels of Rh promoter, but the band reappears in the Rh(2.1)NiAl40-C550-R700 and Rh(4.2)NiAl40-C550-R700 samples. However, the band splits into two: one appearing around 2183 and the other at 2169 cm^{-1}. Similar splitting is also observed in the Pd(2.3)NiAl40-C550-R700 and Pd(4.0)NiAl40-C550-R700 catalysts. A strong absorption is found at 2044 cm^{-1} with a small shoulder at 2078 cm^{-1} on the NiAl40-C550-R700 and the Pd, Rh promoted catalysts with low quantity of Pd or Rh.

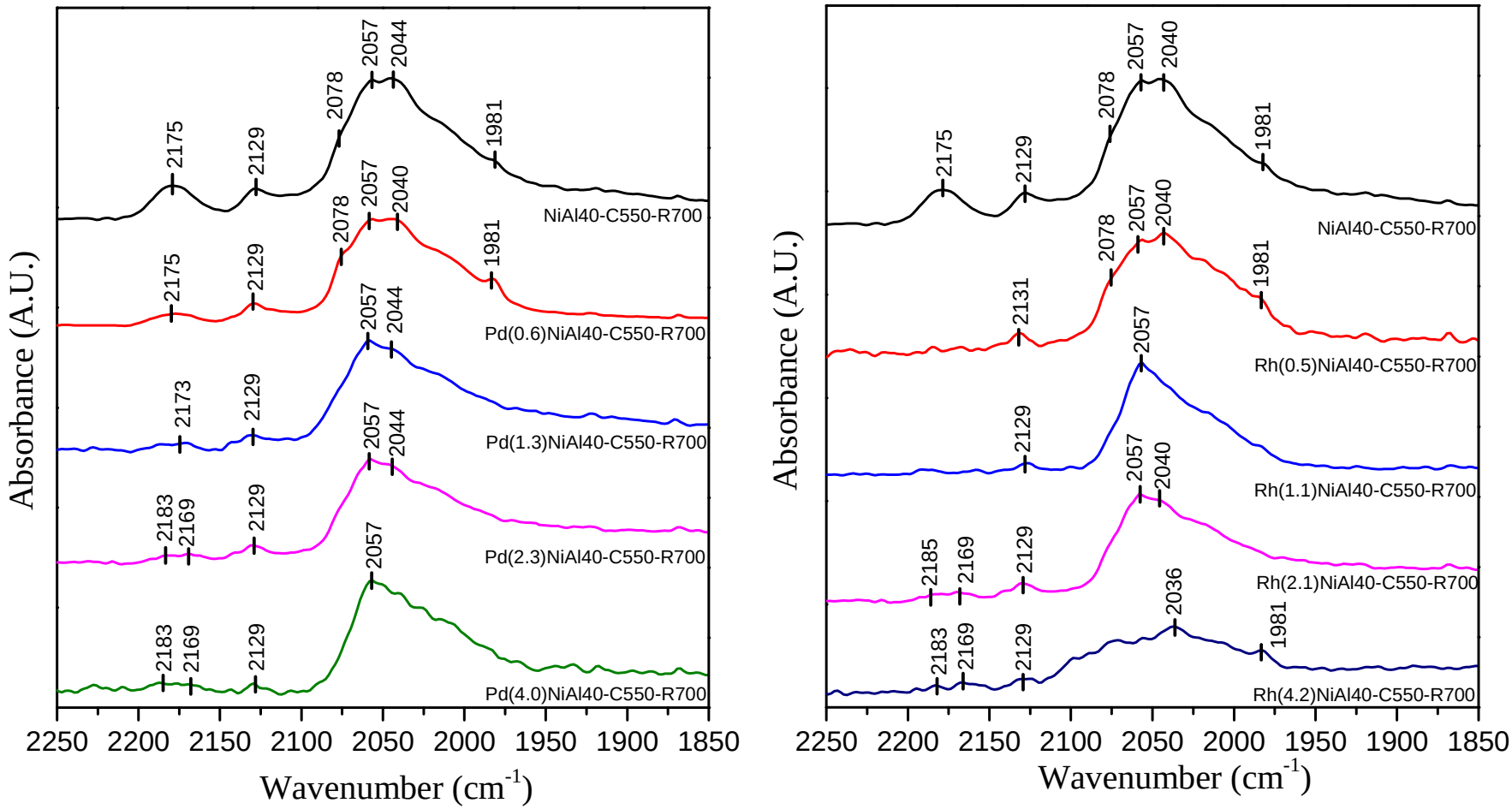


Figure 5.11 FTIR spectra after admission of CO on reduced Ni/Al, and Pd and Rh promoted Ni/Al catalysts at ambient temperature.

Again, this is due to the linear CO being adsorbed on the $Ni^{\delta+}$ sites [226, 227]. This feature also gradually decreases with the increasing Pd or Rh loading. In accordance with the XRD pattern, the result implies an enhancement of catalysts' reducibility by the addition of noble metal promoters.

It may be noted that the shape of the spectrum on Rh(4.2)NiAl40-C550-R700 is different from other Rh promoted catalysts. The band at 2057 cm^{-1} becomes very weak whereas the peak at 2036 cm^{-1} looks dominant in regard to the liner CO adsorption. The shortage of Ni and Rh on the surface-promoted catalysts with high Rh loading as evidenced from the elemental mapping of the EDX images consequently led to poor adsorption ability.

In additional, there is no direct evidence of the adsorption of linear or bridged CO on the promoter metal or promoter ions for the IR spectra. The reason may be due to their low quantities in comparison with Ni and Al either in the surface or in bulk.

5.3.7 TPR analysis

The reduction temperature of the catalysts strongly depends on the promoter content. As discussed in previous chapters, aluminium in the lattice of Ni(Al)O polarises nickel, making nickel more ionic and less reducible. The unpromoted catalyst NiAl40-C550 reduced at 660°C found to be in S.L.M.. When Pd or Rh promoter is incorporated in the lattice, the polarisation effect on nickel is weakened and internal structure of Ni(Al)O is changed. The reduction maximum gradually shifts towards lower temperature range and the structure of the catalyst gets transformed from S.L.M.

to S.N.O with an increase in loading of Pd or Rh promoter. During this process, H_2 consumption at 660°C corresponded to S.L.M. gradually becomes less intensive.

For the Pd promoted Ni(Al)O catalysts series, the reduction temperature shifts to lower temperatures up to Pd content becomes 1.3 % (Pd/(Pd+Ni+Al)%). Any substitution over this amount moves the reduction temperature to higher value (Figure 5.12A). The reason for this behaviour may be due to the segregation of Pd from Ni(Al)O beyond Pd ratios over 1.3 % (Pd/(Pd+Ni+Al)%). On the other hand, small reduction peaks are also found at 120°C in the Pd(1.3)NiAl40-C550 catalyst, corresponding to the reduction in surface-exposed structural palladium. The peak shifts to lower temperature and became more intensive with the increase in Pd loading. In the case of the Pd(2.3)NiAl-C550 catalyst, the peak splits into two: one at 85° and the other at 92°C. The first one could be attributed to the reduction of the segregated PdO, as discussed previous chapters, while the second one could be a result of the substitutional Pd in the catalysts. A clear reduction peak at 68°C in the Pd(4.0)NiAl40-C550 catalyst can be assigned to the large quantity of PdO segregation [204, 205]. The TPR findings correlate well with the XRD results discussed earlier.

In the cases of Rh promoted Ni(Al)O catalysts, the reduction peak continuously shifts to a lower temperature as a function of increased Rh loading, indicating the structure of Ni(Al)O coming closer to pure NiO (Figure 5.12B). Two small additional reduction peaks are also found at lower temperatures. These peaks may be due to the reduction of surface-exposed structural Rh^{3+} at different sites. The small peaks are not dependent on Rh content unlike the Pd promoted where the intensity of the first peak increases with Pd content.

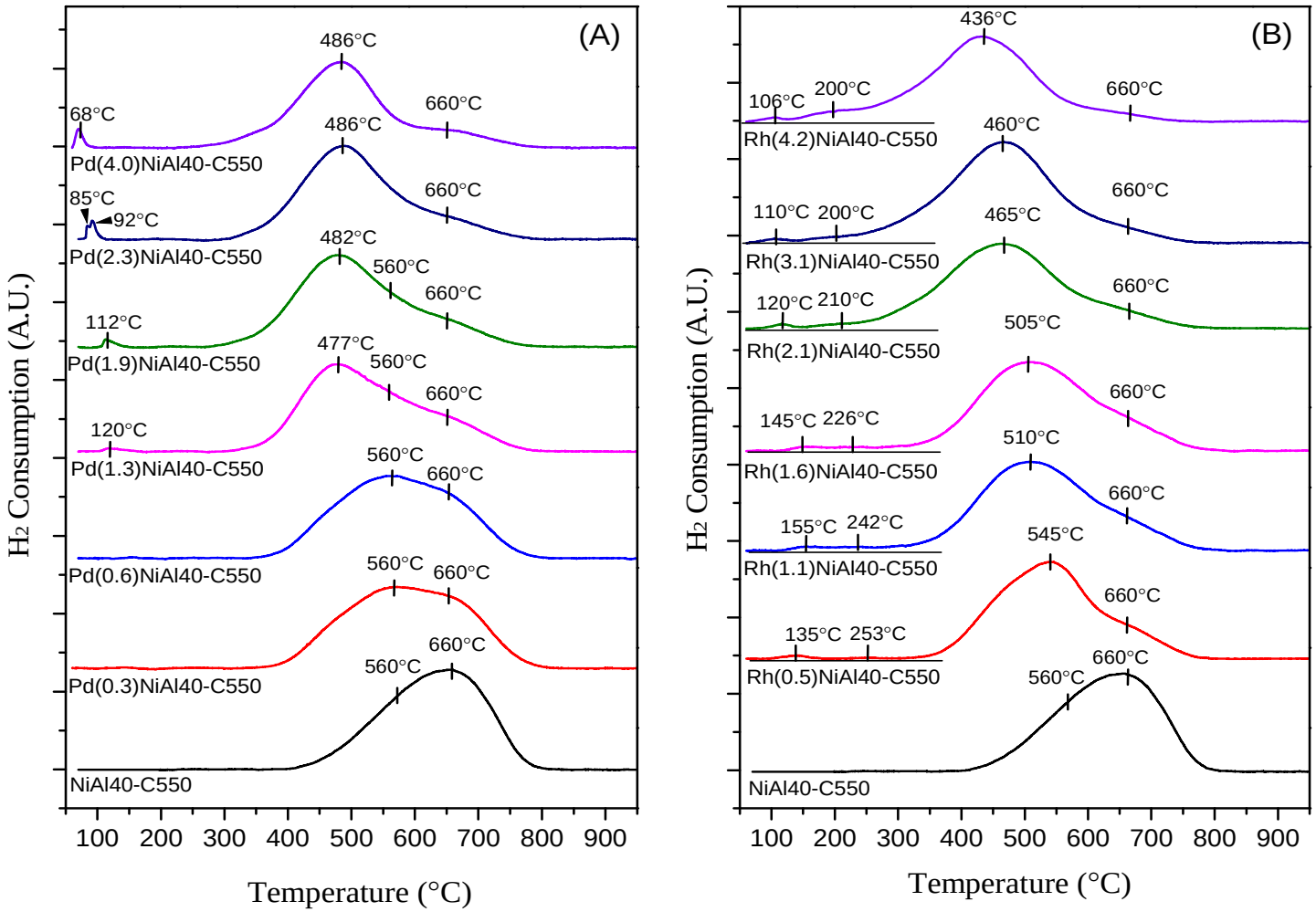


Figure 5.12 TPR profiles of (A) Pd and (B) Rh promoted Ni(Al)O catalysts.

As seen in Figure 5.12B, H_2 consumption at 660°C is gradually going down due to the decrease in quantity of S.L.M. in the catalysts. During this change, more Al^{3+} is incorporated in octahedral sites from tetrahedral sites. By this principle, the quantity of Rh^{3+} tetrahedral sited should not increase. Hence, the second reduction peak at around 200-260°C may be assigned to Rh^{3+} at octahedral sites while the first peak at around 100-160°C is assigned to the Rh^{3+} incorporated at the tetrahedral sites of the Ni(Al)O.

5.3.8 Catalyst activity

Figures 5.13 and 5.14 compare the reforming activities of catalysts with different ratios of promoters. The two series of catalysts show a common trend that both CH_4 consumption and H_2 productivity quickly increase with increasing Pd up to 1.3% or Rh loading up to 1.1%, and then go down in line with a further increase in promoter loading. Best catalytic performances are found in the Pd(1.3)NiAl40-C550-R700 and Rh(1.1)NiAl40-C550-R700, both with enhancement of around 15-20% in methane consumption and H_2 productivity. There is a decline in activity of the catalysts with Pd or Rh loading higher than their optimum ratios (Pd=1.3% or Rh=1.1%) and is mainly due poor distribution of Ni, Pd or Rh, synergetic effect in Ni/Al catalyst is hence weakened.

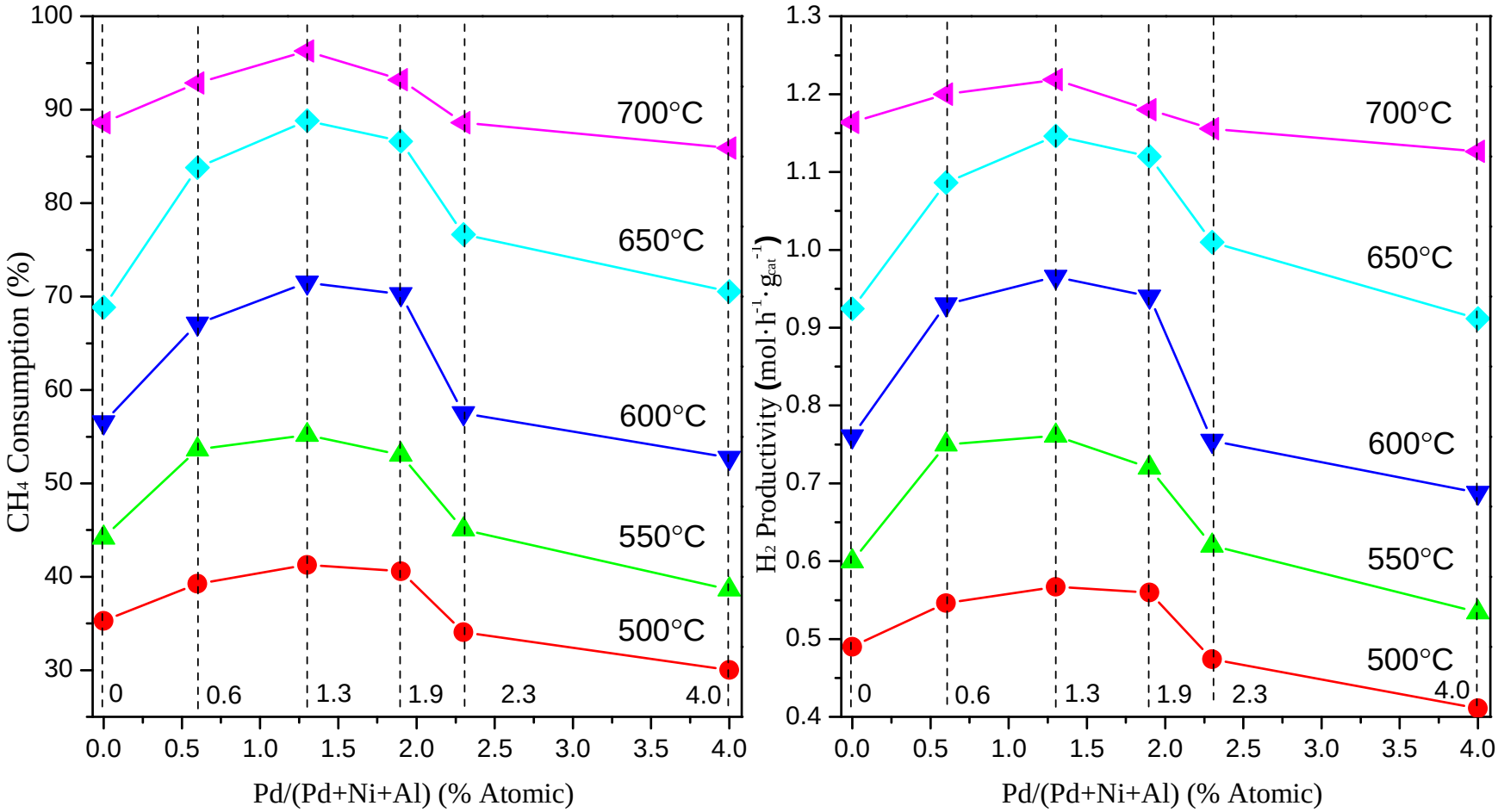


Figure 5.13 CH_4 consumption and H_2 productivity of SMR reactions over Ni/Al and Pd promoted Ni/Al catalyst with different loading amounts of Pd. (CH_{4inlet}= 16.2ml/min, S:C=3:1, 1 atm).

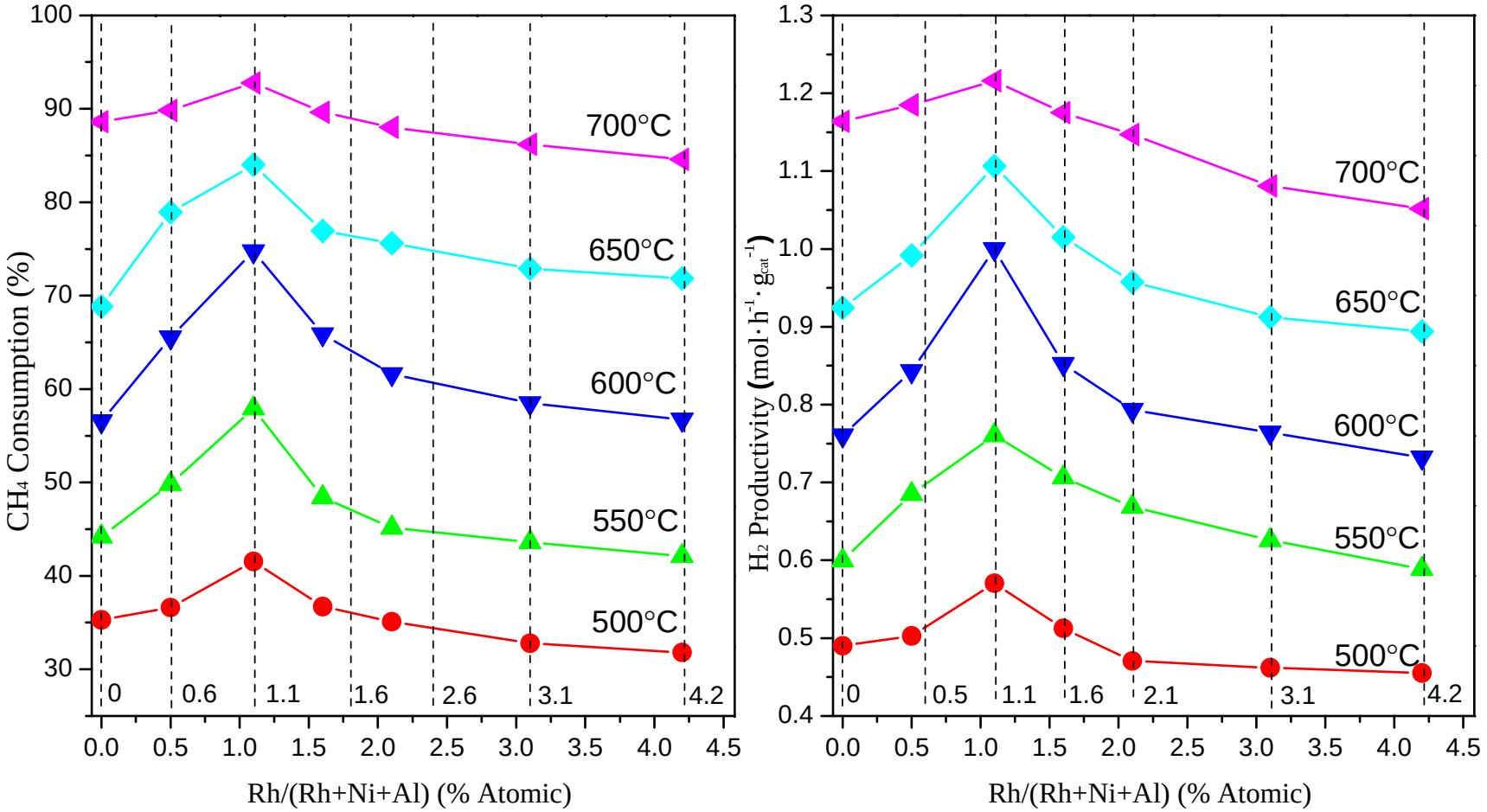


Figure 5.14 CH_4 consumption and H_2 productivity of SMR reactions over Ni/Al and Rh promoted Ni/Al catalyst with different loading amounts of Rh. (CH_{4inlet}= 16.2ml/min, S:C=3:1, 1 atm).

5.4 Conclusions

The incorporation of Pd, or Rh promoters significantly increased the reducibility and catalytic performance of the Ni/Al LDH derived catalysts. However, there is an optimum ratio of doping for the highest performance of the catalyst. The optimum ratio in the case of Pd, is found to be at atomic percentage of 1.3% (Pd/(Pd+Ni+Al)%), while it is 1.1% (Pd/(Pd+Ni+Al)%) for Rh promoted catalysts. Promoted catalysts with these ratios show a relative uniform distribution of Ni and Pd or Rh in the structure as well as a high enhancement on activity. Higher loadings beyond these ratios cause local accumulation of promoters, non-uniform metal distribution, phase segregation (Pd promoted catalyst only), thus lower promotional effect and reduced activity. For catalysts with compositions over 4% Pd or Rh in content, the catalytic activities are found even lower than the unprompted Ni/Al catalyst. As a result, the excessive loading of the promoters play a negative role.

Chapter 6. Development of LDH sol for SOFC anode coating

6.1 Introduction

The most significant advantage of the LDH precursor route over other conventional catalyst preparation methods for SOFC is the uniform and effective coating they produce. Conventional impregnated or precipitated catalysts are difficult to *in-situ* synthesis or fabricate in the SOFC anode. LDH slurry, on the other hand, has good fluidity and stickiness, which can easily be fabricated on the anode surface using jet or spray coating. However, problems such as the non-uniform sizes of LDH clusters, cracking of the coated catalyst layer during calcination and agglomeration of magnetic nickel particles after reduction still exist, and influence the further adoption of this material.

To solve these problems and create a better coating for the SOFC anode, the particle sizes of the LDH clusters, especially their dimension in a 2D direction, have to be reduced. However, general physical and chemical methods, such as soliciting the LDH slurry or reducing the CP temperature and ageing time do not bring significant changes in this aspect. Hence, one of the goals in the present study is to find an effective method to achieve this target. In this chapter, a new chemical approach – acid attack – is developed. CP route prepared LDHs are treated with nitric acid for preparing fine LDH sol. The changes in themselves and their derived catalysts, including structure, chemical compositions, catalyst reduction characteristics, component distribution and catalytic behaviours, are investigated.

6.2 Experimental

Three LDH samples: one basic Ni/Al LDH (NiAl40) and two noble metal substituted LDHs (Pd(1.3)NiAl40 and Rh(1.1)NiAl40), referred to as 'raw-LDHs' were prepared using the CP method at pH=10.0 according to the procedures described in Chapter 3. About 5g samples were prepared for each type of raw-LDH. After precipitation and ageing, the precipitates were filtered and washed several times until no floccules appeared in the last washing. The slurry was centrifuged at 4000 rpm for 5 minutes. The separated water with floccules was decanted off and the raw-LDH prepared was re-dispersed in 300 ml DCDI water, with vigorous stirring until the pH value became stable. Fine LDH sol was prepared from the raw-LDH precipitate by acid attack to split large clusters into small pieces. Nitric acid is selected because NO_3^- can easily be washed compared to other anions. The acid treatment was carried out without pH controls and at an ambient temperature. A small amount of 73% HNO_3 was quickly injected into the raw-LDH slurry with constant stirring until the slurry became translucent, with fine LDH sol thus being obtained. The pH of the sol dropped quickly to around 3.5 to 4.0 during this process. Figures 6.1A and B compare the as-prepared raw-LDH suspension and acid-attacked LDH sol. The sol was stirred for a few minutes at high speed and the solid was then separated following one centrifugation – re-dispersion–centrifugation step. The final pH reached 5.0 to 5.5. A very fine bright precipitate with fine particles was obtained at the end of the last centrifugation. The LDHs prepared by this sol/nitric acid attack method are referred as 'NA-LDHs' (nitric acid-treated LDHs). NA-LDH can easily be distinguished from the parent raw-LDH by the appearance, as seen in Figures 6.1C and D.

The as-prepared NA-LDHs were dried at 90°C for 12 h for a further crystallisation. Then, the dried LDHs were ground into fine powders and calcined at 550°C for 4 h.

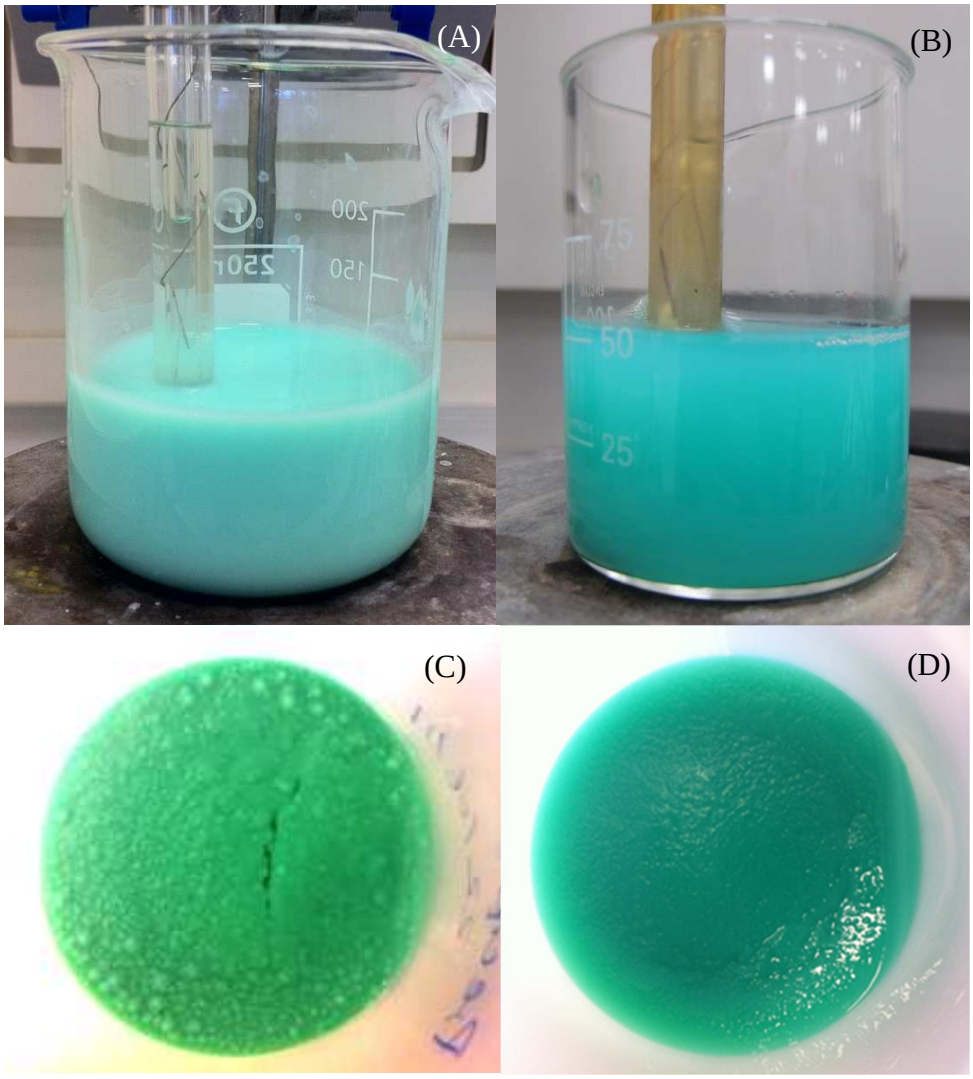


Figure 6.1 Suspension of Ni/Al LDH (A) before and (B) after nitric acid attack treatment. The centrifuged slurry of Ni/Al LDH (C) before and (D) after nitric acid attack.

The NA-LDHs and their related raw-LDHs were characterised by EDX, XRD, SEM, FTIR and TGA and the derived catalysts were characterised by XRD, TEM and TPR. Details of these experiments are given in Section 2.5 of Chapter 2. All catalysts were

pre-reduced at 700°C before SMR. Activity measurements were carried out from 250-700°C as described in Section 2.4.3.1 of Chapter 2.

6.3 Results and discussion

6.3.1 Preparative conditions of NA-LDHs

The preparation of the NA-LDH is a semi-empirical work. The principal work is to split the large raw-LDH clusters into small species while maintaining the layered structure of the LDH. NO_3^- ions may replace some of the CO_3^{2-} at the moment of acid attack [150]. The quantity and the rate of acid injection for are important in terms of the quality of the sol. An appropriate amount of nitric acid should be injected in one quick shot. Unlike to some general ion exchange preparation being designed for intercalations, a slow drop-wise addition of acid could not instantly break the large LDH clusters to make small particles in the suspension. Instead, it gradually destroys the layer structure, forming nickel and aluminium nitrates. On the other hand, an excessive amount of acid applied in shot may also cause a quick drop in pH and hence cause structural damage, with nickel and aluminium nitrates also being formed. It is found the LDH structure can be easily destroyed when local pH is below 3.5. The repeated washing/filtering cycles could not completely remove all nickel and nitrate ions. In both of these cases, the dried NA-LDHs show the presence of nickel nitrate and become hygroscopic. The large lumps formed (LDH and $Ni(NO_3)_2 \cdot 6H_2O$) make these LDHs not applicable for coating on SOFC anode.

Table 6.1 Chemical composition and structural parameters of raw-LDHs and NA-LDHs.

Sample name	Relative quantity of nitric acid (NA) applied	Expected metal molar ratio % (Solution)			Actual metal molar ratio % (Solid, by EDX)			Phase (by XRD)	Crystallite size (nm)[a]	Lattice parameter (Å)	
		A	**Ni**	**Al**	**A**	**Ni**	**Al**			***a***	***c***
NiAl40	-	-	75.0	25.0	-	72.7	27.3	LDH	16.2	3.036	23.091
NA(1.0)-NiAl40	1.0 (optimum)	-	75.0	25.0	-	72.6	27.4	LDH	6.1	3.037	25.317
NA(1.1)-NiAl40	1.1	-	75.0	25.0	-	72.4	26.6	LDH, $Ni(NO_3)_2$	5.5	-	-
NA(1.2)-NiAl40	1.2				-	72.2	26.8	LDH, $Ni(NO_3)_2$	4.6	-	-
		Pd			**Pd**						
Pd(1.3)NiAl40	-	2.0	73.0	25.0	1.3	71.7	27.0	LDH	9.9	3.048	23.136
NA(0.85)-Pd(1.2)NiAl40	0.85 (optimum)	2.0	73.0	25.0	1.2	71.6	27.2	LDH, $Ni(NO_3)_2$	5.2	3.050	25.331
NA(0.9)-Pd(1.0)NiAl40	0.90	2.0	73.0	25.0	1.1	71.5	27.4	LDH, $Ni(NO_3)_2$	4.8	-	-
		Rh			**Rh**						
Rh(1.1)NiAl40	-	1.0	74.0	25.0	1.1	72.2	26.7	LDH	11.5	3.042	23.118
NA(0.88)-Rh(1.0)NiAl40	0.88 (optimum)	1.0	74.0	25.0	1.0	72.2	26.8	LDH	5.7	3.043	25.328

Blue number in the catalyst name indicates the relative quantity of nitric acid applied during preparation of the LDH sol.
Red number in the catalyst name indicates the ratio of Pd and Rh to overall Ni+Al+Pd and Ni+Al+Rh (%).
The prefix NA- stands for nitric acid treated.
[a] Mean values obtained from reflections (003) and (006), ref ICDD 00-015-0087

6.3.2 Compositions of LDHs

A series of Ni/Al and Pd, Rh substituted NA-LDHs were prepared using different quantities of nitric acid. The relative amounts of nitric acid applied for each the preparation and some of the properties of the as-prepared LDHs are listed in Table 6.1. It should be noted that there is a difficulty in preparing pure single-phase Pd substituted NA-LDH since the size of the Pd^{2+} ion is very close to the limit of the brucite layers. Further layer expansion or contraction may lead to leakage of Pd from the brucite layers. Indeed, a similar problem was also found when preparing Rh substituted LDH, although it is less severe. In order to avoid destroying the LDH structure and maintaining the composition of the metal ternary, it is suggested that a slightly lower amount of nitric acid should be used in preparing the Pd or Rh substituted NA-LDHs, compared with the quantity applied for basic NA-LDH.

Nitric acid attacks also marginally influenced the nickel content, causing a slight reduced Ni/Al ratio in all as-prepared NA-LDHs and thus indicating a loss of metal ions during acid treatment. This can be found from the EDX results in Table 6.1.

6.3.3 Structure of LDHs

6.3.3.1 Structure of raw-LDHs and NA-LDHs

The XRD patterns of raw-LDHs and NA-LDHs are shown in Figure 6.2. All the patterns are characteristic of the typical structure of takovite (ICDD: 00-015-0087)

and no obvious new phase is found in the three NA-LDHs. The positions of the two intensive reflections (003) and (006) of NA-LDHs shift to the lower 2θ range. This shift becomes obvious in Pd and Rh substitued NA-LDHs. As shown in Table 6.1, the average lattice parameter *c* of these NA-LDHs are higher than their parent raw-LDHs. This may be due to the exchanging of carbonate ions for nitrate ions in the interlayers.

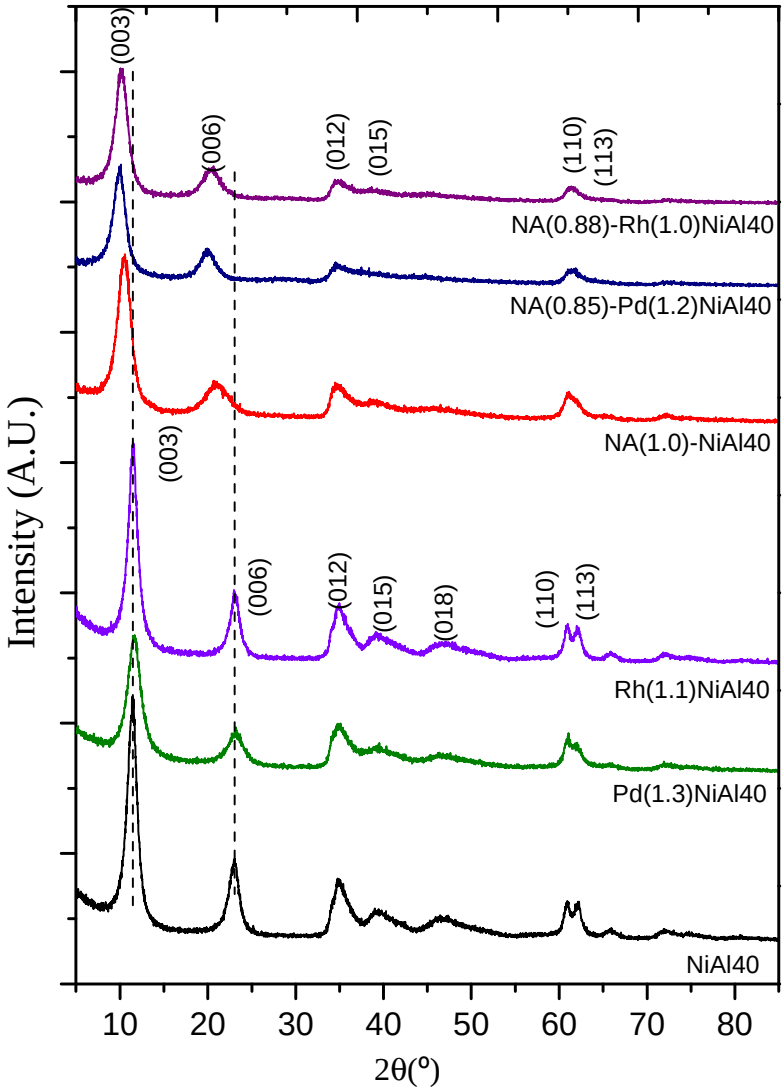


Figure 6.2 XRD patterns of raw-LDHs and NA-LDHs.

Beside the reflections, all other peaks in the NA-LDHs become less intense in comparison with the corresponding raw-LDHs. Some reflections such as (018) and

(113) lines have even disappeared after the acid attack, indicating a decrease in crystallinity and crystallite sizes (Table 6.1).

6.3.3.2 Effect of nitric acid quantity on structure of NA-LDHs

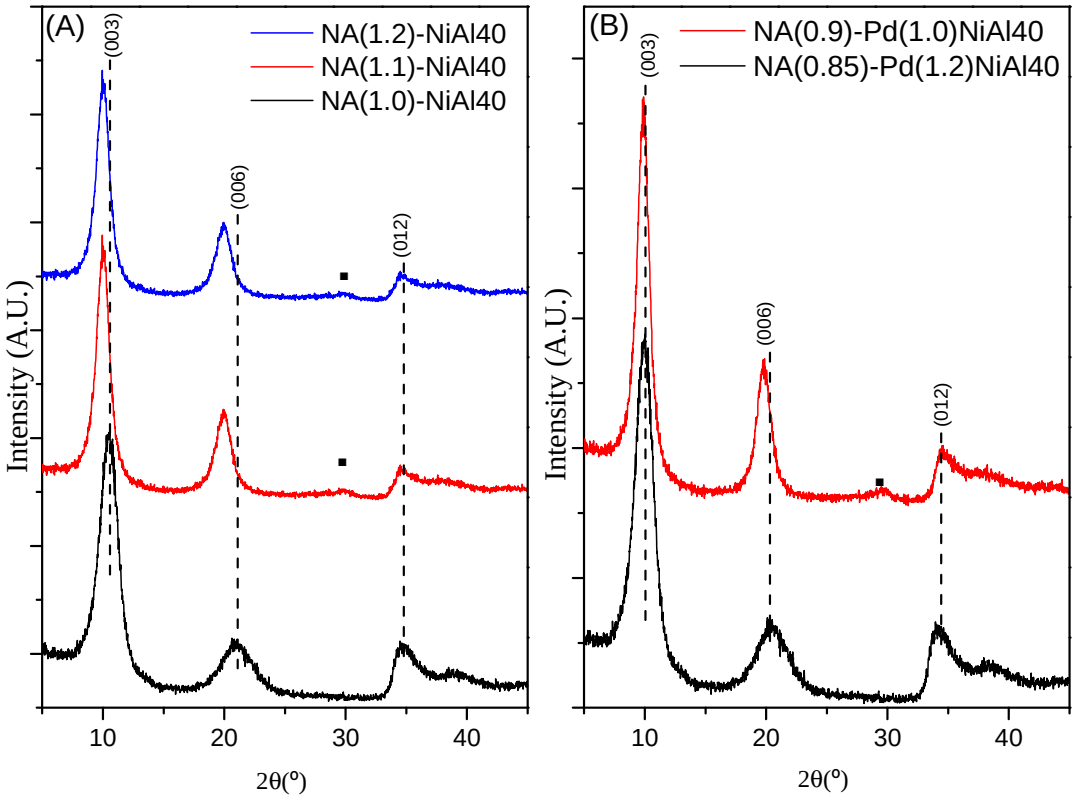


Figure 6.3 XRD patterns of LDHs treated with different quantities of nitric acid (■) $Ni(NO_3)_2 \cdot 6H_2O$.

The XRD patterns of NA-LDHs treated with different amounts of nitric acid are compared in Figure 6.3. The amounts of nitric acid used for preparing these NA(1.1)-NiAl40, NA(1.2)-NiAl40 and NA-NA(0.9)-Pd(1.0)NiAl40 LDHs were higher than the ones used for NA(1.0)-NiAl40 and NA(0.85)-Pd(1.0)NiAl40 LDHs (Table 6.1). A phase segregation is observed at 2θ=29.5° for all these three samples treated with high amount of nitric acid, assigning to the nickel nitrate. A further shift of (003) and (006)

lines to the low 2θ range is also found, implying a further expansion of brucite layer since more nitrate ions are incorporated in the interlayers replacing carbonate ions.

6.3.4 SEM observation

The quality and morphology of raw-LDH and NA-LDHs coated on silica substrate were studied using the SEM technique. An SEM micrograph of the surface of the substrate is shown in Figure 6.4.

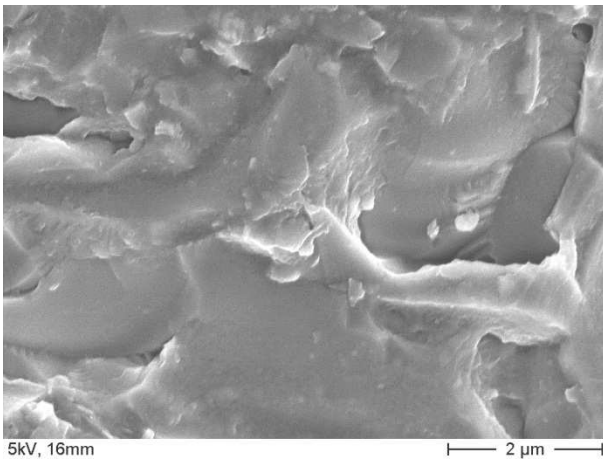


Figure 6.4 SEM image of silica substrate used for spin coating

Figure 6.5A shows the SEM micrograph of raw-LDH NiAl40 coated on silica substrate. The SEM shows plate-shaped particles in a narrow size range. The dispersion is not uniform as the crystal grew in both vertical and horizontal directions. The substrates coated with sols are shown in Figures 6.5B, C and D. These coatings of NA-LDH sols look uniform and smooth and the NA-LDH layer is properly stuck to the surface of the substrate with cotton-like morphology.

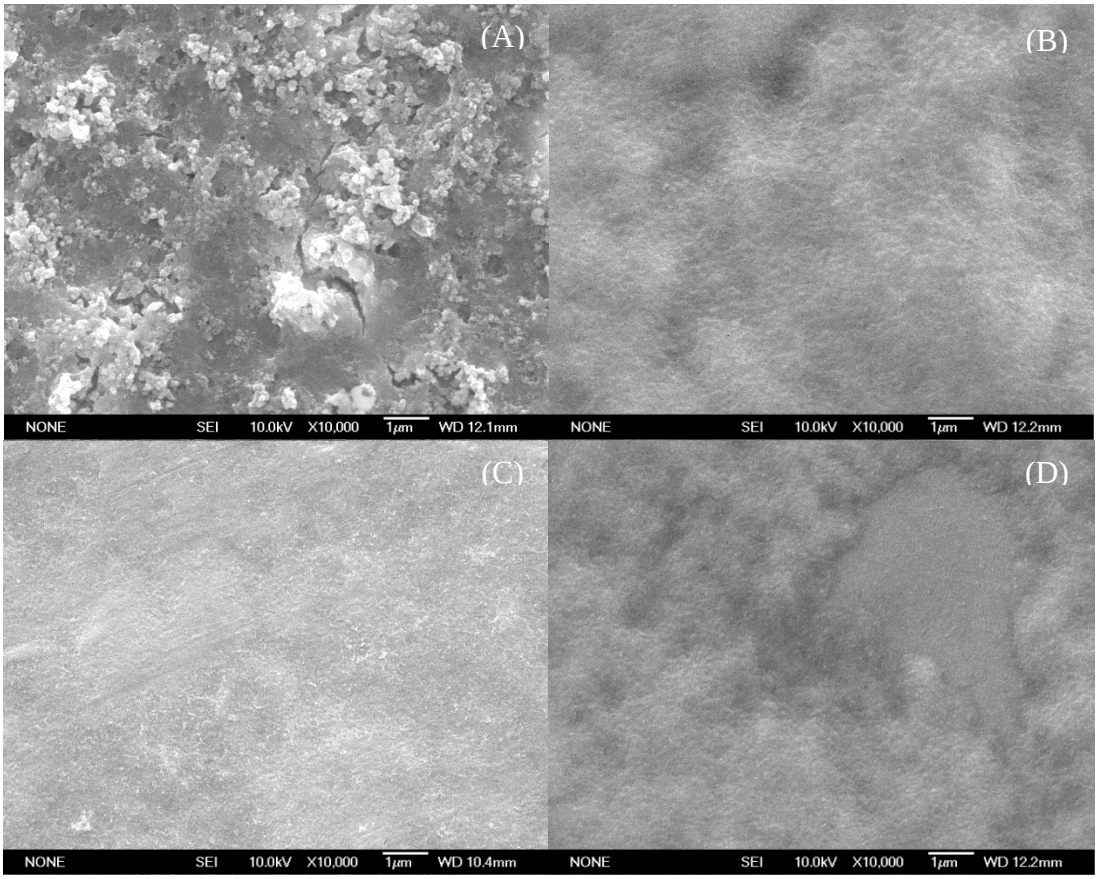


Figure 6.5 SEM images of (A) NiAl40, (B) NA(1.0)-NiAl40, (C) NA(0.85)-Pd(1.3)NiAl40, and (D) NA(0.88)-Rh(1.1)NiAl40 LDHs.

It is likely that the acid attack not only split the large lamellar LDH clusters into small particles but also made their sizes uniform. Therefore, crystallisation in the vertical direction is weakened in comparison to raw-LDHs. In addition, the high uniformity and smaller sizes entail a close combination of the dried LDH particles without large spaces in between.

After calcination, the plated-shape structure is retained in the NiAl40-C550. As shown in Figure 6.6A, the surface becomes rough with a random distribution of large agglomerations of catalyst lumps. In contrast, no evidential agglomeration of particles is observed in the NA(1.0)-NiAl40-C550 catalyst and the catalyst layer is still fine coated on the surface of the substrate, without any obvious agglomeration (Figure

6.6B). Even after reduction, this morphology of the coated catalyst is still retained (Figure 6.6D) with only a few small cracks due to the shrinkage in volume of the catalyst. In contrast, severe agglomeration happens in the NiAl40-C550-R700 sample, with a series of large cracks on the coated layer making the coating less stable on the substrate (Figure 6.6C). The cracks were caused by the shrinkage of the volume of the substance coated on the substrate after thermal decomposition.

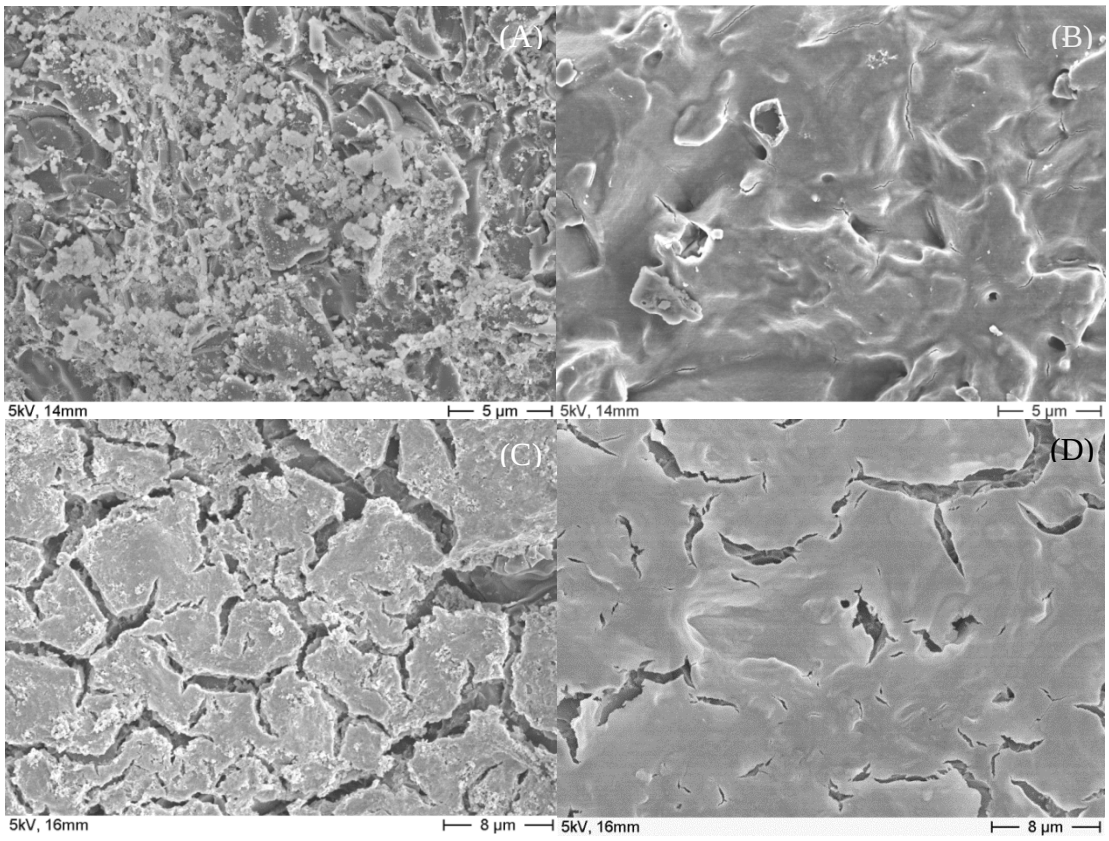


Figure 6.6 SEM images of (A) NiAl40-C550, (B) NA(1.0)-NiAl40-C550, (C) NiAl40-C550-R700, and (D) NA(1.0)-NiAl40-C550-R700 catalysts.

6.3.5 FTIR analysis

Figure 6.7 shows the FTIR spectra of as-prepared NA-LDH and the raw-LDHs. It is found that the absorbance of NA-LDHs is stronger than the raw-LDHs. For the two

series of LDHs, the Pd, Rh substituted LDHs show stronger absorbance than the Ni/Al LDHs.

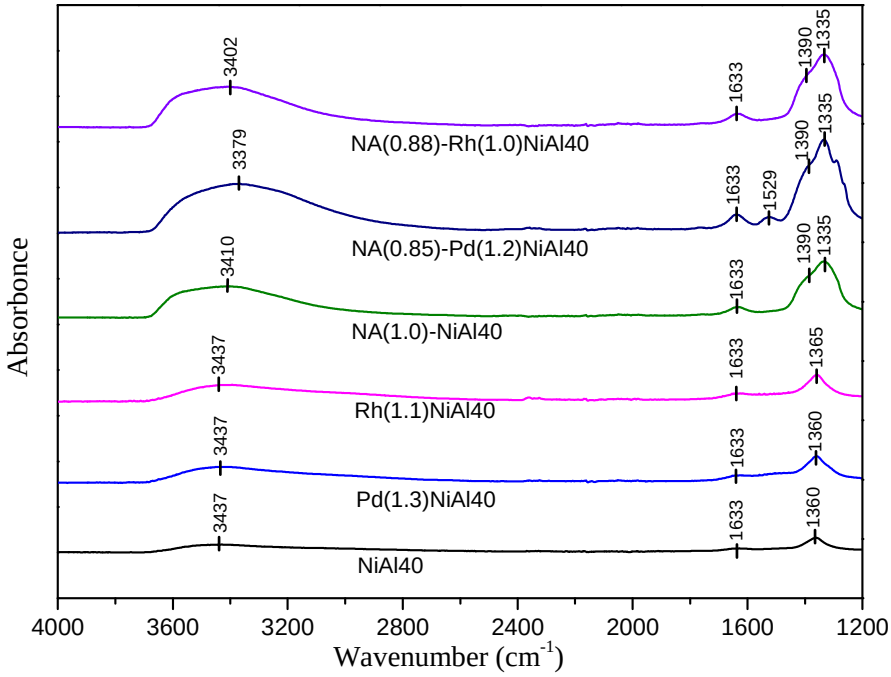


Figure 6.7 FTIR spectra of raw-LDHs and NA-LDHs.

All NA-LDHs show a strong broad band at round 3350 to 3450 cm^{-1} and a less intense peak around the 1633 cm^{-1} region, assigned to the hydroxyls group in the brucite-like layers [208, 228, 229] and water molecules in the interlayers [228, 230] respectively. For the raw-LDHs, the strong 1350 cm^{-1} band is assigned to abroad symmetric carbonate ions the interlayer [141, 208, 231]. After nitric acid treatment, this band was replaced by a higher intensive band at 1335 cm^{-1} with a shoulder at 1390 cm^{-1}. According to Resini *et al.* [147], this new 1335 cm^{-1} is indicative of the formation of abroad antisymmetric stretching carbonates, whereas the higher wavelength shoulder occurring at 1390 cm^{-1} is due to the sharp antisymmetric nitrate ions which were intercalated to the interlayers during nitric attack.

The above results imply the nitric acid attack not only replace some interlayer symmetric carbonate nitrate ions by antisymmtric nitrate ions, but also make the rest of the carbonate ions in the interlayers antisymmetric. In agreement with the displacement of characteristic peaks in the XRD, this ion exchange leads to a lower level electrostatic force for the interlayers, resulting an expansion of the brucite layers in *c* direction.

6.3.6 Thermal decomposition analysis

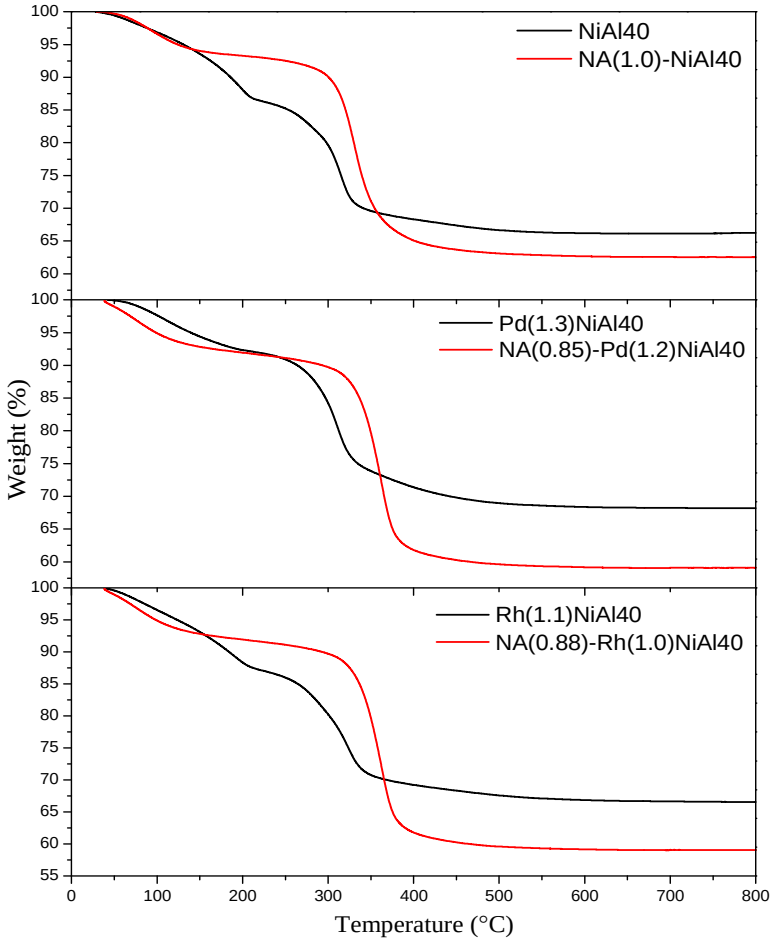


Figure 6.8 TGA curves of raw-LDHs and NA-LDHs.

TGA plots are shown in Figure 6.8 for raw-LDHs and NA-LDHs. All LDHs show a two-step weight loss. A very low temperature, of around 100°C, is sufficient to vapour out the physical adsorbed water whereas the interlayer water is removed at higher temperatures, i.e. between 100 and 250°C. Major weight loss around 300 to 450°C is assigned to the dehydroxylation of brucite layers as well as to the decomposition of compensating ions [200, 232]. Since each CO_3^{2-} ion is replaced with two NO_3^- to balance the charges during ion exchange, the total weight loss in the second stage of NA-LDHs is much higher in comparison with their raw-LDHs. The overall weight loss of NA-LDHs is hence higher. On the other hand, second weight loss starts at a higher temperature in the NA-LDHs (around 380°C compared with 330°C for raw-LDHs), which indicates more energy is consumed in decomposing the nitrate anions at this stage.

6.3.7 Structure of catalysts

6.3.7.1 Structures of catalysts derived from raw-LDHs and NA-LDHs

Figure 6.9 displays the XRD patterns of the Ni(Al)O, Pd and Rh promoted Ni(Al)O catalysts obtained by calcining the relevant raw-LDHs and NA-LDHs at 550°C. All catalysts show similar diffraction patterns of the NiO-like structure (ICDD: 00-047-1049) without any additional phase. As seen in Table 6.2, the crystallite sizes and lattice parameter of each NA-catalyst is slightly smaller than the catalyst derived from raw-LDH. This could be due to a reduction on crysatllinity and a small decrease in the Ni and Pd ratios.

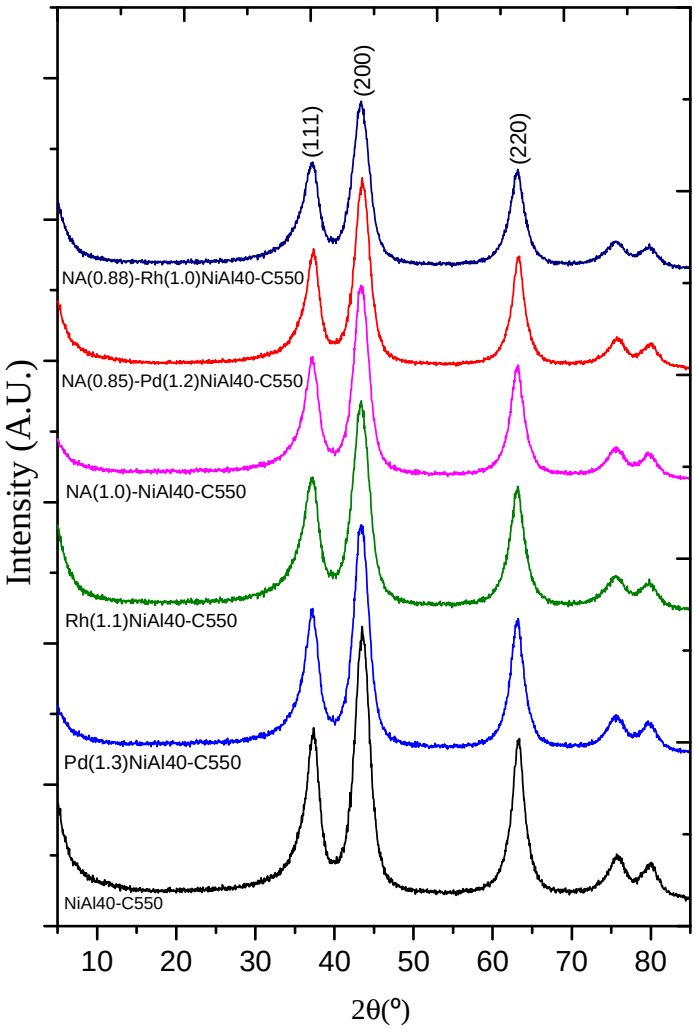


Figure 6.9 XRD patterns of catalysts obtained from calcination of raw-LDHs and NA-LDHs at 550°C for 4 h.

Table 6.2 Structure and composition of calcined catalysts.

Catalyst name	**Phase (by XRD)**	**Crystallite size (nm)[a]**	**Lattice Parameter *a* (Å)**
NiAl40-C550	Ni(Al)O	13.5	4.154
NA(1.0)-NiAl40-C550	Ni(Al)O	11.2	4.152
NA(1.1)-NiAl40-C550	Ni(Al)O, NiO	-	-
NA(1.2)-NiAl40-C550	Ni(Al)O, NiO	-	-
Pd(1.3)NiAl40-C550	Pd/Ni(Al)O	8.4	4.186
NA(0.85)- Pd(1.2)NiAl40-C550	Pd/Ni(Al)O	7.8	4.183
NA(0.9)- Pd(1.0)NiAl40-C550	Pd/Ni(Al)O, (Pd)/NiO, NiO, PdO	-	-
Rh(1.1)NiAl40-C550	Rh/Ni(Al)O	9.7	4.177
NA(0.88)- Rh(1.0)NiAl40-C550	Rh/Ni(Al)O	9.2	4.174

[a] Mean values obtained from reflections (111), (200) and (220): ref ICDD 47-1049

6.3.7.2 Structures of catalysts derived from NA-LDHs treated with different quantities of nitric acid

Nitric acid, if used in excess, breaks the LDH structure, forming metal nitrates. Figure 6.10A shows the diffraction peaks of NiO-like phase becoming sharper and narrower as a function of increasing quantity for acid attacking the LDH precursor. Catalyst NA(1.1)-NiAl40-C550 and NA(1.2)-NiAl40-C550 when the precursors treated with 10% to 20% excessive nitric acid over the optimum amount, show clear phases of nickel oxide (ICDD: 00-047-1049).

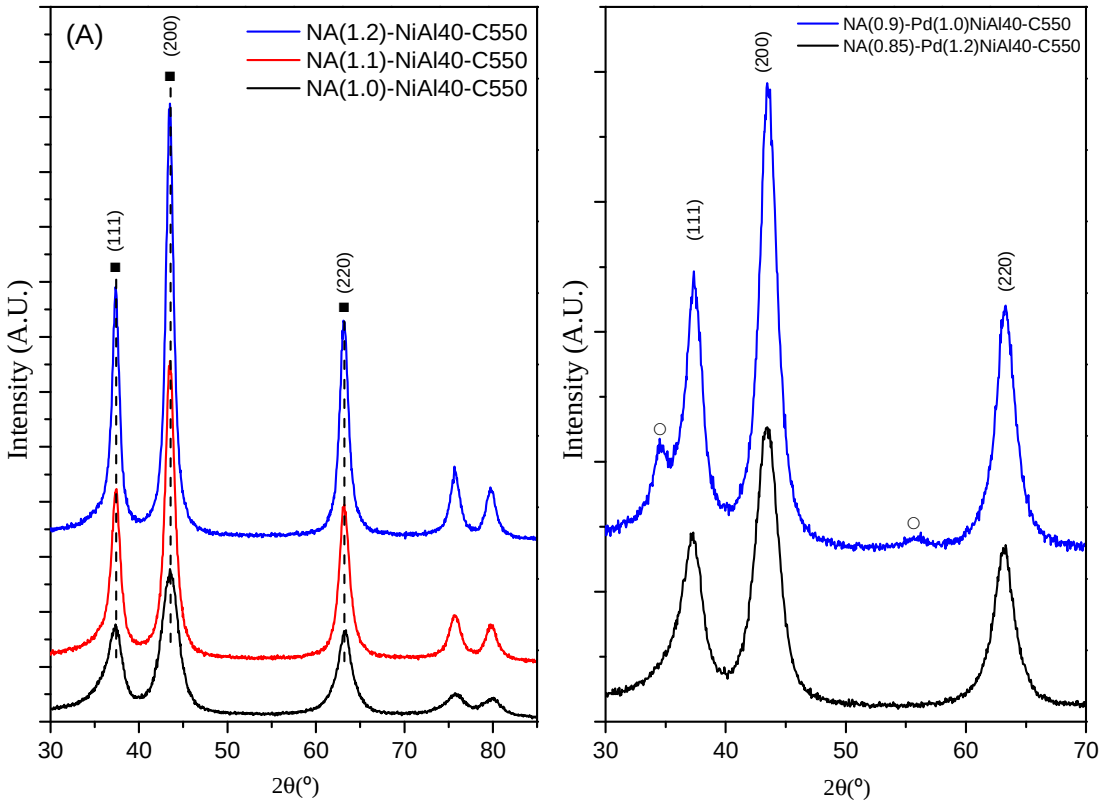


Figure 6.10 Comparison of XRD patterns of (A) Ni(Al)O and (B) Pd promoted Ni(Al)O catalysts derived from LDH precursors treated with different quantities of nitric acid. (■) Ni(Al)O/NiO; (○) PdO

Similarly, a sharp diffraction pattern corresponding to NiO is observed along with diffraction patterns of NA(0.9)-Pd(1.0)NiAl40-C550 sample when precursor is treated with 5% more acid over quantity used in NA(0.85)-Pd(1.2)NiAl40 (Figure 6.10B). Two separate peaks at 2θ=34.5 and 56° are also detected corresponded to PdO (ICDD: 00-002-1432) which may be formed during the acid attack.

6.3.8 TEM observation

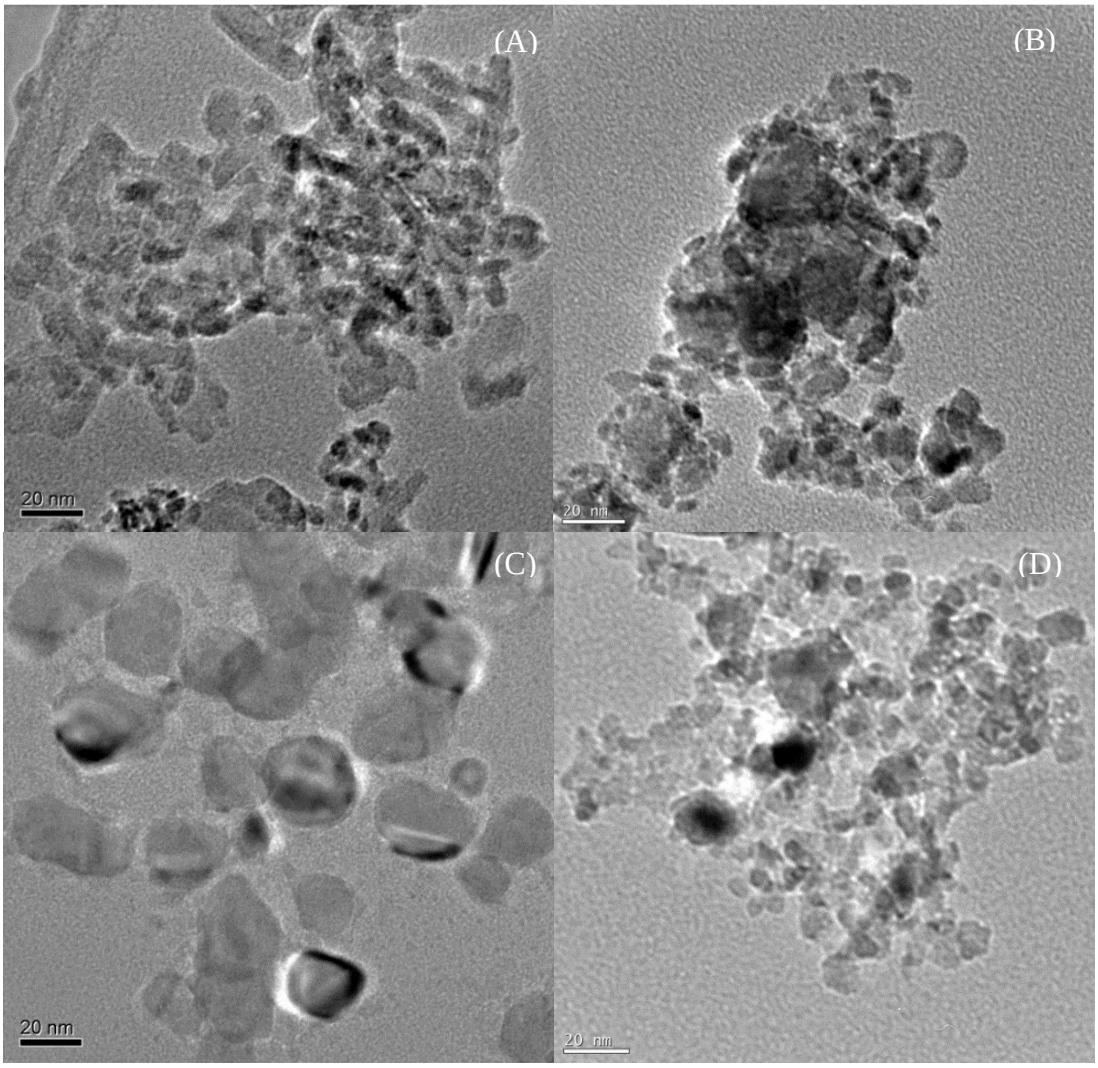


Figure 6.11 HR-TEM images of (A) NiAl40-C550, (B) NA(1.0)-NiAl40-C550, (C) NiAl40-C550-R700 and (D) NA(1.0)-NiAl40-C550-R700.

Figure 6.11A shows the morphology of NiAl40-C550 catalyst with predominantly thin strips and nodular-shaped plates and a small amount of rotundity/elliptical shape plates. In the case of the NA(1.0)-NiAl40-C550 catalyst, rotundity/elliptical plates dominate the morphology and no long strip-shaped particles are observed (Figure 6.11B). The particle sizes range from 5 to 15 nm, which is much smaller than the NiAl40-C550 catalyst (15-30 nm). This result confirms the fact that nitric acid treatment effectively splits the large extended raw-LDH particles into small pieces, suggesting the derived catalyst has a smaller particle size.

After reduction, both the catalysts show similar elliptical nanoparticles with a relatively uniform size distribution (Figure 6.11C and D). The average particle size of the reduced NA(1.0)-NiAl40-C550-R700 catalysts (5-15nm) is retained at the small level, in comparison with the NiAl40-C550-R700 catalysts (15-30 nm).

6.3.9 TPR analysis

The TPR profiles of the catalysts obtained from the calcination of raw-LDHs and NA-LDHs are shown in Figure 6.12. A common feature is that all the catalysts derived from NA-LDHs consume more H_2 than the related catalysts derived from raw-LDHs, indicating a higher dispersion of nickel due to the smaller particle sizes. This shows the agrrement with the findings of TPR analyses in Chapter 3, as the initial preparative condtions show the influnce on calcined catalysts. In Figure 6.12A, the reduction maximum of catalyst NA(1.0)-NiAl40-C550 shifts to the lower temperature when compared with the NiAl40-C550 catalyst. According to Pulxy *et al.* [155], Al^{3+} are located in both tetrahedral and octahedral sites in the Ni(Al)O derived from Ni/Al

LDH. Nitric acid treatment and small particle size of the NA-LDH precursor influence the distribution of Al^{3+} in the derived catalyst. More Al^{3+} ions are incorporated in the octahedral sites after calcination. From the study in the previous chapters, it is inferred that the 'ligand effect' on nickel by aluminium is weakened in this case. As a result, nickel becomes less ionic and the reducibility of the Ni(Al)O is enhanced with its internal structure being transferred from S.L.M. to D.O.S.I. form. However, these changes occur internally within the structure of the Ni(Al)O and are hardly detected by XRD.

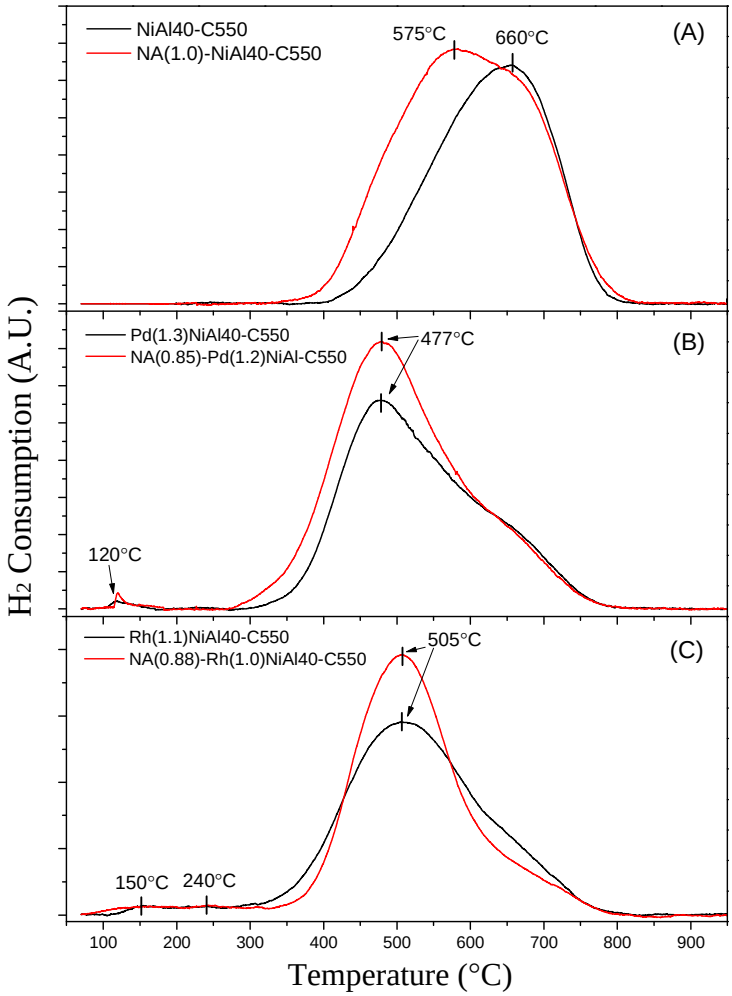


Figure 6.12 TPR profiles of the catalysts derived from raw-LDHs and NA-LDHs.

On the other hand, the reduction situation of the catalysts derived from Pd or Rh substituted NA-LDHs are different. In Figure 6.12B and C, the shapes of their TPR curves are not obviously different from the related raw-LDH derived catalysts. The nitric acid treatment did not cause a change on maximum reduction temperatures of these catalysts but only increase the H_2 consumption at these temperatures. This is because the 'ligand effect' in the promoted catalysts is not obvious due to the synergetic effect of Pd and Rh promoters. Hence, the Ni and Al interaction and internal structure of the noble metal promoted Ni(Al)O catalysts are merely inflected by the nitric acid treatment applied on the precursor LDHs.

6.3.10 Catalyst Activity

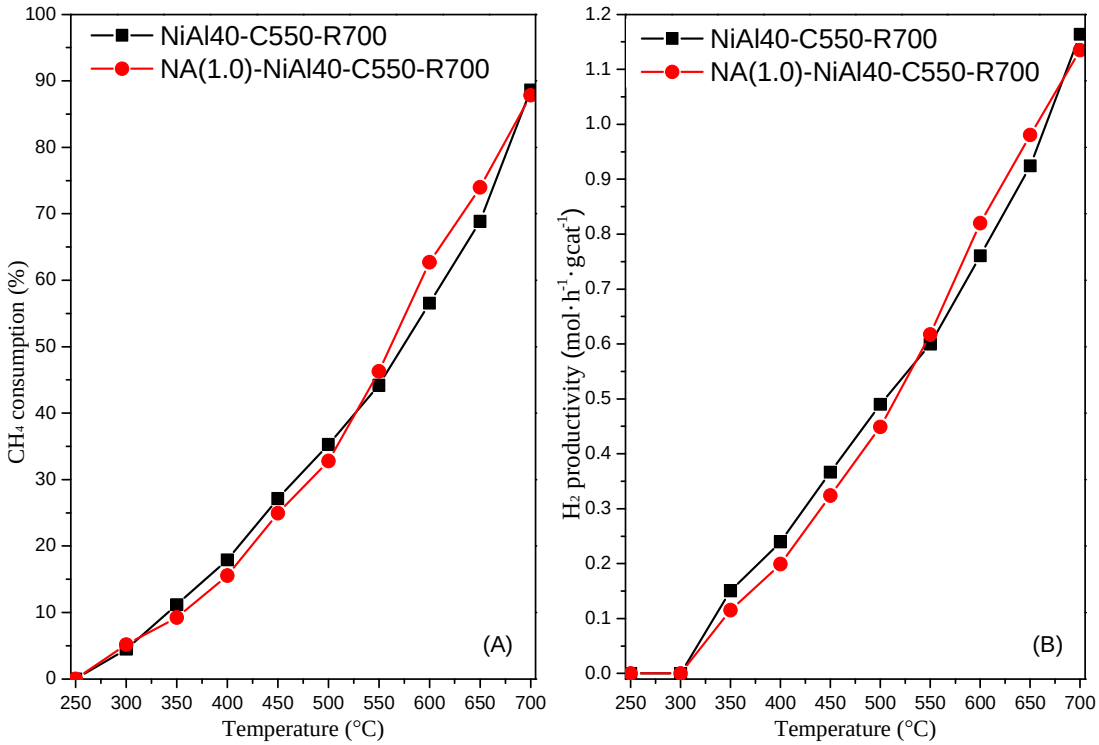


Figure 6.13 Comparison of (A) CH_4 consumption and (B) H_2 productivity of SMR over Ni/Al catalysts derived from raw-LDH and NA-LDH (CH_{4inlet}=16.2ml/min, S:C=3:1, 1 atm).

Figure 6.13 shows the CH_4 consumption and H_2 productivity over Ni/Al catalysts derived from raw-LDH and NA-LDH. The light-off temperature on both the catalysts is around 250 to 300°C. Below 550°C, the activity of NA(1.0)-NiAl40-C550-R700 is slightly lower than NiAl40-C550-R700. Between 550 and 700°C, the activities marginally increase with increasing temperature and NA(1.0)-NiAl40-C550-700 catalyst shows averagely 5% higher than the NiAl40-C550R700 catalyst in both CH_4 consumption and H_2 productivity. This enhancement could be contributed by the small particle sizes and the change of the internal structure of the catalyst.

The activity comparison results over NA-Pd(1.2)NiAl-40-C550-R700 and NA-Rh(1.1)NiAl-40-C550-R700 with Pd(1.3)NiAl-40-C550-R700 and Rh(1.1)NiAl-40-C550-R700 catalysts are shown in Figures 6.14 and 6.15. The activity of the Pd and Rh promoted Ni/Al catalysts derived from NA-LDHs are slightly lower than the ones derived from NA-LDHs, with the maximum difference being below 5%. This phenomenon is not surprising since nitric acid treatments are known to reduce the content of active components (Ni, Pd and Rh). Although the promoted NA-LDH derived catalysts produced smaller particle sizes and higher nickel dispersion, the reduced content of Pd and Rh (in comparison to the optimum ratio) brings down the level of activity.

The above results, again, strongly support the conclusions drawn in the previous chapters as the chemical composition and internal structure of the LDH derived catalysts play significant role in the catalytic activity, being more crucial than other physical issues such as surface area, metal dispersion and particle sizes.

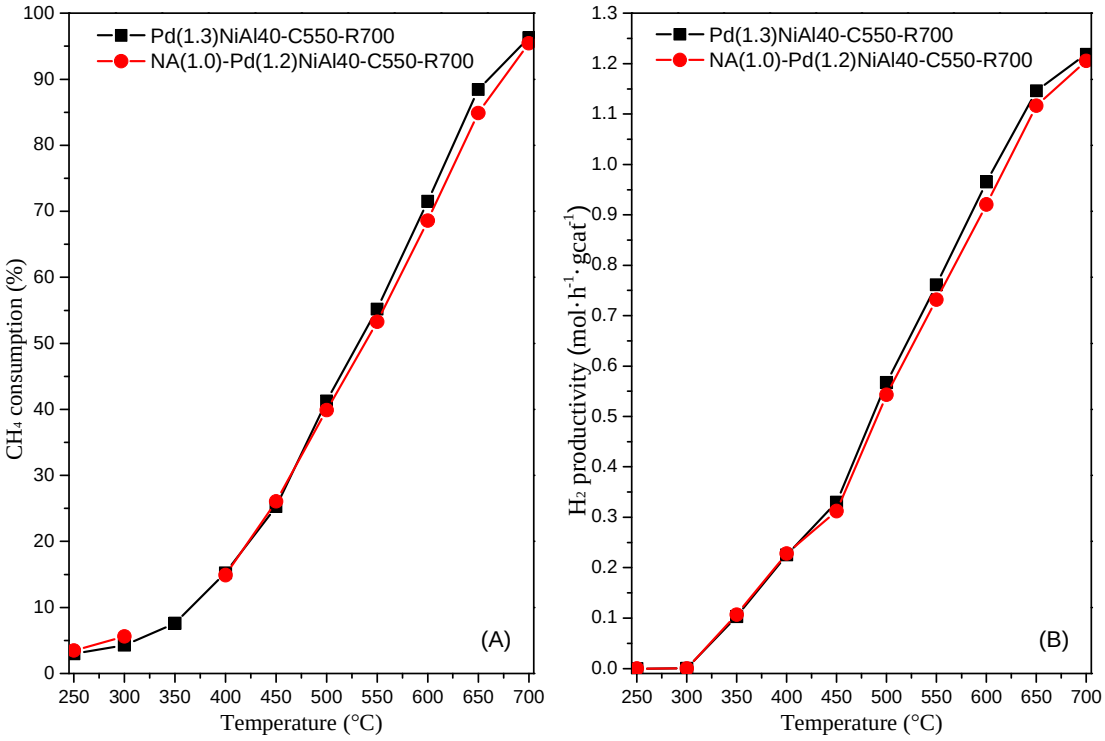


Figure 6.14 Comparison of (A) CH_4 consumption and (B) H_2 productivity of SMR over Pd promoted Ni/Al catalysts derived from raw-LDH and NA-LDH (CH_{4inlet}=16.2ml/min, S:C=3:1, 1 atm).

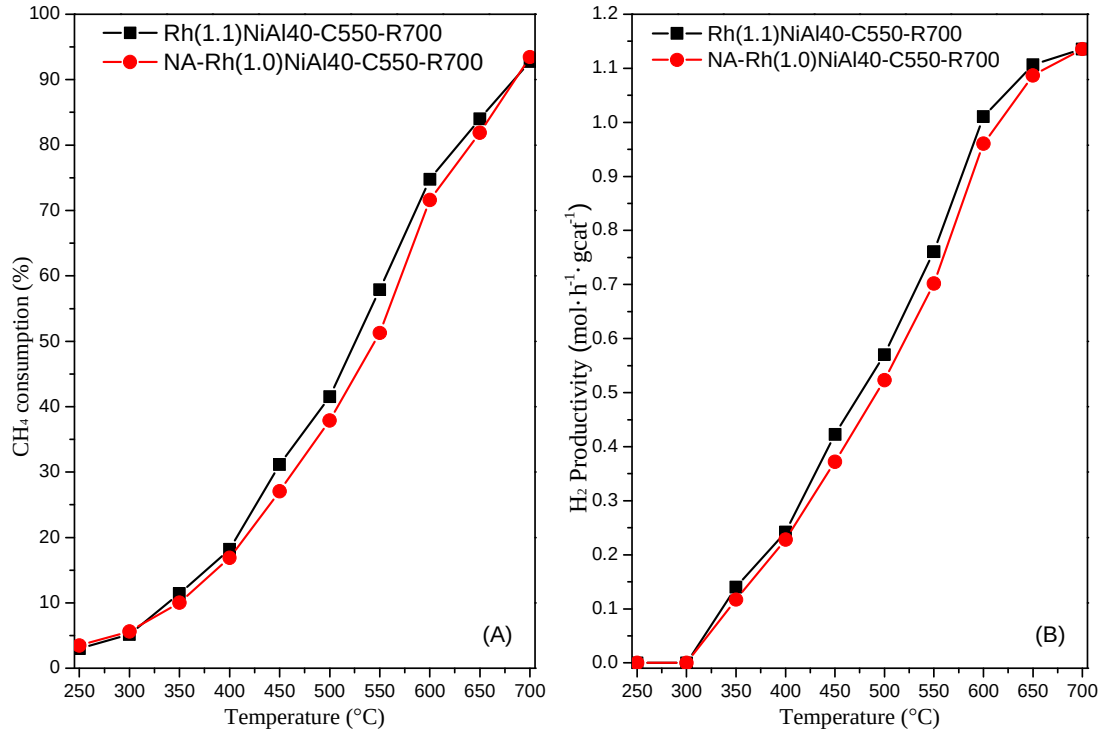


Figure 6.15 Comparison of (A) CH_4 consumption and (B) H_2 productivity of SMR over Rh promoted Ni/Al catalysts derived from raw-LDH and NA-LDH (CH_{4inlet}=16.2ml/min, S:C=3:1, 1 atm).

6.4 Conclusions

Based on the present study, a new method of nitric acid attack method was successfully developed to prepare highly dispersed LDH sol. This method involves peptisation, acid attack and ion exchange. Large LDH clusters were successfully split into small and uniform size particles without significant changing structures, when a suitable amount of nitric acid is used. The sol, with good fluidity and glutinosity, is favours to the subsequent coating work to form a fine and smooth layer covered on the surface of the SOFC anode. The TEM micrograph shows that the particle sizes of calcined and reduced NA-catalysts are smaller than the catalysts derived from raw-LDHs. This method, therefore, effectively improves the usability of the current LDHs prepared by the general CP method. The activity test shows that there are sufficient activities by the NA-LDH derived catalysts. The NA-Ni/Al catalyst has slightly enhanced activity due to the change in internal structure. Nevertheless, Pd and Rh promoted NA-catalysts show a small reduction in their activity compared with the parent raw-LDH analogues due to the decreased quantity of promoter metals.

Chapter 7. Stability, self-activation and self-regeneration studies over LDH derived catalysts

7.1 Introduction

LDH derived Ni/Al catalysts, as described in the previous chapters, show high activity for SMR and can easily be fabricated within an SOFC anode. However, only these qualities are not sufficient for successfully applying them in the commercial SOFC as the real operating conditions play critical roles as well. First, the catalyst is normally incorporated inside the layered structure SOFC stack and it is not realistic to think this can be replaced during the cell's lifetime; resultantly, the lifetime of the catalyst determines the lifetime of the whole SOFC stack. Also, the SMR temperature (equal to the cell reaction temperature) varies during DSS, especially domestic used SOFC (e.g. a stationary power plant or any remote application). In the gap between two operations, the system normally undergoes a purged cooling-down process for security and safety reasons [128]. Common laboratory gases, such as nitrogen, helium, etc., may not be used here due to their high cost. Thus, the normal method is to cut the methane off and leave hot steam as a purging gas. This means the catalyst must have very high stability and tolerance against deterioration in multiple-cycle operations and oxidation conditions. General nickel based catalysts are easily oxidised by steam or oxygen and may not be suitable for operating in these conditions. To solve this problem, as well as to maintain a low cost, promoters are therefore needed. Platinum group metals are frequently reported for their excellent catalytic behaviours in promoting nickel catalyst [126, 128, 140, 154]. In this chapter, the stability, self-activation and self-regeneration behaviours of the Pd and Rh promoted Ni/Al catalysts prepared in the present study are investigated to ensure the competence of these catalysts for fuel-processing in IT-SOFC.

7.2 Experimental

Some of the previously prepared catalysts were selected for this study: NiAl40-C550, Pd(1.3)NiAl40-C550, Rh(1.1)NiAl40-C550, NA(1.0)-NiAl40-C550, NA(0.85)-Pd(1.2)NiAl40-C550 and NA(0.88)-Rh(1.1)NiAl40-C550. The former three catalysts are derived from LDH precursors prepared using the general CP method, and exhibited the best activity during SMR compared with other related catalysts in the series (Ni/Al, Pd and Rh promoted Ni/Al catalyst series in Chapters 3, 4 and 5). The latter three catalysts are derived from LDHs prepared by the newly developed nitric acid attack method (Chapter 6). All LDH precursors were calcined at 550°C for 4 h to obtain the catalysts.

Three different tests were performed on these catalysts: long-term stability, self-activation and self-regeneration ability tests. Details of these experiments are introduced in Section 2.4.3 in Chapter 2. The self-regeneration ability was studied through a steam-purged DSS-like test over all catalysts mentioned above. Beside these, two separate DSS-like tests, over unpromoted catalysts NiAl40-C550 and NA(1.0)-NiAl40-C550, were also carried out without the steam purging. In these tests, steam was cut off after each reaction cycle, leaving only the argon flow to protect the catalysts during the gap prior to entering the next reaction cycle.

XRD and HR-TEM were used to analyse the differences in the catalysts before and after the catalytic studies. Information of handling and specimen preparation are introduced in Section 2.5 in Chapter 2.

7.3 Results and discussion

7.3.1 Long-term stability test

The results of the long-term stability test with time-on-stream at a reaction temperature of 600°C are given in Figure 7.1. All catalysts were very stable, without any fluctuations or decrease in activity during the reaction period. This high stability ensures the catalysts suitable for fundamental commercial application. Figure 7.2 shows the HR-TEM micrograph of NiAl40-C550-R700 catalysts before and after testing. No obvious change in the catalyst morphology is found after the reaction and the used catalyst is still clean, without any evidence of carbon deposition on the surfaces of the catalyst particles.

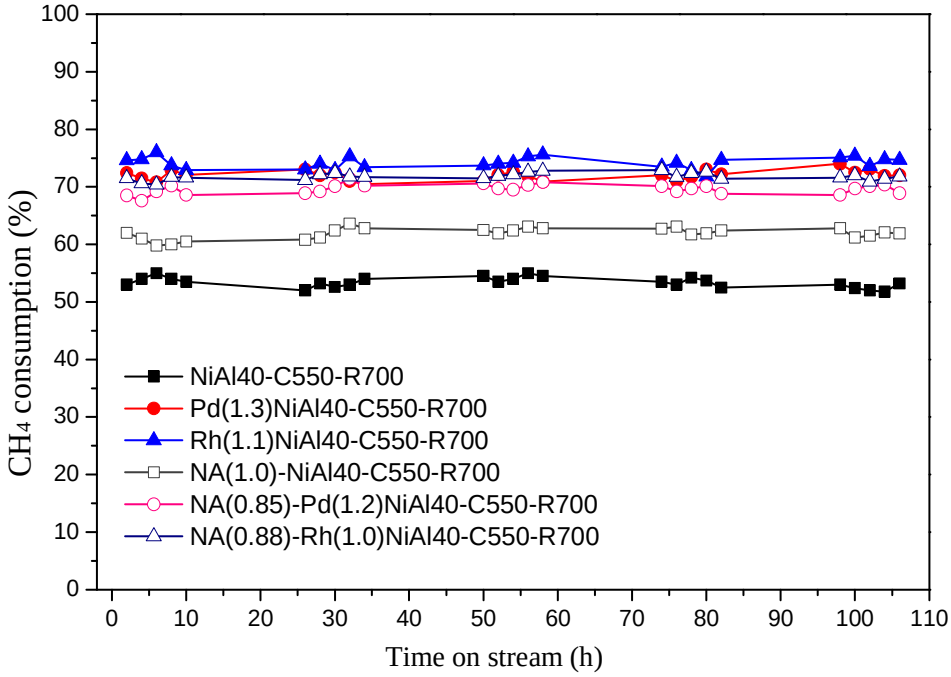


Figure 7.1 CH_4 consumption of long-term SMR at 600°C over tested catalysts (CH_{4inlet}=16.2ml/min, S:C=3:1, 1 atm).

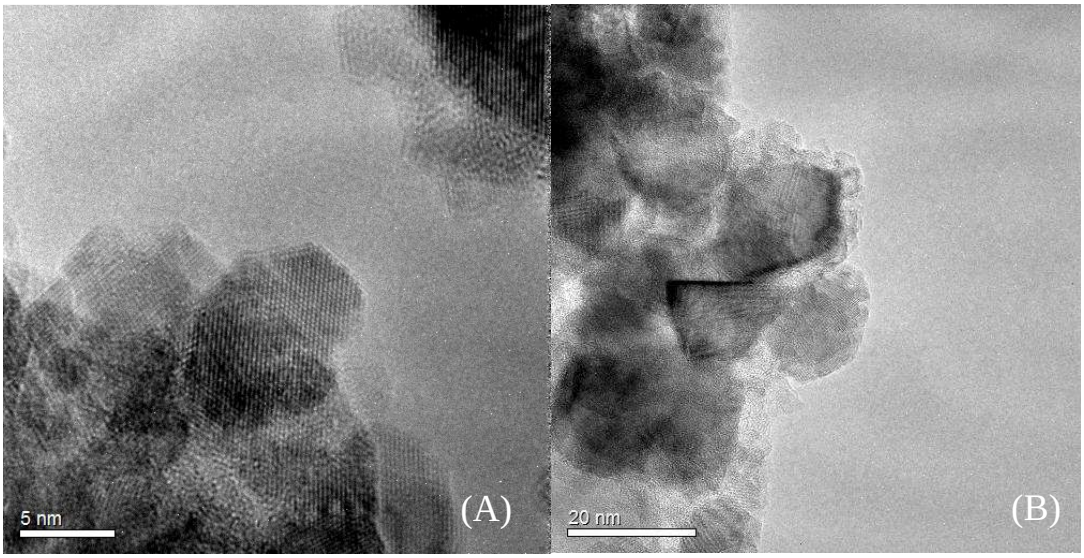


Figure 7.2 HR-TEM images of NiAl40-C550-R700 derived catalyst (A) before and (B) after long-term stability test.

7.3.2 Self-activation of Pd and Rh promoted Ni(Al)O catalysts

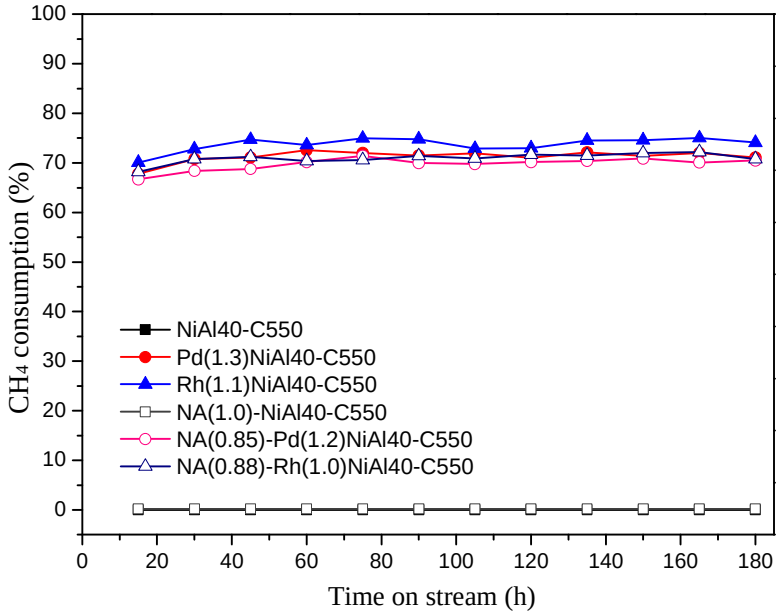


Figure 7.3 Self-activation of the tested catalysts during SMR at 600ºC. (CH_{4inlet}=16.2ml/min, S:C=3:1, 1 atm).

Figure 7.3 shows the self-activation test results. The two unpromoted Ni(Al)O catalysts show no activity during the entire test period. The Pd and Rh promoted Ni(Al)O catalysts were self-activated at the start of the reaction. With a further 10-20 minutes of operation, the activity reached an equilibrium state. It is likely that the surface-exposed Pd and Rh ions were quickly reduced at 600°C under the reaction conditions. The metallic Pd or Rh then dissociated methane to hydrogen atoms and the spilled-over hydrogen atoms migrated and reduced some surface-exposed Ni^{2+}. The reduced nickel then initiated the SMR reactions, producing a large quantity of H_2 which resulted in a further reduction of the neighbouring Ni^{2+} in the bulk. Therefore, the catalysts gradually reduced in a short time [128, 133].

After reaching a steady state, all self-activated catalysts exhibited considerable activity and stability. At 600°C, the activity of all self-reduced catalysts reached almost the same activity level of the pre-reduced catalysts studied in the long-term stability test. This implies that the reduction conditions do not obviously affect the activity of catalysts, except in terms of a delay in attaining a steady state.

7.3.3 Self-regeneration of Pd and Rh promoted Ni/Al catalysts

Figure 7.4 shows the activities of both unprompted NiAl40-C550-R700 and NA-NiAl40-C550-R700 catalysts at standard DSS-like operations for three cycles. The catalysts are stable under these conditions. When the steam purging is introduced, these catalysts were completely deactivated after the first steam-purging process,

indicating a quick oxidation of the active nickel by steam (Figure 7.5). Indeed, the XRD results in Figure 7.6 further confirm that no metallic nickel phase is present in the deactivated catalysts. Similar results were also reported by Takehira and co-workers [128, 130, 132, 154].

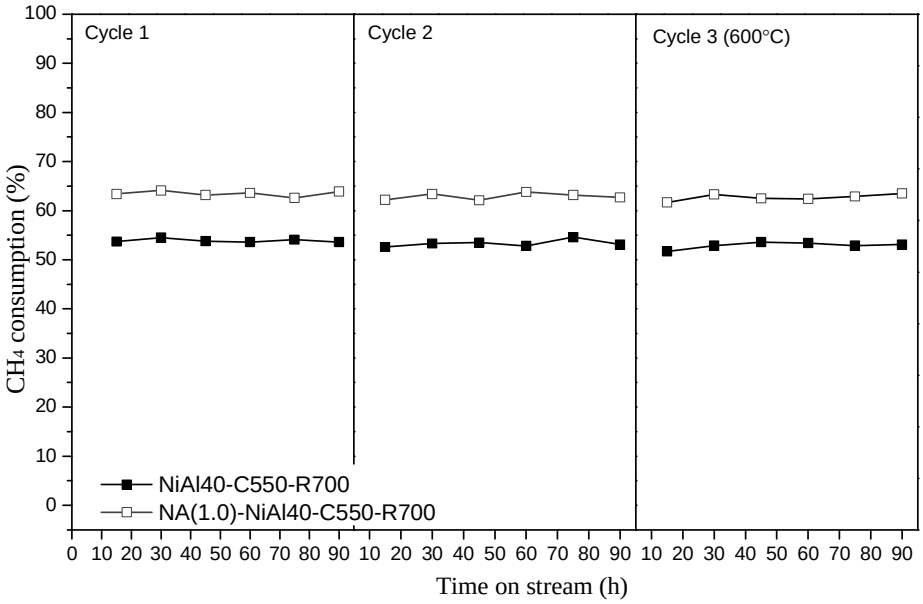


Figure 7.4 CH_4 consumption of SMR under normal DSS-like conditions over NiAl40-C550-R700, NA-NiAl40-C550-R700 catalysts (CH_{4inlet}=16.2ml/min, S:C=3:1, 1 atm).

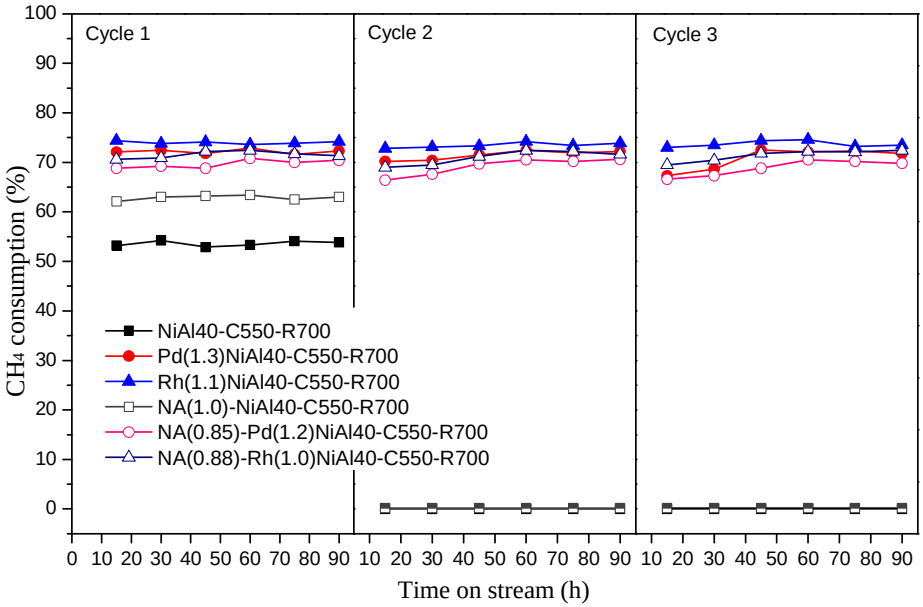


Figure 7.5 CH_4 consumption of SMR under steam-purged DSS-like conditions over tested catalysts at 600°C (CH_{4inlet}=16.2ml/min, S:C=3:1, 1 atm).

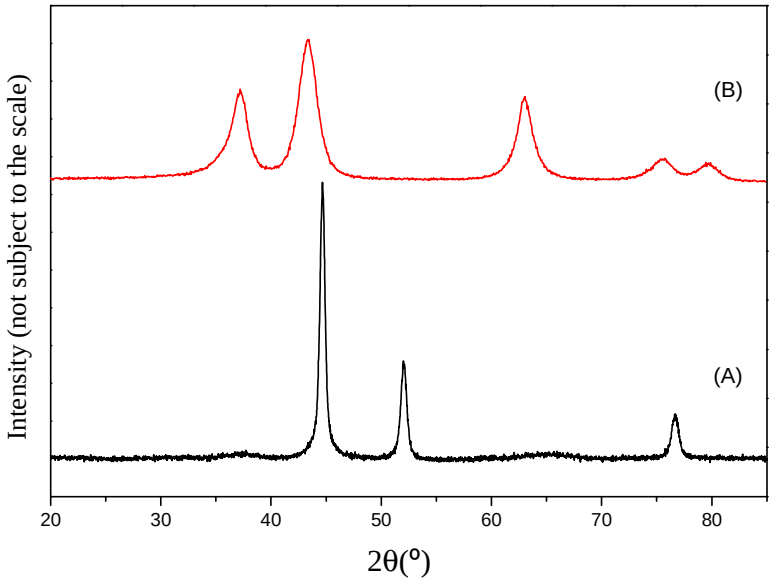


Figure 7.6 XRD patterns of NiAl40-C550-R700 catalysts (A) before and (B) after the steam-purged DSS-like operation.

In contrast, Pd and Rh promoted catalysts exhibit stable activity during the whole test range of the purging experiments. A small drop in activity is found in all the cases at the initial stage of the second and third testing cycles, but activity quickly recovers to the normal level after around 30 minutes' operation when the reaction reaches a steady state. There are two possible mechanisms accounting for this behaviour. First, it could be attributed to a small amount of Pd or Rh promoters protect nickel metal, affecting the catalysts as a result of oxidation under steam-purging conditions. Second, the self-activation behaviour could also have played a role in reducing any oxidised nickel when the catalyst comes into contact with methane. The active nickel is, hence, always regenerated.

7.4 Conclusions

The Ni/Al catalysts derived from takovite LDHs showed high and stable activity in long-term steady and DSS-like SMR operations. However, the catalysts were easily oxidised under purging conditions if there is an absence of the noble metal promoters. The deactivation of this low-cost catalytic material significantly restricts its further adoption in SOFC. Introducing small amount of Pd or Rh promoter effectively enhanced the performance of the catalysts as they not only increased the average activity of the catalysts but also protected the activated nickel against oxidation by steam. Moreover, the promoted catalysts exhibited self-activation and self-regeneration properties, keeping them always in an active state when in contact with steam/methane flow at reaction temperature. Additionally, the promoted catalysts showed excellent activity and stability at the intermediate temperature range after reaching a steady state, which indicates that steam purging did not cause any permanent deactivation of the catalysts.

Chapter 8. Summary and recommendations

8.1 Summary

The experimental findings presented so far help us give answers to the questions raised in the research objectives. (Research objectives and ***questions 1-4*** in Section 1.7.1, Chapter 1).

Research question 1: Are the catalysts suitable for IT-SOFC?

This is the principle research objective of this thesis. To meet the requirements of IT-SOFC, the catalyst must be cost effective, very active and stabile and easy to incorporate within IT-SOFC anode. In this thesis, a series of experiments were performed on catalyst synthesis, characterisations, and performance tests. Testing methods include standard activity test (with gradually elevating operating temperature), long-term stability test, DSS-like test and self-activation and self-regeneration tests.

Three optimised LDH derived catalysts prepared by CP method (NiAl40-C550-R700, Pd(1.3)NiAl40-C550-R700 and Rh(1.1)NiAl40-C550-R700) and another three catalysts derived from their respective sols (NA(1.0)-NiAl40-C550-R700, NA(0.85)-Pd(1.2)NiAl40-C550-R700 and NA(0.88)-Rh(1.1)NiAl40-C550-R700) have been chosen for studying activity (Chapter 3, 6), stability (Chapter 7) as well as self-regeneration behaviours (ICDD: 00-047-1049) (Chapter 7). Sols are prepared by nitric acid attack on the parent LDH samples.

These catalysts show very good activity and stability at intermediate reaction temperatures (550-700°C, particularly at 600°C). Though small quantity of Pd or Rh added will increase the catalyst cost marginally, a significant enhancement in the activity and improved stability will supersede the cost effect. In addition, pre-reduction of the catalyst during the cell fabrication can also be eliminated and hot steam produced from electrochemical reaction within the cell can be used for purged DSS operation and hence will have reduced operational cost. The above facts make these promoted catalysts as ideal fuel-processing choices for the ISMR in IT-SOFC.

Research question 2: How do preparation and calcination conditions influence the catalyst's behaviour?

It is found that the chemical composition, especially the content of noble metal promoters, of the LDH acts as the primary issue inflecting the final catalyst activity among all preparative differences (Chapter 3). The noble metal ion affinity to takovite LDH is in the order $Rh^{3+}>Pd^{2+}>>Pt^{2+}$. Rh^{3+} has favourable to the brucite of the LDH. For the basic Ni/Al and Rh containing LDHs, any changes in CP temperature and aging time only affects the particle size and crystallinity of the LDHs, with no change in the chemical composition. The internal structure and activity of the derived catalysts are barely influenced. Pd^{2+} has size limitation to get incorporated into the brucite layers. Preparative conditions influence the quantity of Pd incorporated in the lattice and thus the activity of the catalysts derived from these precursors vary during SMR. Pt is not favourable for inclusion in the lattice and hence has poor affinity to the LDH precursor. Higher Pd or Rh content over the optimum ratio causes ununiform

distribution of these metals, and even segregation (only found in Pd promoted catalyst) (Chapter 5).

Calcination temperature, beside preparative conditions of the LDH precursors, also influences the finial catalysts' behaviours as it influences the internal structure and component distribution of the catalysts (Chapter 4).

Research question 3: What is the role of the noble metal promoters?

The addition of Pd or Rh noble metals drastically improve the catalytic behaviour of the Ni(Al)O catalyst. Firstly, Pd and Rh promoted Ni/Al catalysts have significant enhancement on catalytic activity over the basic Ni/Al catalysts, due the synergetic effect (Chapter 3). Secondly, the promoters weaken the ligand effect from aluminium and hence maintain the internal structure of the calcined Ni(Al)O catalyst against calcination temperature (Chapter 4). Also, the promoted catalysts exhibit novel features such as self-activation and self-regeneration over the basic Ni/Al catalysts, preventing the catalyst from deactivation (Chapter 7).

Research question 4: Developing a new method for coating the LDH on SOFC anode.

A novel method is developed in this study which involves peptization, acid-attack and ion exchange (Chapter 6). SEM observation shows a uniform, smooth and flat LDH layer located on the simulated SOFC anode surface (silica substrate). TEM study also shows the particles of sol derived LDHs and the catalysts are very fine and uniform in

sizes in comparison with the ones prepared by conventional CP method, indicating a great potential of these materials.

8.2 Recommendations for future study

The investigations of the conventional CP method prepared LDHs and their derived catalysts in this thesis are comprehensive, covering a series of essential aspects. The LDH sol (referred as NA-LDHs in Chapter 6) developed in this study has significant technical advantages in coating and hence further research work has to be conduct to improve the quality of LDHs sols

Some recommendations are summarized below:

The present work focused only on the concept and examined the preparative methods for the production of LDH sol and their activity as discussed in Chapter 6 of this thesis without any optimisation. Since the chemical composition and the catalytic behaviour of unpromoted and Rh promoted catalysts are almost independent of crystallinity and particle size of their precursor LDHs, the CP temperature can be lowered (e.g. to 0°C) and aging time can be shorten to make the raw-LDHs with smaller particle size. This can potentially reduce the quantity of nitric acid used in each injection in sol preparation and hence reduce the difficulty in handling as well as lower the risk of damaging the LDH structure. In contrast, it is suggested to prepare the raw-LDH at critical condition (high CP temperature, boiled aging) to make Pd containing raw-LDHs. This can maximally prevent the loss of expensive palladium.

Nitric acid is injected manually using a syringe in achieving sol in the present study. It is difficult to produce a consistent sol every time with this uncontrolled way. A better design for acid injection (may be multiport and automatic injection) is necessary to ensure uniformity and consistency in sol preparation.

Despite a detailed study for the general CP method prepared LDH derived catalysts (550°C/4 hour) has been completed to optimise the calcination conditions of in this thesis, the same condition is followed to study the NA-LDH derived catalysts without any optimisation. The optimum condition for NA-LDH derived catalysts may be different from their parent catalysts. A detailed optimisation work may bring out many hidden facts about this formulation.

Coating methods (optimised solution for coating) for the actual SOFC anode also need to be developed to study the effect of the anode environment for the compatibility and activity.

Bibliography

[1] J.A. Turner, Science, 285 (1999) 687-689.
[2] M. Ratner, Global Natural Gas: A Growing Resource, DIANE Publishing, 2011.
[3] T.L. Johnson, D.W. Keith, Energy Policy, 32 (2004) 367-382.
[4] U.S.E.I. Administration, Natural Gas Consumption by End Use Database, in, 2009.
[5] OECD/IEA, World Electricity Generation, in, 2008.
[6] H. Goverment, Carbon Budgets Factsheet, in, 2009.
[7] M. Shahidehpour, Y. Fu, T. Wiedman, Proceedings of the IEEE, 93 (2005) 1042-1056.
[8] C. Marchetti, Technological Forecasting and Social Change, 10 (1977) 345-356.
[9] I. Hadjipaschalis, A. Poullikkas, V. Efthimiou, Renewable and Sustainable Energy Reviews, 13 (2009) 1513-1522.
[10] G.J. Stiegel, M. Ramezan, International journal of coal geology, 65 (2006) 173-190.
[11] A. Bauen, Journal of Power Sources, 157 (2006) 893-901.
[12] J.H. Hirschenhofer, D.B. Stauffer, M.G. Klett, Fuel Cell Handbook, Fourth Edition ed., Parsons Corporation, Reading, 1998.
[13] B.J. Holland, J.G. Zhu, L. Jamet, Fuel Cell Technology and Application, in, Faculty of Engineering, University of Technology, Sydney, 2001, pp. 1-6.
[14] P. Atkins, Physical Chemistry. 8th, in, Oxford University Press, Oxford, Melbourne, Tokyo, 2006.
[15] S.M. Haile, Acta Materialia, 51 (2003) 5981-6000.
[16] I. Pilatowsky, R.J. Romero, C.A. Isaza, S.A. Gamboa, P.J. Sebastian, W. Rivera, Congeneration Fule Cell-Sorption Air Conditioning Systems, Springer, New York, 2011.
[17] L.J.M.J. Blomen, M.N. Mugerwa, Fuel Cell Systems, Plenum Press, London, 1993.
[18] The International Fuel Cells, a United Technology Company, Fuel Cells Review, 2000.
[19] G. Hoogers, Fuel Cell Technology Handbook, CRC Press, London, 2003.
[20] J. Larminie, A. Dicks, Fuel Cell Systems Explained, John Wileys and Sons, London, 2000.
[21] M. Andersson, H. Paradis, J. Yuan, B. Sundén, International Journal of Energy Research, 35 (2011) 1340-1350.
[22] M.A. Laguna-Bercero, Journal of Power Sources, 203 (2012) 4-16.
[23] Z. Shao, W. Zhou, Z. Zhu, Progress in Materials Science, 57 (2012) 804-874.
[24] A.J. Appleby, F.R. Foulkes, Fuel Cell Handbook, Van Nostrand Reinold, New York, 1989.
[25] J.T. Brown, Assessment of Research Needs for Advanced Fuel Cells, DOE/AFCWG, 1985.
[26] M. Gasik, Materials for fuel cells, Woodhead Pub. and Maney Pub., 2008.
[27] C. Sun, H. Rob, J. Roller, J Solid State Electrochem, 14 (2010) 1125-1144.
[28] T. Chandra, K. Tsuzaki, M. Militzer, C. Ravindran, Advanced Materials Engineering, 15-17 (2007) 293-298.
[29] E.J. De Guire, Solid Oxide Fuel Cells, in, ProQuest, 2003.
[30] B.C.H. Steele, Journal of Materials Science, 36 (2001) 1053-1068.
[31] B.C.H. Steele, A. Heinzel, Nature, 414 (2001) 345-352.
[32] R.M. Ormerod, Royal Society of Chemistry, 32 (2003) 17-28.
[33] A.B. Stambouli, E. Traversa, Renewable and Sustainable Energy Reviews, 6 (2002) 433-455.

[34] J.P.P. Huijsmans, F.P.F. van Berkel, G.M. Christie, Journal of Power Sources, 71 (1998) 107-110.
[35] D. Georgis, S.S. Jogwar, A.S. Almansoori, P. Daoutidis, Computers & Chemical Engineering, 35 (2011) 1691-1704.
[36] A.J. Mc Evoy, in: Fuel cell technology status and prospects, 1998.
[37] O. Yamamoto, Electrochimica Acta, 45 (2000) 2423-2435.
[38] K. Huang, M. Feng, J.B. Goodenough, C. Milliken, Journal of the Electrochemical Society, 144 (1997) 3620.
[39] Y. Arachi, H. Sakai, O. Yamamoto, Y. Takeda, N. Imanishai, Solid State Ionics, 121 (1999) 133-139.
[40] A.J. Jacobson, Chemistry of Materials, 22 (2009) 660-674.
[41] Z. Shao, S.M. Haile, Nature, 431 (2004) 170-173.
[42] W. Zhu, Z. Lü, S. Li, B. Wei, J. Miao, X. Huang, K. Chen, N. Ai, W. Su, Journal of Alloys and Compounds, 465 (2008) 274-279.
[43] W. Sun, Z. Zhu, Y. Jiang, Z. Shi, L. Yan, W. Liu, International Journal of Hydrogen Energy, (2011).
[44] T. Ishihara, T. Kudo, H. Matsuda, Y. Takita, Journal of the Electrochemical Society, 142 (1995) 1519.
[45] T. Ishihara, K. Shimose, T. Kudo, H. Nishiguchi, T. Akbay, Y. Takita, Journal of the American Ceramic Society, 83 (2000) 1921-1927.
[46] S. Adler, J. Lane, B. Steele, Journal of the Electrochemical Society, 143 (1996) 3554.
[47] D. Waller, J. Lane, J. Kilner, B. Steele, Solid State Ionics, 86 (1996) 767-772.
[48] R. Chiba, F. Yoshimura, Y. Sakurai, Solid State Ionics, 124 (1999) 281-288.
[49] R. Chiba, F. Yoshimura, Y. Sakurai, Solid State Ionics, 152 (2002) 575-582.
[50] R. Chiba, F. Yoshimura, Y. Sakurai, Y. Tabata, M. Arakawa, Solid State Ionics, 175 (2004) 23-27.
[51] E.P. Murray, T. Tsai, S. Barnett, Nature, 400 (1999) 649-651.
[52] E.W. Park, H. Moon, M. Park, S.H. Hyun, International Journal of Hydrogen Energy, 34 (2009) 5537-5545.
[53] O. Costa-Nunes, R.J. Gorte, J.M. Vohs, Journal of Power Sources, 141 (2005) 241-249.
[54] G. Mather, F. Figueiredo, D. Fagg, T. Norby, J. Jurado, J. Frade, Solid State Ionics, 158 (2003) 333-342.
[55] M.D. Gross, J.M. Vohs, R.J. Gorte, Journal of the Electrochemical Society, 153 (2006) A1386.
[56] H. He, R.J. Gorte, J.M. Vohs, Electrochemical and Solid-State Letters, 8 (2005) A279.
[57] S. An, C. Lu, W. Worrell, R. Gorte, J. Vohs, Solid State Ionics, 175 (2004) 135-138.
[58] R.J. Gorte, H. Kim, J.M. Vohs, Journal of Power Sources, 106 (2002) 10-15.
[59] C. Lu, S. An, W.L. Worrell, J.M. Vohs, R.J. Gorte, Solid State Ionics, 175 (2004) 47-50.
[60] Y.H. Huang, R.I. Dass, Z.L. Xing, J.B. Goodenough, Science, 312 (2006) 254-257.
[61] Y. Ji, Y.H. Huang, J.R. Ying, J.B. Goodenough, Electrochemistry communications, 9 (2007) 1881-1885.
[62] A. Lashtabeg, S.J. Skinner, J. Mater. Chem., 16 (2006) 3161-3170.
[63] S.P. Jiang, Materials Science and Engineering: A, 418 (2006) 199-210.
[64] IEA Energy Technology Essentials, in, IEA, 2007.

[65] M. Momirlan, T. Veziroğlu, Renewable and Sustainable Energy Reviews, 3 (1999) 219-231.
[66] M. Momirlan, T.N. Veziroglu, International Journal of Hydrogen Energy, 30 (2005) 795-802.
[67] K. Taylor, J. Anderson, M. Boudart, Catalysis: Science and Technology, (1984).
[68] Y. Matsumura, T. Nakamori, Applied Catalysis A: General, 258 (2004) 107-114.
[69] M. Andersson, H. Paradis, J. Yuan, B. Sundén, International Journal of Energy Research, (2011).
[70] J.-M. Klein, M. Hénault, C. Roux, Y. Bultel, S. Georges, Journal of Power Sources, 193 (2009) 331-337.
[71] M. Boder, R. Dittmeyer, Journal of Power Sources, 155 (2006) 13-22.
[72] P. Dokmaingam, S. Assabumrungrat, A. Soottitantawat, N. Laosiripojana, Journal of Power Sources, 195 (2010) 69-78.
[73] S. Badwal, K. Foger, Ceramics International, 22 (1996) 257-265.
[74] J.M. Klein, Y. Bultel, S. Georges, M. Pons, Chemical Engineering Science, 62 (2007) 1636-1649.
[75] P. Vernoux, J. Guindet, M. Kleitz, Journal of the Electrochemical Society, 145 (1998) 3487.
[76] J.M. Klein, M. Hénault, C. Roux, Y. Bultel, S. Georges, Journal of Power Sources, 193 (2009) 331-337.
[77] M. Andersson, J. Yuan, B. Sundén, Applied Energy, 87 (2010) 1461-1476.
[78] S. Georges, G. Parrour, M. Henault, J. Fouletier, Solid State Ionics, 177 (2006) 2109-2112.
[79] P. Vernoux, M. Guillodo, J. Fouletier, A. Hammou, Solid State Ionics, 135 (2000) 425-431.
[80] N. Laosiripojana, S. Assabumrungrat, Journal of Power Sources, 163 (2007) 943-951.
[81] J. Xu, G.F. Froment, AIChE Journal, 35 (1989) 88-96.
[82] M.A. Rosen, International Journal of Hydrogen Energy, 16 (1991) 207-217.
[83] A.J. ASSIS, C.E. HORI, C.N. ÁVILA-NETO, T.V. FRANCO, Hydrogen production from methane reforming: Thermodynamic assessment, in, 2008.
[84] D. Dalle Nogare, P. Baggio, C. Tomasi, L. Mutri, P. Canu, Chemical Engineering Science, 62 (2007) 5418-5424.
[85] S. Chan, H. Wang, International Journal of Hydrogen Energy, 25 (2000) 441-449.
[86] W. Akers, D. Camp, AIChE Journal, 1 (1955) 471-475.
[87] P. Van Beurden, Energy Research Centre of the Netherlands (ECN), Technical Report I-04-003, (2004).
[88] J.P. Van Hook, Catalysis Reviews—Science and Engineering, 21 (1980) 1-51.
[89] A.E. Lutz, R.W. Bradshaw, J.O. Keller, D.E. Witmer, International Journal of Hydrogen Energy, 28 (2003) 159-167.
[90] M.V. Twigg, M. Twigg, Catalyst handbook, CSIRO, 1989.
[91] J. Rostrupnielsen, J.H.B. Hansen, Journal of Catalysis, 144 (1993) 38-49.
[92] J.R. Rostrup-Nielsen, J. Sehested, J.K. Noerskov, Advances in catalysis, 47 (2002) 65-139.
[93] L. De Rogatis, M. Cargnello, V. Gombac, B. Lorenzut, T. Montini, P. Fornasiero, ChemSusChem, 3 (2010) 24-42.
[94] J. Xu, Catalytic Properties of Nano Ceria in Heterogeneous Catalysis, in: Department of Ingrganic Chemistry, University of Oxford, Oxford, 2010, pp. 61.
[95] H.S. Taylor, Proceedings of the Royal Society of London. Series A, 108 (1925) 105-111.

[96] http://dept.chem.polimi.it/~citterio/SilsisMI/Introduction.pdf, Catalysis-Speeding up the approach to equilibrium, in.
[97] J.R. Rostrup-Nielsen, Catalysis Today, 18 (1993) 305-324.
[98] J.R. Rostrup-Nielsen, Catalysis Today, 37 (1997) 225-232.
[99] J.R. Rostrup-Nielsen, journal of Catalysis, 173 (1973).
[100] E. Kikuchi, S. Tanaka, Y. Yamazaki, Y. Morita, Bulletin of the Japan Petroleum Institute, 16 (1974) 95-98.
[101] D. Qin, J. Lapszewicz, Catalysis Today, 21 (1994) 551-560.
[102] G. Jones, J.G. Jakobsen, S.S. Shim, J. Kleis, M.P. Andersson, J. Rossmeisl, F. Abild-Pedersen, T. Bligaard, S. Helveg, B. Hinnemann, Journal of Catalysis, 259 (2008) 147-160.
[103] M. Boudart, Journal of molecular catalysis, 30 (1985) 27-38.
[104] Z. Ma, F. Zaera, Encyclopedia of Inorganic and Bioinorganic Chemistry, (2005).
[105] G.C. Bond, Catalysis by metals, Academic Press, 1962.
[106] R. Isha, P.T. Williams, Journal of the Energy Institute, 85 (2012) 29-37.
[107] M.C.J. Bradford, M.A. Vannice, Applied Catalysis A: General, 142 (1996) 73-96.
[108] K.P. de Jong, Synthesis of solid catalysts, Wiley-VCH, 2009.
[109] D. Harvey, Modern analytical chemistry, McGraw-Hill Boston, MA, 2000.
[110] http://encyclopedia2.thefreedictionary.com/Coprecipitation, Great Soviet Encyclopedia (Translated in English), in, The Free Dictionary by Farlex, 1979.
[111] P. Patnaik, Dean's analytical chemistry handbook, McGraw-Hill New York, 2004.
[112] J. Li, B. Xiao, R. Yan, X. Xu, Bioresource technology, 100 (2009) 5295-5300.
[113] P. Gayán, C. Dueso, A. Abad, J. Adanez, L.F. De Diego, F. García-Labiano, Fuel, 88 (2009) 1016-1023.
[114] R. Zanella, S. Giorgio, C.R. Henry, C. Louis, The Journal of Physical Chemistry B, 106 (2002) 7634-7642.
[115] S. Wang, G. Lu, Applied Catalysis A: General, 169 (1998) 271-280.
[116] S. Wang, G. Lu, Applied Catalysis B: Environmental, 16 (1998) 269-277.
[117] S. Abelló, D. Verboekend, B. Bridier, J. Pérez-Ramírez, Journal of Catalysis, 259 (2008) 85-95.
[118] L. Smoláková, L. Čapek, Š. Botková, F. Kovanda, R. Bulánek, M. Pouzar, Topics in Catalysis, (2011) 1-12.
[119] R. Hughes, Deactivation of catalysts, Academic press London, 1984.
[120] C.H. Bartholomew, Applied Catalysis A: General, 212 (2001) 17-60.
[121] J. Sehested, J.A.P. Gelten, S. Helveg, Applied Catalysis A: General, 309 (2006) 237-246.
[122] J. Sehested, J.A.P. Gelten, I.N. Remediakis, H. Bengaard, J.K. Nørskov, Journal of Catalysis, 223 (2004) 432-443.
[123] J. Sehested, Journal of Catalysis, 217 (2003) 417-426.
[124] J.A. Rodriguez, D.W. Goodman, Science, 257 (1992) 897-903.
[125] A. Groß, Topics in Catalysis, 37 (2006) 29-39.
[126] D. Li, Y. Nakagawa, K. Tomishige, Applied Catalysis A: General, 408 (2011) 1-24.
[127] E.L. Foletto, R.W. Alves, S.L. Jahn, Journal of Power Sources, 161 (2006) 531-534.
[128] T. Miyata, D. Li, M. Shiraga, T. Shishido, Y. Oumi, T. Sano, K. Takehira, Applied Catalysis A: General, 310 (2006) 97-104.

[129] Z. Hou, P. Chen, H. Fang, X. Zheng, T. Yashima, International Journal of Hydrogen Energy, 31 (2006) 555-561.
[130] D. Li, I. Atake, T. Shishido, Y. Oumi, T. Sano, K. Takehira, Journal of Catalysis, 250 (2007) 299-312.
[131] D. Li, T. Shishido, Y. Oumi, T. Sano, K. Takehira, Applied Catalysis A: General, 332 (2007) 98-109.
[132] D. Li, K. Nishida, Y. Zhan, T. Shishido, Y. Oumi, T. Sano, K. Takehira, Applied Catalysis A: General, 350 (2008) 225-236.
[133] J.H. Jeong, J.W. Lee, D.J. Seo, Y. Seo, W.L. Yoon, D.K. Lee, D.H. Kim, Applied Catalysis A: General, 302 (2006) 151-156.
[134] M. Komiyama, Catalysis Reviews, 27 (1985) 341-372.
[135] J. Geus, J. Van Veen, Studies Surface Sci. Catal, 79 (1993) 355-360.
[136] G. Acres, A. Bird, J. Jenkins, F. King, Spec. Period. Rep. Catal, 4 (1981) 1-30.
[137] J. He, M. Wei, B. Li, Y. Kang, D. Evans, X. Duan, Layered Double Hydroxides, (2006) 89-119.
[138] F. Zhang, X. Xiang, F. Li, X. Duan, Catalysis surveys from Asia, 12 (2008) 253-265.
[139] O. Clause, B. Rebours, E. Merlen, F. Trifiró, A. Vaccari, Journal of Catalysis, 133 (1992) 231-246.
[140] K. Takehira, Journal of Natural Gas Chemistry, 18 (2009) 237-259.
[141] F. Cavani, F. Trifirò, A. Vaccari, Catalysis Today, 11 (1991) 173-301.
[142] M.K. Titulaer, J.B.H. Jansen, J.W. Geus, Clays and clay minerals, 42 (1994) 249-258.
[143] T. Miyata, M. Shiraga, D. Li, I. Atake, T. Shishido, Y. Oumi, T. Sano, K. Takehira, Catalysis Communications, 8 (2007) 447-451.
[144] Y. Zhan, D. Li, K. Nishida, T. Shishido, Y. Oumi, T. Sano, K. Takehira, Applied Clay Science, 45 (2009) 147-154.
[145] W.S. Dong, H.S. Roh, K.W. Jun, S.E. Park, Y.S. Oh, Applied Catalysis A: General, 226 (2002) 63-72.
[146] V. Rives, S. Kannanb, Journal of Materials Chemistry, 10 (2000) 489-495.
[147] C. Resini, T. Montanari, L. Barattini, G. Ramis, S. Presto, P. Riani, R. Marazza, M. Sisani, F. Marmottini, U. Costantino, Applied Catalysis A: General, 355 (2009) 83-93.
[148] F. Prinetto, G. Ghiotti, P. Graffin, D. Tichit, Microporous and Mesoporous Materials, 39 (2000) 229-247.
[149] F. Basile, G. Fornasari, M. Gazzano, A. Vaccari, Applied Clay Science, 16 (2000) 185-200.
[150] D. Bish, Bull. Mineral, 103 (1980) 170-175.
[151] A.I. Khan, D. O'Hare, J. Mater. Chem., 12 (2002) 3191-3198.
[152] G.R. Williams, D. O'Hare, J. Mater. Chem., 16 (2006) 3065-3074.
[153] J. Rocha, M. Del Arco, V. Rives, M. Ulibarri, J. Mater. Chem., 9 (1999) 2499-2503.
[154] Y. Guo, L. Zhou, W. Zhao, J. Chen, M. Sakurai, H. Kameyama, Chemistry Letters, 40 (2011) 201-203.
[155] D. Puxley, I. Kitchener, C. Komodromos, N. Parkyns, Stud Surf Sci Catal, 16 (1983) 237-271.
[156] M. Bellotto, B. Rebours, O. Clause, J. Lynch, D. Bazin, E. Elkaïm, The Journal of Physical Chemistry, 100 (1996) 8535-8542.
[157] H.-S. Roh, I.-H. Eum, D.-W. Jeong, Renewable Energy, 42 (2012) 212-216.

[158] M.G. Beaver, H.S. Caram, S. Sircar, Journal of Power Sources, 195 (2010) 1998-2002.
[159] Y. Sekine, M. Haraguchi, M. Matsukata, E. Kikuchi, Catalysis Today, 171 (2011) 116-125.
[160] D.A.J.M. Ligthart, J.A.Z. Pieterse, E.J.M. Hensen, Applied Catalysis A: General, 405 (2011) 108-119.
[161] M.A. Soria, C. Mateos-Pedrero, A. Guerrero-Ruiz, I. Rodríguez-Ramos, International Journal of Hydrogen Energy, 36 (2011) 15212-15220.
[162] M. Veronica, B. Graciela, A. Norma, L. Miguel, Chemical Engineering Journal, 138 (2008) 602-607.
[163] V. Mas, M.L. Dieuzeide, M. Jobbágy, G. Baronetti, N. Amadeo, M. Laborde, Catalysis Today, 133–135 (2008) 319-323.
[164] C. Qi, J.C. Amphlett, B.A. Peppley, Catalysis Communications, 11 (2009) 71-76.
[165] Y. Chen, C. Liaw, L. Lee, Applied Catalysis A: General, 177 (1999) 1-8.
[166] A. Monzón, E. Romeo, C. Royo, R. Trujillano, F. Labajos, V. Rives, Applied Catalysis A: General, 185 (1999) 53-63.
[167] S. Narayanan, K. Krishna, Applied Catalysis A: General, 198 (2000) 13-21.
[168] A. Corma, V. Fornes, F. Rey, Journal of Catalysis, 148 (1994) 205-212.
[169] N. Mimura, I. Takahara, M. Saito, Y. Sasaki, K. Murata, Catalysis letters, 78 (2002) 125-128.
[170] P. Mitchell, S. Wass, Applied Catalysis A: General, 225 (2002) 153-165.
[171] J.R. Anderson, K.C. Pratt, Introduction to characterization and testing of catalysts, Academic Press, Maryland, 1985.
[172] L. Zhou, Y. Guo, J. Chen, M. Sakurai, H. Kameyama, Fuel, 92 (2012) 373-376.
[173] L. Zhou, Y. Guo, Q. Zhang, M. Yagi, H. Li, J. Chen, M. Sakurai, H. Kameyama, Catalysis Communications, 10 (2008) 325-329.
[174] T. Miyata, D. Li, M. Shiraga, T. Shishido, Y. Oumi, T. Sano, K. Takehira, Applied Catalysis A: General, 310 (2006) 97-104.
[175] S.C. Baek, K.W. Jun, Y.J. Lee, J.D. Kim, D.Y. Park, K.Y. Lee, Research on Chemical Intermediates, (2011) 1-12.
[176] D. Li, K. Nishida, Y. Zhan, T. Shishido, Y. Oumi, T. Sano, K. Takehira, Applied Clay Science, 43 (2009) 49-56.
[177] R.A. van Santen, P.W.N.M. van Leeuwen, J.A. Moulijin, B.A. Averill, Catalysis: an integrated approach, Second ed., Elsevier Science, Amsterdam, 1999.
[178] R. Kellner, J.-M. Mermet, M. Otto, H.M. Widmer, Analytical Chemistry, Wiley-VCH, Weinheim, 1998.
[179] E. Lifshin, X-ray Characterization of Materials, Wiley-VCH Cerlag, Weinheim, 1999.
[180] M.l. Deviney, J.L. Gland, Catalyst Characterization Science: Surface and Solid State Chemistry, Oxford University Press, Oxford, 1985.
[181] D. Kealey, P.J. Haines, Instant Notes, 2nd ed., BIOS Scentific Publishers Ltd, Oxford, 2002.
[182] N. Jespersen, Instrumental Analysis, Allyn and Bacon, Boston, 1986.
[183] D.a. Skoog, F.J. Holder, C. R.Standley, Principles of Instrumental Analysis, 6th ed., Thomson Brooks/Cole., New York, 2006.
[184] R.F. Egerton, Physical principles of electron microscopy : an introduction to TEM, SEM, and AEM, Springer, New York, 2005.
[185] http://serc.carleton.edu, Geochemical Instrumentation and Analysis, Science Education Resource Center, Carteton College.

[186] J. Goldstein, D. Newbury, D. Joy, C. Lyman, P. Echlin, E. Lifshin, L. Sawyer, J. Michael, Scanning Electron Microscopy and X-ray Microanalysis, 3rd ed., Kluwer Academic/Plenum Publishers, New York, 2002.
[187] S.R. Segal, K.B. Anderson, K.A. Carrado, C.L. Marshall, Applied Catalysis A: General, 231 (2002) 215-226.
[188] J. Comas, M. Dieuzeide, G. Baronetti, M. Laborde, N. Amadeo, Chemical Engineering Journal, 118 (2006) 11-15.
[189] C. Qi, J.C. Amphlett, B.A. Peppley, Journal of Power Sources, 171 (2007) 842-849.
[190] C. Qi, J.C. Amphlett, B.A. Peppley, Catalysis letters, 104 (2005) 57-62.
[191] C.E. Daza, J. Gallego, F. Mondragón, S. Moreno, R. Molina, Fuel, 89 (2010) 592-603.
[192] K. Nagaoka, A. Jentys, J.A. Lercher, Journal of Catalysis, 229 (2005) 185-196.
[193] A.C. Canos, A.E.P. Gimeno, J.G.P. Moreno, Bimetallic catalyst for the treatment of water containing nitrates, in, Google Patents, 2003.
[194] N.N. Greenwood, A. Earnshaw, Chemistry of Elements. , Pergamon, , Oxford, 1989.
[195] F. Kovanda, T. Rojka, P. Bezdička, K. Jirátová, L. Obalová, K. Pacultová, Z. Bastl, T. Grygar, Journal of Solid State Chemistry, 182 (2009) 27-36.
[196] J. Zielinski, Applied Catalysis A: General, 94 (1997) 107.
[197] S. Miyata, Clays and clay minerals, 31 (1983) 305-311.
[198] W.T. Reichle, S.Y. Kang, D.S. Everhardt, Journal of Catalysis, 101 (1986) 352-359.
[199] W.T. Reichle, Journal of Catalysis, 94 (1985) 547-557.
[200] A.I. Tsyganok, T. Tsunoda, S. Hamakawa, K. Suzuki, K. Takehira, T. Hayakawa, Journal of Catalysis, 213 (2003) 191-203.
[201] D. Tichit, F. Medina, B. Coq, R. Dutartre, Applied Catalysis A: General, 159 (1997) 241-258.
[202] P.H.M. De Korte, E.B.M. Doesburg, C.P.J. De Winter, L.L. Van Reijen, Solid State Ionics, 16 (1985) 73-80.
[203] P. Arnoldy, M. Franken, B. Scheffer, J. Moulijn, Journal of Catalysis, 96 (1985) 381-395.
[204] B. Yue, R. Zhou, Y. Wang, X. Zheng, Journal of Molecular Catalysis A: Chemical, 238 (2005) 241-249.
[205] N. Iwasa, S. Masuda, N. Ogawa, N. Takezawa, Applied Catalysis A: General, 125 (1995) 145-157.
[206] G.R. Williams, D. O'Hare, Journal of Materials Chemistry, 16 (2006) 3065-3074.
[207] F. Trifirò, A. Vaccari, Solid-state Supramolecular Chemistry: Two-and Three-Dimensional Inorganic Networks, 7 (1996) 251-291.
[208] M. Jitianu, M. Bãlãsoiu, R. Marchidan, M. Zaharescu, D. Crisan, M. Craiu, International Journal of Inorganic Materials, 2 (2000) 287-300.
[209] B. Kneale, J.R.H. Ross, Faraday Discuss. Chem. Soc., 72 (1981) 157-171.
[210] H.S.C. O'Neill, W. Dollase, C. Ross, Physics and Chemistry of Minerals, 18 302-319.
[211] F. Trifirò, A. Vaccari, O. Clause, Catalysis Today, 21 (1994) 185-195.
[212] B. Rebours, J.B. d'Espinose de la Caillerie, O. Clause, Journal of the American Chemical Society, 116 (1994) 1707-1717.
[213] O. Clause, M. Goncalves Coelho, M. Gazzano, D. Matteuzzi, F. Trifirò, A. Vaccari, Applied Clay Science, 8 (1993) 169-186.

[214] F. Basile, L. Basini, G. Fornasari, M. Gazzano, F. Trifirò, A. Vaccari, Chem. Commun., (1996) 2435-2436.
[215] Y. Cesteros, P. Salagre, F. Medina, J.E. Sueiras, Chemistry of Materials, 12 (2000) 331-335.
[216] C. Li, Y.-W. Chen, Thermochimica Acta, 256 (1995) 457-465.
[217] T. Shishido, M. Sukenobu, H. Morioka, M. Kondo, Y. Wang, K. Takaki, K. Takehira, Applied Catalysis A: General, 223 (2002) 35-42.
[218] Z. Jiang, Z. Hao, J. Yu, H. Hou, C. Hu, J. Su, Catalysis letters, 99 (2005) 157-163.
[219] J. Xu, C.M.Y. Yeung, J. Ni, F. Meunier, N. Acerbi, M. Fowles, S.C. Tsang, Applied Catalysis A: General, 345 (2008) 119-127.
[220] K. Hadjiivanov, M. Mihaylov, D. Klissurski, P. Stefanov, N. Abadjieva, E. Vassileva, L. Mintchev, Journal of Catalysis, 185 (1999) 314-323.
[221] S.R. Kirumakki, B.G. Shpeizer, G.V. Sagar, K.V.R. Chary, A. Clearfield, Journal of Catalysis, 242 (2006) 319-331.
[222] T. Lear, R. Marshall, J.A. Lopez-Sanchez, S.D. Jackson, T.M. Klapötke, M. Bäumer, G. Rupprechter, H.J. Freund, D. Lennon, J. Chem. Phys., 123 (2005) 174706-174713.
[223] J.B. Peri, Journal of Catalysis, 86 (1984) 84-94.
[224] S. Derrouiche, D. Bianchi, Applied Catalysis A: General, 313 (2006) 208-217.
[225] K. Hadjiivanov, M. Mihaylov, D. Klissurski, P. Stefanov, N. Abadjieva, E. Vassileva, L. Mintchev, Journal of Catalysis, 185 (1999) 314-323.
[226] C. Crisafulli, S. Scirè, S. Minicò, L. Solarino, Applied Catalysis A: General, 225 (2002) 1-9.
[227] M. Primet, J.A. Dalmon, G.A. Martin, Journal of Catalysis, 46 (1977) 25-36.
[228] H.-y. Zeng, Z. Feng, X. Deng, Y.-q. Li, Fuel, 87 (2008) 3071-3076.
[229] M.J. Dos Reis, F. Silvério, J. Tronto, J.B. Valim, Journal of Physics and Chemistry of Solids, 65 (2004) 487-492.
[230] M.R. Othman, N.M. Rasid, W.J.N. Fernando, Chemical Engineering Science, 61 (2006) 1555-1560.
[231] M. Jitianu, M. Bãlãsoiu, M. Zaharescu, A. Jitianu, A. Ivanov, Journal of Sol-Gel Science and Technology, 19 (2000) 453-457.
[232] H.W. Olfs, L. Torres-Dorante, R. Eckelt, H. Kosslick, Applied Clay Science, 43 (2009) 459-464.

Appendices

Appendix A. List of chemicals and gases used in experiments

Solids and liquids (solution)

Name	Supplier	Purity and other information
$Ni(NO_3)_2 \cdot 6H_2O$	Sigma-Aldrich	Assay>99.8%
$Al(NO_3)_3 \cdot 9H_2O$	Fisher Scientific	Assay>99%
$Pd(NO_3)_2$ solution	Johnson-Matthey	Assay 8.16%
$Rh(NO_3)_3$ solution	Johnson-Matthey	Assay 8.16%
$Pt(NH_3)_4(NO3)_2$	Sigma-Aldrich	99.9995% metals basis
NaOH	Sigma-Aldrich	Reagent Grade≥98%
Na_2CO_3	Fisher Scientific	Assay>99.8%
KCl	Fisher Scientific	>99%
HNO_3	Fisher Scientific	73%
Buffer solution 4.0	Fisher Scientific	pH=4 Reagent
Buffer solution 7.0	Fisher Scientific	pH=7 Reagent
Buffer solution 10.0	Fisher Scientific	pH=10 Reagent
Acetone	Fisher Scientific	>99%
Methanol	Fisher Scientific	>99.9%

Gas

Name	Supplier	Purity and other information
Ar	BOC	Zero Grade (N5.0)>99.999%
H_2	BOC	CP Grade (N5.0)>99.999%
CH_4	BOC	CP Grade (N2.5)>99.5%
CO	BOC	CP Grade (N3.0)>99.9%
CO/Ar	BOC	10% CO in Ar
CO_2/Ar	BOC	40% CO_2 in Ar
He	BOC	Pure shield grade
Air	IAT Building	Compress air line

Appendix B. List of CP method prepared LDHs

Sample name	CP temp (ºC)	Aging time (h)	Metal molar ratio (%)			Crystallite size (nm) [a]	Phase (XRD)	Lattice parameter (Å)		Characterisation result (Figure in this thesis)			
			A	Ni	Al			*a*	*c*	XRD	SEM	TGA	FTIR
NiAl(2:1)40	40	4	-	64.6	35.4	13.3	LDH	2.974	22.694	3.2	-	-	-
NiAl40	40	4	-	72.8	27.2	16.2	LDH	3.036	23.091	3.2	3.5	3.6	6.7
NiAl70	70	4	-	72.4	27.6	23.8	LDH	3.034	23.087	3.2	-	-	-
NiAl70L	70	24	-	72.6	27.4	27.7	LDH	3.031	23.081	3.2	3.5	-	-
Pd(0.3)NiAl40	40	4	0.3	72.4	27.3	14.5	LDH	3.039	23.128	5.3	-	-	-
Pd(0.6)NiAl40	40	4	0.6	72.3	27.1	12.2	LDH	3.045	23.134	5.3	-	-	-
Pd(1.3)NiAl40	40	4	1.3	71.7	27.0	9.9	LDH	3.048	23.136	5.3	3.5	3.6	6.7
Pd(1.9)NiAl40	40	4	1.9	71.2	26.9	9.1	LDH	3.053	23.141	5.3	-	-	-
Pd(2.3)NiAl40	40	4	2.3	70.9	26.8	8.6	LDH	3.055	23.146	5.3	-	-	-
Pd(4.0)NiAl40			4.0	69.8	26.2	7.7	LDH	3.061	23.150	5.3	-	-	-
Pd(1.6)NiAl70	70	4	1.6	71.5	26.9	12.8	LDH	3.049	23.139	3.2	-	-	-
Pd(1.8)NiAl70L	70	24	1.8	71.3	26.9	20.2	LDH	3.052	23.144	3.2	-	-	-
Pd(2.1)NiAl70B	70	100°C/0.5	2.1	71.2	26.7	24.1	LDH	3.057	23.149	3.2	-	3.6	-
Rh(0.5)NiAl40	40	4	0.5	72.6	26.9	15.3	LDH	3.040	23.106	5.3	-	-	-
Rh(1.1)NiAl40	40	4	1.1	72.2	26.7	11.5	LDH	3.042	23.118	5.3	3.5	3.6	6.7
Rh(1.6)NiAl40	40	4	1.6	71.8	26.6	10.1	LDH	3.047	23.122	5.3	-	-	-
Rh(2.1)NiAl40	40	4	2.1	71.4	26.5	9.6	LDH	3.049	23.129	5.3	-	-	-
Rh(3.1)NiAl40	40	4	3.1	70.6	26.3	8.3	LDH	3.052	23.134	5.3	-	-	-
Rh(4.2)NiAl40	40	4	4.2	69.5	26.3	8.9	LDH	3.058	23.142	5.3	-	-	-
Rh(1.1)NiAl70	70	4	1.1	72.3	26.6	14.3	LDH	3.041	23.114	3.2	-	-	-
Rh(1.1)NiAl70L	70	24	1.1	72.2	26.7	21.9	LDH	3.031	23.109	3.2	-	-	-
Pt(0)NiAl40	40	4	0	72.5	27.5	14.0	LDH	3.038	23.089	3.2	-	-	-
Pt(0.1)NiAl70B	70	100°C/0.5	0.1	72.6	27.3	26.5	LDH	3.036	23.081	3.2	-	-	-

[a] Mean value obtained from reflections (003) and (006), ref ICDD 001-015-0087.

Appendix C. List of sol/nitric acid attack method prepared LDHs

Sample name	Parent LDH (raw-LDH)	Relative quantity of nitric acid applied	Metal molar ratio (%)			Crystallite size (nm) [a]	Phase (XRD)	Lattice parameter (Å)		Characterisation result (Figure in this thesis)			
			A	Ni	Al			*a*	*c*	XRD	SEM	TGA	FTIR
NA(1.0)-NiAl40	NiAl40	1.0	-	72.6	27.4	6.1	LDH	3.037	25.317	6.2	6.5	6.8	6.7
NA(1.1)-NiAl40	NiAl40	1.1	-	72.4	26.6	5.5	LDH, $Ni(NO_3)_2$	-	-	6.3	-	-	-
NA(1.2)-NiAl40	NiAl40	1.2	-	72.2	26.8	4.6	LDH, $Ni(NO_3)_2$	-	-	6.3	-	-	6.7
NA(0.85)-Pd(1.2)NiAl40	Pd(1.3)NiAl40	0.85	1.2	71.6	27.2	5.2	LDH	3.050	25.331	6.2	6.5	6.8	-
NA(0.9)-Pd(1.0)NiAl40	Pd(1.3)NiAl40	0.9	1.1	71.5	27.4	4.8	LDH, $Ni(NO_3)_2$	-	-	6.3	-	-	-
NA(0.88)-Rh(1.0)NiAl40	Rh(1.1)NiAl40	0.88	1.0	72.2	26.8	5.7	LDH	3.043	25.328	6.2	6.5	6.8	6.7

[a] Mean value obtained from reflections (003) and (006), ref ICDD 001-015-0087.

Appendix D. List of calcined catalysts derived from LDHs prepared by CP method

Sample name	Calcination temp (°C)	Calcination time (h)	Crystallite Size (nm) [a]	Phase (XRD, TPR)	Lattice parameter *a* (Å)	BET SA (m^2/g)	Characterisation result (Figure in this thesis)				Self-activation Test
							XRD	SEM	TEM	TPR	
NiAl40(2:1)-C550	550	4	11.0	Ni(Al)O	4.104	146.4	3.4	-	-	3.7	-
NiAl40-C450	450	4	10.9	Ni(Al)O	4.165	173.6	4.3	-	3.11	4.5	-
NiAl40-C550	550	4	13.5	Ni(Al)O	4.159	137.7	4.3	6.6	-	4.5	7.3
NiAl40-C550L	550	20	16.2	Ni(Al)O	4.156	123.6	4.4	-	-	-	-
NiAl40-C700	700	4	15.7	Ni(Al)O	4.151	115.9	4.3	-	-	4.5	-
NiAl40-C1000	1000	4	24.8 (NiO)	NiO, $NiAl_2O_4$	4.188 (NiO)	85.72	4.3	-	-	4.7	-
NiAl70-C550	550	4	14.2	NiO	4.153	135.4	3.4	-	-	3.8	-
NiAl70L-C550	550	4	14.6	NiO	4.151	129.2	3.4	-	3.11	3.8	-
Pd(0.3)NiAl40-550	550	4	11.1	NiO	4.173	-	5.4	-			-
Pd(0.6)NiAl40-550	550	4	9.6	NiO	4.186	-	5.4	-			-
Pd(1.3)NiAl40-C450	450	4	5.2	Pd/Ni(Al)O	4.181	202.1	4.3	-	-	4.5	-
Pd(1.3)NiAl40-C550	550	4	8.4	Pd/Ni(Al)O	4.186	184.9	4.3	-	-	4.5	7.3
Pd(1.3)NiAl40-C700	700	4	9.6	Pd/Ni(Al)O	4.176	157.3	4.3	-	-	4.5	-
Pd(1.3)NiAl40-C1000	1000	4	28.7(NiO)	PdO, NiO, Pd/NiO, Pd/Ni(Al)O,	4.192 (NiO)	102.1	4.3	-	-	4.7	-
Pd(1.9)NiAl40-550	550	4	7.2	Pd/Ni(Al)O	4.184	-	5.4	-	-	5.12	-
Pd(2.3)NiAl40-550	550	4	6.2	PdO, Pd/Ni(Al)O	4.187	-	5.4	-	-	5.12	-
Pd(4.0)NiAl40-550	550	4	5.0	Pd/Ni(Al)O	4.188	-	5.4	-	-	5.12	-

Sample name	**Calcination temp (°C)**	**Calcination time (h)**	**Crystallite Size (nm)** [a]	**Phase (XRD, TPR)**	**Lattice parameter *a* (Å)**	**BET SA (m^2/g)**	**Characterisation result (Figure in this thesis)**				**Self-activation Test**
							XRD	SEM	TEM	TPR	
Pd(1.6)NiAl70-C550	550	4	7.7	Pd/Ni(Al)O	4.188	188.0	3.4	-	-	3.10	-
Pd(1.8)NiAl70L-C550	550	4	6.9	Pd/Ni(Al)O	4.197	208.6	3.4	-	-	3.10	-
Pd(2.1)NiAl70B-C550	550	4	6.2	PdO, Pd/Ni(Al)O,	4.201	217.2	3.4	-	-	3.10	-
Rh(0.5)NiAl40-550	550	4	10.8	Rh/Ni(Al)O	4.164	-	5.4	-	-	5.12	-
Rh(1.1)NiAl40-C450	450	4	6.7	Rh/Ni(Al)O	4.173	194.7	4.3	-	-	4.5	-
Rh(1.1)NiAl40-C550	550	4	9.7	Rh/Ni(Al)O	4.177	179.5	4.3	-	-	4.5	7.3
Rh(1.1)NiAl40-C700	700	4	10.8	Rh/Ni(Al)O	4.168	146.2	4.3	-	-	4.5	-
Rh(1.1)NiAl-C1000	1000	4	22.7 (NiO)	Rh/NiO, Rh/$NiAl_2O_4$	4.186 (NiO)	91.3	4.3	-	-	4.7	-
Rh(1.6)NiAl40-550	550	4	7.6	Rh/Ni(Al)O	4.179	-	5.4	-	-	5.12	--
Rh(2.1)NiAl40-550	550	4	6.8	Rh/Ni(Al)O	4.175	-	5.4	-	-	5.12	-
Rh(3.1)NiAl40-550	550	4	6.1	Rh/Ni(Al)O	4.171	-	5.4	-	-	5.12	-
Rh(4.2)NiAl40-550	550	4	5.6	Rh/Ni(Al)O	4.166	-	5.4	-	-	5.12	-
Rh(1.1)NiAl70-C550	550	4	10.2	Rh/Ni(Al)O	4.175	4.175	3.4	-	-	3.9	-
Rh(1.1)NiAl70L-C550	550	4	12.8	Rh/Ni(Al)O	4.172	4.172	3.4	-	-	3.9	-

[a] Mean values obtained from reflections (111), (200) and (220): ref ICDD 47-1049

Appendix E. List of calcined catalysts derived from LDHs prepared by sol/nitric acid attack method

Sample name	**Calcination temp (°C)**	**Calcination time (h)**	**Crystallite Size (nm)** [a]	**Phase (XRD, TPR)**	**Lattice parameter *a* (Å)**	**Characterisation result (Figure in this thesis)**				**Self-activation Test**
						XRD	SEM	TEM	TPR	
NA(1.0)-NiAl40-C550	550	4	11.2	Ni(Al)O	4.152	6.9	6.6	6.11	6.12	7.3
NA(1.1)-NiAl40-C550	550	4	-	Ni(Al)O, NiO	-	6.10	-	-	-	-
NA(1.2)-NiAl40-C550	550	4	-	Ni(Al)O, NiO	-	6.10	-	-	-	-
NA(0.85)-Pd(1.2)NiAl40-C550	550	4	7.8	Pd/Ni(Al)O	4.183	6.9	-	-	6.12	7.3
NA(0.9)-Pd(1.0)NiAl40-C550	550	4	-	Pd/Ni(Al)O, (Pd)/NiO, NiO, PdO	-	6.10	-	-	-	-
NA(0.88)-Rh(1.0)NiAl40-C550	550	4	9.2	Rh/Ni(Al)O	4.174	6.9	-	-	6.12	7.3

[a] Mean values obtained from reflections (111), (200) and (220): ref ICDD 47-1049

Appendix F. List of reduced catalysts derived from LDHs prepared by CP method

Sample name[a]	Lattice parameter *a* (Å)	Characterisation result (Figure in this thesis)					Catalytic study result (Figure in this thesis)		
		XRD	SEM	TEM	FTIR	EDX[b]	Activity test	Stability test	DSS-like test
NiAl40(2:1)-C550-700	-	-	-	-	-	-	3.12	-	-
NiAl40-C450-700	-	-		-	-	-	4.9	-	-
NiAl40-C550-700	3.514	5.5	6.6	5.6	5.11	-	3.12 (4.9)	7.1	7.4, 7.5
NiAl40-C550L-700	-	-	-	-	-	-	4.9	-	-
NiAl40-C700-700	-	-	-	-	-	-	4.9	-	-
NiAl70-C550-700	-	-	-	-	-	-	3.12	-	-
NiAl70L-C550-700	-	-	-	3.11	-	-	3.12	-	-
Pd(0.3)NiAl40-550-700	-	-	-	-	-	-	5.13	-	-
Pd(0.6)NiAl40-550-700	3.529	5.5	-	-	5.11	-	5.13	-	-
Pd(1.3)NiAl40-C450-700	-	-	-	-	-	-	4.10	-	-
Pd(1.3)NiAl40-C550-700	3.538	5.5	-	5.6	5.11	5.7	3.15 (4.10)	7.1	7.5
Pd(1.3)NiAl40-C700-700	-	-	-	-	-	-	4.10	-	-
Pd(1.9)NiAl40-550-700	-	-	-	-	-	-	5.13	-	-
Pd(2.3)NiAl40-550-700	-	-	-	-	5.11	-	5.13	-	-
Pd(4.0)NiAl40-550-700	3.541	5.5	-	5.6	5.11	5.9	5.13	-	-
Pd(1.8)NiAl70L-C550-700	-	-	-	-	-	-	3.15	-	-
Pd(2.1)NiAl70B-C550-700	-	-	-	-	-	-	3.15	-	-
Rh(0.5)NiAl40-550-700	3.516	5.5	-		5.11	-	5.13	-	-
Rh(1.1)NiAl40-C450-700	-	-	-	-		-	4.11	-	-
Rh(1.1)NiAl40-C550-700	3.521	-	-	-	5.11	5.8	3.14 (4.11)	7.1	7.5
Rh(1.1)NiAl40-C700-700	-	-	-	-	-	-	4.11	-	-

Sample name[a]	Lattice parameter *a* (Å)	Characterisation result (Figure in this thesis)					Catalytic study result (Figure in this thesis)		
		XRD	SEM	TEM	FTIR	EDX[b]	Activity test	Stability test	DSS-like test
Rh(1.6)NiAl40-550-700	-	-	-	-	-	-	5.13	-	-
Rh(2.1)NiAl40-550-700	-	-	-	-	5.11	-	5.13	-	-
Rh(3.1)NiAl40-550-700	-	-	-	-	-	-	5.13	-	-
Rh(4.2)NiAl40-550-700	3.554	5.5	-	5.6	5.11	5.10	5.13	-	-
Rh(1.1)NiAl70-C550-700	-	-	-	-	-	-	3.14	-	-
Rh(1.1)NiAl70L-C550-700	-	-	-	-	-	-	3.14	-	-

a. All catalysts are reduced at 700ºC for1h.
b. For elemental mapping.

Appendix G. List of reduced catalysts derived from LDHs prepared by sol/nitric acid attack method

Sample name[a]	Characterisation result (Figure in this thesis)		Catalytic study result (Figure in this thesis)		
	SEM	TEM	Activity test	Stability test	DSS-like test
NA(1.0)-NiAl40-C550-R700	6.6	6.11	6.13	7.1	7.5
NA(0.85)- Pd(1.2)NiAl40-C550-R700	-	-	6.14	7.1	7.5
NA(0.88)- Rh(1.0)NiAl40-C550-R700	-	-	6.15	7.1	7.5

a. All catalysts are reduced at 700ºC for1h.